

The effects of sulfur on heteroleptic copper (I) complexes for the potential application in light emitting electrochemical cells

Inauguraldissertation

zur

Erlangung der Würde eines Doktorats der Philosophie

vorgelegt der

Philosophisch-Naturwissenschaftlichen Fakultät

der Universität Basel

von

Isaak Nohara

2022

Originaldokument gespeichert auf dem Dokumentenserver der Universität Basel
edoc.unibas.ch

Genehmigt von der Philosophisch-Naturwissenschaftlichen Fakultät auf Antrag von

Prof. Dr. Edwin C. Constable

Prof. Dr. Oliver Wenger

Prof. Dr. Jean-François
Nierengarten

Basel, den 21. September 2021

Prof. Dr. Marcel Mayor

Dekan

2

“Put sulfur in [the molecule] and it does something interesting.”

Prof. Dr. Edwin C. Constable

Acknowledgements

First of all, I would like to thank Prof. Dr. Catherine Housecroft and Prof. Dr. Edwin Constable for four wonderful years in their group. You always showed a lot of warmth and heart and your door was always open to talk and discuss. I remember the first year when Catherine and I spent hours upon hours assigning the NMR spectra of my first complexes. Although that was not particularly easy, it had a huge impact on future assignments. Furthermore, to witness the accumulated knowledge between the two of you, particularly in the subgroup meetings, was a true inspiration. You understood to motivate and push people in the right direction, each at their own pace. Even during the last year, which certainly was not the easiest in terms of organization, you put the health of the group members first and encouraged working in the home office whenever possible – something that I think a lot of supervisors did not pursue as diligently. Despite the spatial separation of workplaces, the communication during the time of the pandemic was smooth and the feeling that we always had the open door to come to you with a question or a concern was always there. I think this is not necessarily a given and deserves another huge ‘thank you’.

A big thank you goes to Prof. Dr. Oliver Wenger and Prof. Dr. Jean-François Nierengarten, who agreed to be my co-examiners in the first six months of my PhD without having any idea where the project would be going. Furthermore, I want to thank Prof. Dr. Christof Sparr, who agreed to be the chair of the exam on relatively short notice.

A huge thanks goes to all former and current member of the Constable – Housecroft group. My first supervisor was Dr. Jonas Schönle with a small Schlussversuchs project that got me interested in the general topic I would later pursue in my PhD. In my Wahlpraktikum Dr. Andreas Bünzli really opened up the field of luminescent compounds to me, which carried over to my master thesis, supervised by Dr. Cathrin Ertl and Dr. Alexanders Stephens. But not only were my supervisors great in capturing my interest, the whole group created such a friendly work environment that one instantly felt welcome. In that regard, I want to thank in particular the LEC subgroup, Dr. Sarah Keller, Dr. Fabian Brunner, Dr. Paola Forero – Cortes and Marco Meyer, it was a truly enjoyable experience working with you. Furthermore, I want to thank my newfound friends and especially Vanessa Wyss for accompanying me on my way.

I also want to especially mention Dr. Mariia Becker. We started our PhD at the nearly same time and when I look back at the past four years, it was always a pleasure discussing with her about every topic imaginable.

I want to thank Dr. Christina Wegeberg from the Wenger research group, for her support and measurements of the 77 K frozen matrix spectra. With her help we were able to improve the scope of this project immensely and the discussions with her in this regard were highly educational and interesting.

A big thank you goes to Dr. Alessandro Prescimone who was in charge of measuring all the X-ray structures and who gave me an introduction into making these measurements myself.

A big thank you goes to Sylvie Mittelheisser, Jonas Zurflüh and Michael Pfeffer, our analytics team, who were in charge of the EA and HR ESI-MS measurements and were always quick to help if there were any problems with the ESI-MS of the Constable – Housecroft group.

I want to thank Prof. Dr. Daniel Häussinger and his team Daniel Joss, Raphael Vogel and Pascal Rieder, for keeping the NMR machines running and helping with more special experiments, that would be difficult to carry out ourselves.

I want to thank Prof. Dr. Catherine Housecroft, Dr. Paola Forero – Cortes, Dr. Christina Wegeberg, Marco Meyer, Aramis Keller and Ricky Duff for proofreading my PhD thesis.

I want to thank my four Wahlpraktikums students, Zlatko Jovov, Aramis Keller, Philip Meyer and especially Fabian Schürch, who decided to do his Master's thesis in the Constable – Housecroft group. Their work, although often difficult, yielded valuable data and allowed more detailed insight into the mechanisms of my PhD project.

I want to thank Beatrice Erismann, who organized a lot and could help with every administrative task imaginable. Additionally, it was a pleasure, drinking coffee and talking about so many different things with her in the mornings. Thank you also to Isa Worni, who took over Beatrice's administrative tasks later in my PhD.

Thank you to Dr. Henk Bolink and his team, especially Dr. Michele Sessolo and Christina Momblona, at the university of Valencia for building and measuring the LEC device.

To the Werkstatt-team, Markus Ast, Pascal Andrek, Andreas Sohler, Andreas Koller and Hisni Meha goes a special shout out, without their support, a lot of things could not have been fixed in a timely manner. Furthermore, a big thank you to Marcus Hauri, Susanne Foley and Oliver Ilg who are in charge of ordering the chemicals and lab equipment we need. They really are the backbone of our research community.

My gratitude also extends to my two best friends, Simon Loosli and Philip Helbling. Simon has been accompanying me since the first year of apprenticeship and even if we did not have the opportunity to meet so often over the last years, I always knew he was there. Philip has been a great friend over the last decade and has been a great support throughout.

Of course, a big 'Thank you' also goes to my parents, Simone and Claudio Nohara, who always supported my decisions, and instilled that curiosity that ultimately led to me pursuing this PhD. To my sisters, with whom I laughed and argued my whole life, I extend my gratitude as well.

I also cannot thank my roommates Celine Döbelin, Benjamin Schmidlin and Aramis Keller enough. It was a great thing to know you were around during this last months. I could not wish for better roommates.

I want to thank Dan Reilly for talking to me nearly every day over the last eight months, taking my fear and anxiousness serious and calm me down when needed.

Last but not least, I want to thank the people from the Puerto Lobos Discord server, who were always around when help was needed, who created little distractions and were always kind and supportive, no matter the issue.

List of abbreviations

°	degree
°C	degree Celsius
Å	Ångström ($1 \text{ Å} = 10^{-10} \text{ m}$)
a,b,c	unit cell axes
acac	acetylacetone / acetylacetonate
ACQ	aggregation caused quenching
Alq ₃	<i>tris</i> (-8-quinolinolato)aluminium(III)
BDOH-PF	poly(9,9-bis(3,6-dioxaheptyl)-fluorene-2,7-diyl)
bdpp	1,2-bis(diphenylphosphane)benzene
BINAP	2'-bis(diphenylphosphano)-1,1'-binaphthalene
bpy	2,2'-bipyridine
Br ₂ phen	dibromo-1,10-phenanthroline
cd	candela
Cl ₂ phen	dichloro-1,10-phenanthroline
cm	centimetre
COSY	correlation spectroscopy
CRI	colour rendition index
CSD	Cambridge Structural Database
CV	cyclic voltammogram
d	doublet (NMR)
Dc	calculated density
dd	doublet of doublet (NMR)
ddd	doublet of doublet of doublet (NMR)
DFT	density functional theory
dm	decimetre
dpe	<i>cis</i> -1,2-bis-(diphenylphosphino)ethylene
dppdtbpf	1-diphenylphosphino-10-di-tert-butylphosphinoferrocene
dt	doublet of triplets (NMR)
e ⁻	electron
e.g.	for example
ECA	exciton-charge annihilation
ECDM	electrochemical doping model
EDL	electric double layer
EDM	electrodynamic model
EIL	electron injection layer
$E_{1/2}^{\text{ox}}$	oxidation potential
E_{pa}	anodic peak potential
E_{pc}	cathodic peak potential
eqv.	equivalent
eq.	equation

EQE	external quantum yield
ESI-MS	electrospray ionisation mass spectrometry
<i>et al.</i>	and others
Et ₂ O	diethyl ether
Etbpy	6-ethyl-2,2'-bipyridine
ETL	electron transport layer
EtO	ethoxy
EtObpy	6-ethoxy-2,2'-bipyridine
EtS	ethylsulfanyl
EtSbpy	6-ethylsulfanyl-2,2'-bipyridine
eV	electron Volt
EXSY	exchange spectroscopy
Fc/Fc ⁺	ferrocene/ferrocenium
h ⁺	hole
HIL	hole injection layer
HMBC	heteronuclear multiple-bond correlation spectroscopy
HMQC	heteronuclear multiple quantum coherence spectroscopy
HOMO	Highest Occupied Molecular Orbital
HR ESI-MS	high resolution electrospray ionisation mass spectrometry
HTL	hole transport layer
IC	internal conversion
IPr	1,3-bis(2,6-di- <i>iso</i> -propylphenyl)imidazole-2-ylidene
<i>i</i> PrSPy	2-((<i>iso</i> -propylsulfanyl)methyl)pyridine
IQE	internal quantum efficiency
irrev	irreversible
ISC	inter system crossing
iTMC	ionic transition metal complex
<i>J</i>	coupling constant
K	Kelvin
<i>K</i> _d	dissociation constant
kg	kilogram
LEC	light emitting electrochemical cell
LED	light emitting diode
lm	lumen
LUMO	Lowest Unoccupied Molecular Orbital
M	molar (mol/litre)
m	multiplet (NMR)
Me ₂ bpy	6,6'-dimethyl-2,2'-bipyridine
Mebpy	6-methyl-2,2'-bipyridine
MeCN	acetonitrile
MeO	methoxy
MeObpy	6-methoxy-2,2'-bipyridine

MeS	methylsulfanyl
MeSbpy	6-methylsulfanyl-2,2'-bipyridine
MeSPy	2-((methylsulfanyl)methyl)pyridine
Me-THF	2-methyltetrahydrofuran
MeThMePy	2-(5-methylthiophen-2-yl)-6-methylpyridine
MeThPy	2-(5-methylthiophen-2-yl)pyridine
Mg	mega-gram
MHz	mega-Hertz
min	minute
MLCT	metal to ligand charge transfer
mmol	milli-mol
ms	milli-second
ⁿ Bu	<i>n</i> -butyl
NCS	thiocyanate / thiocyanato
n-doped	negative doped
NHC	N-heterocyclic carbene
nm	nano-meter
NMR	Nuclear Magnetic Resonance (spectroscopy)
NOESY	nuclear Overhauser effect spectroscopy
ns	nano-second
OLED	organic light emitting diode
p-doped	positive doped
PECDM	preferential electrochemical doping model
PEO	poly(ethylene oxide)
PET	poly(ethylene terephthalate)
Ph	phenyl
PJ	peta-joule
PLEC	polymer light emitting electrochemical cell
PLQY	photoluminescence quantum yield
PMMA	poly (methyl methacrylate)
POP	<i>bis</i> (2-(diphenylphosphano)phenyl)
PPh ₂	diphenylphosphano
PPh ₃	triphenylphosphane
ppm	parts per million
ppy	phenyl pyridine
PtOEP	2,3,7,8,12,13,17,18-octaethyl-21H,23H-porphine platinum(II)
PVK	poly(<i>N</i> -vinylcarbazole)
Ref.	reference
RISC	reverse inter system crossing
ROESY	rotating-frame nuclear Overhauser effect spectroscopy
RSC	Royal Society of Chemistry

s	second, singlet (NMR)
S ₀	electronic ground state
S ₁	lowest -lying singlet excited state
SSL	solid state lighting
t	triplet (NMR)
T	temperature
T ₁	lowest-lying triplet excited state
t _{1/2}	device half lifetime
TADF	thermally activated delayed fluorescence
TAZ	3-(4'-tert-butylphenyl)-4-phenyl-5-(4''-biphenyl)-1,2,4-triazole
tBu	<i>tert</i> -butyl
tBuSPy	2-((<i>tert</i> -butylsulfanyl)methyl)pyridine
td	triplet of doublets (NMR)
TD-DFT	time dependent density functional theory
tfbp	tetrakis[3,5-bis(trifluoromethyl)phenyl]borate
THF	tetrahydrofuran
ThMepy	2-(thiophen-2-yl)-6-methylpyridine
ThPy	2-(thiophen-2-yl)pyridine
TTA	triplet-triplet annihilation
UV	ultra-violet
V	Volt
W	Watt
wt.	weight
xantphos	4,5-bis(diphenylphosphano)-9,9-dimethylxanthene
Z	number of formula units in the unit cell
α, β, γ	unit cell angles
δ	chemical shift
ε	molar extinction coefficient
λ	wavelength
λ _{exc}	excitation wavelength
λ _{em} ^{max}	emission maximum wavelength
λ _{abs} ^{max}	absorption maximum wavelength
μm	micro-meter
μs	micro-second
μW	micro-Watt

List of publications

Part of this work has been published.

I. Nohara, A. Prescimone, D. Häussinger, C. E. Housecroft, and E. C. Constable, *RSC Adv.*, 2019, 9, 13646–13657. DOI: 10.1039/c9ra02617g

I. Nohara, A. Keller, N. Tarassenko, A. Prescimone, E. C. Constable, and C. E. Housecroft, *Inorganics.*, 2020, 8, 4. DOI: 10.3390/inorganics8010004

I. Nohara, A. Prescimone, C. E. Housecroft, and E. C. Constable, *Inorganics.*, 2019, 7, 11. DOI: 10.3390/inorganics7010011

Material and Methods

^1H , $^{13}\text{C}\{^1\text{H}\}$ and $^{31}\text{P}\{^1\text{H}\}$ NMR spectra were recorded on a Bruker Avance 500 spectrometer at 298 K, unless otherwise stated. ^1H and ^{13}C NMR chemical shifts were referenced to the residual solvent peaks with respect to $\delta(\text{TMS}) = 0$ ppm and ^{31}P NMR chemical shifts with respect to $\delta(85\% \text{ aqueous } \text{H}_3\text{PO}_4) = 0$ ppm.

Solution absorption spectra were measured using a Shimadzu UV2600 spectrophotometer or an Agilent 8453 spectrophotometer. Solution emission spectra were recorded using a Shimadzu RF-5301PC spectrofluorometer or a Shimadzu RF-6000 spectrofluorometer. Quantum yields (CH_2Cl_2 solution and powder) were measured using a Hamamatsu absolute photoluminescence quantum yield spectrometer C11347 Quantaaurus-QY. Powder emission spectra as well as excited-state lifetimes for powders and CH_2Cl_2 solutions were measured with a Hamamatsu Compact Fluorescence lifetime Spectrometer C11367 Quantaaurus-Tau with an LED light source ($\lambda_{\text{exc}} = 340, 365$ or 405 nm). THF solution state and frozen matrix 2-Me-THF at 77 K emission spectra as well as excited-state lifetimes were obtained on an LP920-KS apparatus from Edinburgh Instruments. The excitation at 410 nm was performed by a frequency-tripled Nd:YAG laser (Quantel Brilliant, *ca.* 10 ns pulse width) equipped with a Rainbow optical parameter oscillator (OPO). The typical pulse energy was 6 mJ at 410 nm. A beam expander (GBE02-A from Thorlabs) was used to improve the excitation homogeneity in the detection volume. Detection of emission spectra (THF solution and at 77K) occurred on an ICCD camera (Andor), and the kinetic data at single wavelengths were recorded using a photomultiplier tube. Photophysical measurements were acquired on oxygen free solutions by either employing three freeze-pump-thaw cycles or minimum 15 min purging of the solution with Ar or N_2 .

A Shimadzu LCMS-2020 instrument or a Bruker esquire 3000plus was used to record electrospray (ESI) mass spectra; high resolution ESI (HR-ESI) mass spectra were measured on a Bruker maXis 4G QTOF instrument.

Electrochemical measurements used a CH Instruments 900B potentiostat or an Ametek Scientific Instruments VersaStat 3F with $[\text{Bu}_4\text{N}][\text{PF}_6]$ (0.1 M) as supporting electrolyte and a scan rate of 0.1 V s^{-1} ; the solvent was CH_2Cl_2 and solution concentrations were *ca.* $2 \times 10^{-3} \text{ mol dm}^{-3}$. The working electrode was glassy carbon, the reference electrode was a leakless Ag^+/AgCl (eDAQ ET069-1) and the counter-electrode was a platinum wire. Final potentials were internally referenced with respect to the Fc/Fc^+ redox couple.

Data collection of single crystals was carried out on an APEX-II diffractometer (Cu $\text{K}\alpha$ radiation) or using a STOE StadiVari diffractometer equipped with a Pilatus300K detector and with a Metaljet D2 source (Ga $\text{K}\alpha$ radiation). Data reduction, solution and refinement was achieved using SAINT¹, APEX or APEX2,² SuperFlip³, Crystals⁴, Olex or Olex2,⁵ ShelXT, ShelXL-2014/7⁶ or ShelXL-2018/3⁷. Structure analysis was carried out using Mercury CSD v. 3.5.1, 3.8, 4.1.0 or 4.3.1.⁸⁻¹⁰ A solvent mask¹¹ was used to treat the solvent region and all the numbers and formulae were adapted to keep account of the removed electrons. Disordered rings were refined as rigid bodies, and the disordered pyridine ring in $[\text{Cu}(\text{POP})(i\text{PrSPy})][\text{PF}_6]$ was refined isotropically.

The DFT calculations in Chapter 2 were performed with Spartan 16 (v. 2.0.10)¹². A 6-31G* basis set on all atoms was selected to optimize computer time. Initial geometry energy optimization was carried out at a semi-empirical (PM3) level.

Microwave reactions were carried out with a Biotage Initiator+ microwave reactor.

Chemicals were purchased Sigma-Aldrich, Acros Organics, Fluorochem, TCI, Alfa Aesar or Apollo Scientific and used as received. Inert reactions were carried out under N₂ atmosphere in flame dried glassware and the used dry solvents purchased from Acros Organics. All other reactions were carried out under normal conditions with reagent grade solvents. Analyses were carried out in HPLC grade solvents. Column chromatography was performed with Silicycle SiliaFlash P60 or with a Biotage Selekt with Biotage Sfar Silica HC D prepact columns.

[Cu(MeCN)₄][PF₆] was prepared according to the literature.¹³

Abstract

The aim of this project was the synthesis and characterisation of heteroleptic copper(I) compounds that emit light in the visible spectrum (400–800 nm), with the goal to incorporate these complexes as emitting species in light emitting electrochemical cells (LECs). LECs have several advantages when compared to organic light emitting diodes (OLEDs) and light emitting diodes (LEDs), and some challenges that need to be overcome before large scale applications can be considered. These advantages and challenges will be discussed in Chapter 1: Introduction, together with a brief overview over the history of lighting and an introduction to LEDs and OLEDs.

Typically, the cation in such a light emitting copper(I) complex consists of the copper centre, a diphosphane – in the case of this project the commercially available bis(2-(diphenylphosphano)phenyl) (POP) and 4,5-bis(diphenylphosphano)-9,9-dimethylxanthene (xantphos) – and a diimine such as 2,2'-bipyridine (bpy) or 1,10-phenanthroline (phen). Often, the bpy or phen carries alkylic or aromatic substituents.

The overarching theme of this project was the incorporation of heteroatom substituents into these complexes. In Chapter 2 sulfur replaces one of the chelating nitrogens, and thereby takes an active role in binding to the Cu(I) centre. The first series of complexes with only one aromatic ring (pyridine), did not show significant luminescence. The second series, which used a 2-(thiophen-2-yl)pyridine as a chelating ligand, featured a yellow emission in solid-state with photoluminescence quantum yields (PLQYs) up to 10.8% and a blue emission, with significant ligand-based contributions, in solution with PLQYs up to 33.2%.

Chapter 3 focuses on classical $[\text{Cu}(\text{P}^{\wedge}\text{P})(\text{N}^{\wedge}\text{N})][\text{PF}_6]$ compounds, with $\text{N}^{\wedge}\text{N}$ being a dibromo-1,10-phenanthroline. In this series of complexes, the influence of substituents in the 2- and 9-positions of the phen on the emission wavelength and PLQY are clearly visible. The complexes do not feature a PLQY >1% in deaerated CH_2Cl_2 solution, but in the solid state they are yellow to orange emitters with a PLQY up to 45%.

Chapter 4 investigates the influence of chalcogen substituents in the 1,10-phenanthroline backbone. The introduction of either alkylsulfanyl or alkoxy substituents has significant influence on the photophysical properties of the complexes. The complexes are yellow to orange emitters with a PLQY of up to 9.4% in deaerated CH_2Cl_2 solution and up to 60% in the solid state. 2,9-Alkylsulfanyl substituted phenanthrolines feature a notable blue shift compared to 3,8- and 4,7-substituted ones with a significantly higher PLQY. In the solid state these complexes exhibit excited state lifetimes in the μs regime with the longest being 19 μs . To investigate the nature of these emissions further measurement in a frozen matrix of 2-methyltetrahydrofuran at 77 K were carried out, where most of the complexes exhibited a considerable blue-shift and dual emission.

At the end of this work a short summary of the work at hand and a glance into the future of light emitting Cu(I) complexes and LECs awaits.

Table of Contents

Acknowledgements	4
List of abbreviations	6
List of publications	10
Material and Methods	11
Abstract	13
Table of Contents	14
Chapter 1: Introduction	18
1.1 Solid state lighting – towards higher power efficiency	18
1.1.1 LEDs	18
1.1.2 OLEDs	19
1.1.2a Fluorescence, Phosphorescence and Thermally Activated Delayed Fluorescence	20
1.1.2b Structure and working principle of OLEDs	22
1.1.2c Advantages and challenges of OLEDs	23
1.1.3 Light emitting electrochemical cells	24
1.1.3a Working mode of LECs	25
1.1.3b Challenges in designing LECs	27
1.1.3c Emissive compounds for LECs	30
Chapter 2: Replacing one chelating N with sulfur: [Cu(P [^] P)(N [^] S)][PF ₆] complexes	36
2.1 Motivation	36
2.2 Synthesis	37
2.2.1 Ligand synthesis	37
2.2.2 Complex synthesis	38
2.3 Spatial distribution of the HOMO and LUMO	39
2.4 Structural analysis	39
2.4.1 Solution NMR spectroscopic characterization	39
2.4.1a ³¹ P{ ¹ H} NMR experiments	39
2.4.2b ¹ H NMR experiments	40
2.4.2 Crystal structures	45
2.5 Electrochemistry	49
2.6 Photophysical properties	51
2.6.1 UV-VIS absorption spectra	51
2.6.2 Emission properties	52
	14

2.6.2a	Solution emission properties of [Cu(P [^] P)(N [^] S)]PF ₆ with 2-(alkylsulfanyl)pyridine ligands	52
2.6.2b	Solution emission properties of [Cu(P [^] P)(N [^] S)]PF ₆ with 2-(thiophen-2-yl)pyridine ligands	52
2.6.2c	Solid-state emission properties of [Cu(P [^] P)(N [^] S)]PF ₆ with 2-(alkylsulfanylmethyl)pyridine ligands	54
2.6.2d	Solid-state emission properties of [Cu(P [^] P)(N [^] S)]PF ₆ with 2-(thiophen-2-yl)pyridine ligands	54
2.6.2e	Testing of [Cu(xantphos)(ThPy)]PF ₆ thin film and LEC configuration	55
2.7	Investigation of the stability of [Cu(P [^] P)(N [^] S)]PF ₆ compounds in solution	55
2.7.1	The effect of added chloride ions on the solution absorption and ¹ H NMR spectra	55
2.7.2	Crystal structure of [Cu(xantphos)(MeCN) ₂][PF ₆] \cdot 0.5Et ₂ O	57
2.8	Conclusion	58
2.9	Experimental	59
2.9.1	Ligand Synthesis	59
2.9.1a	MeThMePy	59
2.9.2	Complex synthesis	59
2.9.2a	[Cu(POP)(iPrSPy)]PF ₆	59
2.9.2b	[Cu(xantphos)(iPrSPy)]PF ₆	60
2.9.2c	[Cu(POP)(tBuSPy)]PF ₆	60
2.9.2d	[Cu(xantphos)(tBuSPy)]PF ₆	60
2.9.2e	[Cu(POP)(ThPy)]PF ₆	61
2.9.2f	[Cu(xantphos)(ThPy)]PF ₆	61
2.9.2g	[Cu(POP)(ThMePy)]PF ₆	61
2.9.2h	[Cu(xantphos)(ThMePy)]PF ₆	61
2.9.2i	[Cu(POP)(MeThPy)]PF ₆	62
2.9.2j	[Cu(xantphos)(MeThPy)]PF ₆	62
2.9.2k	[Cu(POP)(MeThMePy)]PF ₆	62
2.9.2l	[Cu(xantphos)(MeThMePy)]PF ₆	63
Chapter 3:	Influencing the photophysical properties of [Cu(P [^] P)(N [^] N)]PF ₆ complexes with bromo-substituents on 1,10-phenanthroline	64
3.1	Motivation	64
3.2	Synthesis	65
3.3	Structural characterization	65
3.3.1	NMR spectroscopy	65
3.3.2	Crystal structures	68
		15

3.4 Electrochemistry	72
3.5 Photophysical properties	73
3.5.1 UV-Vis absorption spectra	73
3.5.2 Solution emission properties	73
3.5.3 Solid-state emission properties	75
3.6 Conclusion	76
3.7 Experimental	77
3.7.1 General synthesis procedures for Cu(I)-complex synthesis	77
3.7.1a [Cu(POP)(2,9-Br ₂ phen)][PF ₆]	77
3.7.1b [Cu(POP)(3,8-Br ₂ phen)][PF ₆]	77
3.7.1c [Cu(POP)(4,7-Br ₂ phen)][PF ₆]	77
3.7.1d [Cu(xantphos)(2,9-Br ₂ phen)][PF ₆]	78
3.7.1e [Cu(xantphos)(3,8-Br ₂ phen)][PF ₆]	78
3.7.1f [Cu(xantphos)(4,7-Br ₂ phen)][PF ₆]	78
Chapter 4: The effect of alkylsulfanyl and alkyloxy substituents on 1,10-phenanthroline on the photophysical and electrochemical properties of [Cu(P [^] P)(N [^] N)][PF ₆] complexes.	80
4.1 Motivation	80
4.2 Synthesis	81
4.2.1 Ligand synthesis	81
4.2.2 Complex synthesis	81
4.3 Structural characterization	81
4.3.1 NMR spectroscopy	81
4.3.2 Crystal structures	82
4.4 Electrochemistry	87
4.5 Photophysical properties	88
4.5.1 UV-Vis absorption spectra	88
4.5.2 Solution emission properties	90
4.5.2a Emission properties in THF solution and in frozen glass matrices at 77 K	93
4.5.3 Solid-state emission properties	94
4.5.4 Comparison of solid-state and 77 K frozen matrix emission measurements	95
4.6 Conclusion	95
4.7 Experimental	96
4.7.1 (MeS) ₂ phen ligand synthesis	96
4.7.1a 3,8-(MeS) ₂ phen	96

4.7.1b 4,7-(MeS) ₂ phen	97
4.7.2 (MeO) ₂ phen ligand synthesis	97
4.7.3 (EtS) ₂ phen ligand synthesis	97
4.7.3a 2,9-(EtS) ₂ phen	97
4.7.3b 3,8-(EtS) ₂ phen	97
4.7.3c 4,7-(EtS) ₂ phen	97
4.7.4 Complex synthesis	98
4.7.4a [Cu(POP)(2,9-(MeS) ₂ phen)][PF ₆]	98
4.7.4b [Cu(POP)(3,8-(MeS) ₂ phen)][PF ₆]	98
4.7.4.c [Cu(POP)(4,7-(MeS) ₂ phen)][PF ₆]	99
4.7.4d [Cu(xantphos)(2,9-(MeS) ₂ phen)][PF ₆]	99
4.7.4e [Cu(xantphos)(3,8-(MeS) ₂ phen)][PF ₆]	99
4.7.4f [Cu(xantphos)(4,7-(MeS) ₂ phen)][PF ₆]	99
4.7.4g [Cu(POP)(2,9-(MeO) ₂ phen)][PF ₆]	100
4.7.4h [Cu(POP)(3,8-(MeO) ₂ phen)][PF ₆]	100
4.7.4i [Cu(POP)(4,7-(MeO) ₂ phen)][PF ₆]	100
4.7.4J [Cu(xantphos)(2,9-(MeO) ₂ phen)][PF ₆]	101
4.7.4k [Cu(POP)(2,9-(EtS) ₂ phen)][PF ₆]	101
4.7.4l [Cu(POP)(3,8-(EtS) ₂ phen)][PF ₆]	101
4.7.4.m [Cu(POP)(4,7-(EtS) ₂ phen)][PF ₆]	102
4.7.4n [Cu(xantphos)(2,9-(EtS) ₂ phen)][PF ₆]	102
4.7.4o [Cu(xantphos)(3,8-(EtS) ₂ phen)][PF ₆]	102
4.7.4p [Cu(xantphos)(4,7-(EtS) ₂ phen)][PF ₆]	102
Conclusion and Outlook	104
Bibliography	107
Appendix	121

Chapter 1: Introduction

Life as we know it is bound to the perpetual cycle of day and night. Every organism on the surface of the earth follows the day-night cycle, driven by hormones. With the discovery and controlled use of fire some 500'000 years ago, humans began to break free from the confines of the natural light provided by the sun.¹⁴ Fire, be it from burning wood, oil, gas or another medium, was the only artificial light source for millennia to come. This began to change when in the 1830s the arc lamp proved that a constant light from an electric source was possible.¹⁵ Thus began the investigation of incandescent light bulbs. The first patent was filed in the United Kingdom by Joseph Swan for a carbon filament incandescent light bulb, operating in a partial vacuum in 1860. Thomas Edison, who is often mistakenly named the inventor of the incandescent light bulb, joined forces with Swan in 1883 to commercialize more efficient light bulbs, which Swan developed around 1880.¹⁶

Incandescent light bulbs emit light over the whole visible spectrum; hence, its colour rendering capabilities are remarkably high and its CRI (colour rendition index) value is close to 100. The big disadvantages of the light bulb are its comparatively short lifetime and its very low efficiency in converting electric energy to visible light. About 95% of the input electricity is wasted as infrared radiation. A more efficient method of creating light was developed with the fluorescent light tube by General Electric in 1937. The fluorescent tube uses electric discharges to excite mercury vapour which in turn emits ultraviolet (UV) light, which is converted into visible light by a phosphor coating on the inside of the tube. Its superior efficiency of typically 25% and its largely increased lifetime of 7,500–30,000 hours made it a strong competitor against the incandescent light bulb. Particularly, the commercialisation of the compact fluorescent lamps in the early 1980s was a strong contender against the light bulb.¹⁶ All the described light sources, from fire to the compact fluorescent lamp, have one thing in common: The emission of visible light is just a by-product, while the primary product is heat, thus leading to a huge unproductive use in energy. In Switzerland, artificial lighting is responsible for the electricity consumption of nearly 20 PJ (Peta-joule = 10^{15} Joule) in 2019. While this only represents 2.7% of the total amount of energy used, it is still an enormous quantity.¹⁷ Electricity consumption for lighting inside buildings on the globe has peaked in the year 2015 and is stagnating since then, due to the use of high efficiency lighting technologies.^{18,19} Switzerland has reduced its electricity consumption for lighting appliances by more than 20% or 5 PJ in the timespan between 2000 and 2019. Given that the majority of electricity on the globe is still produced by burning fossil fuels,²⁰ the use of more efficient devices is needed to diminish the use of electricity. This strategy can lead to a decrease in CO₂ emissions. It has to be said, however, that more efficient devices don't automatically lead to less CO₂ emissions, due to curtailment of renewable electricity.^{21,22}

1.1 Solid state lighting – towards higher power efficiency

1.1.1 LEDs

The report of solids emitting light predates the invention of the fluorescent tube by two decades. In 1907 H. J. Round reported the yellow – green emission of a carborundum (silicon carbide) crystal when a bias of only 10 V was applied. However, he also noted that only very few crystals emitted the light at this bias and only at 110 V a large number began to shine.²³ A young Russian by the name of Oleg Vladimirovich Losev made similar observations in his work with radio transmitters in 1920. In the following years he investigated the phenomenon and assembled what is nowadays recognized as the first LED.²⁴ The next

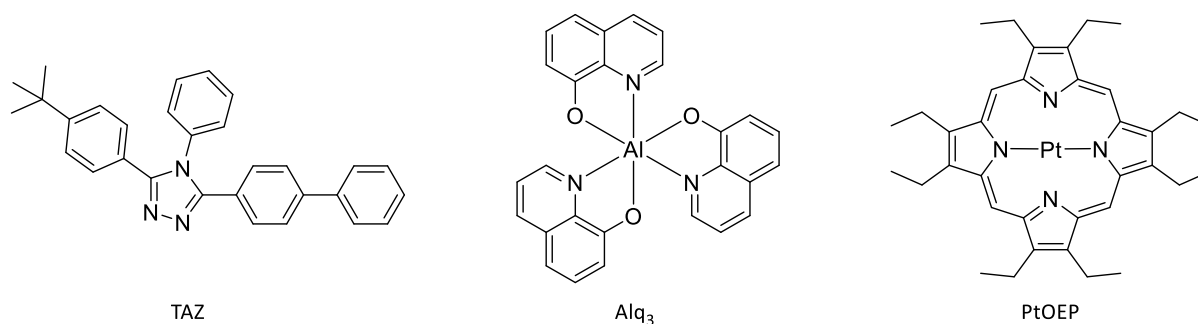
step in solid state lighting was made over thirty years after Losev's patent on a 'light relay' in 1929. In 1962 Holonyak and Bevacqua demonstrated the red light emission from a Ga(As_{1-x}P_x) inorganic diode.²⁵ However, the efficiency of this LED was very low and it would take about another 20 years and the implementation of quantum wells until these red LEDs reached an efficacy (lm/W) of 2 lm/W, which was about the same as Edison's first incandescent light bulb.^{16,26} With the development of blue light emitting InGaN LEDs in 1993 by Nakamura, the step to white light emitting diodes, and consequently making LEDs a viable alternative to traditional light sources, was not far away anymore. Nowadays there are a couple of ways to achieve white light emission from LEDs. Since the diodes themselves only emit in a narrow bandgap the white light cannot be achieved by one single type of semiconductor. Instead, two general approaches are used to generate white light from LEDs. In the first, phosphors are used to downconvert wavelengths of higher energy light. This allows the fabrication of relatively cheap devices. The second approach is the combination of LEDs with different primary colours, with each LED controlled independently.¹⁴ In contrast to fire, light bulbs and fluorescent tubes, the light emission in LEDs is not a product of heating or an electric discharge, but the primary product of the applied bias and their efficiency is consequently higher. During the last decade the typical efficacy of LEDs has increased by about 6-8 lm/W each year and surpassed the average efficacy of linear fluorescent tubes in 2019.¹⁸

LEDs are nowadays found in a multitude of applications, ranging from normal lighting devices to the use as a backlight in liquid crystal displays (LCDs), lighting to support plant growth in green houses and some applications in medicine.²⁷

1.1.2 OLEDs

Ten years before Holonyak *et al.* reported their red emitting inorganic diode,²⁵ luminescence in organic materials was demonstrated by Bernanose *et al.* with the luminescence of an acridine orange doped cellulose film.²⁸ Around the same time as the red LED was reported, Pope, Kallmann, and Magnante described the luminescence in a single crystal of anthracene, however they needed high voltages for the luminescence to occur.²⁹ Because of the needed high electric field, the low luminance and low efficiency, the interest in the emission of organic molecules was mostly scientific and not geared towards practical applications. This began to change when Tang and VanSlyke reported a device in 1987 with a high luminance at relatively low driving voltages (up to 1000 cd/m² at 10 V). With 100 cd/m² and a driving voltage of 5.5 V, the power conversion efficiency of this device was still only 0.46% with 1.5 lm/W, but this already represented a nearly tenfold increase in efficiency.^{30,31} With the inclusion of a hole transport layer using an aromatic diamine they laid the basis for the future, highly complex multilayer design of OLEDs. With the report of this device the field of OLEDs began to attract more attention, not only from the academic community, but also from industry. With the first report of a white light emitting OLED in 1994 by Kido *et al.*,³² OLEDs became interesting for lighting applications and – using colour filters – full colour displays. Kido built on and expanded on the foundation of Tang's and VanSlyke's group and included multiple additional layers. In contrast to VanSlyke and Tang, they didn't employ a separate hole transporting layer, instead they used doped poly(*N*-vinylcarbazole) (PVK) as a combined hole transport and emitting layer. However, they introduced an electron injection layer using Alq₃ (*tris*-(8-quinolinolato)aluminium(III)) and a hole blocking, electron transporting 3-(4'-*tert*-butylphenyl)-4-phenyl-5-(4''-biphenyl)-1,2,4-triazole (TAZ) layer (Scheme 1.1). Although the power to light conversion efficiency was lower than for VanSlyke's device, with 0.83 lm/W at 10 V with a luminance of 50 cd/m², it was still a

significant step forward, since the white light emission could be used in applications such as a backlight in LCD displays.³² In their report, Kido *et al.* stated that the doping of the emitting layer with several fluorescent type dyes via vacuum deposition is quite challenging, since multiple evaporation processes need to be controlled simultaneously. As an alternative they give doped polymer layers, in which any number of fluorescent dyes can be mixed with a polymer solution and applied onto the OLED with simple coating methods. Despite this, vacuum evaporation techniques are still the most common way to prepare the different layers in OLEDs to this day.³¹ While the device of Tang and VanSlyke used four separate layers, Kido already increased this number to six. Indeed, to achieve the highest possible external quantum efficiency (EQE), up to 15 distinct layers are nowadays employed.^{33,34}



Scheme 1.1: Structure of compounds used in a) electron transporting layers 3-(4'-tert-butylphenyl)-4-phenyl-5-(4''-biphenyl)-1,2,4-triazole (TAZ), b) emissive and host compound (tris(8-quinolinolato)aluminium(III)) (Alq₃), and c) guest emitter 2,3,7,8,12,13,17,18-octaethyl-21H,23H-porphine platinum(II) (PtOEP).

1.1.2a Fluorescence, Phosphorescence and Thermally Activated Delayed Fluorescence

When a molecule absorbs light it reaches an excited state, and from there are several deactivation processes that can occur. Via internal conversion the molecule will lose a certain amount of some energy until it reaches the S_1 or – via inter system crossing (ISC) – the T_1 state from where it can either decay non-radiatively or under the emission of light (Figure 1.1).

At this point it may be prudent to talk about selection rules. For electronic transitions, two main principles must be obeyed. The first is the conservation of the electronic spin during an electronic transition, the second is that there must be a change in parity of the involved orbitals (Laporte rule). Effectively that means only $s \rightarrow p$, $p \rightarrow d$ and $d \rightarrow f$ transitions are allowed. While these rules must be obeyed, there are certain effects that mix electronic states and make formerly forbidden transitions ‘allowed’.³⁵ The coupling of spin and angular momentum (spin–orbit coupling) plays an important role, especially for heavier d -block metals, since its effect is strongly dependent on the effective nuclear charge (‘heavy atom effect’,³⁶ equation (eq.) 10 in reference 37). For first row transition metals this effect is therefore not very dominant, instead ‘vibronic coupling’ an effect where the symmetry of the molecules is disturbed by the molecular vibration, makes the mixing of states temporarily possible. This effect is stronger in non-centrosymmetric (e.g. tetrahedral) than in centrosymmetric (e.g. octahedral) compounds.³⁵

Fluorescence describes spin allowed transitions, typically relaxation of the excited S_1 state back to the ground state S_0 under the emission of a photon. In purely fluorescent compounds, the excited state lifetime is very short (picosecond to the nanosecond regime). In contrast, phosphorescence is the spin forbidden transition of an electron from a, relative to the singlet excited state, long-lived triplet excited

state. Because the transition is of spin forbidden of nature, the excited state lifetimes of the T_1 state is usually much longer than for the S_1 state and non-radiative decay mechanisms have a higher probability to occur. As described above, the use of heavy metal atoms which feature large spin-orbit coupling constants,³⁸ such as Pt or Ir, facilitate intersystem crossing and mix the triplet and singlet states, thereby making the transition more allowed (Figure 1.1).^{39–41}

Because of the statistical distribution of singlet and triplet excitons (bound electron-hole pair, with the electron in an excited state) of 1:3, the internal quantum yield (IQE) of a fluorophore cannot exceed 25%. This also sets an inherent limitation on OLEDs using purely fluorescent compounds. This problem was addressed with the report of the first phosphorescent OLED in 1998 by Baldo *et al.* They found that with the introduction of 2,3,7,8,12,13,17,18-octaethyl-21H,23H-porphine platinum(II) (PtOEP) (Scheme 1.1) into an Alq₃ host matrix that would transfer energy onto the phosphorescent compound, they could increase the EQE up to 4%,⁴² from a stated maximum of 2% using only the Alq₃ host⁴³.

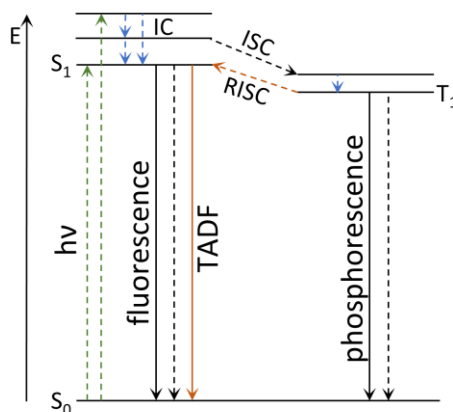


Figure 1.1: Jablonski diagram illustrating relevant transitions upon light excitation. Dashed arrows = non-radiative transitions; solid lines = radiative transitions. IC = internal conversion; ISC = intersystem crossing; RISC = reverse intersystem crossing; TADF = thermally activated delayed fluorescence; this process only takes place if S_1 and T_1 are separated by a small ΔE and requires RISC to take place.

Further improvements were made, especially if Ir and Pt compounds were employed as luminophores. These heavy metal complexes feature efficient spin-orbit coupling,^{44,45} which facilitates the spin forbidden transition from the triplet excited state to the singlet ground state. As such, they can be very efficient phosphors. In 2001 Adachi *et al.* reported a high efficiency OLED with an IQE of around 90% using bis(2-phenylpyridine) iridium(III)acetylacetonate ($[(ppy)_2Ir(acac)]$) (Scheme 1.2) as the guest luminophore in an TAZ host layer.⁴⁴ This was a significant finding since it proved that the theoretical maximum of 100% IQE could be approached by phosphorescent compounds.

Even though these findings were a breakthrough, increasing the efficiency of pure fluorophores remained a topic of interest. A particular area of interest was the high EQE of some fluorescent devices^{46,47} that could not be attributed solely to a better outcoupling efficiency but was attributed to triplet-triplet annihilation (TTA).⁴⁸ Depending on the mechanism the up-conversion of triplet to singlet excitons via TTA could lead to an increase in IQE from 15% to 37.5%, and thereby potentially more than double the IQE of a purely fluorescent emitter.⁴⁹

With the introduction of TADF (thermally activated delayed fluorescence) emitters in OLEDs another way of harvesting triplets was explored. In compounds exhibiting TADF the energy difference between the S_1 and T_1 state is so small, that the ambient temperature is enough to repopulate the S_1 state from the T_1 state via reverse intersystem crossing (RISC) (Figure 1.1). According to Uoyama and co-workers, the optimal energy difference between the S_1 and T_1 state is smaller than 0.1 eV, while the radiative decay rate (fluorescence) is higher than 10^6 s^{-1} to avoid significant nonradiative decay. However, these two metrics are in direct competition to each other, making a careful design of the HOMO (Highest Occupied Molecular Orbital) and LUMO (Lowest Unoccupied Molecular Orbital) necessary. Additionally, a geometry change/distortion of the molecular conformation upon excitation should be prevented to suppress non-radiative relaxations. Applying these principles, they were able to build OLEDs with an IQE approaching 100% with purely organic emitters.⁵⁰

1.1.2b Structure and working principle of OLEDs

While the use of both triplet and singlet excitons is an important aspect to have the highest possible IQE, it is by no means the only contributing factor. Eq. 1 states the dependence the IQE (η_{int}), from emissive exciton production efficiency (η_r), charge carrier balance (q) and radiative quantum yield (γ).³¹

$$\eta_{int} = \eta_r * q * \gamma \quad (1)$$

When it is possible to use all generated excitons in a device, be it via phosphorescence or TADF, η_r can be assumed as 1. Although the possibility of using all excitons is a fundamental part of the equation, it says nothing about the radiative decay of these excitons. q gives the ratio of nonradiative to radiative decays in a given compound and, with the right molecular design of the emitter, can approach 100%.^{51–53} Charge carrier balance is a critical issue in OLEDs and the devices need to be constructed in a way that $\gamma = 1$ for maximum efficiency. To achieve that goal, as has been mentioned before, OLEDs employ a multilayer structure. The careful implementation of electron and hole injection and transport layers (Figure 1.2), sometimes combined with blocking layers for either one or both charge carriers, is used to let the electrons and holes only recombine in the emissive layer.⁴¹

When a bias is applied to the device, holes from the anode and electrons from the cathode are injected and travel through their respective injection and transport layers, which have to be carefully chosen to facilitate the migration of the charge carriers. To improve the charge balance, it is crucial that there is only a gradual increase in the energy levels of HOMOs – for holes – and a decrease in energy levels for LUMOs – for electrons – between neighbouring layers.⁴¹ In the emissive layer the electrons and holes recombine to form an exciton which then decays under the emission of a photon.

The luminophores, especially phosphors, are often doped into a host material with a slightly higher LUMO than the one of the emitters. There are several benefits of using a host–guest system, from avoiding aggregation caused quenching (ACQ) over trapping of the charges in the emitting layer to improving device stability. As such the host material plays a crucial role in OLEDs and its properties will be regarded more closely in the following section.

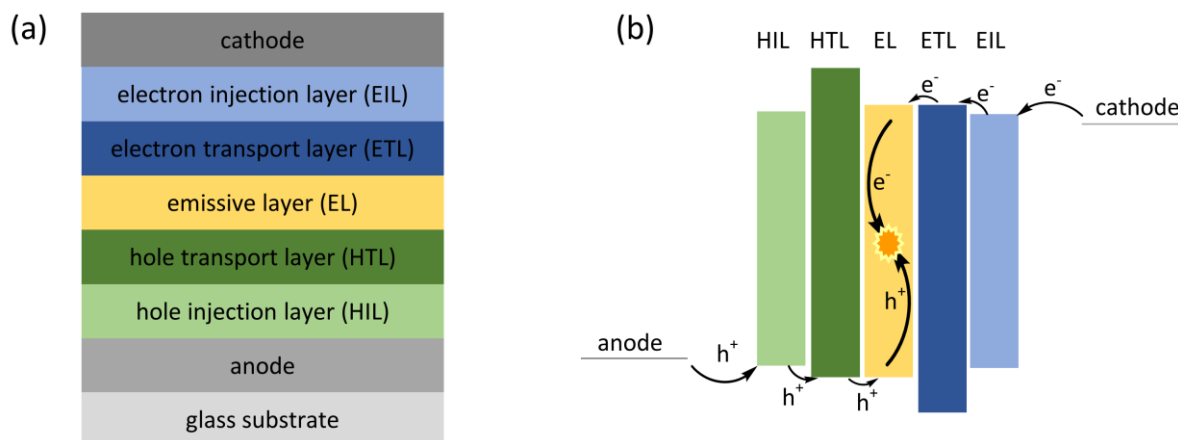


Figure 1.2: (a) Representation of the layer structure of an OLED. (b) Schematic illustration of energy levels in an OLED. HTL and ETL optimally work as electron blocking, respectively hole blocking layers. Electrons (e^-) and holes (h^+) are injected from the respective electrodes via their injection layers, transported to the emissive layer, where they recombine to form an exciton, which then can relax back to the ground state with concomitant emission of light.

1.1.2c Advantages and challenges of OLEDs

One of the main advantages of OLEDs over LEDs is their flexibility. Where LEDs are brittle and rigid, OLEDs are thin, lightweight devices that can be used in handheld and wearable electronics and have enabled the emergence of foldable smartphones. They have only a small power consumption, a high power efficiency, they feature wide viewing angles, are able to emit over the whole visible spectrum and can cover large areas.⁵⁴

One of the biggest challenges OLEDs face is their relatively high manufacturing cost.^{55,56} The thermal vacuum evaporation technique commonly used makes poor use of the material, is not easily scalable, has high equipment costs, and uses complicated processes.⁵⁷ Even though alternative wet processes, such as ink-jet printing and spin coating, have been researched for years, vacuum evaporation still is the dominant manufacturing technique, since it allows the exact control over the multilayer structure needed for a balanced charge carrier injection.^{31,56} Additionally, the cathodes commonly consist of low work function metals such as Ca, Mg, Ba to provide efficient electron injection into either the electron injection or electron transport layer, depending on the structure of the OLED. These metals readily react with oxygen or water making the careful encapsulation of the cathodes and the exclusion of air during the application of the cathode a requirement.³⁴ Often the cathode and the EIL are combined and referred to as cathode.³¹ Typical materials are Mg doped with either Al or Ag, or a combination of ionic species such as LiF or CsF with a metal like Al or Ca.^{30,58–60}

All of the aforementioned luminescence types – fluorescence, phosphorescence and TADF – can exhibit aggregation caused quenching at increased concentration of the luminophore. The mechanism for the self-quenching in TADF emitters is, according to recent reports, based on short range Dexter energy transfer,^{61–63} while the quenching for traditional fluorophores and phosphors is caused by Förster energy transfer.^{61,64–66} With the doping of the emitter into a host material at relatively low concentrations ACQ can be prevented. The use of a host material decreases the occurrence of ACQ, though it is not the only benefit of using a host–guest system, but there are some specific requirements for the host. The triplet

states of the host should energetically lie above the triplet states of the guest, the HOMO and LUMO of the host should be matched to the ones of the neighbouring layers to minimize charge injection barriers and it should have good charge carrier transport properties.⁶⁷⁻⁷⁰ If the host is chosen carefully, it confines excitons to the recombination zone and prevents not only ACQ but also triplet-triplet annihilation;⁷¹ thereby helping to make the most out of the generated excitons.

It has been established previously that phosphorescent and TADF emitters are preferred as luminophores, due to their potential ability to make use of all generated excitons. While there are a multitude of red, yellow and green emitting compounds of these two categories,^{40,45,72-83} OLEDs using blue emitters with the potential of 100% IQE are relatively rare. Blue phosphorescent emitters have particularly high demands for their host material.^{31,68} In addition, blue phosphors show problems with colour purity and stability,^{84,85} which is why deep blue fluorescent emitters are still employed in OLEDs despite their low maximum IQE.⁸⁶ While molecules with blue emission based on a TADF mechanism have been reported,⁸⁷⁻⁹⁰ there is a lack of data concerning the stability of these devices.⁸⁶ Additionally, TADF emitters tend to exhibit a red shift when the concentration is increased in the host material. It has been proposed that this red shift is caused by aggregation and high local electric fields in the host as a form of solvatochromism.^{91,92} Recently, a new model has been suggested in which at higher concentrations of the emitter, excitons can jump from one emitter molecule to another, thereby thermalizing and losing energy, leading to the described red shift.⁹³

One last issue that has to be mentioned, but will not be discussed in detail, is light outcoupling. Only a fraction of the photons created can escape from the device; others are refracted or reabsorbed inside the it. Due to these unwanted effects, only about 20% of the generated photons are able to leave the OLED.⁵⁶

1.1.3 Light emitting electrochemical cells

While OLEDs were actively researched and developed in the 1990s, Pei and co-workers constructed a new SSL (solid state lighting) device in 1995 by incorporating ions into the organic semiconductor.⁹⁴ Although the design of the device was similar to that of an early OLED, with only a minimal amount of layers sandwiched in between two electrodes, the working principles turned out to be vastly different. Pei already stated in the initial paper that light emitting electrochemical cells have some important advantages over OLEDs: They need a lower bias for luminescence to occur, they don't need to employ low work function metals, therefore air stable metals can be used as electrodes, the work function does not need to match the HOMO and LUMO energy of the emitter and the thickness of the emitting layer isn't as crucial a factor as in OLEDs. All of these aspects allow for much simpler manufacturing methods and a simpler device architecture when compared to OLEDs (Table 1.1). The relative independence of the thickness of the active layer in LECs opens up the possibility for two different device architectures, that allow different aspects of the LECs to be researched (Figure 1.3). Planar LECs are suitable to examine the growing of n and p doped fronts^{95,96}, for example, while stacked LECs can be used to investigate light outcoupling techniques⁹⁷.

Table 1.1: Comparison of some key device parameters between OLED and LEC. Based on reference 98

Parameter	OLED	LEC
Number of layers	4 or more	1 or 2
Typical thickness of layers	Between 1 and 40 nm	Up to multiple 100s of nm
Cathode material	Air sensitive, low work function metals	Air stable, not dependent on work function
Encapsulation requirements	High	Low

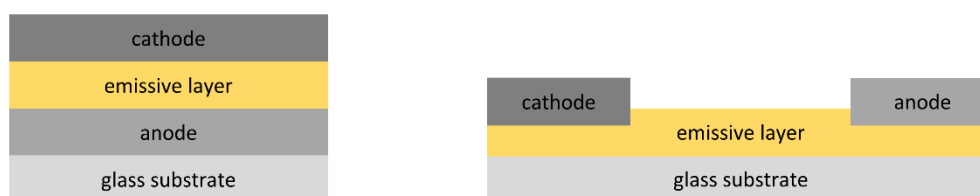


Figure 1.3: Stacked (left) and planar (right) LEC device architecture with the simplest possible layout.

The use of simple solution-based processing techniques for the construction of LECs paves the way for interesting applications, different from conventional lighting. LECs can be fabricated on top of a wide range of materials ranging from paper⁹⁹ over poly(ethylene terephthalate) (PET)¹⁰⁰ to metal forks¹⁰¹. While these examples were mainly used to showcase different printing and fabrication methods, they highlight the versatility of LECs. One particular interesting behaviour has been reported by Shih *et al.*. They reported multistate memristive behaviour in a LEC device using carbohydrate-based block – copolymers for ion capturing, leading to a device with three distinct states (OFF, ON1, ON2) which was retained over time that could potentially be used in high density data storage devices.¹⁰² LECs face some challenges, that need to be overcome for large scale practical applications, which will be discussed in a later sub-chapter (Section 1.1.3b).

1.1.3a Working mode of LECs

While the basic principles for light emission in an OLED (charge injection, charge migration, exciton formation and radiative recombination, see Figure 2b) can be applied to LECs as well, the underlying electrochemical processes are very different. The inclusion of four charged particles (cations, anions, electrons, and holes), makes the understanding of the working principle of the LECs particularly challenging.⁹⁶ Since the first mention of the LECs there have been three models proposed for the working mode of a LEC, the electrodynamic model (EDM), the electrochemical doping model (ECDM), and the preferential electrochemical doping model (PECDM).

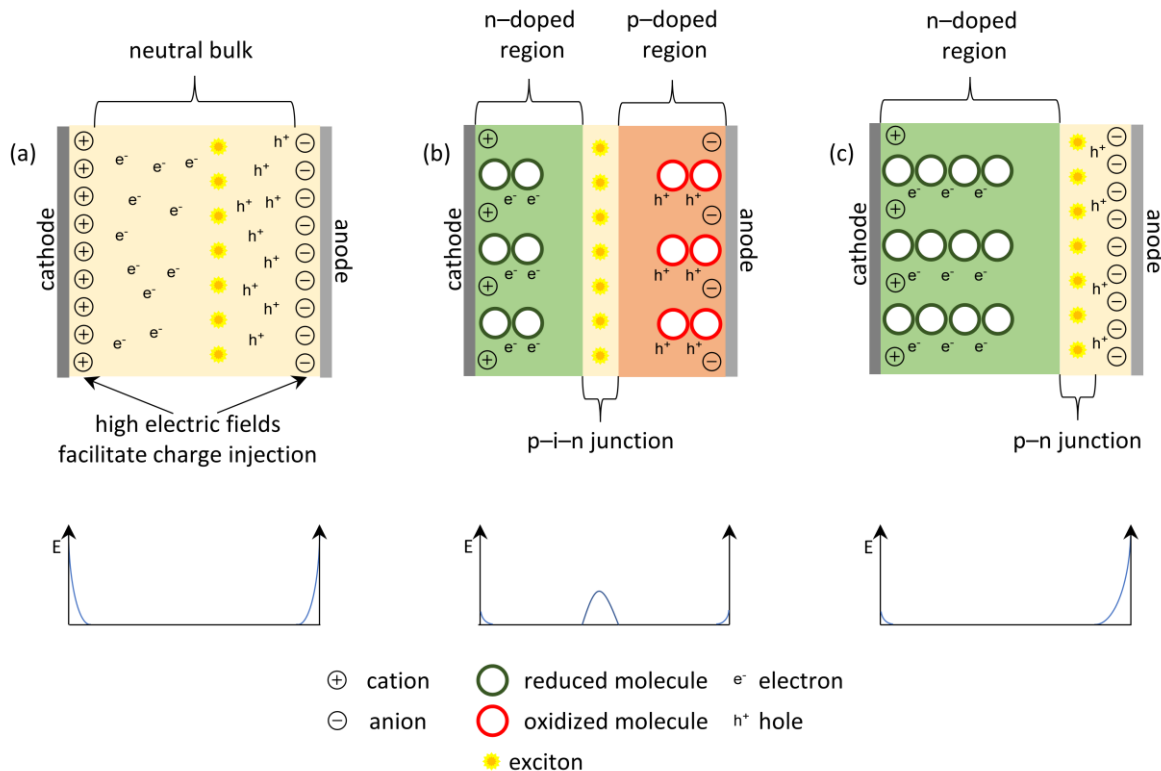


Figure 1.4: Graphical representation of (a) electrodynamic model, (b) electrochemical doping model and (c) preferential electrochemical doping model. The electric field distribution for each model is represented underneath. Adapted from reference 98.

Electrodynamic model

The electrodynamic model was proposed deMello *et al.*¹⁰³ It suggests that, when a bias is applied, the mobile ions redistribute and form an electrical double layer (EDL) near the respective electrodes. These electrical double layers are typically very thin (less than 1 nm) and the electrical field within them is therefore very large, in the order of 10^9 V/m. This leads to a bending of the energy levels (= potential drop) at the electrode – active layer interface and dissipation of the potential until the injection barrier has been overcome. Once this has happened, the injection of charge carriers into the active material begins. Because the bulk material is shielded by the EDLs, consequently there is no electric field in the bulk, practically no doping takes place and no p–i–n junction is formed. Because of this, exciton formation and light emission can occur in the whole field free region.^{34,96,104–107} (Figure 1.4a)

Electrochemical doping model

In the electrochemical doping model, promoted by Pei and Heeger, EDLs are predicted to form as well, but only to a point where ohmic contacts form and charge injection occurs.¹⁰⁶ The injected electrons and holes represent space charges, which are compensated with redistribution of cations and anions. This compensation leads to the formation of growing n-doped (holes compensated by anions) and p-doped (electrons compensated by cations) regions, akin to the (static) doping in inorganic semiconductors, hence the name electrochemical doping. Because the number of injected charge carriers is unlimited, while the number of cations and anions is not, eventually a complete separation of cations and anions occur. The two highly conductive doped regions ultimately meet, only separated by a thin, undoped region, forming

a p–i–n (positive-intrinsic-negative) junction. In this undoped region a sharp drop in voltage takes place and the excitons are formed.^{34,95,105,106,108} (Figure 1.4b)

Preferential electrochemical doping model

Proposed by Leger, Carter and Ruhstaller in 2005, this is a special case of the electrochemical doping model, in which only one ohmic contact is formed and only type of doping occurs, hence the light emission takes place close to one of the electrodes within a p–n junction.^{109,110} (Figure 1.4c)

The main difference of the models is the distribution of the electric field in the bulk material. While in the ED model the field is limited to a narrow region at the electron – semiconductor interface, in the ECD model the field is distributed over the whole emitting layer, with exception of an intrinsic region where the light emission occurs. In fact, all models have been found to be valid and to coexist side by side.^{98,110} van Reenen *et al.* described the different models as a consequence of the ability of the device to form non-injection limited ohmic contacts. In the case of the ECD model there is no injection limit, ohmic contacts are formed and anions and cations become fully spatially separated and thereby forming doped regions and EDLs at the contacts. If the charge carrier injection is limited – either by electrode oxidation or electrochemical side reactions – a transition to the ED model can occur, in which the doping is less pronounced but the EDLs are strengthened until the bulk material is shielded from the external electric field.^{34,96,98,106,111}

1.1.3b Challenges in designing LECs

Turn-on time and the importance of mobile ions

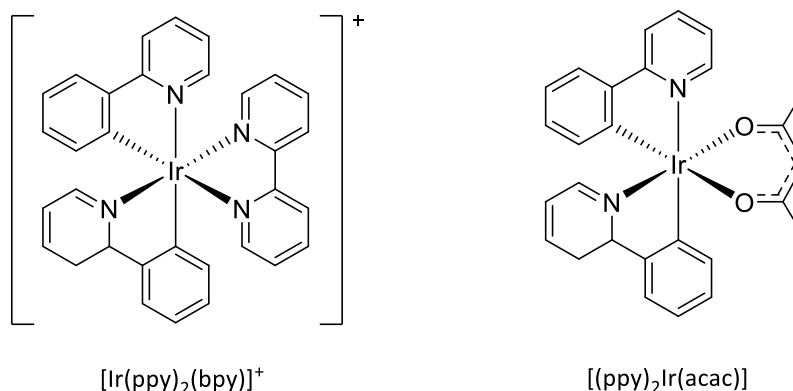
The turn-on time, commonly defined as the time until maximum luminance is reached,¹¹² is highly dependent on the mobile ions in the active layer of a LEC. While the transport of charge carriers in organic semiconductors is efficient enough to reach a quasi-steady state in less than a second, the movement of ions is much slower, since it involves the physical displacement through a solid state material.⁹⁸ This may lead to long turn-on times from an instantaneous response to several hours.^{113–116} For applications that are required to have a fast turn-on time, such as displays or lighting devices, this is not suitable and a lot of effort has been appointed to decrease the turn-on time in LECs.

To overcome the initial low conductivity of the cell, driving the cell with a fixed current instead of a fixed voltage can lead to improved turn-on times, due typically high initial biases.^{98,117} van Reenen *et al.* showed that increasing the temperature of the device shortened the turn-on time significantly to seconds for both ionic transition metal complexes (iTMC) - LECs and polymer LECs (PLECs), attributed to a higher ion conductivity and facilitated anion/cation dissociation.¹¹⁸ Creating frozen junction LECs, by preheating and applying a pre-bias or by chemical means, the device can also lead to a significantly improved response time.¹¹⁹

In iTMC LECs, the cations are normally large ions which, under an applied bias, can be viewed as generally immobile. This is not only disadvantageous for fast response times, but also leads to an imbalance in charge carrier injection, since the accumulation of cations at the anode is – at best – severely hampered.^{120,121} The first approach to address this issue was the addition of poly(ethylene oxide) (PEO) together with a salt, making use of similar materials as were used in PLECs.¹²² While the turn-on time could be reduced by this approach, the EQE was very low. The use of ionic liquids (IL) (salts with melting points below 100 °C) delivered promising results in terms of decreasing the turn-on time, even at low

concentrations. On the other hand, higher concentration of ILs lead to reduced device lifetimes and only marginally increased luminescence.¹²³ Studies investigating the effect of ILs on the performance showed that this effect can be attributed to a higher conductivity in the film.^{124,125} It was also found that a higher intrinsic conductivity of an ionic liquid can lead to a higher luminance of the device.^{125,126}

A different approach to the low ion mobility of the cation is the addition of a salt with a small cation. Li⁺ salts proved to be the most effective, while K⁺ and NH₄⁺ were already too large to have a considerable impact on the device metrics. Even small amounts of a Li⁺ salt have a measurable effect on the device performance in terms of turn-on time, power efficiency and luminance. Slinker *et al.* investigated the influence of the concentration of Li[PF₆] (PF₆⁻ = hexafluorophosphate) on a device with the archetypical [Ir(ppy)₂(bpy)][PF₆] (bpy = 2,2'-bipyridine) (Scheme 1.2) as emitter.



Scheme 1.2: Typical representatives of a cationic and a neutral Ir(III) complex; [Ir(ppy)₂(bpy)]⁺(right) and [(ppy)₂Ir(acac)](left)

The Li⁺ makes up for the lack of mobility of the Ir-cation and they found that already an amount of only 0.2% wt. about halves the thickness of the EDL at the cathode and leads to improved device performance. They determined that the optimal salt concentration was 0.5% wt., which led to the thinnest EDL and stating that this enhances current injection, and a balanced injection of charge carrier, which in turn has a positive influence on luminance and efficiency of the device.¹²⁷

Degradation of the active layer, luminescence quenching and reabsorption

Decreasing efficiency is commonly observed in LECs during operation. The growing n and p doped zones can quench excitons, especially long-lived triplet excitons, therefore a stabilisation of the p-i-n junction and slowing down of the doping fronts improves the device lifetime and device performance.¹¹⁷ Frozen junction devices have been mentioned before to achieve faster turn-on times but as the name suggests, they also possess a stable p-i-n junction. A different way to achieve the same goal is the use of a pulsed current driving scheme. Using this method Tordera and co-workers presented a LEC with a fast turn-on time and long device lifetime.¹¹⁷ Additionally, it has been shown that the doping of the LEC is not permanent and can be reversed.^{128,129}

While LECs do not need to undergo a similarly vigorous sealing as OLEDs, and in fact residual solvent and water can have a beneficial impact on the turn-on time and brightness of a device¹³⁰, generally, the exclusion of water and oxygen in the preparation of a LEC is necessary to prevent the formation of H₂, the consequent formation of bubbles and delamination of the emissive layer.¹³¹ Particularly, Al cathodes are

susceptible to electrochemical side reactions, leading to shorter device lifetimes and decreased luminescence^{132–134}, therefore, different high work function metals and metal oxides have been investigated as possible cathode materials.^{135,136}

PLECs also suffer from irreversible degradation if the conduction band of the ion transport polymer lies above the reduction level of the electrolyte.^{137,138} In this case the injection of electrons can reduce either the electrolyte or the polymer, thereby possibly hindering the injection of electrons, ultimately causing a charge carrier imbalance which, in the worst case, leads to microshorts if a doped region reaches the opposite electrode.¹³⁹ This irreversible degradation can be prevented by carefully choosing the polymer and electrolytes with a high electrochemical stability window.¹³⁸

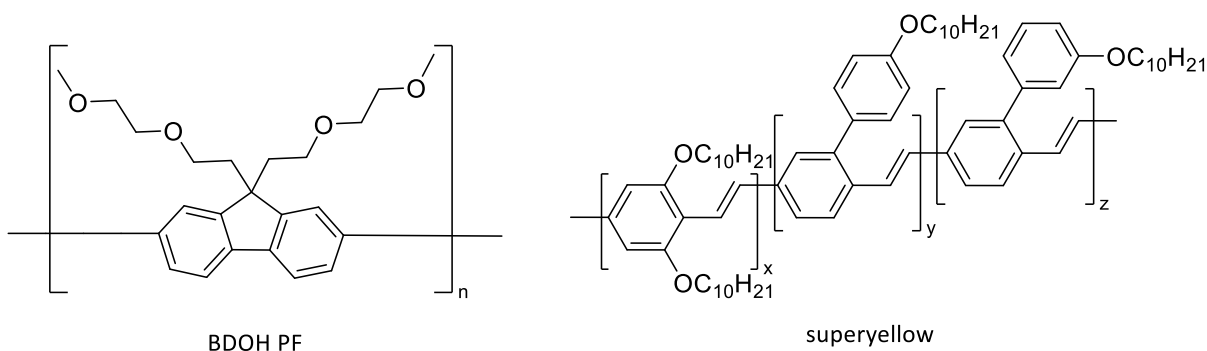
Similar to OLEDs, the loss of charge carriers by non-radiative recombination or the loss of the charge carrier at the electrode of the opposite polarity needs to be avoided to achieve the best efficiencies. Due to the formation of n- and p-doped regions in the ECD model, such losses are prevented by high doping densities. However, in the PECD and ED models, the recombination zones are much closer to the electrodes and quenching in these manners can occur, hence LECs employing the non-injection limited ECD model are preferred for applications. Furthermore, the recombination zone tends to move during the operation of the LEC, hence a stabilisation of the p–i–n junction is necessary. To prevent quenching of charges at the electrodes and improve the charge carrier balance, sometimes electron or hole transport layers are incorporated.^{140,141} While quenching at the electrodes can be avoided, there are other quenching mechanisms, namely quenching via exciton-charge annihilation (ECA),¹⁴² by other excitons,¹⁴³ by polarons,¹⁴⁴ and large electric fields¹⁴⁵ are not as easily prevented. The exciton polaron quenching is particularly important in this case, since achieving higher brightness is achieved through increased current density, which leads to a higher doping density which in turn leads to an increase in exciton–polaron quenching. In other words, if the current density is increased beyond a certain point, the brightness of the cell will diminish. Additionally, aggregation caused quenching is an issue in LECs too; a fact that is addressed with doping of the emitter into an inert host material such as poly (methyl methacrylate) (PMMA) and – in case of iTMC–LECs – the addition of bulky ligands on the metal centre.^{146,147} On the other hand, the increased resistance from the inert polymer at lower doping concentrations leads to reduced brightness and power efficiency.¹³²

Lastly, extracting the generated photons from the device can be challenging. It has been found that the electrochemical doping of the active layer can lead to reabsorption of the photons, since the doping gives rise to an additional absorption band, with a similar energy as the generated photon.^{148,149} Although the occurrence of the luminescent region is not dependent on the thickness of the active layer, it plays an important role in the reabsorption of the photons. Kaihorvita found a sevenfold increase in absorption when increasing the thickness of the active layer from 100 nm to 1 μm .¹⁴⁸ As such it can be said, that generally thinner devices are preferable to obtain the highest efficiencies in LECs. Additionally, as in OLEDs, light outcoupling is an important topic in the engineering of the devices which needs to be optimized for the best outcome.

1.1.3c Emissive compounds for LECs

Polymers

Since the first report of a LEC by Pei *et al.*, polymers have been investigated as possible luminophores in these devices. Tuning the emission wavelength based on polymers is relatively easy and can be achieved by exchanging repeating units.¹⁵⁰ A different approach is to modify the periphery, e.g., including phosphors to not only tune the emission wavelength but also enhance the IQE of the device.¹⁵¹ While the HOMO–LUMO gap can be changed by synthetic chemistry, enabling emissions from white to red, the addition of side chains to the rigid conjugated backbone allows the solubility in common organic solvents. However, to build a LEC, mobile ions are needed and the addition of an electrolyte is necessary for PLECs. In this lies one of the major drawbacks of PLECs, since there are often issues with phase separation between the polymer and the electrolyte. The phase separation decreases the EQE of the devices, but it can be exploited as well, as has been shown by Pei and Yang in 1997. When they built a PLEC with poly(9,9-bis(3,6-dioxaheptyl)-fluorene-2,7-diyl) (BDOH-PF) and added PEO as an electrolyte they found that the EQE decreased from 4% – for a device without PEO – to 2.5%, but the emission colour also changed from blue-green to white.¹⁵² This was attributed to conformational changes in the polymer–electrolyte blend and the resulting aggregation induced red shift of the emission. The phase separation is an important contributing factor to the device lifetime ($t_{1/2}$, time until half of the maximum luminance is reached) which is usually rather short. It is, however, possible with the correct stoichiometry of emitter, electrolyte and copolymers to achieve relatively long lifetimes, as has been demonstrated with the polymer superyellow by Heeger *et al.*¹⁵³



Scheme 1.3: Structures of the repeating unit of the polymers BDOH-PF and superyellow with $x:y:z = 1:12:12$.

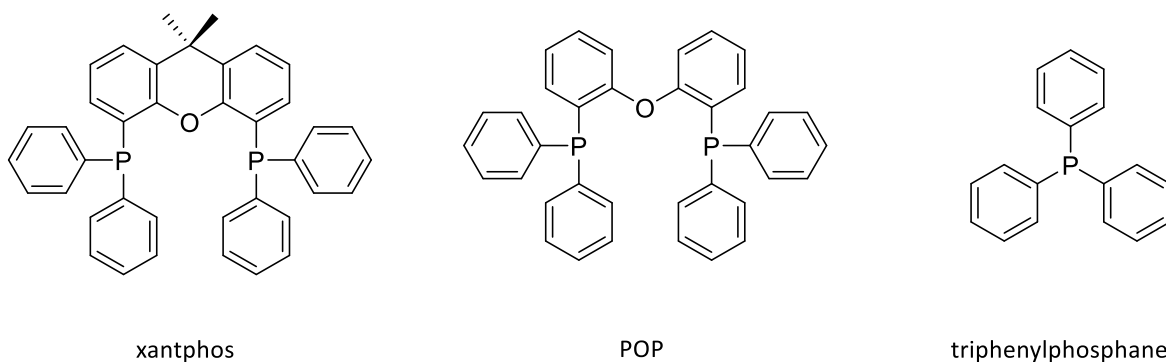
Ionic transition metal complexes

Comparable to phosphors in OLEDs, emitters with a *d*-block metal, especially of the second and third row of the periodic table, are interesting because of the potential for triplet harvesting. Early on, the focus lay on Ru(II)-complexes, but because of limited colour tunability, dominant orange red emission^{154,155} and the poor stability of the compounds, complexes incorporating other metals were desirable. Ir(III) complexes emerged as promising candidates with colour tunability over the whole visible spectrum and high complex stability.¹⁵⁶ The typical Ir(III) complex in a LEC carries two ppy and one bpy ligand (giving the $[\text{Ir}(\text{ppy})_2(\text{bpy})]^+$ cation) (Scheme 1.2). In this cation, the HOMO is located on the Ir and the two cyclometalating ligands (ppy) while the LUMO is situated on the bpy alone. This spatial separation allows an independent tuning of the HOMO and the LUMO levels, respectively.³⁴ With the strategy of HOMO stabilization with electron withdrawing fluoro-groups on the ppy and LUMO destabilization with electron donating dimethylamino

groups on the bpy, De Angelis and co-workers were able to design a deep blue emitting complex.¹⁵⁷ On the other hand, red emissions can be achieved via LUMO stabilisation, for example by substituting ester groups onto the bpy.¹⁵⁸ Of course, the limited availability of Ir and other heavy *d*-block metals plays an important role in the development of sustainable and cheap iTMCs, where the use of rare earth metals is rather detrimental.

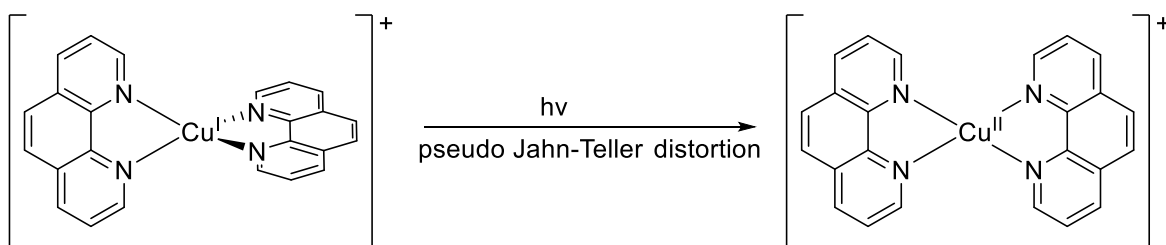
As an alternative, copper(I) complexes emerged due to the high abundance and low cost of copper (abundance of Cu vs. Ir in earth crust: 27 ppm vs. 0.000037 ppm,¹⁵⁹ price of Cu vs. Ir as of June 15, 2021 : 10.03 \$/kg vs. 196119.55 \$/kg¹⁶⁰). The emission of cationic copper(I) complexes originates from a metal-to-ligand charge transfer (MLCT). The absence of low-lying metal centred (MC) states in the d^{10} electronic ground state of Cu(I) prevents undesirable deactivation pathways.¹⁶¹ The basis for luminescent copper(I) complexes was laid in the late 1970s by McMillin and co-workers with the homoleptic $[\text{Cu}(\text{dmp})_2][\text{BF}_4]$ complex (dmp = bis(2,9-dimethyl-1,10-phenanthroline)).¹⁶² Recently, homoleptic bis(phenanthroline)Cu(I) complexes with long-lived excited states and PLQY <5% in solution have been reported.¹⁶³ However, homoleptic bis(diimine)copper(I) complexes have never achieved PLQYs which were high enough for application in LECs. Note that the photoluminescence is only an indicator and not a definitive assurance for electroluminescence.^{161,164} Parallel to the homoleptic Cu(I) complexes, Buckner and McMillin also investigated heteroleptic cationic Cu(I) complexes incorporating phosphanes, diphosphanes and diimine ligands. While the emission of the homoleptic $[\text{Cu}(\text{dmp})_2]^+$ complex was too weak and the measurement method too insensitive for the emitted wavelength ($\lambda_{\text{em}}^{\text{max}}$), the heteroleptic complexes $[\text{Cu}(\text{PPh}_3)(\text{bpy})]^+$ and $[\text{Cu}(\text{dpe})(\text{bpy})]^+$ (dpe = cis-1,2-bis-(diphenylphosphino)ethylene) showed a measurable, albeit very short-lived, luminescence with a notably blue shifted emission originating from a MLCT state.¹⁶⁵ Indeed, the incorporation of the phosphane and consequent formation of heteroleptic complexes generally leads to a blue shifted emission, higher PLQYs and longer excited state lifetimes in comparison to homoleptic diimine complexes.¹⁶¹

The introduction of phosphanes (in particular wide bite-angle diphosphanes) has therefore been a crucial step in improving the photophysical properties of heteroleptic $[\text{Cu}(\text{P}^{\wedge}\text{P})(\text{N}^{\wedge}\text{N})]^+$ and $[\text{Cu}(\text{P}_2)(\text{N}^{\wedge}\text{N})]^+$ complexes, where P is a phosphane, $\text{P}^{\wedge}\text{P}$ a diphosphane ligand, $\text{N}^{\wedge}\text{N}$ is a diimine ligand and + denoting the need for an anion. The effects of the phosphane ligands are thereby not only limited to increased bulk and stabilization of the pseudo-tetrahedral geometry of Cu(I) (see next paragraph) but they also serve as σ donors and π acceptors, whereby the π acidity is dependent on the substituents of the phosphorus and is particularly pronounced for aryl groups. This electron withdrawing effect of the phosphanes stabilizes the HOMO, consequently leading to a larger HOMO–LUMO gap and a blue shift in emission.¹⁶⁶ In solution it has been shown that Cu(I) complexes with two coordinating triphenylphosphanes ligands (Scheme 1.3) show significantly lower PLQY and shorter luminescence lifetimes than Cu(I) complexes which carry a diphosphane ligand such as such as xantphos or POP (Scheme 1.3). This has been attributed to a higher rigidity of the diphosphane ligands, which prevents ligand dissociation, exciplex quenching and to some extent excited state distortion.^{167,168}



Scheme 1.4: Schematic representation of 4,5-bis(diphenylphosphano)-9,9-dimethylxanthene (xantphos), bis(2-(diphenylphosphano)phenyl)ether (POP) and triphenylphosphane.

In his initial research with $[\text{Cu}(\text{N}^{\wedge}\text{N})_2]^+$ complexes, McMillin noted the flattening of the pseudo-tetrahedral geometry of Cu(I) towards a square planar conformation (which is adopted by Cu(II) compounds) upon excitation of the compound.^{167,169} Exciting an electron from the d -orbitals of copper leads to a formal oxidation to Cu(II) (d^9 configuration) and pseudo Jahn–Teller distortion.¹⁷⁰



Scheme 1.5: Schematic representation of the flattening motion of Cu(I) complexes upon photoexcitation and the accompanying formal oxidation of the copper centre exemplified by $[\text{Cu}(\text{phen})_2]^+$.

Not only is the flattening of the geometry adding new non-radiative decay pathways, it also opens up a new coordination site on the copper, where a solvent or dioxygen molecule can coordinate, opening up the possibility for exciplex quenching.¹⁷¹ Preventing this flattening distortion is therefore key to improve the photophysical properties of these complexes. Bulky diphosphane ligands carrying phenyl groups¹⁷² and substituents in ortho-position to the coordinating nitrogen (2/9 position for phen and 6/6' position in bpy) were shown to increase the HOMO–LUMO gap, yield higher PLQYs and longer excited state lifetimes.^{114,173} This is most significant for emission in solution, but the benefit of the sterically hindered substituents can also be found in thin films and solid state.¹⁶¹ It has to be noted, however, that the decrease in flexibility of the diphosphane can also have a negative impact on the PLQY of luminescent Cu(I) species.¹⁷⁴

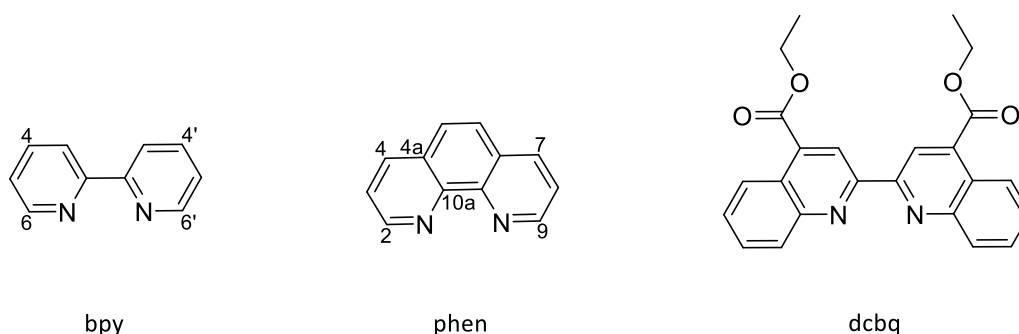
Prompt fluorescence is normally not observed in $[\text{Cu}(\text{P}^{\wedge}\text{P})(\text{N}^{\wedge}\text{N})]^+$ complexes, leading to excited state lifetimes in the microsecond regime. However, both TADF and phosphorescence (Figure 1.1) can be observed in these compounds and, in fact, both emission pathways can exist in the same molecule.¹⁷⁵ Usually, the HOMO is located on the copper with contributions from the phosphane ligand, while the LUMO is located on the diimine. The spatial separation of the HOMO and the LUMO has been demonstrated multiple times with computational methods,^{173,176–180} and allows the independent tuning of the frontier orbitals, similar to Ir(III) complexes. To tune the emissive properties of $[\text{Cu}(\text{P}^{\wedge}\text{P})(\text{N}^{\wedge}\text{N})]^+$

complexes both structural elements as well as electronic influences have to be considered; research has thereby mainly been focused on the diimine ligand.^{114,173,181–187} In 2017 Weber *et al.* proposed guidelines for ligand design using the σ -Hammett parameter of different substituents. While the work was only focused on the 4,4' position of bpy, it laid important groundwork for rationalizing and fine-tuning the photophysical properties. They found that substituents with more σ -donating character (i.e. more negative σ -Hammett parameter) destabilized the LUMO, thus increasing the HOMO–LUMO gap.¹⁸⁸

The two most commonly investigated N^N ligands are bpy and phen (Scheme 1.4). [Cu(P^P)(bpy)]⁺ or [Cu(P^P)(phen)]⁺ complexes both exhibit ligand centred (LC) absorptions in the region of 250 – 350 nm as well as weaker absorption bands usually assigned to MLCT absorptions between 350 – 450 nm. While the emission wavelength (λ_{em}) and the PLQY is heavily dependent on the substituents, substitution pattern, and the environment (solid state, thin-film or solution), generally it can be said for most of the [Cu(P^P)(N^N)]⁺ complexes that λ_{em} lies in the range of 550 – 700 nm with some noteworthy blue-shifted outliers (Table 1.2).^{161,189}

Table 1.2: Photophysical properties of some [Cu(P^P)(N^N)]⁺ complexes in solid state.

N^N ligand	P^P ligand	λ_{em} [nm]	PLQY [%]	τ [μ s]	Ref.
dmp	POP	527	28	27.5	190
6,6'-Me ₂ -4,4'-(CF ₃)-bpy	xantphos	517	50.3	2.7	114
6,6'-Cl ₂ bpy	POP	584	14.8	2.3	115
6,6'-Cl ₂ bpy	xantphos	587	17.1		115
6-MeObpy	POP	565	17	3.3	116
6-MeObpy	xantphos	566	19	4.7	116
6-PhObpy	POP	585	5	1.5	116
6-PhObpy	xantphos	572	12	2.7	116
dcbq	xantphos	671	56	1.85	191

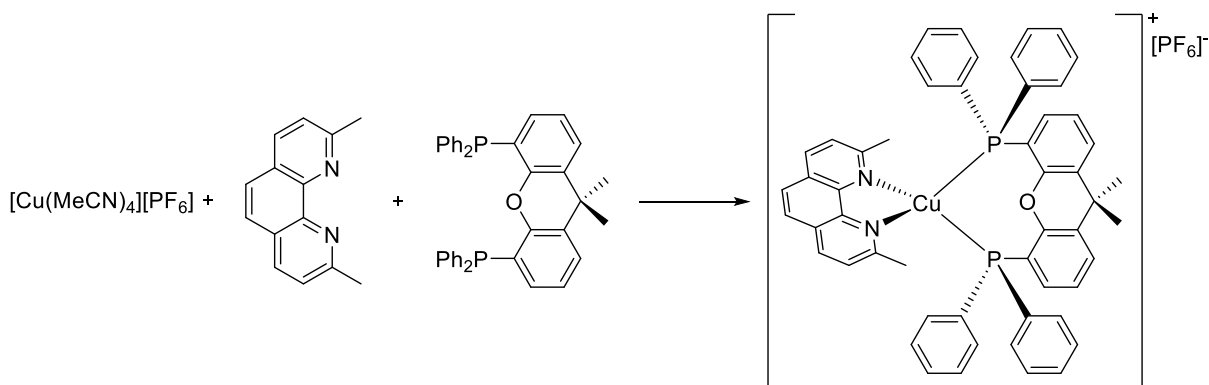


Scheme 1.6: Structure and labelling scheme of 2,2'-bipyridine (left) and 1,10-phenanthroline (middle) and 4,4'-diethylester-2,2'-biquinoline (dcbq) (right).

To achieve white light emission from LECs, developing blue and deep red emitting compounds is a necessity. However, Cu(I) complexes featuring such emissions have been elusive and only in the last decade progress, particularly with blue emitting complexes, has been made. These complexes commonly exchange the P^P ligand with a sterically demanding N-heterocyclic carbene (NHC). Based on this concept,

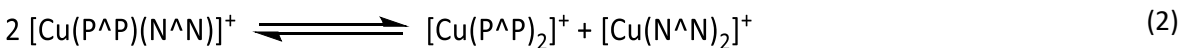
Marion *et al.* prepared complexes with different dipyriddyamine ligands and the NHC ligand 1,3-bis(2,6-di-iso-propylphenyl)imidazole-2-ylidene (IPr) with blue emission and high PLQY in the solid state.^{192,193} The incorporation of these complexes into LECs by the same group led to blue emitting devices, which could compete with state of the art blue emitting Ir(III) complexes in terms of efficacy and luminance. However, these devices only possessed a short lifetime of about 15 min. This behaviour was attributed to uncontrolled oxidation and reduction processes.¹¹³ In a follow up publication, they investigated the influence of the bridging atom of the N^N ligand. This led to devices with emissions from light blue to green. Similarly, to other complexes, they found that stabilizing the Cu(I) geometry in the excited state was key to improve the PLQY value of the complexes. While they outperformed the previously built LECs, the device lifetime was very short in these light-blue to yellow emitting devices.¹⁹⁴

Only one deep-red emitting Cu(I) complex employed in LECs has been reported to date, based on [Cu(4,4'-diethylester-2,2'-biquinoline)(xantphos)][PF₆].¹⁹¹ The complex exhibited a PLQY of 56% and the corresponding device “showed a promising electroluminescent response, that is, stable deep-red emission centred at around 671 nm, x/y CIE colour coordinates: 0.66/0.32, with an irradiance of ≈100 μW cm⁻², and stabilities of almost a day” (Table 1.2).¹⁸⁹ Using this red emitting complex, the group was able to build the first white emitting LEC via incorporating the complex into the blue emitting, hole transport host material 4,4'-Bis(*N*-carbazolyl)-1,1'-biphenyl. A device, with a weight ratio of 15% guest, 85% host for the active layer featured a moderate luminance of 4 cd/m² with a CRI of 0.92.



Scheme 1.7: Representative reaction scheme for the synthesis of [Cu(P^A P)(N^A N)]⁺[PF₆]⁻ complexes, exemplified by [Cu(xantphos)(dmp)]⁺[PF₆]⁻.

Although the synthesis of the [Cu(P^A P)(N^A N)]⁺ complexes generally follows a simple pathway (Scheme 1.5) it has been reported that during synthesis, or when in solution over an extended period of time, other species, e.g. [Cu(N^A N)₂]⁺ and [Cu(P^A P)₂]⁺, are readily formed (Eq. 2).^{195,196}



In order to minimize the formation of the homoleptic complexes, two preparation methods have been established, depending on whether or not the phosphane ligand forms a stable homoleptic [Cu(P^A P)₂]⁺ complex. In the sequential preparation, the P^A P ligand is added as solid to a solution of [Cu(MeCN)₄][PF₆], stirred and after some time the N^A N, again as solid, is added. In the parallel method, both ligands are dissolved and added to the [Cu(MeCN)₄][PF₆] (MeCN = acetonitrile) solution at the same time. The instability of the complexes poses a serious issue, and not only requires optimized synthesis routes, but

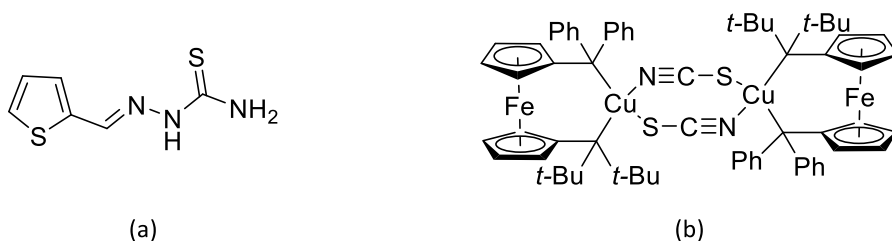
also careful control of the purification and device assembly to exclude the homoleptic species and particularly $[\text{Cu}(\text{N}^{\wedge}\text{N})_2]^+$ since it represents an efficient quencher. However, even with the best preparative techniques it cannot be ruled out that these species form during the operation of the LEC.¹⁹⁵ This issue has been addressed with a publication from Mohankumar *et al.* by the introduction of a pseudorotaxanes macrocycle into the phenanthroline framework. The synthesized Cu(I) complexes with the pseudorotaxanes and POP as P^P ligand were then compared to $[\text{Cu}(\text{POP})(\text{dmp})][\text{BF}_4]$. The results were remarkably similar in terms of UV-VIS absorption and emission properties, PLQY and luminescence lifetime. Cyclic voltammetry measurements showed higher oxidation potentials for the $\text{Cu}^+ \rightarrow \text{Cu}^{2+}$ oxidation for the complexes incorporating the larger macrocycles when compared to the reference complex, which was rationalised with an improved stabilisation of the Cu(I) pseudo-tetrahedral geometry. When the complexes are cooled down, all of the complexes exhibit a red shift in emission, expected for TADF emitters. However, in dichloromethane at 77 K the complexes show a significant blue shift compared to at 298 K, ascribed to rigidochromic effects overtaking all electronic ones. The OLED they constructed using the largest macrocycle as luminophore exhibited good stability when comparing to an OLED with the $[\text{Cu}(\text{POP})(\text{dmp})][\text{BF}_4]$ luminophore; this was, in part, attributed to a decrease in ligand dissociation.¹⁹⁰ Despite these promising findings, the incorporation of such complexes into LECs has not yet happened and work that focuses on more stable mononuclear heteroleptic Cu(I) complexes for the use in LECs are notably absent.

Chapter 2: Replacing one chelating N with sulfur: [Cu(P[^]P)(N[^]S)][PF₆] complexes

The contents of this chapter are based on references 197 and 198.

2.1 Motivation

As it has been established, luminescent Cu(I) complexes with P[^]P and N[^]N ligands have been widely investigated, but additionally in some cases the phosphane and imine were combined in one molecule to incorporate a hard and soft donor moiety on the same ligand.^{199–201} A different hard – soft donor set has been used in [Cu(P[^]P)(N[^]S)]⁺ complexes, where N[^]S describes a thiosemicarbazone. They are interesting compounds in pharmacology, catalysis and analytical chemistry. Furthermore, they exhibit multiple binding modes in Cu complexes depending on other ligands, such as PPh₃ or halides, and oxidation state of the copper.^{202–204} It has been shown that sulfur can engage in a bridging binding mode, which is also the case for thiocyanato (NCS) ligands.²⁰⁵

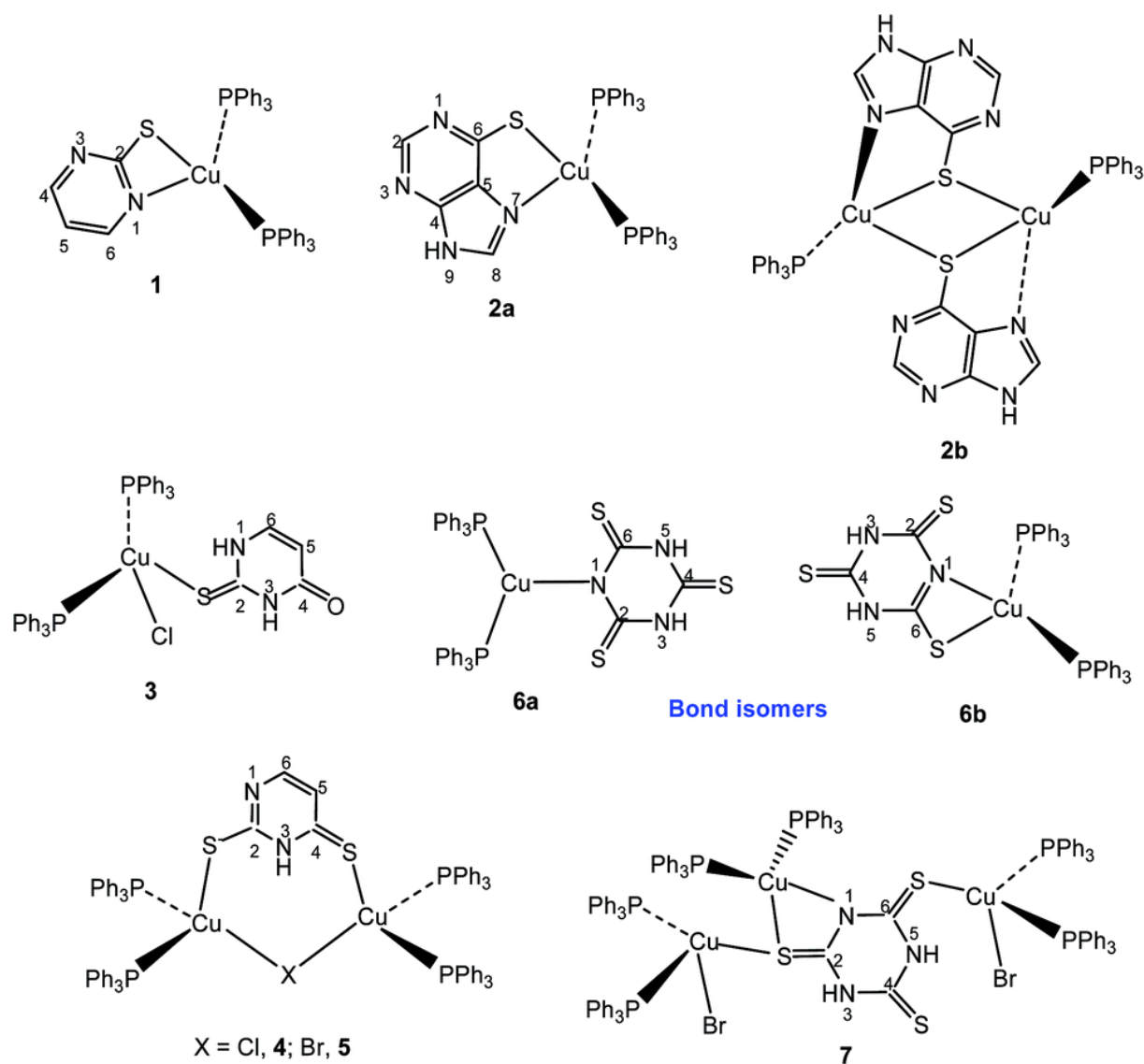


Scheme 2.1: Structures of (a) one of the thiosemicarbazones used by Lobana et al.^{204,206} and (b) 1-diphenylphosphino-10-di-tert-butylphosphinoferrocene.

For [Cu₂(dppdtbpf)(μ-NCS)₂] (dppdtbpf = 1-diphenylphosphino-10-di-tert-butylphosphinoferrocene), a broad emission with a λ_{em}^{max} around 500 nm was reported.²⁰⁷ A series of [Cu(PPh₃)₂(N[^]S)]⁺ complexes, with N[^]S being a thioamide, which featured different binding modes depending on the respective structure of the ligand, exhibited absorptions from 260 – 450 nm, often with two distinct absorption bands, assigned to a π* ← π for the higher energy band and π* ← n for the lower energy band. When excited between 270–291 nm these complexes feature a broad emission band centred around 490–495 nm.²⁰⁸

Although N[^]N (e.g. bpy) and simple bidentate N[^]S (e.g. 2-(thiophen-2-yl)pyridine, (ThPy)) ligands have similarities in terms of coordination to Cu, the ‘replacement’ of an N with an S has serious stereo-electronic consequences due to the two lone pairs of sulfur. This leads to a distortion of the N–C–S dihedral angle when coordinated to Cu(II).^{209,210} Even though similar studies with Cu(I) complexes had not been previously carried out, analogous distortions are expected, which could potentially have implications for the stability of these complexes. Nevertheless, with Cu(I) being a classical soft metal centre, a Cu–S coordination bond is considered likely to form.

The lack of data surrounding the properties of [Cu(P[^]P)(N[^]S)]⁺ complexes, with P[^]P being POP or xantphos and N[^]S being 2-((alkylsulfanyl)methyl)pyridines or 2-(thiophen-2-yl)pyridines (scheme 2.1) and the potential for light emission from these compounds sparked the interest for this project and prompted the investigation of several [Cu(P[^]P)(N[^]S)][PF₆] complexes.



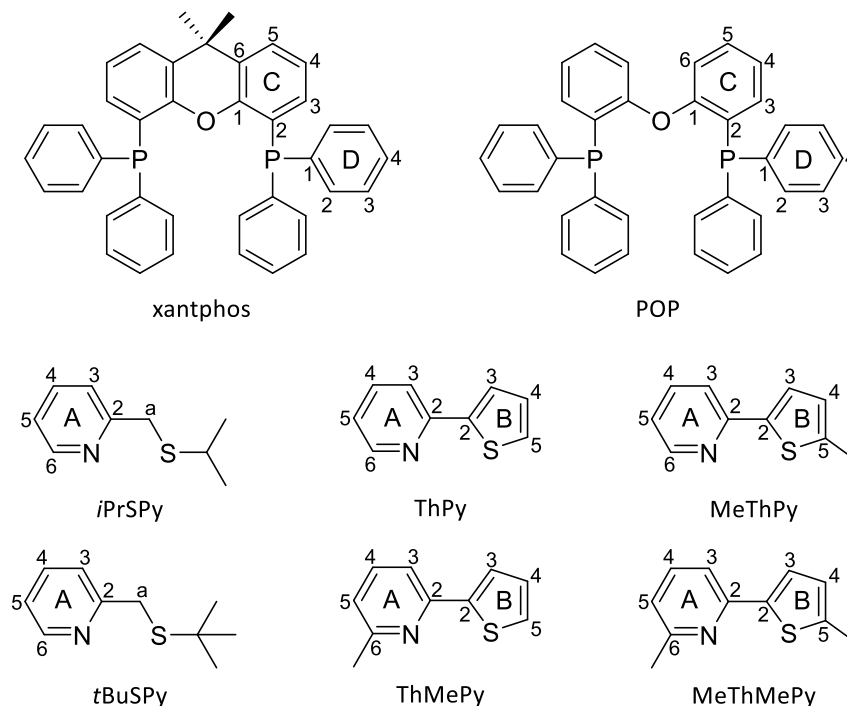
Scheme 2.2: Structure and bonding pattern of Cu complexes incorporating several thioamides synthesized by Lobana et al.. Reproduced with permission of the Royal Society of Chemistry from reference 208; permission conveyed through Copyright Clearance Centre, Inc.

2.2 Synthesis

2.2.1 Ligand synthesis

The synthesis of 2-(*iso*-propylsulfanylmethyl)pyridine (*i*PrSPy) and 2-(*tert*-butylsulfanylmethyl)pyridine (*t*BuSPy) (Scheme 2.1) were previously reported.^{211,212} 6-Methyl-2-(thiophen-2-yl)-pyridine (ThMePy) and 2-(5-methylthiophen-2-yl)pyridine (MeThPy) (Scheme 2.1) were prepared by Suzuki-coupling as previously reported and the NMR spectroscopic data of all ligands matched the literature.^{213,214} 6-Methyl-2-(5-methylthiophen-2-yl)pyridine (MeThMePy) was synthesized in an analogous manner to the other 2-(thiophen-2-yl)pyridines via Suzuki-coupling reaction (see experimental section 2.8.1) with 2-bromo-6-methylpyridine and 4,4,5,5-tetramethyl-2-(5-methyl-2thienyl)-1,3,2-dioxaborolan. MeThMePy was

isolated as yellow oil. ESI-MS (electrospray mass spectrometry) showed the highest mass and base peak at m/z 190.00, which was assigned to $[\text{MeThMePy} + \text{H}]^+$. Assignment of the ^1H and ^{13}C NMR spectra was done with COSY, NOESY, HMQC and HMBC 2D NMR experiments and are consistent with the proposed structure (Scheme 2.1).



Scheme 2.3: Structures of $P^A P$ and $N^A S$ ligands used in the synthesis of $[\text{Cu}(P^A P)(N^A S)][\text{PF}_6]$ complexes with labelling scheme used for ^1H and ^{13}C NMR spectroscopy assignment.

2.2.2 Complex synthesis

Even though different synthesis protocols for the assembly of $[\text{Cu}(P^A P)(N^A N)]^+$ complexes exist, it was found that the addition of the $N^A S$ ligand to a 1:1 mixture of $[\text{Cu}(\text{MeCN})_4][\text{PF}_6]$ and the respective diphosphane in CH_2Cl_2 provided the complexes as colourless solids in yields from 40–75% after purification. Interestingly, the two synthesis protocols were developed to address different stabilities of $\text{Cu}(\text{I})$ -bisphosphane complexes. Indeed, it has been shown that between POP and xantphos, only xantphos adopts a $[\text{Cu}(P^A P)_2]^+$ structure, while POP forms a tricoordinate $[\text{Cu}(P^A P-\kappa^2 P)(P^A P-\kappa^1 P)]^+$ cation due to its greater steric hindrance.²¹⁵ While one would assume the replacement of a $P^A P-\kappa^2 P$ (as is the binding mode for xantphos in $[\text{Cu}(P^A P)_2]^+$) is less favoured than the substitution of a $P^A P-\kappa^1 P$ and consequently a lower yield would be expected if the homoleptic complexes were allowed to assemble first, such a trend was not observed.

For each of the complexes the $[\text{Cu}(P^A P)(N^A S)]^+$ cation peak was found in the ESI mass spectrum as well as a corresponding $[\text{Cu}(P^A P)]^+$ fragment at m/z 601.1 for $[\text{Cu}(\text{POP})]^+$ and 641.1 for $[\text{Cu}(\text{xantphos})]^+$, respectively and the isotope pattern was in accordance with calculations. The solution ^1H , $^{13}\text{C}\{^1\text{H}\}$ and $^{31}\text{P}\{^1\text{H}\}$ NMR spectroscopy in acetone- d_6 was consistent with the proposed structure (Scheme 2.2). The elemental composition was corroborated by elemental analysis. In addition, for $[\text{Cu}(\text{POP})(i\text{PrSPy})][\text{PF}_6]$ and $[\text{Cu}(\text{POP})(t\text{BuSPy})][\text{PF}_6]$ as well as $[\text{Cu}(\text{POP})(\text{ThPy})][\text{PF}_6]$, $[\text{Cu}(\text{POP})(\text{MeThPy})][\text{PF}_6]$,

[Cu(xantphos)(ThPy)][PF₆], [Cu(xantphos)(ThMePy)][PF₆] and [Cu(xantphos)(MeThMePy)][PF₆] crystal structures were obtained by X-ray diffraction (section 2.4).

2.3 Spatial distribution of the HOMO and LUMO

In the introduction the spatial distribution of the HOMO – mainly located on the Cu centre and the phosphane – and LUMO – primarily situated on the diimine – in [Cu(P[^]P)(N[^]N)]⁺ complexes, and the associated independent tuning of energy levels and promotion of TADF have been discussed (see sections 1.1.2a and 1.1.3c). Ground state DFT (density functional theory) calculations on [Cu(POP)(MeSPy)]⁺ (MeSPy = 2-((methylsulfanylmethyl)pyridine) demonstrated a LUMO

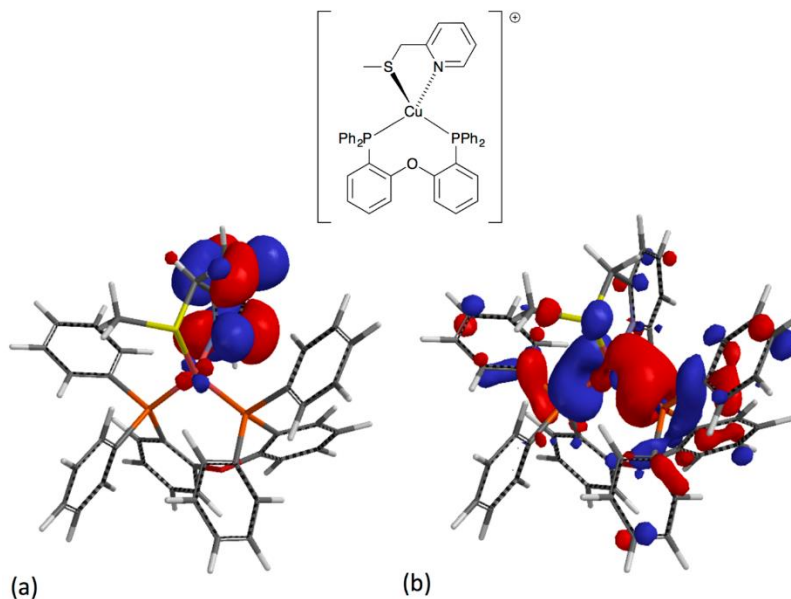


Figure 2.1: Localisation of the (a) LUMO and (b) HOMO of the model [Cu(POP)(MeSPy)]⁺ calculated at a DFT level (6-31-G* basis set in vacuum). Reproduced from reference 198 under the terms of the CC-BY license.

largely centred on the N[^]S ligand while the HOMO is located mainly on the Cu with various smaller ligand contributions (Figure 2.1). Based on these findings, and by analogy with the spatial separation of the frontier orbitals in [Cu(P[^]P)(N[^]N)]⁺, a mostly independent LUMO energy tuning should be possible.

2.4 Structural analysis

2.4.1 Solution NMR spectroscopic characterization

Unless otherwise stated, the assignment of ¹H and ¹³C{¹H} NMR spectra was carried out using COSY, NOESY, HMQC and HMBC NMR techniques.

2.4.1a ³¹P{¹H} NMR experiments

All of the complexes show characteristic ³¹P signals in the ³¹P{¹H} NMR experiment. One signal from the PF₆⁻ anion arises at δ -144.2 to -144.3 ppm as a septet. The coordinated diphosphanes give rise to a broadened signal between δ -12.6 and -15.7 ppm (see materials and methods section). Due to the remaining lone pair of the coordinated sulfur atom, the S is a stereogenic centre which can undergo inversion. If this inversion were slow on the NMR time scale this would lead to inequivalent environments

and therefore a splitting of the ^{31}P signals would occur, but this was not observed neither at 298 K nor at low temperatures of 238 K and 198 K, indicating a low energy barrier for the sulfur inversion.

On the other hand, the bridging $\text{C}(\text{Me})_2$ unit makes xantphos a less flexible diphosphane ligand than POP. It has been shown that the inversion of the xanthene 'bowl' leads to two conformers that may be distinguishable at low temperatures (Figure 2.2).^{183,216,217} At 198 K the broadened singlet for the coordinated P in $[\text{Cu}(\text{xantphos})(\text{tBuSPy})][\text{PF}_6]$ splits up into two signals with a ratio of 5:1 which is the same ratio as for the major to minor species in the ^1H NMR spectra of the same complex at 198 K (see section 2.4.1b).

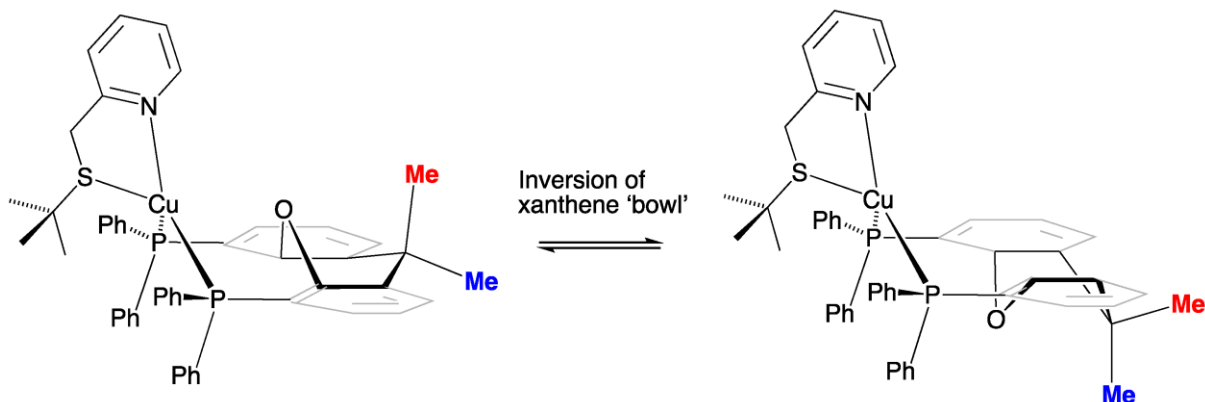


Figure 2.2: Two possible conformers of $[\text{Cu}(\text{xantphos})(\text{tBuSPy})]^+$ accessed through inversion of the xanthene unit. Reproduced from reference 198 under the terms of the CC-BY license.

2.4.2b ^1H NMR experiments

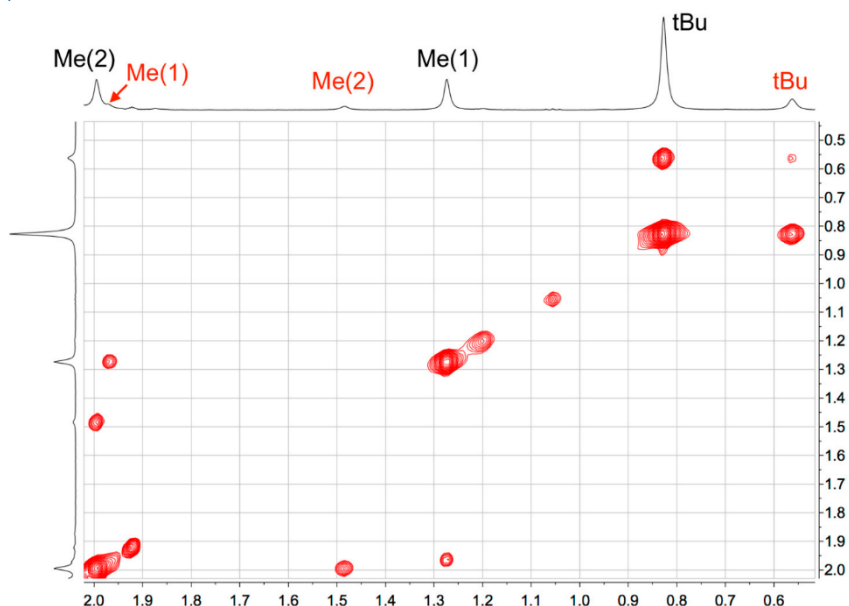


Figure 2.3: Alkyl region of the ROESY spectrum of $[\text{Cu}(\text{xantphos})(\text{tBuSPy})][\text{PF}_6]$ (500 MHz, acetone- d_6 , 238 K) showing EXSY crosspeaks between the major (black labels) and the minor (red labels) species. Chemical shifts are given in δ/ppm . Reproduced from reference 198 under the terms of the CC-BY license.

At 298 K the ^1H NMR spectra of the $[\text{Cu}(\text{P}^\wedge\text{P})(2\text{-alkylsulfanyl)methylpyridine}]^+$ complexes show sharp peaks for the N $^\wedge$ S ligand and broadened peaks for the aromatic protons of the P $^\wedge$ P ligand – in particular of the pending phenyl rings – suggesting dynamic behaviour (Figure 2.6 and 2.7). While the aliphatic region in $[\text{Cu}(\text{POP})(i\text{PrSPy})][\text{PF}_6]$ and $[\text{Cu}(\text{POP})(t\text{BuSPy})][\text{PF}_6]$ remain basically unchanged over the whole temperature range of 298 K to 238 K, the same cannot be said for the two respective xantphos complexes. Upon cooling down, the signals for the $\text{C}(\text{Me})_2$ and the $t\text{Bu}$ groups split up into two sets of signals with a ratio of 5:1 (Figure 2.3). Furthermore, ROESY NMR experiments present EXSY peaks for these two groups, showing the interconversion between two conformers. Important in that regard is the exchange peak of the inner and outer methyl group of $\text{C}(\text{Me})_2$, which is only possible with inversion of the xanthene bowl and thereby creating two conformers. On the other hand, the stereogenic sulfur centre has no apparent effect on the NMR spectrum, indicative of fast inversion at the coordinated sulfur atom at 198 K.

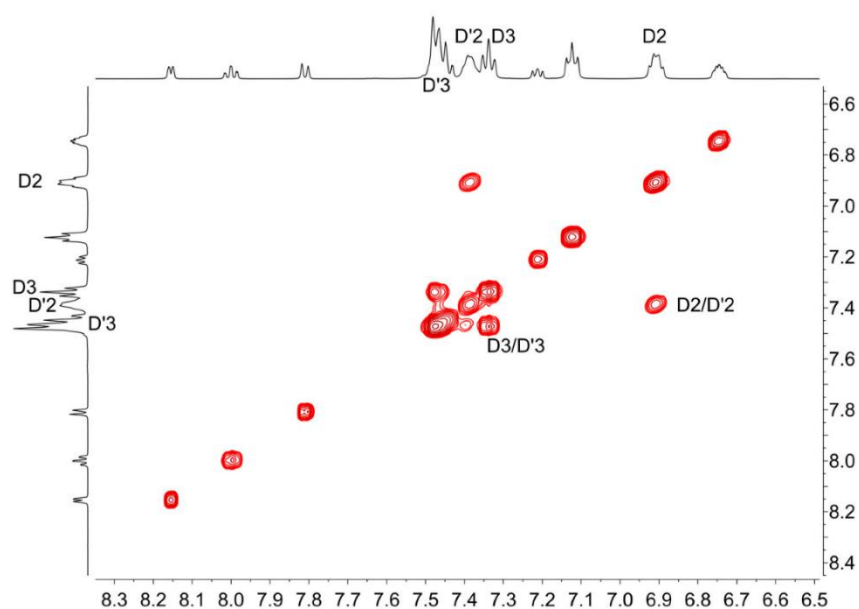


Figure 2.4: Aromatic region of the ROESY spectrum of $[\text{Cu}(\text{POP})(t\text{BuSPy})][\text{PF}_6]$ (500 MHz, acetone- d_6 , 238 K) showing EXSY crosspeaks for protons on the pending phenyl rings, for atom labelling see Scheme 2.1. Chemical shifts are given in δ/ppm . Reproduced from reference 198 under the terms of the CC-BY license.

The broad aromatic features at 298 K are partially resolved at a temperature of 238 K. For $[\text{Cu}(\text{POP})(i\text{PrSPy})][\text{PF}_6]$ and $[\text{Cu}(\text{POP})(t\text{BuSPy})][\text{PF}_6]$ two sets of signals arise from the pending phenyl rings, labelled D and D'. In ROESY at 238 K EXSY exchange peaks for the protons $\text{H}^{\text{D}2}/\text{H}^{\text{D}'2}$ and $\text{H}^{\text{D}3}/\text{H}^{\text{D}'3}$ can be found, indicating motion of the POP backbone that is frozen out at lower temperatures (Figure 2.4). In addition, a low intensity NOESY crosspeak between $\text{H}^{\text{D}2}$ and $\text{H}^{\text{A}6}$ in the spectrum of $[\text{Cu}(\text{P}^\wedge\text{P})(t\text{BuSPy})][\text{PF}_6]$ was found, while there was no correlation between $\text{H}^{\text{A}6}$ to $\text{H}^{\text{D}'2}$. This leads to the conclusion that the D rings are pointing upwards to the N $^\wedge$ S ligand with the D' rings pointing away (Figure 2.5). However, it has to be noted that for compounds with a molecular weight of around 700 g/mol, it is expected for NOESY peaks in a ROESY spectrum to have a near zero intensity.²¹⁸

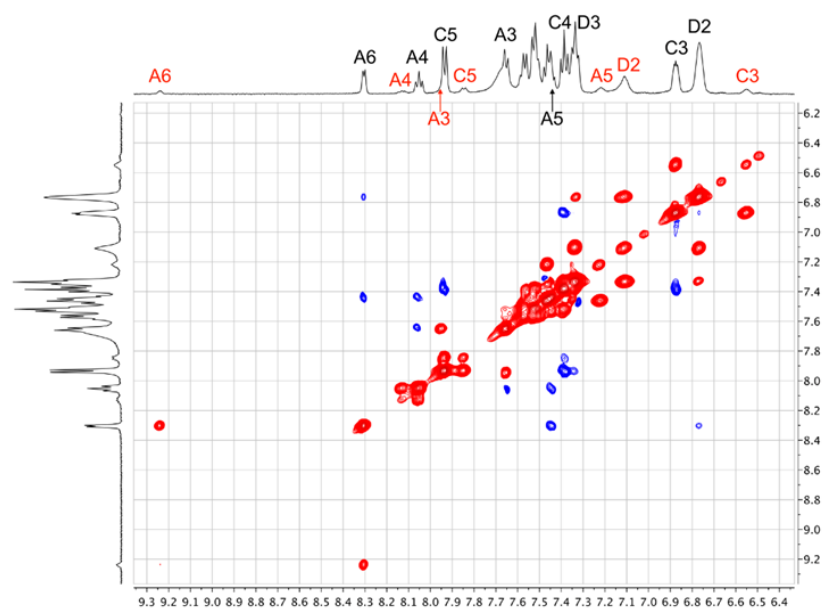


Figure 2.5: Aromatic region of the ROESY spectrum of $[\text{Cu}(\text{xantphos})(\text{tBuSPy})][\text{PF}_6]$ (500 MHz, acetone- d_6 , 198 K) showing EXSY (red) and NOESY (blue) crosspeaks. Black labels represent the major, red labels the minor species. See section 2.8.2d for full assignment of the major species, for atom labelling see Scheme 2.1. Chemical shifts are given in δ/ppm . Reproduced from reference 198 under the terms of the CC-BY license.

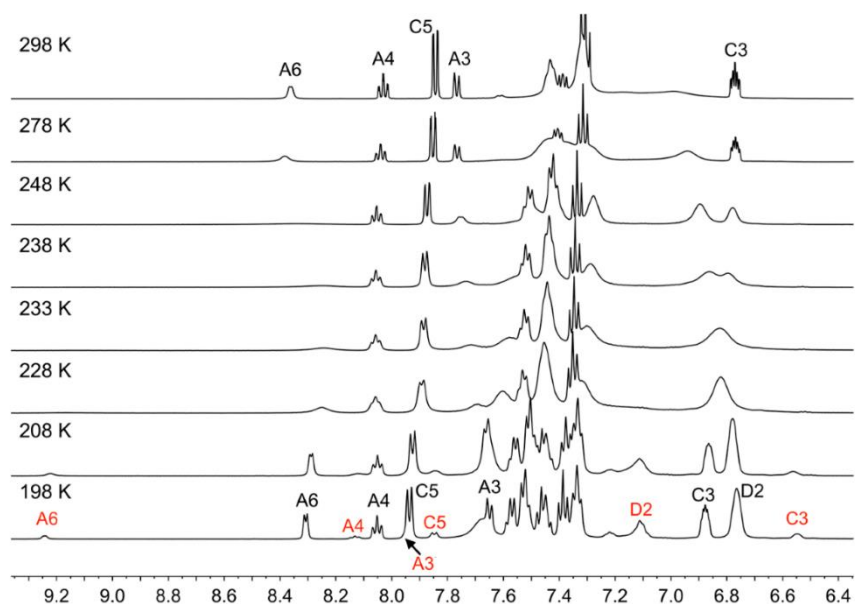


Figure 2.6: Variable temperature ^1H NMR spectra of the aromatic region of $[\text{Cu}(\text{xantphos})(\text{tBuSPy})][\text{PF}_6]$ (500 MHz, acetone- d_6). The major species at 198K is annotated with black labels, the minor species with red ones. For a full assignment of the major species see section 2.8.2d, for atom labelling see Scheme 2.1. Chemical shifts are given in δ/ppm . Reproduced from reference 198 under the terms of the CC-BY license.

As previously stated, at a temperature of 198 K the spectra of $[\text{Cu}(\text{xantphos})(i\text{PrSPy})][\text{PF}_6]$ and $[\text{Cu}(\text{xantphos})(\text{tBuSPy})][\text{PF}_6]$ split into a major and a minor species in the ratio of 5:1. EXSY peaks from the ROESY spectrum allow the identification of some peaks of the minor species, but there is still significant overlap. Therefore, only the major species was fully assigned. The correlating proton signals undergo some

significant shifts, none more so than H^{A6} of the pyridine, highlighting the different environments of the two conformers (Figure 2.6).

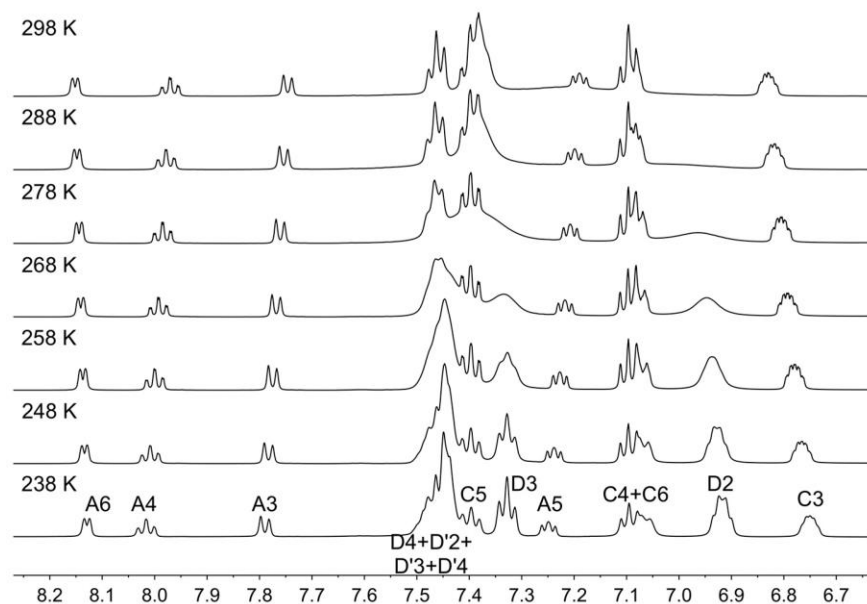


Figure 2.7: Variable temperature ¹H NMR spectra of the aromatic region of [Cu(POP)(iPrSPy)][PF₆] (500 MHz, acetone-d₆). For a full assignment of the major species see section 2.8.2a, for atom labelling see Scheme 2.1. Chemical shifts are given in δ/ppm. Reproduced from reference 198 under the terms of the CC-BY license.

The absence of H^{C6} in [Cu(xantphos)(N^{AS})] [PF₆] is consistent with the introduction of the C(Me)₂ bridge in xantphos when compared to POP (Figure 2.6 and 2.7). Similarly, the loss of the H^{A6} signal for [Cu(P^{AP})(ThMePy)][PF₆] and [Cu(P^{AP})(MeThMePy)][PF₆], as well as the loss of the H^{B5} signal for [Cu(P^{AP})(MeThPy)][PF₆] and [Cu(P^{AP})(MeThMePy)][PF₆] are in agreement with the introduction of a methyl group at the respective positions of the 2-(thiophen-2-yl)pyridine ligands. The H^{Me-B5} methyl group in [Cu(POP)(MeThMePy)][PF₆] gives rise to a doublet with a coupling constant of $J_{H-H} = 0.8$ Hz, which is confirmed by a COSY crosspeak to H^{B4}. This coupling was not observed in [Cu(xantphos)(MeThMePy)][PF₆] nor in [Cu(POP)(MeThPy)][PF₆] or [Cu(xantphos)(MeThPy)][PF₆]. A big difference in the ¹H NMR spectra between the 2-(alkylsulfanylmethyl)pyridine and the 2-(thiophen-2-yl)pyridine-derivative complexes is the resolution of the aromatic proton signals of the P^{AP} ligands, which are well resolved for the latter and broadened for the former at 298 K (Figures 2.6 – 2.8). This is indicative of higher energy barriers for dynamic processes for complexes with the 2-(thiophen-2-yl)pyridine ligands compared to those with the 2-(alkylsulfanylmethyl)pyridine ligands.

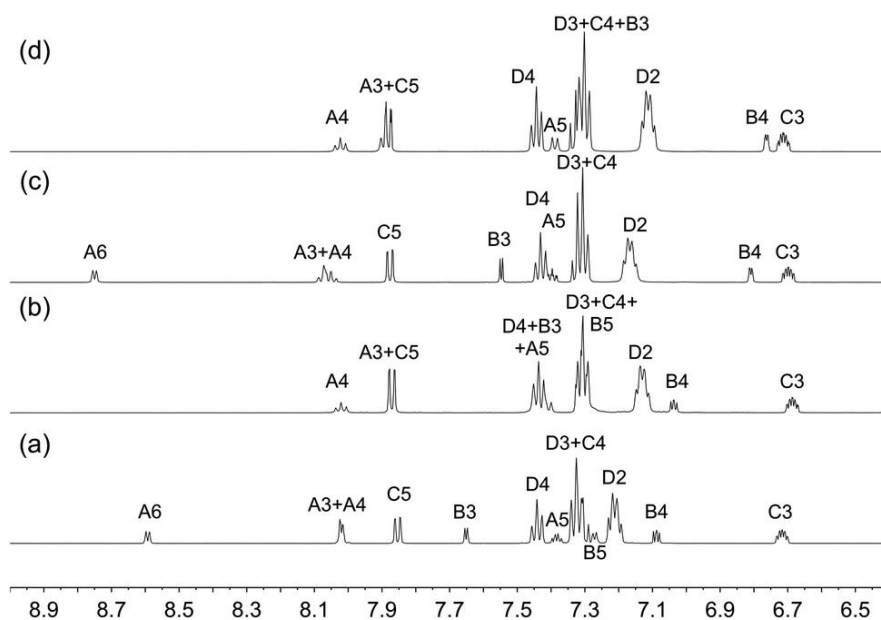


Figure 2.8: Aromatic region in the ^1H NMR spectra (500 MHz, acetone- d_6 , 298 K) of (a) $[\text{Cu}(\text{xantphos})(\text{ThPy})][\text{PF}_6]$, (b) $[\text{Cu}(\text{xantphos})(\text{ThPy})][\text{PF}_6]$, (c) $[\text{Cu}(\text{xantphos})(\text{ThPy})][\text{PF}_6]$ and (d) $[\text{Cu}(\text{xantphos})(\text{ThPy})][\text{PF}_6]$. For atom labelling see Scheme 2.1. Chemical shifts are given in δ/ppm . Reproduced from reference 197 under the terms of the CC-BY-NC license.

2.4.2 Crystal structures

Table 2.1: Crystallographic data for [Cu(P[^]P)(N[^]S)][PF₆] compounds.

Compounds	[Cu(POP)(iPrSPy)][PF ₆]	[Cu(POP)(tBuSPy)][PF ₆]
Formula	C ₄₅ H ₄₁ CuF ₆ NOP ₃ S	C ₄₆ H ₄₀ CuF ₆ NOP ₃ S,
Formula weight	914.35	928.37
Crystal colour and habit	Colourless block	Colourless block
Crystal system	Monoclinic	Monoclinic
Space group	<i>P</i> 2 ₁ / <i>c</i>	<i>P</i> 2 ₁ / <i>c</i>
<i>a</i> , <i>b</i> , <i>c</i> /Å	14.0474(11), 17.4236(14), 18.3028(13)	13.8102(4), 18.4985(6), 18.0974(6)
α , β , γ /°	90, 109.786(2), 90	90, 107.74558(16), 90
<i>V</i> /Å ³	4215.2(6)	4403.3(2)
<i>D_c</i> /Mg m ⁻³	1.441	1.400
<i>Z</i>	4	4
μ (Cu-K α)/mm ⁻¹	2.81	2.699
<i>T</i> /K	123	123
Refln. collected (<i>R</i> _{int})	33404 (0.028)	25698 (0.030)
Unique refln.	7650	7939
Refln. for refinement	7275	6739
Parameters	541	532
Threshold	2 σ	2 σ
<i>R</i> ₁ (<i>R</i> ₁ all data)	0.0743 (0.0762)	0.0530 (0.0617)
<i>wR</i> ₂ (<i>wR</i> ₂ all data)	0.1724 (0.1724)	0.1350 (0.1388)
Goodness of fit	0.9944	0.9911
CCDC REFCODE	KOXHUD	KOXJAL

Compounds	[Cu(POP)(ThPy)][PF ₆]	[Cu(POP)(MeThPy)][PF ₆]-CH ₂ Cl ₂	[Cu(xantphos)(ThPy)][PF ₆]
Formula	C ₄₅ H ₃₅ CuF ₆ NOP ₃ S	C ₄₇ H ₃₉ Cl ₂ CuF ₆ NOP ₃ S	C ₄₈ H ₃₉ CuF ₆ NOP ₃ S
Formula weight	908.3	1007.2	948.36
Crystal colour and habit	Colourless block	Colourless needle	Colourless block
Crystal system	Triclinic	Triclinic	Monoclinic
Space group	<i>P</i> -1	<i>P</i> -1	<i>P</i> 2 ₁ / <i>n</i>
<i>a</i> , <i>b</i> , <i>c</i> /Å	10.8352(14), 12.0146(15), 16.754(2)	10.5738(10), 12.4356(12), 18.8853(17)	10.5055(13), 21.487(3), 19.094(2)
α , β , γ /°	92.081(3), 98.546(3), 107.937(3)	71.646(3), 75.679(3), 70.826(3)	90, 95.118(4), 90
<i>V</i> /Å ³	2044.2(4)	2197.3(4)	4293.0(9)
<i>D_c</i> /Mg m ⁻³	1.476	1.522	1.467
<i>Z</i>	2	2	4
μ (Cu-K α)/mm ⁻¹	2.897	3.848	2.785
<i>T</i> /K	123	130	123
Refln. collected (<i>R</i> _{int})	26 148 (0.027)	28 575 (0.027)	56 802 (0.033)
Unique refln.	7456	7961	7797
Refln. for refinement	7376	7776	7732
Parameters	523	669	602
Threshold	2 σ	2 σ	2 σ
<i>R</i> ₁ (<i>R</i> ₁ all data)	0.0388 (0.0389)	0.0383 (0.0390)	0.0504 (0.0505)
<i>wR</i> ₂ (<i>wR</i> ₂ all data)	0.0933 (0.0933)	0.0922 (0.0927)	0.0877 (0.0877)
Goodness of fit	0.9868	1.05	0.9592
CCDC REFCODE	POFQUZ	POFQEJ	POFQIN

Single crystals of [Cu(POP)(iPrSPy)][PF₆] and [Cu(POP)(tBuSPy)][PF₆] were grown by diffusion of diethyl ether (Et₂O) in acetone solutions of the complexes, while [Cu(POP)(ThPy)][PF₆], [Cu(POP)(MeThPy)][PF₆], [Cu(xantphos)(ThMePy)][PF₆] and [Cu(xantphos)(MeThMePy)][PF₆] were grown from diffusion Et₂O into a CH₂Cl₂ solution of the complexes. The κ^2 binding mode for N[^]S ligands was confirmed in crystal structures of [Cu(POP)(iPrSPy)][PF₆] and [Cu(POP)(tBuSPy)][PF₆] as well as [Cu(POP)(ThPy)][PF₆], [Cu(POP)(MeThPy)][PF₆], [Cu(xantphos)(ThPy)][PF₆], [Cu(xantphos)(ThMePy)][PF₆] and [Cu(xantphos)(MeThMePy)][PF₆].

Table 2.1 (continuation): Crystallographic data for $[\text{Cu}(\text{P}^{\wedge}\text{P})(\text{N}^{\wedge}\text{S})][\text{PF}_6]$ compounds.

Compounds	$[\text{Cu}(\text{xantphos})(\text{ThMePy})][\text{PF}_6]$	$[\text{Cu}(\text{xantphos})(\text{MeThMePy})][\text{PF}_6]$	$[\text{Cu}(\text{xantphos})(\text{NCMe}_2)_2][\text{PF}_6] \cdot 0.5\text{Et}_2\text{O}$
Formula	$\text{C}_{49}\text{H}_{41}\text{CuF}_6\text{NOP}_3\text{S}$	$\text{C}_{50}\text{H}_{43}\text{CuF}_6\text{NOP}_3\text{S}$	$\text{C}_{45}\text{H}_{43}\text{CuF}_6\text{N}_2\text{O}_{1.5}\text{P}_3$
Formula weight	962.39	976.36	863.42
Crystal colour and habit	Colourless block	Colourless plate	Colourless plate
Crystal system	Orthorhombic	Triclinic	Triclinic
Space group	<i>Pbca</i>	<i>P-1</i>	<i>P-1</i>
<i>a</i> , <i>b</i> , <i>c</i> /Å	19.1120(14), 20.3777(15), 22.2356(16)	11.5350(5), 12.1924(6), 17.0548(8)	9.7193(10), 14.8522(17), 17.864(2)
α , β , γ /°	90, 90, 90	82.221(3), 71.606(3), 88.977(3)	110.080(5), 99.380(5), 102.758(5)
<i>V</i> /Å ³	8659.8(11)	2254.30(19)	2280.5(4)
<i>D_c</i> /Mg m ⁻³	1.476	1.438	1.257
<i>Z</i>	8	2	2
$\mu(\text{Cu-K}\alpha)$ /mm ⁻¹	2.769	2.668	2.188
<i>T</i> /K	130	130	130
Refln. collected (<i>R</i> _{int})	38 128 (0.033)	27 121 (0.045)	25 739 (0.0412)
Unique refln.	7944	8187	8116
Refln. for refinement	7100	6150	7338
Parameters	559	572	554
Threshold	2 σ	2 σ	2 σ
<i>R</i> ₁ (<i>R</i> ₁ all data)	0.0338 (0.0382)	0.0603 (0.0842)	0.0789 (0.0839)
<i>wR</i> ₂ (<i>wR</i> ₂ all data)	0.0868 (0.0903)	0.1525 (0.1695)	0.2135 (0.2179)
Goodness of fit	0.9988	1.025	1.114
CCDC REFCODE	POFRAG	POFQOT	POFROU

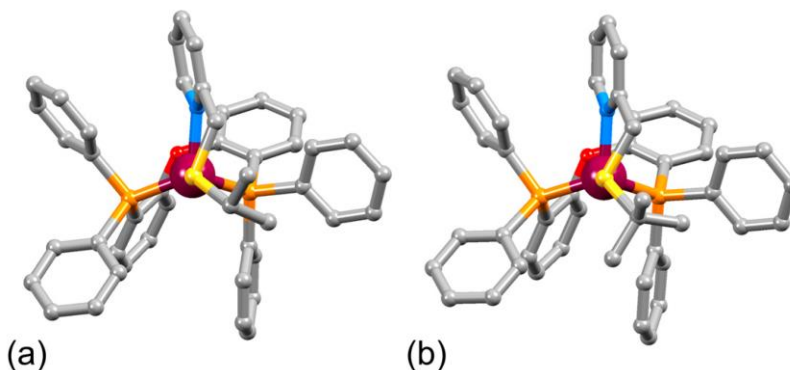


Figure 2.9: View along the S–Cu bond of the crystal structures of (a) $[\text{Cu}(\text{POP})(i\text{PrSPy})]^+$ and (b) $[\text{Cu}(\text{POP})(t\text{BuSPy})]^+$. H atoms are omitted for clarity. Reproduced from reference 198 under the terms of the CC-BY license.

$[\text{Cu}(\text{POP})(i\text{PrSPy})][\text{PF}_6]$ and $[\text{Cu}(\text{POP})(t\text{BuSPy})][\text{PF}_6]$ crystallise in the monoclinic $P2_1/c$ space group. The phenyl ring involving C40 in $[\text{Cu}(\text{POP})(i\text{PrSPy})][\text{PF}_6]$ exhibited disorder and was modelled over two sites. Both complexes are chiral and the two enantiomers for each are present in the unit cell. Intracation π –stacking interactions between aromatic rings, as is observed in a number of $[\text{Cu}(\text{P}^{\wedge}\text{P})(\text{N}^{\wedge}\text{N})]^+$ cations,^{103,155} is not observed in either $[\text{Cu}(\text{POP})(i\text{PrSPy})]^+$ or $[\text{Cu}(\text{POP})(t\text{BuSPy})]^+$. It has to be noted that no intra-cation π –stacking of aromatic rings were observed in the PM3 optimized geometry of $[\text{Cu}(\text{POP})(\text{MeSPy})]^+$.

$[\text{Cu}(\text{xantphos})(\text{ThMePy})][\text{PF}_6]$ crystallises in the orthorhombic *Pbca* group, while $[\text{Cu}(\text{xantphos})(\text{ThPy})][\text{PF}_6]$ crystallises in the monoclinic $P2_1/n$ space group. $[\text{Cu}(\text{POP})(\text{ThPy})][\text{PF}_6]$, $[\text{Cu}(\text{POP})(\text{MeThPy})][\text{PF}_6]$ and $[\text{Cu}(\text{xantphos})(\text{MeThMePy})][\text{PF}_6]$ crystallise in the triclinic space group *P-1*. Unit cell dimensions can be found in Table 2.2 and angles and bond lengths surrounding the Cu centre can be found in Table 2.3. Each of the copper atoms is in a distorted tetrahedral environment. Houser *et al.* defined the τ_4 parameter as a function of the angles α and β (with α and β being the two largest angle θ around the metal centre (Equation 2.1), which gives a measurement of the distortion of the tetrahedron.

$$\tau_4 = \frac{360^\circ - (\alpha + \beta)}{144^\circ} \quad (2.1)$$

For a perfect tetrahedral geometry with α and $\beta = 109.5^\circ$ the equation returns a value of 1 while, for a square planar geometry $\tau_4 = 0$. The τ_4 values between 0.76 and 0.89 for the $[\text{Cu}(\text{P}^\wedge\text{P})(\text{N}^\wedge\text{S})]$ cations indicate a trigonal pyramidal (C_{3v} , $\tau_4 = 0.85$) type geometry.²¹⁹

Table 2.2: Bond angles and bond lengths surrounding the Cu(I) centre. ^a τ_4 parameter as defined by Houser et al..²¹⁹ ^b values measured in Mercury due to disorder of the *iPrSPy* ligand.⁸⁻¹⁰

Cation in [Cu(P [∧] P)(N [∧] S)][PF ₆]	P–Cu–P/ ^o	N–Cu–S/ ^o	N–Cu–P/ ^o	S–Cu–P/ ^o	τ_4^a	P–Cu/Å	N–Cu/Å	S–Cu/Å
[Cu(POP)(<i>iPrSPy</i>)] ⁺	111.84(4)	82.56/ 84.01 ^b	115.91/106.61/ 104.79/112.86 ^b	114.22(5)/ 123.57(5)	0.92/ 0.88	2.2550(10)/ 2.2722(11)	2.114(5)	2.3229(12)
[Cu(POP)(<i>t</i> BuSPy)] ⁺	110.81(3)	83.17(7)	107.337(7)/ 111.10(7)	113.79(3)/ 126.12(3)	0.85	2.2584(7)/ 2.2817(8)	2.0999(2)	2.3332(7)
[Cu(POP)(ThPy)] ⁺	115.38(2)	81.34(5)	110.83(5)/ 115.14(5)	110.02(2)/ 119.44(2)	0.89	2.2406(5)/ 2.2655(5)	2.0640(15)	2.4470(5)
[Cu(POP)(MeThPy)] ⁺	116.02(2)	78.2(3)	116.9(3)/ 123.4(3)	100.95(4)/ 110.40(5)	0.85	2.2649(6)/ 2.2770(6)	2.151(9)	2.5567(16)
[Cu(xantphos)(ThPy)] ⁺	117.89(2)	80.52(5)	112.83(5)/ 128.30(5)	96.66(2)/ 103.47(2)	0.81	2.2534(6)/ 2.2897(7)	2.013(2)	2.6403(9)
[Cu(xantphos)(ThMePy)] ⁺	127.804(19)	80.34(5)	102.04(4)/ 124.62(4)	99.701(19)/ 109.172(19)	0.76	2.660(5)/ 2.2874(5)	2.0558(16)	2.5789(6)
[Cu(xantphos)(MeThMePy)] ⁺	120.86(4)	79.40(10)	111.35(10)/ 121.48(10)	96.23(4)/ 118.75(4)	0.83	2.2559(11)/ 2.2621(11)	2.044(3)	2.6780(12)

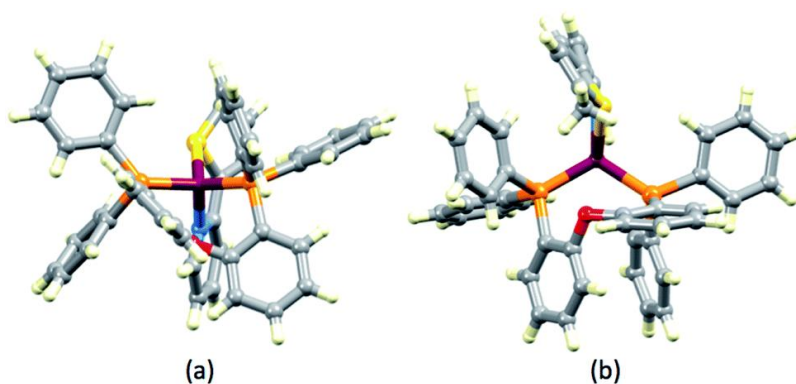


Figure 2.10: Crystal structure of (a) $[\text{Cu}(\text{POP})(\text{ThPy})]^+$ and (b) $[\text{Cu}(\text{POP})(\text{MeThPy})]^+$, highlighting the pseudo-tetrahedral Cu(I) centre in (a), the twisted nature of MeThPy in (b) and the stereogenic coordinated S-atoms in both. Reproduced from reference 197 under the terms of the CC-BY-NC license.

In Figure 2.10 the structures of $[\text{Cu}(\text{POP})(\text{ThPy})]^+$ and $[\text{Cu}(\text{POP})(\text{MeThPy})]^+$ highlight the pseudo-tetrahedral geometry in the former and the twisting of the 2-(5-methylthiophen-2-yl)pyridine ligand in the latter. The distortion of the 2-(thiophen-2-yl)pyridines are found in all five complexes with a coordinated 2-(thiophen-2-yl)pyridine derivative and can be associated with the sulfur lone pair (Figure 2.10). Its deviation from planarity can be exemplified by measuring the angle between the least squares plane of the thiophene and pyridine ring. The smallest distortion is measured for the MeThPy with 17.4° while the largest twist is found in MeThMePy with an angle between the least squares planes of 32.1° . These compare to angles of 4.8° and 7.8° for bpy and 6,6'-dimethylbipyridine (Me_2bpy) respectively in $[\text{Cu}(\text{POP})(\text{bpy})][\text{PF}_6]$ and $[\text{Cu}(\text{xantphos})(\text{Me}_2\text{bpy})][\text{PF}_6]$.^{178,217}

The large N–Cu–P angle in $[\text{Cu}(\text{xantphos})(\text{ThPy})][\text{PF}_6]$ can be explained with tight anion⋯cation binding. The PF_6^- anion sits in a pocket between the phenyl and pyridine rings with C–H⋯F contacts in the range of 2.48–2.82 Å (Figure 2.11), with the van der Waals radii of H and F between 1.10–1.20 and 1.35–1.47 Å, respectively.²²⁰ However, the crystal packing in $[\text{Cu}(\text{P}^{\wedge}\text{P})(\text{N}^{\wedge}\text{N})][\text{PF}_6]$ unavoidably involves extensive to close C–H⋯F interactions. Only in $[\text{Cu}(\text{POP})(\text{MeThPy})][\text{PF}_6]$ solvent molecules are incorporated in the crystal lattice. Furthermore, close Cu–O contacts within the sum of van der Waals radii for Cu and O (using the radii for Cu from Batsanov²²⁰ and Hu²²¹) are found for all $[\text{Cu}(\text{P}^{\wedge}\text{P})(\text{N}^{\wedge}\text{S})][\text{PF}_6]$ complexes with 2-(thiophen-2-yl)pyridine ligands. For $[\text{Cu}(\text{xantphos})(\text{ThMePy})][\text{PF}_6]$ and $[\text{Cu}(\text{POP})(\text{ThPy})][\text{PF}_6]$ these contacts are particularly close with 2.8260(13) Å and 2.8405(13) Å, while for $[\text{Cu}(\text{xantphos})(\text{ThPy})][\text{PF}_6]$ (3.008(2) Å), $[\text{Cu}(\text{POP})(\text{MeThPy})][\text{PF}_6]$ (3.019(1) Å) and $[\text{Cu}(\text{xantphos})(\text{MeThMePy})][\text{PF}_6]$ (3.066(3) Å) the distances are a bit larger.

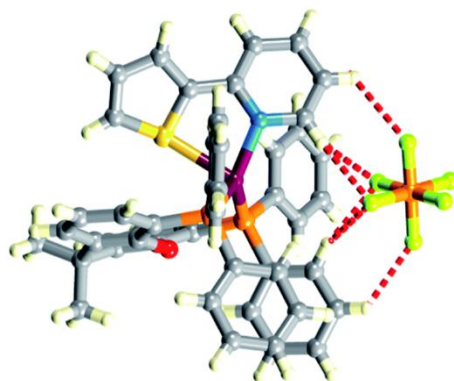


Figure 2.11: Crystal structure of $[\text{Cu}(\text{xantphos})(\text{ThPy})][\text{PF}_6]$, emphasizing the close cation⋯anion C–H⋯F contacts. Reproduced from reference 197 under the terms of the CC-BY-NC license.

The $\text{N}^{\wedge}\text{S}$ ligands of $[\text{Cu}(\text{POP})(\text{MeThPy})][\text{PF}_6]$ and $[\text{Cu}(\text{xantphos})(\text{ThPy})][\text{PF}_6]$ show disorder in the orientation of the $\text{N}^{\wedge}\text{S}$ ligand, once facing towards and once away from the O atom of POP and have been modelled over two sites with 0.8:0.2 and 0.75:0.25 occupancies respectively. As discussed earlier, the backbone of xantphos is structurally more rigid and features the xanthene bowl (Figure 2.2). It has been shown that the preferred orientation for 6-methylpyridine (Mebpy) and 6-ethylpyridine (Etbpy) in $[\text{Cu}(\text{xantphos})(\text{N}^{\wedge}\text{N})][\text{PF}_6]$ complexes is such that the alkyl substituent lies over the xanthene bowl,²¹⁷ and the same behaviour is found in $[\text{Cu}(\text{xantphos})(\text{ThMePy})][\text{PF}_6]$ and $[\text{Cu}(\text{xantphos})(\text{MeThMePy})][\text{PF}_6]$ (Figure 2.12).

The ligand disorder of ThPy in $[\text{Cu}(\text{xantphos})(\text{ThPy})][\text{PF}_6]$ imply that there is little energy difference for the two orientations in the crystal lattice for ligands without substituents.

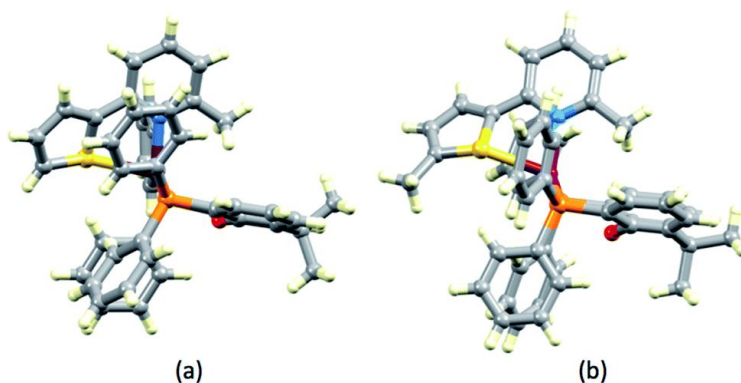


Figure 2.12: Crystal structures of [Cu(xantphos)(ThMePy)]⁺ and (b) of [Cu(xantphos)(MeThMePy)]⁺ showing the positioning of the 6-methyl group of the pyridine of the N[^]S ligands situated over the xanthene 'bowl'. Reproduced from reference 197 under the terms of the CC-BY-NC license.

2.5 Electrochemistry

The electrochemical properties of [Cu(P[^]P)(N[^]S)][PF₆] complexes were investigated using cyclic voltammetry and the cyclic voltammograms (CVs) were referenced to the Fc/Fc⁺ (ferrocene/ferrocenium) redox couple = 0 V. Measurements were carried out in CH₂Cl₂ solution with [tBuN][PF₆] as supporting electrolyte. All of the complexes feature a partially reversible or irreversible oxidation process between +0.79 V and +1.11 V. This is assigned to the Cu⁺/Cu²⁺ oxidation process. In comparison, the Cu⁺/Cu²⁺ oxidation potentials for the benchmark [Cu(POP)(bpy)][PF₆] and [Cu(xantphos)(bpy)][PF₆] are slightly lower with +0.72 V and +0.76 V, respectively.¹¹⁴ This observation can be rationalized by the interplay of two opposing effects. While the change from an N[^]N to a less π-accepting N[^]S ligand should result in an easier Cu⁺ → Cu²⁺ oxidation, on the other hand, the soft S-donor favours the soft Cu(I) oxidation state. Furthermore, Sivasankar *et al.* performed DFT ground state calculations on a Cu(I) centre with different numbers of soft (PH₃ and H₂S) and hard (NH₃, H₂O) electron donors. Their calculations led to the conclusion Cu(I) preferred three soft and one hard donor atoms,²²² which in the case of the [Cu(P[^]P)(N[^]S)][PF₆] would be met. However, it has to be noted that the ligands used for the calculations are simple, monodentate ligands and are not good representatives of the used N[^]S ligands. Additionally, it was shown that the used 6-31G(d,p) and 6-31G basis sets were not able to accurately predict various parameters for transition metals, especially of later rows.^{223,224} Therefore, while Sivasankar's findings are certainly interesting and may give an additional clue why the Cu⁺/Cu²⁺ oxidation potential is shifted to higher potentials, they need to be considered with caution. A second, irreversible oxidation is observed if the forward CV scan is taken beyond +1.1 V for [Cu(P[^]P)((2-(alkylsulfanyl)methyl)pyridine)][PF₆] and past + 1.2 V for [Cu(P[^]P)(N[^]S)][PF₆] (where N[^]S is a 2-(thiophen-2-yl)pyridine derivative), which is assigned to phosphane oxidation.

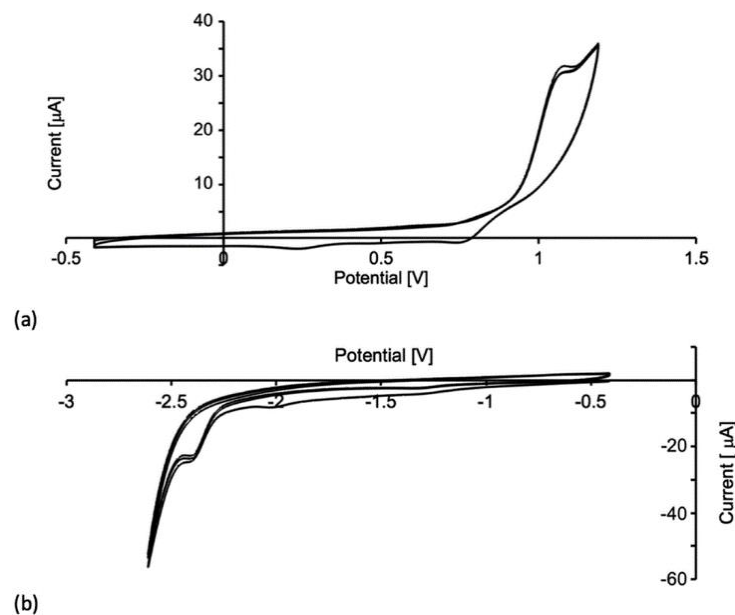


Figure 2.13: Three successive cycles in the voltammogram of $[\text{Cu}(\text{xantphos})(\text{MeThMePy})][\text{PF}_6]$ in CH_2Cl_2 ($c \approx 2 \times 10^{-5} \text{ M}$, referenced to $\text{Fc}/\text{Fc}^+ = 0\text{V}$, $[\text{nBu}_4\text{N}][\text{PF}_6]$ as supporting electrolyte, scan rate = 0.1 V s^{-1}). (a) oxidative scans to $+1.2 \text{ V}$, (b) reductive scans to -2.6 V . Reproduced from reference 197 under the terms of the CC-BY-NC license.

Irreversible reduction processes of the N^{^S} ligand are only observed for $[\text{Cu}(\text{POP})(\text{ThMePy})][\text{PF}_6]$ at -2.37 V and for $[\text{Cu}(\text{xantphos})(\text{MeThMePy})][\text{PF}_6]$ and $[\text{Cu}(\text{xantphos})(\text{MeThMePy})][\text{PF}_6]$ at -2.40 V while the remaining complexes show only poorly resolved or no reduction processes in the solvent accessible window.

All cyclic voltammetry data are summarised in Table 2.3 and a representative example of the positive and negative scan cyclic voltammograms, exemplified by $[\text{Cu}(\text{xantphos})(\text{MeThMePy})][\text{PF}_6]$, is given in Figure 2.13.

Table 2.3: Cyclic voltammetry data for $[\text{Cu}(\text{P}^\wedge\text{P})(\text{N}^\wedge\text{S})][\text{PF}_6]$ complexes in CH_2Cl_2 ($1 - 5 \times 10^{-3} \text{ M}$, referenced to internal $\text{Fc}/\text{Fc}^+ = 0.0 \text{ V}$, $[\text{nBu}_4\text{N}][\text{PF}_6]$ as supporting electrolyte, scan rate = 0.1 V s^{-1}). *irrev* = irreversible.

Compounds	Oxidative Process			Reductive Processes
	$E_{1/2}^{\text{ox}}/\text{V}$	E_{pc}/V	$E_{\text{pc}} - E_{\text{pa}}/\text{mV}$	E_{pa}/V
$[\text{Cu}(\text{POP})(i\text{PrSPy})][\text{PF}_6]$	+0.86		220	
$[\text{Cu}(\text{POP})(t\text{BuSPy})][\text{PF}_6]$		+0.96 (irrev)		
$[\text{Cu}(\text{xantphos})(i\text{PrSPy})][\text{PF}_6]$	+1.02		220	
$[\text{Cu}(\text{xantphos})(t\text{BuSPy})][\text{PF}_6]$	+0.92		240	
$[\text{Cu}(\text{POP})(\text{ThPy})][\text{PF}_6]$	+0.79		210	
$[\text{Cu}(\text{POP})(\text{ThMePy})][\text{PF}_6]$	+0.89		265	-2.37 (irrev)
$[\text{Cu}(\text{POP})(\text{MeThPy})][\text{PF}_6]$	+0.84		240	
$[\text{Cu}(\text{POP})(\text{MeThMePy})][\text{PF}_6]$		+1.11 (irrev)		
$[\text{Cu}(\text{xantphos})(\text{ThPy})][\text{PF}_6]$		+1.06 (irrev)		
$[\text{Cu}(\text{xantphos})(\text{ThMePy})][\text{PF}_6]$		+1.11 (irrev)		
$[\text{Cu}(\text{xantphos})(\text{MeThPy})][\text{PF}_6]$	+0.95		245	-2.40 (irrev)
$[\text{Cu}(\text{xantphos})(\text{MeThMePy})][\text{PF}_6]$	+0.92		310	-2.40 (irrev)

2.6 Photophysical properties

2.6.1 UV-VIS absorption spectra

Solution absorption spectra for $[\text{Cu}(\text{P}^{\wedge}\text{P})(\text{N}^{\wedge}\text{S})][\text{PF}_6]$ were recorded in CH_2Cl_2 , since acetone (solvent used for NMR spectroscopy) is not suitable because of the cut-off at 330 nm. All complexes feature high energy absorptions assigned to spin allowed $\pi^* \leftarrow \pi$ and $\pi^* \leftarrow n$ transitions. (Figure 2.14 and Table 2.5) It can be clearly seen that the introduction of a second aromatic ring red shifts the absorptions and leads to higher molar extinction coefficients ϵ (Table 2.5). Compared to the absorption maxima ($\lambda_{\text{abs}}^{\text{max}}$) of $[\text{Cu}(\text{POP})(\text{bpy})][\text{PF}_6]$ and $[\text{Cu}(\text{xantphos})(\text{bpy})][\text{PF}_6]$,¹¹⁴ the $\lambda_{\text{abs}}^{\text{max}}$ of the $[\text{Cu}(\text{P}^{\wedge}\text{P})(\text{N}^{\wedge}\text{S})][\text{PF}_6]$ compounds are blue shifted.

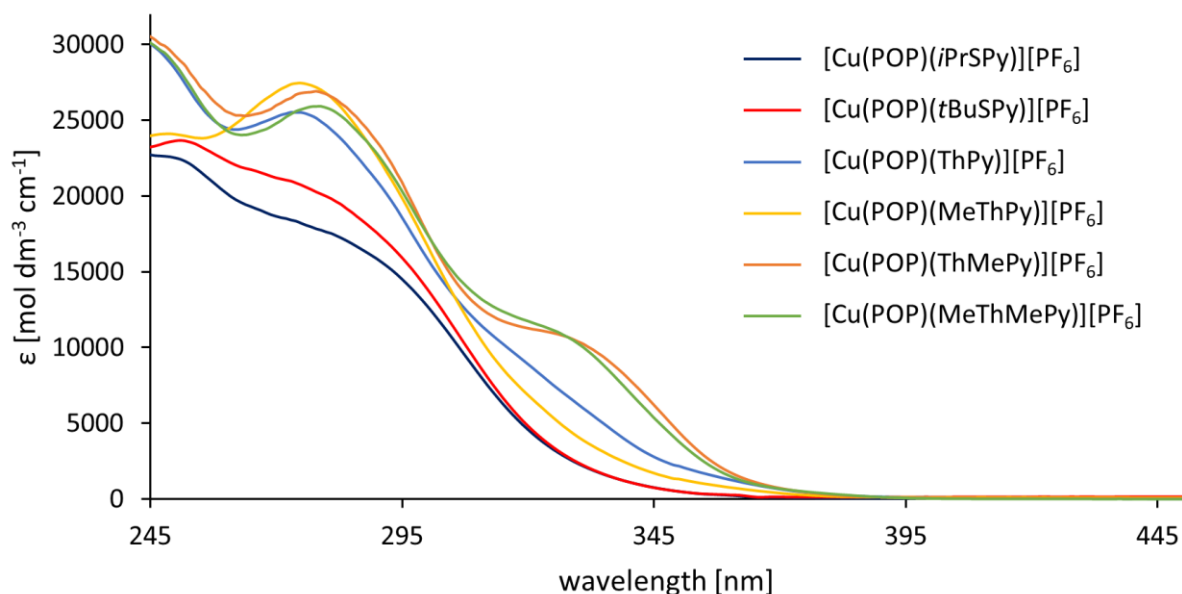


Figure 2.14: UV-Vis absorption spectra of $[\text{Cu}(\text{POP})(\text{N}^{\wedge}\text{S})][\text{PF}_6]$ complexes in CH_2Cl_2 with $c = 2.5 \times 10^{-5} \text{ M}$ for $[\text{Cu}(\text{POP})(i\text{PrSPy})][\text{PF}_6]$ and $[\text{Cu}(\text{POP})(t\text{BuSPy})][\text{PF}_6]$, for all other complexes $c = 5 \times 10^{-5} \text{ M}$.

2.6.2 Emission properties

A summary of emission properties for all [Cu(P[^]P)(N[^]S)][PF₆] compounds can be found in Table 2.4.

Table 2.4: Summary of the photophysical data for [Cu(P[^]P)(N[^]S)][PF₆] complexes at room temperature. ^ac = 2.5 × 10⁻⁵ M. ^bc = 5 × 10⁻⁵ M. ^cnon-emissive. ^dλ_{exc} = 250, 275, 320 or 360 nm. ^eλ_{exc} = 360 nm. ^fλ_{exc} = 280 nm. ^gλ_{exc} = 365 nm.

Compounds	Absorption λ _{abs} ^{max} /nm (ε _{max} /dm ³ mol ⁻¹ cm ⁻¹)	Emission			
		Deaerated Solution		Powder	
		λ _{em} ^{max} /nm	PLQY/%	λ _{em} ^{max} /nm ^f	PLQY/%
[Cu(POP)(iPrSPy)][PF ₆]	248 (22600), 280 (17600) ^a	c	c	470	<1 ^f
[Cu(POP)(tBuSPy)][PF ₆]	250 (23600), 275 (20700) ^a	c	c	490	<1 ^f
[Cu(xantphos)(iPrSPy)][PF ₆]	269 (24300) ^a	c	c	475	<2 ^f
[Cu(xantphos)(tBuSPy)][PF ₆]	272 (26600) ^a	c	c	490	<1 ^f
[Cu(POP)(ThPy)][PF ₆]	275 (25500) ^b	394, 352 ^d	<1 ^e	547	<1 ^g
[Cu(POP)(ThMePy)][PF ₆]	275 (27500) ^b	399, 354 ^d	30.8 ^e	555	3.1 ^g
[Cu(POP)(MeThPy)][PF ₆]	278 (26900), 327 (10400) ^b	414, 369 ^d	1.5 ^e	569	<1 ^g
[Cu(POP)(MeThMePy)][PF ₆]	279 (25900), 327 (10800) ^b	413, 360 ^d	33.2 ^e	546	<1 ^g
[Cu(xantphos)(ThPy)][PF ₆]	277 (33500), 326 (11500) ^b	392, 358 ^d	4.5 ^e	555	10.8 ^g
[Cu(xantphos)(ThMePy)][PF ₆]	275 (32900), 326 sh (7700) ^b	394, 355 ^d	4.8 ^e	552	4.7 ^g
[Cu(xantphos)(MeThPy)][PF ₆]	277 (32800), 329 (11300) ^b	418, 367 ^d	4.5 ^e	555	9.4 ^g
[Cu(xantphos)(MeThMePy)][PF ₆]	277 (33600), 329 (11300) ^b	422, 369 ^d	17.2 ^e	560	2.9 ^g

2.6.2a Solution emission properties of [Cu(P[^]P)(N[^]S)][PF₆] with 2-(alkylsulfanyl)pyridine ligands

[Cu(P[^]P)(iPrSPy)][PF₆] and [Cu(P[^]P)(tBuSPy)][PF₆] are non-emissive in argon purged CH₂Cl₂ solution.

2.6.2b Solution emission properties of [Cu(P[^]P)(N[^]S)][PF₆] with 2-(thiophen-2-yl)pyridine ligands

All [Cu(P[^]P)(N[^]S)][PF₆] complexes are blue emitters in argon purged CH₂Cl₂ solution and exhibit a dual emission with an λ_{em}^{max} between 352–369 nm for the higher energy band and 394–422 nm for the lower energy band. In all of these complexes, except [Cu(xantphos)(ThMePy)][PF₆], the lower energy band is dominant (Figure 2.15). That the higher energy band originates from free ligand emission from the P[^]P ligands can be ruled out since in CH₂Cl₂ solution the POP and xantphos emit at 320 and 344 nm respectively. On the other hand, the λ_{em}^{max} of the N[^]S ligands (ThPy = 349 nm, ThMePy = 349 nm, MeThPy = 361 nm, MeThMePy = 359 nm) coincides relatively well with these higher energy emission bands. Measuring the PLQY of ThMePy, as a representative of these ligands, only yielded 2.4% in deaerated (Ar purge for 15 min) CH₂Cl₂ solution (λ_{exc} = 310 nm). It can therefore be assumed that there is significant ligand character in the emission of the complexes in solution. Consistent with the solution absorption spectra and previously reported [Cu(POP)(N[^]N)][PF₆] and [Cu(xantphos)(N[^]N)][PF₆] or [Cu(POP)(N[^]S)][PF₆] and [Cu(xantphos)(N[^]S)][PF₆] solution absorption and emission, the two P[^]P ligands have little effect on λ_{em}^{max}.^{115,116,217}

The red shift of the λ_{em}^{max} when introducing a methyl group on the thiophenyl ring can be observed in both the ligands and the complexes. To confirm the origin of the emissions, excitation spectra were recorded. They confirm the origins of the higher and lower emission bands in the region of 311–317 nm and 353–380 nm, respectively, for [Cu(POP)(N[^]S)][PF₆] and 302–317 nm and 344–371 nm, respectively, for [Cu(xantphos)(N[^]S)][PF₆] complexes (Figure 2.16). Based on the absorption spectra of the N[^]S ligands with λ_{abs}^{max} between 306–314 nm, these are further evidence for ligand character in the higher energy emission,

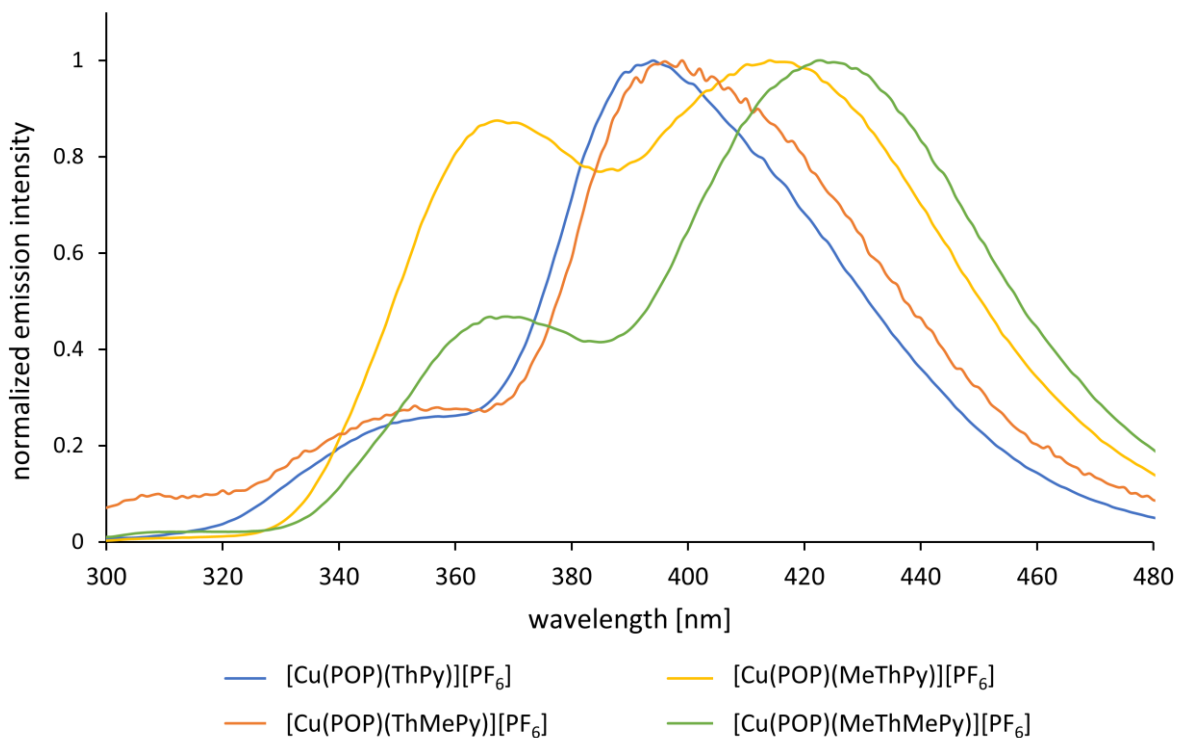


Figure 2.15: Normalized solution emission spectra of $[Cu(POP)(N^A S)](PF_6)$ complexes in CH_2Cl_2 ($c = 2.5 \times 10^{-5} - 5 \times 10^{-5} M$). $\lambda_{exc} = 275$ nm for ThPy, 280 nm for MeThPy, 250 nm for ThMePy and 270 nm for MeThMePy. Adapted from reference 197 under the terms of the CC-BY-NC license.

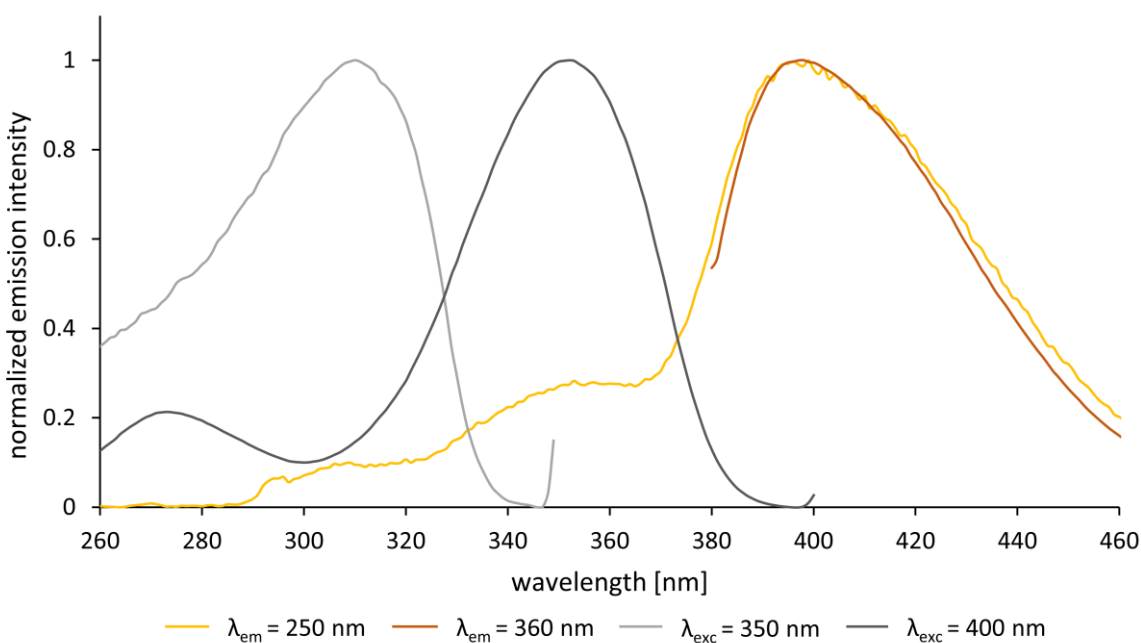


Figure 2.16: Normalized solution emission (yellow and orange) and excitation (light and dark grey) for $[Cu(POP)(ThMePy)](PF_6)$ in CH_2Cl_2 solution ($c = 2.5 \times 10^{-5} - 5 \times 10^{-5}$). Adapted from reference 197 under the terms of the CC-BY-NC license.

while the lower energy bands might arise from MLCT. The PLQY was measured in deaerated (Ar purge for 15 min) CH₂Cl₂ solutions. The highest values were observed for complexes with a methyl group in the 6-position of the pyridine ring. All the excited state lifetimes of the Cu(I) complexes were determined to be <5 ns.

2.6.2c Solid-state emission properties of [Cu(P[^]P)(N[^]S)]PF₆ with 2-(alkylsulfanylmethyl)pyridine ligands

One broad emission band is found in the solid-state for [Cu(P[^]P)(iPrSPy)][PF₆] and [Cu(P[^]P)(tBuSPy)][PF₆]. The emission is significantly blue shifted (λ_{em}^{max} between 470 nm and 490 nm) in comparison to [Cu(P[^]P)(bpy)][PF₆] (λ_{em}^{max} = 581 nm for POP and 587 nm for xantphos, λ_{exc} = 365 nm) when excited at 280 nm. The PLQY in the solid-state of these complexes is significantly lower than for many [Cu(P[^]P)(N[^]N)][PF₆] compounds^{114,116,184} and is below 2%. However, for unsubstituted [Cu(P[^]P)(bpy)][PF₆] the PLQY is not particularly high with 3% for POP and 1.7% for xantphos either, and improved PLQYs are achieved only with the introduction of substituents on the bpy.

2.6.2d Solid-state emission properties of [Cu(P[^]P)(N[^]S)][PF₆] with 2-(thiophen-2-yl)pyridine ligands

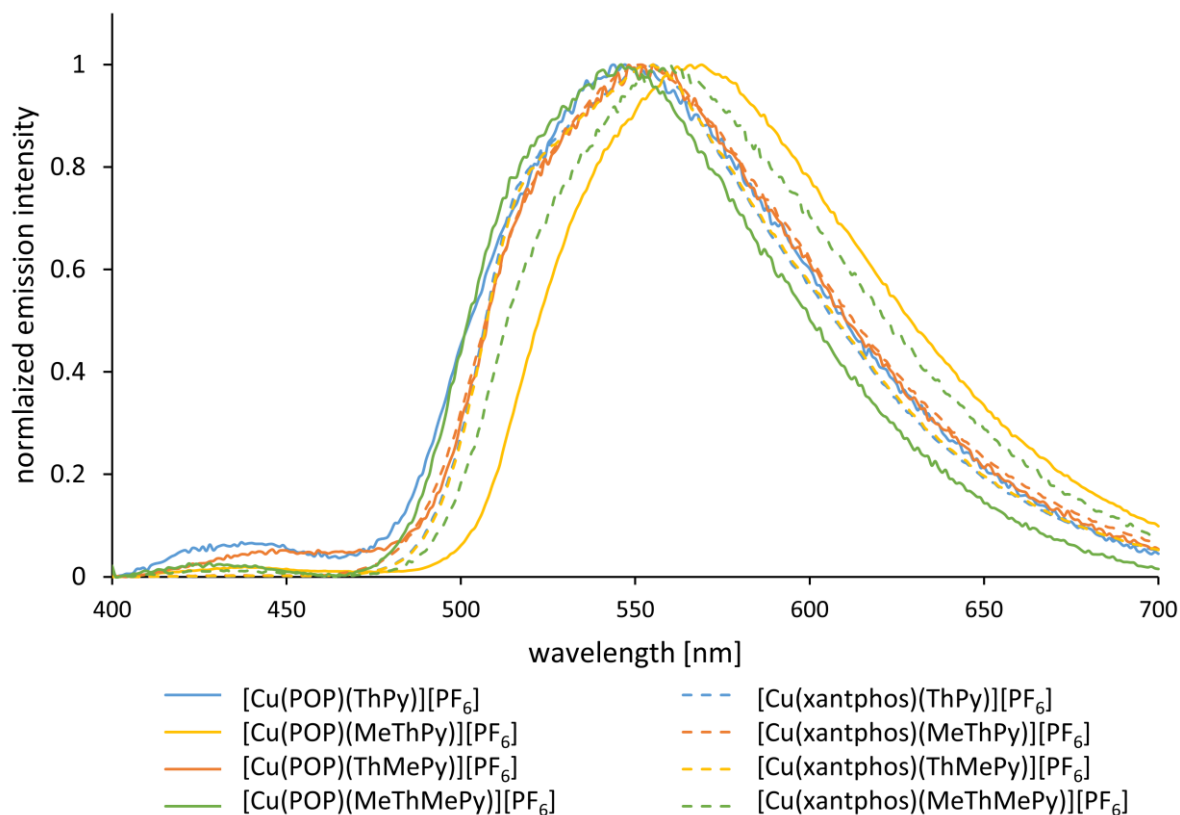


Figure 2.17: Normalized emission spectra of powder samples of [Cu(P[^]P)(N[^]S)]PF₆ compounds when excited with λ_{exc} = 365 nm. Adapted from reference 197 under the terms of the CC-BY-NC license.

In the solid-state, this series of complexes only shows one dominant emission band between 546 nm and 569 nm (Figure 2.17) when excited at 365 nm. Considering the emission profiles of the solid-state and solution emission spectra, it is reasonable to assume this emission corresponds to the lower energy emission. With this assumption, the red shift is in the range from 133 nm to 163 nm on going from solution to powder. The low intensity emission in the solid-state spectra may arise from free or coordinated POP

or xantphos, which emit at λ_{em}^{max} 443 nm and 455 nm, respectively.²¹⁵ The PLQY for these complexes is lower in the solid-state than in solution, with exception of [Cu(POP)(ThPy)][PF₆] and [Cu(xantphos)MeThPy)][PF₆]. This may be associated with ACQ, however, this normally is observed with π -stacking of planar molecular species and in the crystal structures no apparent π -stacking interactions were observed.^{225,226} In this regard, it is interesting to note that the complex with the highest PLQY ([Cu(xantphos)(ThPy)][PF₆]) does not feature substituents that help inhibit the flattening of the pseudo-tetrahedral Cu(I) geometry upon excitation.

2.6.2e Testing of [Cu(xantphos)(ThPy)][PF₆] thin film and LEC configuration

The investigations in this section were carried out by Dr. Michele Sessolo and Cristina Momblona in Valencia. As the most promising candidate in the solid-state, [Cu(xantphos)(ThPy)][PF₆] was tested in thin film with ionic liquid, but no PLQY could be measured since the PL signal was below the detection limit. In a LEC setup no electroluminescence was measured, even when the LEC was driven under a high bias of 18 V. The poor performance may be attributed to a bad charge transport behaviour in device configuration, possibly due to the tight ion-pairing observed in crystal structures (Section 2.4.2 and Figure 2.11), on top of poor emissive properties.

2.7 Investigation of the stability of [Cu(P^AP)(N^AS)][PF₆] compounds in solution

H³ and H^{3'} in bpy (analogous to H^{A3} in 2-(thiophen-2-yl)pyridine ligands)) are relatively acidic. They can undergo orthometallation in Ir(III)^{227,228}, Ni(II), Pd(II) and Pt(II)^{229,230} complexes containing bpy and H/D exchange in [Ru(bpy)₃]²⁺ in basic environment.²³¹ For both [Ir(ppy)₂(bpy)]⁺ and [Ru(bpy)₃]²⁺ derivatives, strong ion pairing between the bpy H³ and H^{3'} and chloride ions has been reported.^{231,232} The observed cation-anion interaction observed in the crystal structures, as well as the behaviour of H³ and H^{3'} in bpy raised the question if similar observations could be made for [Cu(P^AP)(N^AS)][PF₆] compounds.

2.7.1 The effect of added chloride ions on the solution absorption and ¹H NMR spectra

As an example, complex [Cu(POP)(MeThPy)][PF₆] was used. The addition of [ⁿBu₄N]Cl led to a significant change in the profile of the absorption spectrum (Figure 2.18) of the compound.

To confirm the stability of the complex a 5 x 10⁻⁵ M solution of [Cu(POP)(MeThPy)][PF₆] in CH₂Cl₂ was maintained over three days at room temperature. Absorption spectra recorded over the course of these three days remained essentially unchanged. The effects of the added chloride on [Cu(POP)(MeThPy)][PF₆] were further investigated with ¹H NMR spectroscopy in acetone-*d*₆ with increasing amounts of [ⁿBu₄N]Cl (Figure 2.19).

The spectrum undergoes significant changes in the aromatic region, with the signals for H^{A3} and H^{A4} steadily shifting to lower frequencies. Figure 2.20a shows the most affected protons are H^{A3}, H^{A4} and the protons of the methyl group of MeThPy. The adduct with a 1:1 stoichiometry was confirmed with a Job's plot (Figure 2.20b).

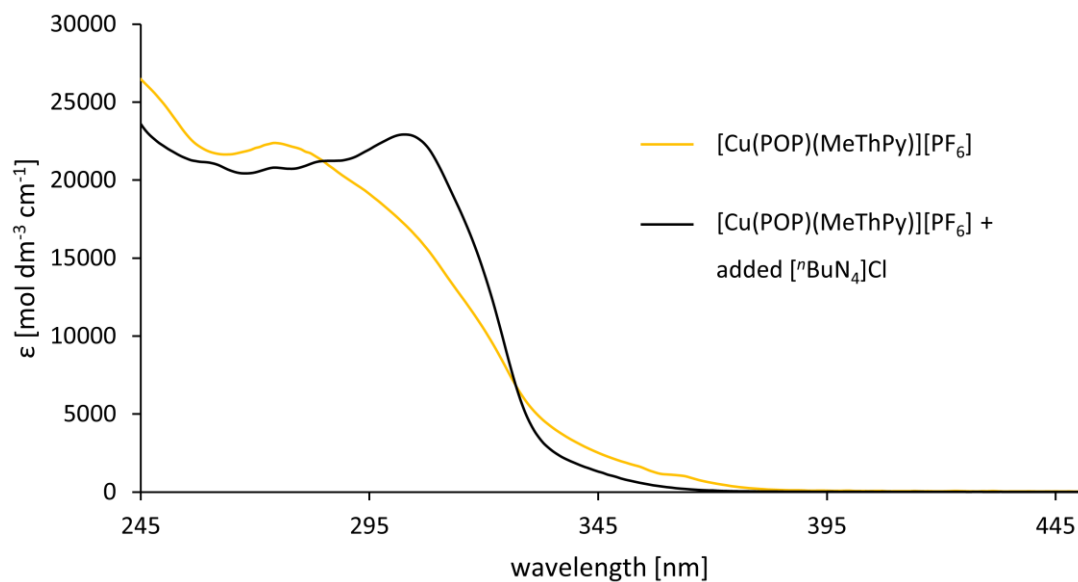


Figure 2.18: Solution absorption spectra of $[\text{Cu}(\text{POP})(\text{MeThPy})][\text{PF}_6]$ in CH_2Cl_2 ($c = 7 \times 10^{-5} \text{ M}$) with and without added chloride ions. Adapted from reference 197 under the terms of the CC-BY-NC license.

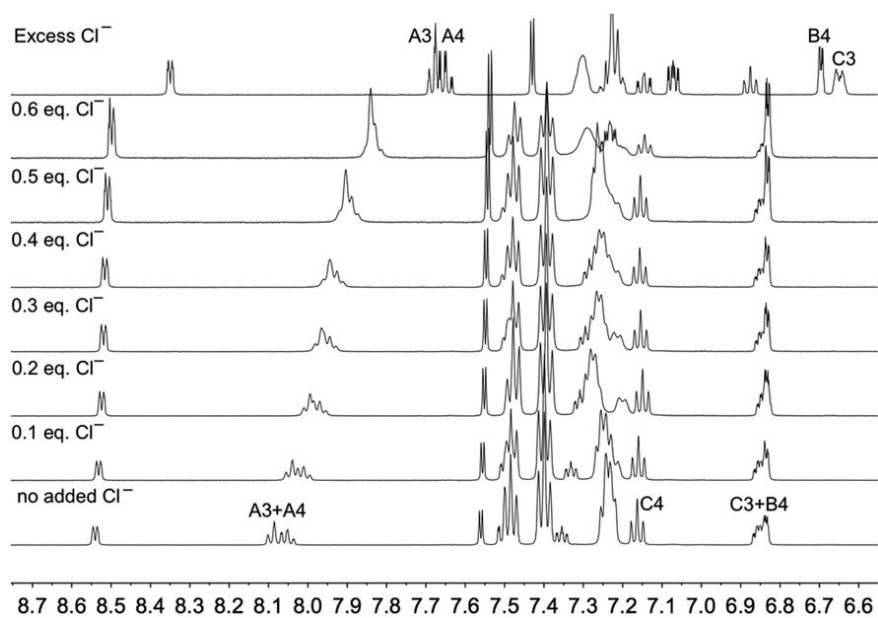


Figure 2.19: Aromatic region of the ^1H NMR spectrum (500 MHz, acetone- d_6 , 0.01 M) of $[\text{Cu}(\text{POP})(\text{MeThPy})][\text{PF}_6]$, showing the changes in the signals for $\text{H}^{\text{A}3}$, $\text{H}^{\text{A}4}$, $\text{H}^{\text{B}4}$ and $\text{H}^{\text{C}3}$ under increasing amounts of chloride ions ($[\text{nBu}_4\text{N}]\text{Cl}$). See scheme 2.1 for atom labelling. Reproduced from reference 197 under the terms of the CC-BY-NC license.

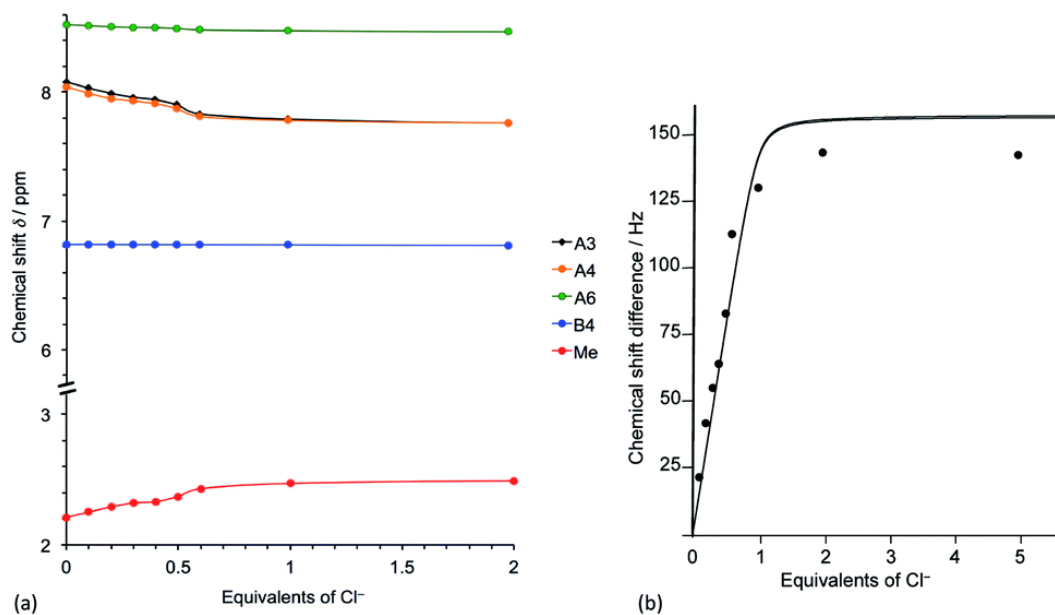


Figure 2.20: (a) Changes in the chemical shifts of the N^{AS} ligand of $[\text{Cu}(\text{POP})(\text{MeThPy})][\text{PF}_6]$ with H^{A3}, H^{A4}, H^{A6} lying on the pyridine ring) and H^{B4} and H^{Me} lying on the thiophene ring, with increasing amounts of Cl^- ions. H^{A5} and H^{B3} behave like H^{B4}. (b) Job's plot for the methyl resonance of $[\text{Cu}(\text{POP})(\text{MeThPy})][\text{PF}_6]$ as function of added chloride ions. The numerical two-parameter fit according to ref. ²³³, eqn. (6) is shown. Reproduced from reference 197 under the terms of the CC-BY-NC license.

The analysis of the methyl resonance reveals a K_d value of $0.14 \pm 0.03 \text{ mM}$.²³⁴ This is comparable to a K_d reported for the ion pairing of iodine and 1-methylquinoxalinium in acetone, which suggests the formation of an ion pair between the complex and the chloride, rather than the coordination of the chloride to form a five coordinate complex. No examples of five coordinate $\{\text{Cu}(\text{P}^{\wedge}\text{P})(\text{N}^{\wedge}\text{N})\text{Cl}\}$ or $\{\text{Cu}(\text{P}^{\wedge}\text{P})(\text{N}^{\wedge}\text{N})\text{Cl}\} \text{Cu}(\text{I})$ complexes are reported (Cambridge Structural Database, CSD v.5.42.²³⁵ searched using Conquest 2020.3.0²³⁶)

2.7.2 Crystal structure of $[\text{Cu}(\text{xantphos})(\text{MeCN})_2][\text{PF}_6] \cdot 0.5\text{Et}_2\text{O}$

The instability of the $[\text{Cu}(\text{P}^{\wedge}\text{P})(\text{N}^{\wedge}\text{S})][\text{PF}_6]$ complexes (with N^{AS} being a 2-(thiophen-2-yl)pyridine) was furthermore investigated with the attempted crystallisation of $[\text{Cu}(\text{xantphos})(\text{ThPy})][\text{PF}_6]$ from an MeCN solution of the Cu(I) complex with vapour diffusion of Et_2O . Before undergoing crystallization, the integrity of the bulk $[\text{Cu}(\text{xantphos})(\text{ThPy})][\text{PF}_6]$ was confirmed by NMR spectroscopy and mass spectrometry. $[\text{Cu}(\text{xantphos})(\text{MeCN})_2][\text{PF}_6] \cdot 0.5\text{Et}_2\text{O}$ crystallised as colourless plates, confirming the replacement of ThPy by the coordinating solvent. $[\text{Cu}(\text{xantphos})(\text{MeCN})_2][\text{PF}_6] \cdot 0.5\text{Et}_2\text{O}$ crystallises in the triclinic space group *P*-1, other unit cell parameters can be found in Table 2.1 and selected bond parameters are given in the figure caption to the depiction of the $[\text{Cu}(\text{xantphos})(\text{MeCN})_2]^+$ cation (Figure 2.21a). The atom Cu(I) is in a distorted tetrahedral environment with a Houser τ_4 parameter of 0.91. The P2-Cu1-P1 angle of $113.73(4)^\circ$ is smaller than for $[\text{Cu}(\text{xantphos})(\text{ThPy})][\text{PF}_6]$, $[\text{Cu}(\text{xantphos})(\text{ThMePy})][\text{PF}_6]$ and $[\text{Cu}(\text{xantphos})(\text{MeThMePy})][\text{PF}_6]$, but similar to previously reported crystal structure of $[\text{Cu}(\text{xantphos})(\text{MeCN})_2][\text{PF}_6] \cdot \text{CHCl}_3$ CSD v.5.42.²³⁵, accessed via Conquest 2020.3.0²³⁶.²¹⁵ The close association of the cation and anion in $[\text{Cu}(\text{xantphos})(\text{MeCN})_2][\text{PF}_6]$ is noteworthy and the related C–H \cdots F contacts, highlighted in Figure 2.21b, lie in the same range as those in $[\text{Cu}(\text{xantphos})(\text{ThPy})][\text{PF}_6]$ with

values between 2.54 and 2.87 Å. Other structural features of $[\text{Cu}(\text{xantphos})(\text{MeCN})_2][\text{PF}_6] \cdot 0.5\text{Et}_2\text{O}$ are unexceptional.

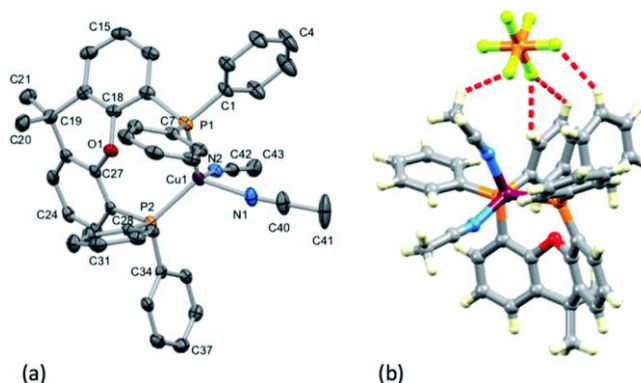


Figure 2.21: (a) ORTEP-style plot of the $[\text{Cu}(\text{xantphos})(\text{MeCN})_2]^+$ cation in $[\text{Cu}(\text{xantphos})(\text{MeCN})_2][\text{PF}_6] \cdot 0.5\text{Et}_2\text{O}$ with ellipsoids plotted at 40% probability level. H atoms and solvent molecules are omitted. Selected bond parameters: $\text{Cu1} - \text{P2} = 2.2593(11)$, $\text{Cu1} - \text{P1} = 2.2676(12)$, $\text{Cu1} - \text{N2} = 2.032(4)$, $\text{Cu1} - \text{N1} = 2.016(4)$, $\text{O1} - \text{C27} = 1.391(5)$, $\text{O1} - \text{C18} = 1.388(5)$ Å; $\text{P2} - \text{Cu1} - \text{P1} = 113.73(4)$, $\text{N2} - \text{Cu1} - \text{P2} = 109.72(11)$, $\text{N2} - \text{Cu1} - \text{P1} = 114.98(11)$, $\text{N1} - \text{Cu1} - \text{P2} = 116.10(13)$, $\text{N1} - \text{Cu1} - \text{P1} = 107.63(14)$, $\text{N1} - \text{Cu1} - \text{N2} = 93.16(16)$, $\text{C18} - \text{O1} - \text{C27} = 114.1(3)$. (b) Short C–H···F contacts between $[\text{Cu}(\text{xantphos})(\text{MeCN})_2]^+$ and $[\text{PF}_6]^-$ ions. Reproduced from reference 197 under the terms of the CC-BY-NC license.

2.8 Conclusion

A series of $[\text{Cu}(\text{POP})(\text{N}^{\wedge}\text{S})][\text{PF}_6]$ and $[\text{Cu}(\text{xantphos})(\text{N}^{\wedge}\text{S})][\text{PF}_6]$ complexes in which $\text{N}^{\wedge}\text{S}$ is either *i*PrSPy, *t*BuSPy or a 2-(thiophen-2-yl)pyridine were synthesized. The complexes are stable with respect to ligand dissociation which was shown using NMR and absorption spectroscopies in either acetone or CH_2Cl_2 . ^1H and $^{31}\text{P}\{^1\text{H}\}$ variable temperature NMR spectroscopy reveal dynamic behaviour of the diphosphane backbone. At 238 K, the motion of the POP ligand is frozen out, while the complexes coordinated to xantphos give rise to two sets of signals at 198 K in the ratio of $\approx 5:1$ in the ^1H and $^{31}\text{P}\{^1\text{H}\}$ NMR spectra. The observation of EXSY peaks in the ROESY spectrum confirm the exchange between the two conformers. In all four complexes containing *i*PrSPy or *t*BuSPy the inversion of the stereogenic sulfur atom is fast on the NMR timescale over the studied temperature range and does not lead to the observation of additional species. In comparison to $[\text{Cu}(\text{P}^{\wedge}\text{P})(\text{bpy})][\text{PF}_6]$, the $\text{Cu}^+/\text{Cu}^{2+}$ oxidation is shifted to higher potentials for all $[\text{Cu}(\text{P}^{\wedge}\text{P})(\text{N}^{\wedge}\text{S})][\text{PF}_6]$ compounds.

Single crystal structures of a number of complexes confirm the distorted tetrahedral geometry of the Cu(I) centre and the chelating nature of the $\text{N}^{\wedge}\text{S}$ ligands. Furthermore, close cation···anion C–H···F contacts were observed, particularly in $[\text{Cu}(\text{xantphos})(\text{ThPy})][\text{PF}_6]$. Investigation of these cation···anion interactions revealed significant changes in the absorption and ^1H NMR spectra of $[\text{Cu}(\text{POP})(\text{MeThPy})][\text{PF}_6]$ in CH_2Cl_2 (or CD_2Cl_2) upon the addition of Cl^- ions. Coordinating solvents are able to replace the $\text{N}^{\wedge}\text{S}$ ligand, as has been shown by the crystallisation of $[\text{Cu}(\text{xantphos})(\text{MeCN})_2][\text{PF}_6]$ out of a MeCN solution of $[\text{Cu}(\text{xantphos})(\text{ThPy})][\text{PF}_6]$.

Complexes with a 2-(thiophen-2-yl)pyridine as $\text{N}^{\wedge}\text{S}$ ligand are blue emitters in solution, with notable quantum yields of up to 33.2%. The highest quantum yields were achieved for $\text{N}^{\wedge}\text{S}$ ligands with a methyl in 6-position of the pyridine ring. $[\text{Cu}(\text{P}^{\wedge}\text{P})(\text{iPrSPy})][\text{PF}_6]$ and $[\text{Cu}(\text{P}^{\wedge}\text{P})(\text{tBuSPy})][\text{PF}_6]$ are non-emissive in solution and only weak emitters blue emitters in solid-state with PLQY <2%. Complexes with a 2-(thiophen-

2-yl)pyridine derivative are yellow emitters in the solid-state with a significant red-shift of 133 – 163 nm on going from solution to powder. The most brightly emitting compound was [Cu(xantphos)(ThPy)][PF₆] with a PLQY of 10.8%. All complexes had very short excited state lifetimes (<5 ns). [Cu(xantphos)(ThPy)][PF₆] was tested in a LEC setup but showed poor electroluminescence possibly to poor charge transport characteristics.

2.9 Experimental

2.9.1 Ligand Synthesis

2.9.1a MeThMePy

A solution of 2-bromo-6-methylpyridine (1000 mg, 0.66 mL, 5.8 mmol), 4,4,5,5-tetramethyl-2-(5-methyl-2-thienyl)-1,3,2-dioxaborolane (1300 mg, 1.4 mL, 5.8 mmol), toluene (6 mL), aqueous Na₂CO₃ (2 M, 6 mL) and EtOH (3 mL) was degassed for 10 min. with N₂, then [Pd(PPh₃)₄] (388 mg, 0.34 mmol) was added. The reaction was heated to 90 °C and stirred under N₂ atmosphere for 5 h. After cooling the reaction mixture to room temperature, it was diluted with water (20 mL). The combined organic phases were washed with water (20 mL) and brine (20 mL), dried over MgSO₄ and the solvent was removed under reduced pressure. The crude product was purified by column chromatography using a Biotage Selekt automated column (CH₂Cl₂/hexane, 30% → 50% CH₂Cl₂) to give MeThMePy as a pale, yellow oil (740 mg, 3.9 mmol, 67%). ¹H (500MHz, CDCl₃, 298 K) δ/ppm: 7.52 (t, *J* = 7.7 Hz, 1H, H^{A4}), 7.37 (overlapping m, 2H, H^{A3+B3}), 6.95 (d, *J* = 7.5 Hz, 1H, H^{A5}), 6.74 (m, 1H, H^{B4}), 2.55 (s, 3H, H^{Me-A6}), 2.51 (s, 3H, H^{Me-B5}). ¹³C{¹H} (126 MHz, CDCl₃, 298 K) δ/ppm: 158.4 (C^{A6}), 152.4 (C^{A2}), 142.8 (C^{B2}), 142.1 (C^{B5}), 136.8 (C^{A4}), 126.3 (C^{B4}), 124.5 (C^{B3}), 121.1 (C^{A5}), 115.5 (C^{A3}), 24.7 (C^{MeA6}), 15.8 (C^{MeB5}). UV-Vis (CH₂Cl₂, 6.0 × 10⁻⁵ mol dm⁻³) λ/nm 290 sh (ε/dm³mol⁻¹cm⁻¹ 5000), 316 (8800). ESI-MS *m/z* 190.00 [MeThMePy + H]⁺ (calc. 190.06). Found: 69.41, H 5.75, N 7.48; C₁₁H₁₁NS requires C 69.80, H 5.86, N 7.40.

2.9.2 Complex synthesis

All Cu(I) complexes were prepared according to the following general procedure, unless otherwise stated. A solution of POP (1.0 eqv.) or xantphos (1.0 eqv.) and [Cu(MeCN)₄][PF₆] (1.0 eqv.) was stirred for 1 – 2 h. Then the N^AS ligand (1.0 eqv.) was added and the reaction mixture was stirred for an additional hour. The solvents were subsequently removed under reduced pressure and the residue was washed with Et₂O. All products were purified by vapour diffusion of Et₂O into a CH₂Cl₂ solution of the crude compound.

2.9.2a [Cu(POP)(iPrSPy)][PF₆]

The reagents were [Cu(MeCN)₄][PF₆] (0.23 g, 0.62 mmol), POP (0.33 g, 0.62 mmol) and 2-((*iso*-propylsulfanyl)methyl)pyridine (0.10 g, 0.62 mmol). [Cu(POP)(iPrSPy)][PF₆] was obtained as colourless crystals (0.38 g, 0.41 mmol, 67%). ¹H NMR (500 MHz, acetone-*d*₆, 248 K) δ/ppm 8.13 (d, *J* = 5.1 Hz, 1H, H^{A6}), 8.01 (td, *J* = 7.7, 1.7 Hz, 1H, H^{A4}), 7.78 (d, *J* = 7.8 Hz, 1H, H^{A3}), 7.52–7.42 (m, 12, H^{D4+D'2+D'3+D'4}), 7.40 (m, 2H, H^{C5}), 7.33 (m, 4H, H^{D3}), 7.24 (m, 1H, H^{A5}), 7.14–7.00 (m, 4H, H^{C4+C6}), 6.98–6.84 (m, 4H, H^{D2}), 6.77 (m, 2H, H^{C3}), 4.13 (s, 2H, H^a), 2.57 (septet, *J* = 6.6 Hz, 1H, H^{Pr-CH}), 0.97 (d, *J* = 6.6 Hz, 6H, H^{Pr-Me}). ¹³C{¹H} NMR (126 MHz, acetone-*d*₆, 248 K) δ/ppm 158.3 (C^{C1}), 156.3 (C^{A2}), 149.8 (C^{A6}), 139.5 (C^{A4}), 134.7 (C^{C3}), 134.5/132.9/129.3 (C^{D'2,3,4}), 132.9 (C^{C5}), 132.7 (C^{D2}), 131.2 (C^{D'1}), 130.7 (C^{D4}), 130.0/125.7 (C^{C6+C4}), 129.5 (C^{D3}), 125.5 (C^{D1}), 125.1 (C^{A3}), 124.6 (C^{A5}), 120.8 (C^{C2}), 38.6 (C^{a+Pr-CH}), 21.9 (C^{Pr-Me}). ³¹P{¹H} NMR (202 MHz, acetone-*d*₆, 298 K) δ/ppm -12.6 (POP), -144.3 (septet, *J*_{PF} = 710 Hz, PF₆⁻). ESI-MS: *m/z* 768.2

[Cu(POP)(*i*PrSPy)]⁺ (base peak, calc. 768.2). Found: C 58.97, H 4.73, N 1.61; and C₄₅H₄₁CuF₆NOP₃S requires C 59.11, H 4.52, N 1.53.

2.9.2b [Cu(xantphos)(*i*PrSPy)][PF₆]

The reagents were [Cu(MeCN)₄][PF₆] (0.23 g, 0.62 mmol), xantphos (0.36 g, 0.62 mmol) and 2-((*iso*-propylsulfanyl)methyl)pyridine (0.10 mg, 0.62 mmol). [Cu(xantphos)(*i*PrSPy)][PF₆] was obtained as a colourless solid (0.32 g, 0.35 mmol, 57%). ¹H NMR (500 MHz, acetone-*d*₆, 238 K) Major species (see text): δ/ppm 8.11–7.98 (m, 2H, H^{A6+A4}), 7.88 (d, *J* = 7.7 Hz, 2H, H^{C5}), 7.73 (d, *J* = 7.8 Hz, 1H, H^{A3}), 7.53–7.39 (m, 12H, H^{D4+D'2+D'3+D'4}), 7.38–7.27 (m, 7H, H^{A5+C4+D3}), 6.84 (m, 4H, H^{D2}), 6.74 (m, 2H, H^{C3}), 3.74 (s, 2H, H^a), 2.60 (m, 1H, H^{Pr-CH}), 1.95 (s, 3H H^{xantphos-Me}), 1.40 (s, 3H H^{xantphos-Me}), 0.89–0.86 (m, 6H, H^{Pr-Me}). ¹³C{¹H} NMR (126 MHz, acetone-*d*₆, 238 K) δ/ppm 156.8 (C^{A2}), 155.1 (C^{C1}), 149.8 (C^{A6}), 140.1 (C^{A4}), 134.4 (C^{C6}), 134.3/130.9/129.9 (C^{D4+D'2+D'3+D'4}), 132.9 (C^{D2}), 132.8 (C^{D1}), 132.0 (C^{C3}), 131.4 (C^{D'1}), 129.8 (C^{D3}), 129.0 (C^{C5}), 125.8 (C^{A3+C4}), 125.7 (C^{A5}), 120.1 (C^{C2}), 39.0 (C^a), 38.5 (C^{Pr-CH}), 36.4 (C^{xantphos-bridge}), 32.0/24.9 (C^{xantphos-Me}), and 21.8 (C^{Pr-Me}). ³¹P{¹H} NMR (202 MHz, acetone-*d*₆, 298 K) δ/ppm –13.1 (xantphos), –144.3 (septet, *J*_{PF} = 710 Hz, PF₆[–]). ESI-MS: *m/z* 808.2 [Cu(xantphos)(*i*PrSPy)]⁺ (base peak, calc. 808.2). Found: C 61.06, H 4.89, N 1.48; C₄₈H₄₅CuF₆NOP₃S requires C 60.41, H 4.75, N 1.47.

2.9.2c [Cu(POP)(*t*BuSPy)][PF₆]

The reagents were [Cu(MeCN)₄][PF₆] (0.20 g, 0.62 mmol), POP (0.30 g, 0.62 mmol) and 2-((*tert*-butylsulfanyl)methyl)pyridine (0.10 g, 0.55 mmol, 0.9 eqv.). [Cu(POP)(*t*BuSPy)][PF₆] was obtained as colourless crystals (0.21 g, 0.23 mmol, 42%). ¹H NMR (500 MHz, acetone-*d*₆, 238 K) δ/ppm 8.15 (d, *J* = 5.0 Hz, 1H, H^{A6}), 8.00 (td, *J* = 7.7, 1.5 Hz, 1H, H^{A4}), 7.81 (d, *J* = 8.0 Hz, 1H, H^{A3}), 7.52–7.42 (m, 10H, H^{C5+D4+D'3+D'4}), 7.42–7.37 (m, 4H, H^{D'2}), 7.34 (m, 4H, H^{D3}), 7.24–7.17 (m, 1H, H^{A5}), 7.16–7.06 (m, 4H, H^{C4+C6}), 6.97–6.86 (m, 4H, H^{D2}), 6.79–6.70 (m, 2H, H^{C3}), 4.25 (s, 2H, H^a), 1.01 (s, 9H, H^{*t*-Bu}). ¹³C{¹H} NMR (126 MHz, acetone-*d*₆, 238 K) δ/ppm 158.8 (C^{C1}), 157.4 (C^{A2}), 149.9 (C^{A6}), 139.6 (C^{A4}), 135.0 (C^{C3}), 134.7 (C^{D'1}), 134.5 (C^{D'2}), 133.2 (C^{C5+D1}), 133.1 (C^{D'3+D'4}), 132.9 (C^{D2}), 129.9 (C^{D4}), 129.6 (C^{D3}), 125.8 (C^{C6/C4}), 121.0 (C^{C6/C4}), 125.1 (C^{A3}), 124.5 (C^{A5}), 124.1 (C^{C2}), 47.8 (C^{Bu-Cq}), 37.7 (C^a), 29.5 (C^{*t*-Bu}). ³¹P{¹H} NMR (202 MHz, acetone-*d*₆, 298 K) δ/ppm –12.6 (POP), –144.3 (septet, *J*_{PF} = 710 Hz, PF₆[–]). ESI-MS: *m/z* 782.2 [Cu(POP)(*t*BuSPy)]⁺ (base peak, calc. 782.2). Found: C 59.43, H 4.76, N 1.70; C₄₆H₄₃CuF₆NOP₃S requires C 59.51, H 4.67, N 1.53.

2.9.2d [Cu(xantphos)(*t*BuSPy)][PF₆]

The reagents were [Cu(MeCN)₄][PF₆] (0.20 g, 0.62 mmol), xantphos (0.32 g, 0.62 mmol) and 2-((*tert*-butylsulfanyl)methyl)pyridine (0.10 g, 0.55 mmol, 0.9 eqv.). [Cu(xantphos)(*t*BuSPy)][PF₆] was obtained as a colourless solid (0.28 g, 0.28 mmol, 51%). ¹H NMR (500 MHz, acetone-*d*₆, 198 K) major species (see text, integrals of some signals are affected by minor species and are not stated): δ/ppm 8.31 (d, *J* = 5.1 Hz, 1H, H^{A6}), 8.05 (t, *J* = 7.3 Hz, 1H, H^{A4}), 7.94 (d, *J* = 7.6 Hz, 2H, H^{C5}), 7.74–7.62 (m, H^{A3+D'4}), 7.60–7.49 (m, H^{D'2+D'3}), 7.49–7.42 (m, H^{A5+D4}), 7.39 (m, 2H, H^{C4}), 7.34 (m, 4H, H^{D3}), 6.88 (m, 2H, H^{C3}), 6.80–6.73 (m, 4H, H^{D2}), 3.40 (s, 2H, H^a), 2.00 (s, 3H, H^{xantphos-Me}), 1.27 (s, 3H, H^{xantphos-Me}), 0.83 (s, 9H, H^{*t*-Bu}). ¹³C{¹H} NMR (126 MHz, acetone-*d*₆, 198 K) δ/ppm 157.7 (C^{A2}), 154.7 (C^{C1}), 149.5 (C^{A6}), 139.7 (C^{A4}), 134.5 (C^{D'4}), 133.9 (C^{C6}), 132.3 (C^{C3}), 132.1 (C^{D2}), 131.4 (C^{D'2/D'3}), 130.5 (C^{D4}), 130.4 (C^{D1}), 129.6 (C^{D'2/D'3}), 129.4 (C^{D3}), 129.0 (C^{C5}), 125.4 (C^{C4}), 124.9 (C^{D'1}), 124.8 (C^{A5}), 124.5 (C^{A3}), 119.6 (C^{C2}), 47.9 (C^{Bu-Cq}), 36.9 (C^a), 35.9 (C^{xantphos-bridge}), 33.0 (H^{xantphos-Me}), 23.8 (H^{xantphos-Me}), 28.7 (C^{*t*-Bu}). ³¹P{¹H} NMR (202 MHz, acetone-*d*₆, 298 K) δ/ppm –14.4 (xantphos), –144.3 (septet, *J*_{PF} = 710 Hz, PF₆[–]). ESI-MS: *m/z* 822.2 [Cu(xantphos)(*t*BuSPy)]⁺ (base peak, calc. 822.2). Found: C 60.82, H 4.95, N 1.55; C₄₉H₄₇CuF₆NOP₃S requires C 60.77, H 4.89, N 1.45.

2.9.2e [Cu(POP)(ThPy)][PF₆]

The reagents were POP (367 mg, 0.68 mmol), [Cu(MeCN)₄][PF₆] (231 mg, 0.62 mmol) and ThPy (100 mg, 0.62 mmol). [Cu(POP)(ThPy)][PF₆] was isolated as a colourless solid (158 mg, 0.45 mmol, 75%). ¹H NMR (500 MHz, acetone-*d*₆) δ/ppm 8.39 (ddd, *J* = 5.3, 1.4, 0.9 Hz, 1H, H^{A6}), 8.14 (dt, *J* = 8.1, 1.2 Hz, 1H, H^{A3}), 8.08 (td, *J* = 7.7, 1.6 Hz, 1H, H^{A4}), 7.73 (dd, *J* = 3.7, 1.1 Hz, 1H, H^{B5}), 7.51 (dd, *J* = 5.0, 1.1 Hz, 1H, H^{B3}), 7.50–7.43 (m, 6H, H^{C5+D4}), 7.41–7.33 (m, 9H, H^{A5+D3}), 7.25–7.17 (m, 10H, H^{C6+D2}), 7.16–7.11 (m, 3H, H^{B4+C4}), 6.82 (m, 2H, H^{C3}). ¹³C{¹H} NMR (126 MHz, acetone-*d*₆) δ/ppm 158.7 (t, *J*_{PC} = 6 Hz, C^{C1}), 152.8 (C^{A2}), 150.3 (C^{A6}), 143.5 (C^{B2}), 140.1 (C^{A4}), 135.2 (C^{C3}), 134.2 (t, *J*_{PC} = 6 Hz, C^{D2}), 133.5 (C^{C5}), 131.5 (C^{D4}), 130.7 (t, *J*_{PC} = 20 Hz, C^{D1}), 130.1 (C^{B4}), 130.0 (t, *J*_{PC} = 5 Hz, C^{D3}), 128.5 (C^{B3+B5}), 126.0 (t, *J*_{PC} = 2 Hz, C^{C4}), 124.7 (C^{A5}), 123.7 (t, *J*_{PC} = 17 Hz, C^{C2}), 122.9 (C^{A3}), 121.1 (C^{C6}). ³¹P{¹H} NMR (202 MHz, acetone-*d*₆, 298 K) δ/ppm -15.3 (POP), -144.2 (septet, *J*_{PF} = 707 Hz, PF₆⁻). ESI-MS positive mode *m/z* 762.10 [Cu(POP)(ThPy)]⁺ (calc. 762.12), 601.10 [Cu(POP)]⁺ (base peak, calc. 601.09). Found: C 59.74, H 3.95, N 1.67; C₄₅H₃₅CuF₆NOP₃S requires C 59.51, H 3.88, N 1.54.

2.9.2f [Cu(xantphos)(ThPy)][PF₆]

The reagents were xantphos (316 mg, 0.50 mmol), [Cu(MeCN)₄][PF₆] (185 mg, 0.50 mmol) and ThPy (80 mg, 0.50 mmol). [Cu(xantphos)(ThPy)][PF₆] was isolated as a colourless solid (126 mg, 0.37 mmol, 75%). ¹H NMR (500 MHz, acetone-*d*₆) δ/ppm 8.59 (d, *J* = 5.2 Hz, 1H, H^{A6}), 8.02 (overlapping m, 2H, H^{A3+A4}), 7.85 (d, *J* = 6.6 Hz, 2H, H^{C5}), 7.65 (d, *J* = 3.7 Hz, 1H, H^{B3}), 7.44 (t, *J* = 7.4 Hz, 4H, H^{D4}), 7.39 (m, 1H, H^{A5}), 7.35–7.28 (m, 10H, H^{C4+D3}), 7.27 (d, *J* = 4.9 Hz, 1H, H^{B5}), 7.23–7.19 (m, 8H, H^{D2}), 7.09 (dd, *J* = 5.0, 3.9 Hz, 1H, H^{B4}), 6.72 (m, 2H, H^{C3}), 1.74 (s, 6H, H^{xantphos-Me}). ¹³C{¹H} NMR (126 MHz, acetone-*d*₆) δ/ppm 155.1 (C^{C1}), 153.1 (C^{A2}), 150.5 (C^{A6}), 143.9 (C^{B2}), 139.4 (C^{A4}), 134.6 (C^{C6}), 134.1 (t, *J*_{PC} = 8 Hz, C^{D2}), 132.3 (C^{C3}), 131.4 (C^{D4}), 131.1 (t, *J*_{PC} = 20 Hz, C^{D1}), 130.4 (C^{B4}), 129.9 (t, *J*_{PC} = 5 Hz, C^{D3}), 129.0 (C^{C5}), 128.2 (C^{B5}), 127.5 (C^{B3}), 126.2 (t, *J*_{PC} = 2 Hz, C^{C4}), 124.3 (C^{A5}), 122.0 (C^{A3}), 119.9 (C^{C2}), 42.5 (C^{xantphos-bridge}), 28.9 (C^{xantphos-Me}). ³¹P{¹H} NMR (202 MHz, acetone-*d*₆, 298 K) δ/ppm -14.9 (xantphos), -144.2 (septet, *J*_{PF} = 707 Hz, PF₆⁻). ESI-MS positive mode *m/z* 802.15 [Cu(xantphos)(ThPy)]⁺ (calc. 802.15), 641.10 [Cu(xantphos)]⁺ (base peak, calc. 641.12). Found: C 60.66, H 4.95, N 1.62; C₄₈H₃₉CuF₆NOP₃S requires C 60.79, H 4.15, N 1.48

2.9.2g [Cu(POP)(ThMePy)][PF₆]

The reagents were POP (215 mg, 0.40 mmol), [Cu(MeCN)₄][PF₆] (150 mg, 0.40 mmol) and ThMePy (69.9 mg, 0.40 mmol). [Cu(POP)(ThMePy)][PF₆] was isolated as a colourless solid (154 mg, 0.17 mmol, 42%). ¹H NMR (500 MHz, acetone-*d*₆) δ/ppm 7.98 (t, *J* = 7.6 Hz, 1H, H^{A4}), 7.85 (d, *J* = 7.6 Hz, 1H, H^{A3}), 7.64 (d, *J* = 4.9 Hz, 1H, H^{B3}), 7.59 (d, *J* = 3.7 Hz, 1H, H^{B5}), 7.51–7.44 (m, 6H, H^{D4+C5}), 7.38 (t, *J* = 7.5 Hz, 8H, H^{D3}), 7.34 (d, *J* = 7.6 Hz, 1H, H^{A5}), 7.24–7.10 (m, 13H, H^{D2+C6+C4+B4}), 6.85–6.76 (m, 2H, H^{C3}), 2.32 (s, 3H, H^{Me}). ¹³C{¹H} NMR (126 MHz, acetone-*d*₆) δ/ppm 159.4 (C^{A6}), 158.5 (C^{C1}), 152.9 (C^{A2}), 143.7 (C^{B2}), 139.8 (C^{A4}), 135.2 (C^{C3}), 134.1 (t, *J*_{PC} = 8 Hz, C^{D2}), 133.5 (C^{C5}), 131.5 (C^{D4}), 130.9 (C^{D1}), 130.7 (C^{B4}), 130.0 (t, *J*_{PC} = 5 Hz, C^{D3}), 128.0 (C^{B3}), 127.8 (C^{B5}), 126.1 (C^{C4}), 124.3 (C^{A5}), 123.6 (C^{C2}), 121.2 (C^{C6}), 119.9 (C^{A3}), 24.9 (C^{Me}). ³¹P{¹H} NMR (202 MHz, acetone-*d*₆, 298 K) δ/ppm -16.0 (POP), -144.2 (septet, *J*_{PF} = 707 Hz, PF₆⁻). ESI-MS positive mode *m/z* 776.15 [Cu(POP)(ThMePy)]⁺ (calc. 776.14), 601.10 [Cu(POP)]⁺ (base peak, calc. 601.09). Found: C 59.34, H 4.21, N 1.50; C₄₆H₃₇CuF₆NOP₃S requires C 59.90, H 4.04, N 1.52.

2.9.2h [Cu(xantphos)(ThMePy)][PF₆]

The reagents were xantphos (231 mg, 0.40 mmol), [Cu(MeCN)₄][PF₆] (150 mg, 0.40 mmol) and ThMePy (69.9 mg, 0.40 mmol). [Cu(xantphos)(ThMePy)][PF₆] was isolated as a colourless solid (183 mg, 0.19 mmol, 48%). ¹H NMR (500 MHz, acetone-*d*₆) δ/ppm 8.02 (t, *J* = 7.8 Hz, 1H, H^{A4}), 7.87 (m, 3H, H^{C5+A3}), 7.48–7.38 (m,

6H, H^{D4+B3+A5}), 7.36–7.27 (m, 11H, H^{D3+C4+B5}), 7.16–7.09 (m, 8H, H^{D2}), 7.04 (dd, *J* = 5.0, 3.7 Hz, 1H, H^{B4}), 6.72–6.65 (m, 2H, H^{C3}), 2.40 (s, 3H, H^{Me-A6}), 1.76 (s, 6H, H^{xantphos-Me}). ¹³C{¹H} NMR (126 MHz, acetone-*d*₆) δ/ppm 159.0 (C^{A6}), 155.1 (t, *J*_{PC} = 6 Hz, C^{C1}), 152.7 (C^{A2}), 143.6 (C^{B2}), 140.0 (C^{A4}), 134.5 (t, *J*_{PC} = 2 Hz, C^{C6}), 133.8 (t, *J*_{PC} = 8 Hz, C^{D2}), 132.2 (C^{C3}), 131.5 (C^{D4}), 131.0 (t, *J*_{PC} = 19 Hz, C^{D1}), 130.5 (C^{B4}), 130.0 (t, *J*_{PC} = 5 Hz, C^{D3}), 129.1 (C^{C5}), 127.9 (C^{B3}), 127.6 (C^{B5}), 126.3 (t, *J*_{PC} = 2.5 Hz, C^{C4}), 124.8 (C^{A5}), 120.2 (C^{A3}), 120.1 (C^{C2}), 36.6 (C^{xantphos-bridge}), 28.9 (C^{xantphos-Me}), 25.1 (C^{Me-A6}). ³¹P{¹H} NMR (202 MHz, acetone-*d*₆, 298 K) δ/ppm –14.2 (xantphos), –144.2 (septet, *J*_{PF} = 707 Hz, PF₆[–]). ESI-MS positive mode *m/z* 816.15 [Cu(xantphos)(ThMePy)]⁺ (calc. 816.17), 641.10 [Cu(xantphos)]⁺ (base peak, calc. 641.12). Found: C 61.18, H 4.27, N 1.46; C₄₉H₄₁CuF₆NOP₃S requires C 61.15, H 4.29, N 1.46.

2.9.2i [Cu(POP)(MeThPy)][PF₆]

The reagents were POP (153 mg, 0.29 mmol), [Cu(MeCN)₄][PF₆] (106 mg, 0.29 mmol) and MeThPy (49.9 mg, 0.29 mmol). [Cu(POP)(MeThPy)][PF₆] was isolated as a colourless solid (154 mg, 0.17 mmol, 59%). ¹H NMR (500 MHz, acetone-*d*₆) δ/ppm 8.53 (d, *J* = 5.2 Hz, 1H, H^{A6}), 8.10 (d, *J* = 8.1 Hz, 1H, H^{A3}), 8.09–8.02 (m, 1H, H^{A4}), 7.54 (d, *J* = 3.7 Hz, 1H, H^{B3}), 7.52–7.44 (m, 6H, H^{D2+C5}), 7.37 (m, 9H, H^{D3+A5}), 7.25–7.18 (m, 10H, H^{D2+C6}), 7.15 (t, *J* = 7.6 Hz, 2H, H^{C4}), 6.86–6.79 (m, 3H, H^{C3+B4}), 2.19 (s, 3H, H^{Me}). ¹³C{¹H} NMR (126 MHz, acetone-*d*₆) δ/ppm 158.9 (t, *J*_{PC} = 6 Hz, C^{C1}), 153.0 (C^{A2}), 150.0 (C^{A6}), 143.4 (C^{B5}), 140.8 (C^{B2}), 140.0 (C^{A4}), 135.2 (C^{C3}), 134.1 (t, *J*_{PC} = 8 Hz, C^{D2}), 133.5 (C^{C5}), 131.5 (C^{D4}), 130.8 (t, *J*_{PC} = 19 Hz, C^{D1}), 130.0 (t, *J*_{PC} = 5 Hz, C^{D3}), 129.6 (C^{B4}), 129.0 (C^{B3}), 126.2 (t, *J*_{PC} = 2.5 Hz, C^{C4}), 124.3 (C^{A5}), 123.8 (t, *J*_{PC} = 16 Hz, C^{C2}), 122.7 (C^{A3}), 121.3 (t, *J*_{PC} = 2 Hz, C^{C6}), 15.4 (C^{Me}). ³¹P{¹H} NMR (202 MHz, acetone-*d*₆, 298 K) δ/ppm –14.7 (POP), –144.2 (septet, *J*_{PF} = 707 Hz, PF₆[–]). ESI-MS positive mode *m/z* 776.10 [Cu(POP)(MeThPy)]⁺ (calc. 776.14), 601.05 [Cu(POP)]⁺ (base peak, calc. 601.09). Found: C 56.63, H 4.04, N 1.56; C₄₆H₃₇CuF₆NOP₃S·CH₂Cl₂ requires C 56.05, H 3.90, N 1.39.

2.9.2j [Cu(xantphos)(MeThPy)][PF₆]

The reagents were xantphos (330 mg, 0.57 mmol), [Cu(MeCN)₄][PF₆] (213 mg, 0.57 mmol) and MeThPy (100 mg, 0.57 mmol). [Cu(xantphos)(MeThPy)][PF₆] was isolated as a colourless solid (237 mg, 0.25 mmol, 43%). ¹H NMR (500 MHz, acetone-*d*₆) δ/ppm 8.75 (d, *J* = 5.2 Hz, 1H, H^{A6}), 8.10–8.03 (m, 2H, H^{A3+A4}), 7.88 (dd, *J* = 7.8, 1.4 Hz, 2H, H^{C5}), 7.55 (d, *J* = 3.7 Hz, 1H, H^{B4}), 7.43 (t, *J* = 7.5 Hz, 4H, H^{D4}), 7.39 (m, 1H, H^{A5}), 7.34–7.28 (m, 10H, H^{D3+C4}), 7.17 (m, 8H, H^{D2}), 6.81 (m, 1H, H^{B3}), 6.69 (m, 2H, H^{C3}), 1.90 (s, 3H, H^{Me-B5}), 1.75 (s, 6H, H^{xantphos-Me}). ¹³C{¹H} NMR (126 MHz, acetone-*d*₆) δ/ppm 155.2 (t, *J*_{PC} = 6 Hz, C^{C1}), 152.8 (C^{A2}), 150.4 (C^{A6}), 140.0 (C^{A4}), 143.3 (C^{B5}), 140.1 (C^{B2}), 134.8 (t, *J*_{PC} = 2 Hz, C^{C6}), 134.0 (t, *J*_{PC} = 8 Hz, C^{D2}), 132.3 (C^{C3}), 131.5 (C^{D4}), 131.0 (t, *J*_{PC} = 19 Hz, C^{D1}), 130.0 (t, *J*_{PC} = 5 Hz, C^{D3}), 129.3 (C^{B4}), 129.1 (C^{C5}), 128.9 (C^{B3}), 126.3 (t, *J*_{PC} = 3 Hz, C^{C4}), 124.4 (C^{A5}), 122.5 (C^{A3}), 120.3 (dd, *J*_{PC} = 16 Hz, C^{C2}), 36.8 (C^{xantphos-bridge}), 28.7 (C^{xantphos-Me}), 14.9 (C^{Me-B5}). ³¹P{¹H} NMR (202 MHz, acetone-*d*₆, 298 K) δ/ppm –14.2 (xantphos), –144.2 (septet, *J*_{PF} = 707 Hz, PF₆[–]). ESI-MS positive mode *m/z* 816.15 [Cu(xantphos)(MeThPy)]⁺ (calc. 816.17), 641.10 [Cu(xantphos)]⁺ (base peak, calc. 641.12). Found: C 60.36, H 4.39, N 1.41; C₄₉H₄₁CuF₆NOP₃S requires C 61.15, H 4.29, N 1.46.

2.9.2k [Cu(POP)(MeThMePy)][PF₆]

The reagents were POP (116 mg, 0.22 mmol), [Cu(MeCN)₄][PF₆] (80.0 mg, 0.22 mmol) and MeThMePy (40.7 mg, 0.22 mmol). [Cu(POP)(MeThMePy)][PF₆] was isolated as a colourless solid (134 mg, 0.14 mmol, 67%). ¹H NMR (500 MHz, acetone-*d*₆) δ/ppm 8.00 (t, *J* = 7.8 Hz, 1H, H^{A4}), 7.86 (d, *J* = 7.9 Hz, 1H, H^{A3}), 7.54–7.45 (m, 6H, H^{D4+C5}), 7.40–7.36 (m, 9H, H^{D3+B3}), 7.34 (d, *J* = 7.7 Hz, 1H, H^{A5}), 7.28–7.23 (m, 2H, H^{C6}), 7.19–7.09 (m, 10H, H^{D2+C4}), 6.88–6.81 (m, 3H, H^{C3+B4}), 2.39 (d, *J* = 1.1 Hz, 3H, H^{Me-B5}), 2.34 (s, 3H, H^{Me-A6}). ¹³C{¹H}

NMR (126 MHz, acetone- d_6) δ /ppm 159.3 (C^{A6}), 158.7 (t, $J_{PC} = 6$ Hz, C^{C1}), 153.0 (C^{A2}), 142.9 (C^{B5}), 140.8 (C^{B2}), 140.3 (C^{A4}), 135.1 (C^{C3}), 133.9 (t, $J_{PC} = 8$ Hz, C^{D2}), 133.3 (C^{C5}), 131.6 (C^{D4}), 130.9 (t, $J_{PC} = 19$ Hz, C^{D1}), 130.0 (t, $J_{PC} = 5$ Hz, C^{D3}), 129.7 (C^{B3}), 129.5 (C^{B4}), 126.3 (t, $J_{PC} = 2$ Hz, C^{C4}), 124.4 (C^{A5}), 123.5 (C^{C2}), 121.2 (t, $J_{PC} = 2$ Hz, C^{C6}), 120.0 (C^{A3}), 25.2 (C^{Me-A6}), 15.6 (C^{Me-B5}). $^{31}P\{^1H\}$ NMR (202 MHz, acetone- d_6 , 298 K) δ /ppm -15.5 (POP), -144.2 (septet, $J_{PF} = 707$ Hz, PF_6^-). ESI-MS positive mode m/z 790.10 [Cu(POP)(MeThMePy)] $^+$ (calc. 790.15), 601.05 [Cu(POP)] $^+$ (base peak, calc. 601.09). Found: C 60.57, H 4.11, N 1.78; $C_{47}H_{39}CuF_6NOP_3S$ requires C 60.29, H 4.20, N 1.50.

2.9.21 [Cu(xantphos)(MeThMePy)][PF₆]

The reagents were, xantphos (124 mg, 0.22 mmol), [Cu(MeCN)₄][PF₆] (80.1 mg, 0.22 mmol) and MeThMePy (40.7 mg, 0.22 mmol). [Cu(xantphos)(MeThMePy)][PF₆] was isolated as a colourless solid (157 mg, 0.16 mmol, 75%). 1H NMR (500 MHz, acetone- d_6) δ /ppm 8.02 (t, $J = 7.8$ Hz, 1H, H^{A4}), 7.92–7.86 (m, 3H, H^{C5+A3}), 7.44 (t, $J = 7.5$ Hz, 4H, H^{D4}), 7.39 (d, $J = 7.6$ Hz, 1H, H^{A5}), 7.35–7.28 (m, 11H, $H^{D3+C4+B3}$), 7.12 (m, 8H, H^{D2}), 6.76 (m, 1H, H^{B4}), 6.71 (m, 2H, H^{C3}), 2.46 (s, 3H, H^{Me-A6}), 2.08 (s, 3H, H^{Me-B5}), 1.76 (s, 6H, $H^{xantphos-Me}$). $^{13}C\{^1H\}$ NMR (126 MHz, acetone- d_6) δ /ppm 158.6 (C^{A6}), 155.1 (t, $J_{PC} = 6$ Hz, C^{C1}), 152.8 (C^{A2}), 142.9 (C^{B5}), 140.5 (C^{B2}), 140.0 (C^{A4}), 134.8 (t, $J_{PC} = 2$ Hz, C^{C6}), 133.8 (t, $J_{PC} = 8$ Hz, C^{D2}), 132.2 (C^{C3}), 131.5 (C^{D4}), 131.0 (t, $J_{PC} = 19$ Hz, C^{D1}), 130.0 (t, $J_{PC} = 5$ Hz, C^{D3}), 129.5 (C^{B4}), 129.1 (C^{C5+B3}), 126.5 (t, $J_{PC} = 2.5$ Hz, C^{C4}), 124.6 (C^{A5}), 120.3 (C^{A3}), 120.1 (dd, $J_{PC} = 16$ Hz, C^{C2}), 36.6 ($C^{xantphos-bridge}$), 28.3 ($C^{xantphos-Me}$), 25.5 (C^{Me-A6}), 15.2 (C^{Me-B5}). $^{31}P\{^1H\}$ NMR (202 MHz, acetone- d_6 , 298 K) δ /ppm -14.4 (xantphos), -144.2 (septet, $J_{PF} = 707$ Hz, PF_6^-). ESI-MS positive mode m/z 830.19 [Cu(xantphos)(MeThMePy)] $^+$ (calc. 830.18), 641.10 [Cu(xantphos)] $^+$ (base peak, calc. 641.12). Found: C 61.83, H 5.13, N 1.48; $C_{50}H_{43}CuF_6NOP_3S$ requires C 61.51, H 4.44, N 1.43.

Chapter 3: Influencing the photophysical properties of [Cu(P^P)(N^N)][PF₆] complexes with bromo-substituents on 1,10-phenanthroline

This chapter is based on reference 196. Synthesis of the complexes and part of the measurements were carried out by Nikolai Tarrassenko and Aramis Keller.

3.1 Motivation

LUMO energy tuning in [Cu(P^P)(N^N)]⁺ complexes by introducing substituents on the N^N ligand has been discussed in section 1.1.3c. For a majority of the used ligands these substituents are limited to trifluoroalkyl, alkyl or aryl substituents.^{114,161,179,183,237,238} The report of Weber *et al.* correlated σ -donating capacity of the substituent to a blue-shift in emission and higher quantum yield. [Cu(xantphos)(4,4'-dimethoxy-2,2'-bipyridine)][BF₄] (with the methoxy (MeO) substituent having the most negative σ -Hammett parameter of the series) was featured as the complex with the highest PLQY and highest energy λ_{em}^{max} .¹⁸⁸ On the other hand, the comparison of [Cu(xantphos)(6-MeObpy)][PF₆] to [Cu(xantphos)(6-Mebpy)][PF₆] shows a diminished PLQY and lower energy λ_{em}^{max} for the former.^{116,217} This shows that the introduction of a substituent with a more negative σ -Hammett parameter does not automatically lead to improvement in photophysical properties. It has to be noted that the values of the σ -Hammett parameter are dependent on the position on the aromatic ring (*ortho*, *meta*, *para*) and while the σ -meta and σ -para values correlate well with experimental observations, the σ -ortho value does not. One of the reasons why it is hard to predict the σ -ortho value is the influence of sterics,²³⁹ which in [Cu(P^P)(N^N)]⁺ complexes plays a particularly important role as has been described earlier (section 1.1.3c).

Studies involving phen and bpy ligands with a heteroatom directly attached to the diimine have been surprisingly rare and involved mostly alkyloxy and halogen substituents.^{115,116,240–242} An investigation by Keller *et al.* of derivatives incorporating 6-halo and 6,6'-dihalo-2,2'-bipyridines with Cl and Br have shown these halogens to be less effective in enhancing the emission of [Cu(P^P)(N^N)][PF₆] than methyl substituents. Since halogens are electron withdrawing and considering σ -Hammett parameters this seems intuitively correct, but it is also possible that the halogens offer additional non-radiative decay pathways. Still, the halogenated complexes exhibited fairly good photophysical properties with PLQYs of 14.8%, 17.1% and 16.3% for [Cu(xantphos)(6,6'-Cl₂bpy)][PF₆], [Cu(POP)(6,6'-Cl₂bpy)][PF₆] and [Cu(xantphos)(6-Brbpy)][PF₆], respectively, in solid state measurements. In LEC devices [Cu(POP)(6,6'-Cl₂bpy)][PF₆] and [Cu(xantphos)(6,6'-Cl₂bpy)][PF₆] had short turn-on times of <12 s and featured maximum luminance values of 64 cd m⁻² and 140 cd m⁻² at an average current density of 50 A m⁻². These is in comparison to a turn on time of 10 min and a maximum luminance of 145 cd m⁻² for [Cu(xantphos)(6,6'-Me₂bpy)][PF₆] at the same current density.^{115,217}

In the family of [Cu(P^P)(N^N)][PF₆] complexes only a few reports involve simple halogenated phen ligands. Feng *et al.* reported the emission of [Cu(xantphos)(3,8-Br₂bpy)][ClO₄] and [Cu(BINAP)(3,8-Br₂bpy)][ClO₄] (BINAP = 2'-bis(diphenylphosphano)-1,1'-binaphthalene) at 565 nm and 606 nm (λ_{exc} = 365 nm), respectively, but no PLQY values were given. Other examples include [Cu(bdpp)(phen)][ClO₄] and [Cu(bdpp)(3,8-Br₂phen)][ClO₄] (bdpp = 1,2-bis(diphenylphosphane)benzene (3,8-Br₂phen is shown in scheme 3.1) with a PLQY of 18.33% and 3.58% (λ_{exc} = 300–430 nm) in solid state and [(3,8-Br₂phen)Cu(μ -

$\text{Ph}_2\text{P}(\text{CH}_2)_5\text{PPh}_2)_2\text{Cu}(3,8\text{-Br}_2\text{phen})][\text{ClO}_4]_2$ which emits at 559 nm when excited at 330 nm with a PLQY of 17.4%.^{243,244}

In continuation of the work carried out in the Constable – Housecroft group by Keller *et al.* and motivated by the lack of data surrounding $[\text{Cu}(\text{P}^\wedge\text{P})(\text{Br}_2\text{phen})][\text{PF}_6]$ with either POP or xantphos, a series of six complexes were synthesized. The employed Br_2phen isomers are presented in scheme 3.1.

3.2 Synthesis

The ligands were either commercially available (3,8- Br_2phen and 4,7- Br_2phen) or synthesized following a previously described route (2,9- Br_2phen) and the NMR ^1H and $^{13}\text{C}\{^1\text{H}\}$ data matched those reported.²⁴⁵

The optimized synthesis procedures with xantphos and the Br_2phen added in parallel, and the sequential addition of POP and subsequently the N^\wedgeN ligand, to a solution of $[\text{Cu}(\text{MeCN})_4][\text{PF}_6]$ in CH_2Cl_2 were used. The total reaction time for both procedures was about 2 h. The complexes were recrystallized by vapour diffusion of Et_2O into a CH_2Cl_2 solution of the crude material.

For $[\text{Cu}(\text{POP})(2,9\text{-Br}_2\text{phen})][\text{PF}_6]$, $[\text{Cu}(\text{POP})(3,8\text{-Br}_2\text{phen})][\text{PF}_6]$ and $[\text{Cu}(\text{POP})(4,7\text{-Br}_2\text{phen})][\text{PF}_6]$, the cation peak was found in the ESI mass spectrum of each compound at m/z 939.02, 938.96 and 938.98, respectively, with an additional peak assigned to $[\text{Cu}(\text{POP})]^+$ at m/z 601.09, 601.06 and 601.11, respectively. Similarly, for $\text{Cu}(\text{xantphos})(2,9\text{-Br}_2\text{phen})[\text{PF}_6]$, $[\text{Cu}(\text{xantphos})(3,8\text{-Br}_2\text{phen})][\text{PF}_6]$ and $[\text{Cu}(\text{xantphos})(4,7\text{-Br}_2\text{phen})][\text{PF}_6]$, a peak arising from the $[\text{Cu}(\text{P}^\wedge\text{P})(\text{N}^\wedge\text{N})]^+$ ion was found at m/z 979.03, 979.00 and 979.03, respectively, with an additional $[\text{Cu}(\text{xantphos})]^+$ peak at m/z 641.12, 641.13 and 641.15, respectively. $[\text{Cu}(\text{POP})]^+$ and $[\text{Cu}(\text{xantphos})]^+$ represented the base peak for the $[\text{Cu}(\text{P}^\wedge\text{P})(2,9\text{-Br}_2\text{phen})]^+$ compounds, whereas with the other 3,8- and 4,7- Br_2phen isomers, they represented a minor species. This may be attributed to increased steric effects for the 2,9- Br_2phen when compared to the other two isomers and will be discussed in more detail in section 3.3.2.

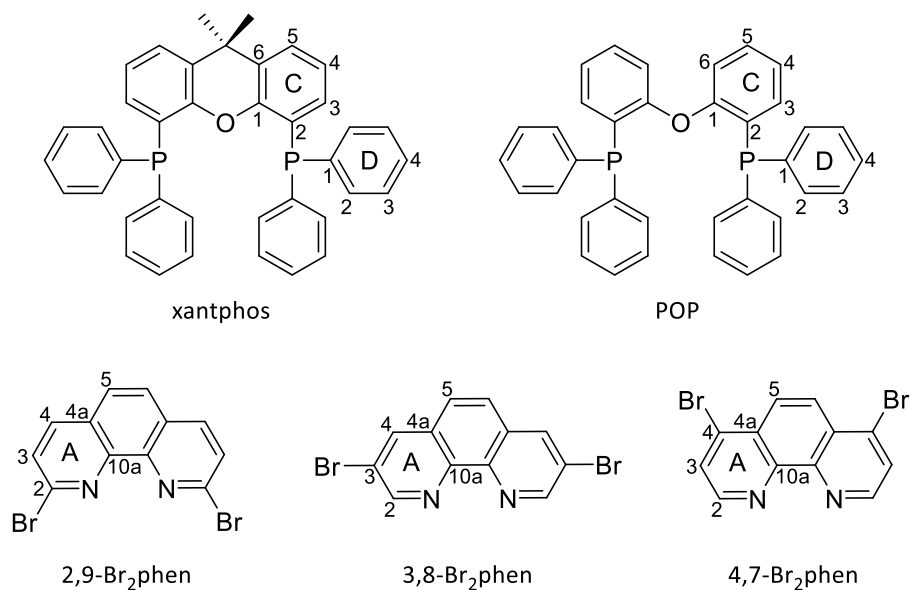
For all complexes except $[\text{Cu}(\text{POP})(2,9\text{-Br}_2\text{phen})][\text{PF}_6]$, satisfactory elemental analysis was obtained. Because the elemental composition of $[\text{Cu}(\text{POP})(2,9\text{-Br}_2\text{phen})][\text{PF}_6]$ could not be corroborated by elemental analysis, a high resolution ESI-MS was recorded. Further structural characterizations of the six complexes were made by assignment of the ^1H , $^{13}\text{C}\{^1\text{H}\}$ and ^{31}P NMR spectra and X-ray diffraction, which are discussed in section 3.3.

3.3 Structural characterization

3.3.1 NMR spectroscopy

The solution NMR ^1H , $^{13}\text{C}\{^1\text{H}\}$, $^{31}\text{P}\{^1\text{H}\}$, COSY, NOESY, HMQC and HMBC spectra were recorded in acetone- d_6 at 298 K.

In the $^{31}\text{P}\{^1\text{H}\}$ NMR spectrum a septet at δ -144.2 ppm was assigned to the PF_6^- anion in addition to a broadened singlet between δ -10.1 and -12.4 ppm arising from a coordinated POP or xantphos ligand. In the ^1H NMR spectra, the disappearance of $\text{H}^{\text{C}6}$ and the change in multiplicity of $\text{H}^{\text{C}5}$ when going from $[\text{Cu}(\text{POP})(\text{Br}_2\text{phen})][\text{PF}_6]$ to $[\text{Cu}(\text{xantphos})(\text{Br}_2\text{phen})][\text{PF}_6]$ complexes, is in accordance with the introduction of the xantphos $\text{C}(\text{Me})_2$ unit. On the NMR time scale at room temperature only one set of signals is observed in the NMR spectra which is consistent with dynamic behaviour akin to observations made for related $[\text{Cu}(\text{P}^\wedge\text{P})(\text{bpy})][\text{PF}_6]$ complexes.^{183,217} Comparing Figure 3.1a which shows the aromatic



Scheme 3.1: Structures of $P^A P$ and $Br_2 phen$ ligands used in the synthesis of $[Cu(P^A P)(Br_2 phen)][PF_6]$ complexes with labelling scheme used for 1H and ^{13}C NMR spectroscopic assignments.

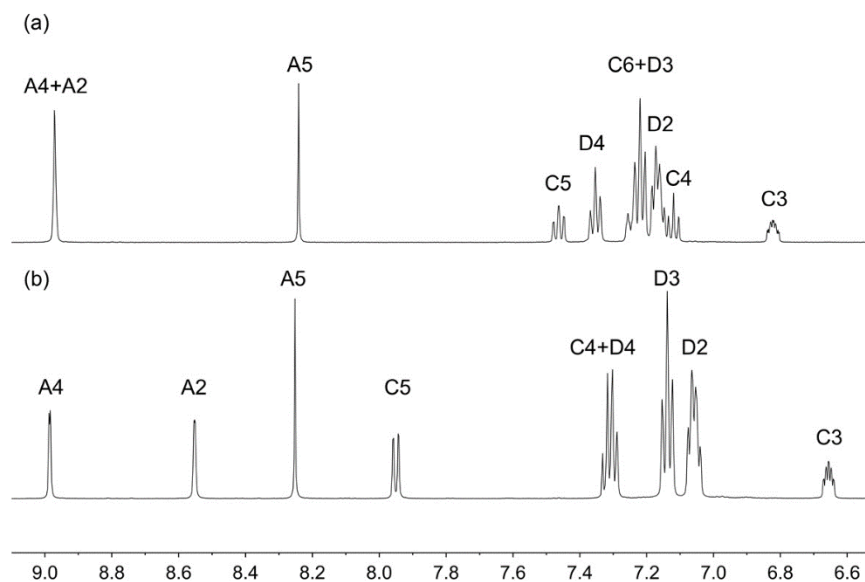


Figure 3.1: Aromatic region of the 1H NMR spectra (500 MHz, acetone- d_6 , 298 K) of (a) $[Cu(POP)(3,8-Br_2 phen)][PF_6]$ and $[Cu(xantphos)(3,8-Br_2 phen)][PF_6]$. Due to the introduction of the $C(Me)_2$ unit in xantphos, the signal for H^{C6} disappears in (b). Chemical shifts are given in δ/ppm , for atom labelling see Scheme 3.1. Reproduced from reference 196 under the terms of the CC-BY license.

region of $[Cu(POP)(3,8-Br_2 phen)][PF_6]$ to the same region of $[Cu(xantphos)(3,8-Br_2 phen)][PF_6]$, shown in Figure 3.1b, a significant shift in the signal for H^{A2} is seen. This is attributed to H^{A2} lying over the previously described xanthene bowl (see section 2.4), which has a significant effect on the chemical shift of the proton. The signal of H^{A6} in $[Cu(xantphos)(6-Rbpy)][PF_6]$ complexes (in unsubstituted bpy the 6 position is

ortho-position to the N) has been shown to have vastly different shifts depending on if the proton lies over the bowl or is directed away from it.^{183,217} Since at room temperature the inversion of the xanthene bowl is not hindered, the phen unit is rendered C_2 symmetric and hence both H^{A2} (to be more precise H^{A2} and H^{A9}) protons experience the same effect.

To confirm the stability of the complexes in CH_2Cl_2 , which was used as solvent in electrochemical and solution photophysical measurements, NMR spectra in CD_2Cl_2 were recorded. The 1H NMR spectra of $[Cu(POP)(4,7-Br_2phen)][PF_6]$ did not change over a period of 6 hours and an H^{A2} (located on the Br_2phen) – H^{D2} (located on POP phenyl ring) crosspeak in the NOESY spectrum strongly supports the presence of the heteroleptic complex.

3.3.2 Crystal structures

Table 3.1: Crystallographic data for [Cu(P[^]P)(N[^]S)][PF₆] compounds.

Compounds	[Cu(POP)(2,9-Br ₂ phen)][PF ₆] ·0.5CH ₂ Cl ₂	[Cu(POP)(3,8-Br ₂ phen)][PF ₆] ·0.8CH ₂ Cl ₂ ·0.9H ₂ O	[Cu(POP)(4,7-Br ₂ phen)][PF ₆] ·0.5CH ₂ Cl ₂
Formula	C ₅₀ H ₃₉ Br ₂ CuF ₆ N ₂ O _{1.5} P ₃	C _{48.8} H _{37.4} Br ₂ Cl _{1.6} CuF ₆ N ₂ O _{1.9} P ₃	C ₄₉ H ₃₆ Br ₂ Cl ₂ CuF ₆ N ₂ OP ₃
Formula weight	1122.10	1169.20	1169.97
Crystal colour and habit	Yellow block	Yellow plate	Yellow block
Crystal system	Triclinic	Monoclinic	Triclinic
Space group	<i>P</i> -1	<i>P</i> 2/ <i>c</i>	<i>P</i> -1
<i>a</i> , <i>b</i> , <i>c</i> /Å	15.1949(10), 29.53222(12), 18.5423(13)	12.9120(7), 14.0896(8), 27.1332(13)	12.4032(9), 18.9805(14), 22.0591(17)
<i>α</i> , <i>β</i> , <i>γ</i> /°	107.867(2), 104.444(2), 101.088(2)	90, 94.491(2), 90	70.330(3), 77.791(3), 87.292(3)
<i>V</i> /Å ³	4603.2(5)	4921.0(5)	5432.5(4)
<i>D_c</i> /Mg m ⁻³	1.619	1.578	1.490
<i>Z</i>	4	4	4
<i>μ</i> (Cu-Kα)/mm ⁻¹	4.260	4.797	5.128
<i>T</i> /K	130	130	130
Refin. collected (<i>R</i> _{int})	38972 (0.0241)	30196 (0.0313)	42627
Unique refin.	16488	8930	17481
Refin. for refinement	15466	8307	16297
Parameters	1182	556	1135
Threshold	2σ	2σ	2σ
<i>R</i> ₁ (<i>R</i> ₁ all data)	0.0369 (0.0389)	0.0870 (0.0905)	0.0327 (0.0350)
<i>wR</i> ₂ (<i>wR</i> ₂ all data)	0.0952 (0.0971)	0.2489 (0.2516)	0.0817 (0.0834)
Goodness of fit	1.028	1.124	1.011
CCDC REFCODE	ZUFWEF	ZUFVUU	ZUFWIJ
Compounds	[Cu(xantphos)(2,9-Br ₂ phen)][PF ₆] ·1.1CH ₂ Cl ₂	[Cu(xantphos)(3,8-Br ₂ phen)][PF ₆] ·1.1CH ₂ Cl ₂ ·0.7Et ₂ O	[Cu(xantphos)(4,7-Br ₂ phen) ₂][PF ₆] ·CH ₂ Cl ₂ ·0.9Et ₂ O
Formula	C _{52.1} H _{40.2} Br ₂ Cl _{2.2} CuF ₆ N ₂ OP ₃	C _{54.9} H _{47.2} Br ₂ Cl _{2.2} CuF ₆ N ₂ O _{1.7} P ₃	C _{55.6} H ₄₉ Br ₂ Cl ₂ CuF ₆ N ₂ O _{1.9} P ₃
Formula weight	1218.52	1270.40	1276.74
Crystal colour and habit	Yellow plate	Yellow block	Yellow block
Crystal system	Monoclinic	Triclinic	Triclinic
Space group	<i>C</i> 2/ <i>m</i>	<i>P</i> -1	<i>P</i> -1
<i>a</i> , <i>b</i> , <i>c</i> /Å	33.3182(16), 14.1050(6), 11.8205(5)	10.1768(8), 13.7501(11), 20.1505(16)	10.9300(4), 14.2927(6), 19.2894(8)
<i>α</i> , <i>β</i> , <i>γ</i> /°	90, 102.059(5), 90	90.204(2), 98.120(2), 99.535(2)	70.366(3), 86.491(3), 73.206(3)
<i>V</i> /Å ³	5432.(4)	2751.9(4)	2715.0(2)
<i>D_c</i> /Mg m ⁻³	1.490	1.533	1.562
<i>Z</i>	4	2	2
<i>μ</i> (Cu-Kα)/mm ⁻¹	4.895	4.597	4.864
<i>T</i> /K	130	130	130
Refin. collected (<i>R</i> _{int})	15005 (0.0515)	35741 (0.0264)	32020 (0.0795)
Unique refin.	5607	10241	10645
Refin. for refinement	4802	9939	9958
Parameters	417	728	624
Threshold	2σ	2σ	2σ
<i>R</i> ₁ (<i>R</i> ₁ all data)	0.0728 (0.0863)	0.0382 (0.0391)	0.0858 (0.0904)
<i>wR</i> ₂ (<i>wR</i> ₂ all data)	0.1853 (0.1973)	0.01039 /0.1101)	0.2317 (0.2384)
Goodness of fit	1.034	1.073	1.059
CCDC REFCODE	ZUFVOO	ZUFWII	ZUFWAB

Layering CH₂Cl₂ solutions of the heteroleptic Cu(I) complexes with Et₂O yielded yellow single crystals of [Cu(POP)(2,9-Br₂phen)][PF₆].0.5Et₂O, [Cu(POP)(3,8-Br₂phen)][PF₆].0.8CH₂Cl₂.0.9H₂O, [Cu(POP)(4,7-Br₂phen)][PF₆].CH₂Cl₂, [Cu(xantphos)(2,9-Br₂phen)][PF₆].1.1CH₂Cl₂, [Cu(xantphos)(3,8-Br₂phen)][PF₆].1.1CH₂Cl₂.0.7Et₂O and [Cu(xantphos)(4,7-Br₂phen)][PF₆].CH₂Cl₂.0.9Et₂O. A summary of the crystallographic data can be found in Table 3.1. It should be mentioned that the unit cell dimensions for [Cu(POP)(2,9-Br₂phen)][PF₆].Et₂O are very close to those reported for [Cu(POP)(2,9-Br₂phen)][PF₆].Et₂O. The xantphos ligand in [Cu(xantphos)(4,7-Br₂phen)][PF₆].CH₂Cl₂.0.9Et₂O is disordered and has been modelled over two sites with equal occupancies. The complex [Cu(xantphos)(4,7-Br₂phen)][PF₆].CH₂Cl₂.0.9Et₂O crystallizes in the monoclinic space group *C*2/*m*. The xantphos ligand in the

latter compound is disordered and has been modelled over two sites with equal occupancies which are related by a mirror plane. The asymmetric unit contains half of the 2,9-Br₂phen, while the other half is generated by the mirror plane. Three of the four xantphos phenyl rings of the PPh₂ unit are associated with the disorder. Due to the extensive disorder in this crystal structure, it will not be discussed in detail. However, as a singular comment, the crystal structure confirms the chelating binding mode for the 2,9-Br₂phen despite the steric hindrance of the two bromo substituents being in *ortho*-position to the N-donors.

The structures of the remaining [Cu(P[^]P)(N[^]N)]⁺ cations are shown in Figures 3.2 and 3.3. Bond lengths and bond angles surrounding the Cu(I) centre are compared in Table 3.2. Phen with its fused aromatic rings only offers a very limited flexibility, so that the N–Cu–N angle only slightly deviates from 80° in all complexes. The flexibility of the P[^]P ligands plays an important role in the P–Cu–P bite angle and while the trend of decreasing angles (2,9-Br₂phen > 3,8-Br₂phen > 4,7-Br₂phen) is observable in both POP and xantphos complexes, the changes are bigger the former (Table 3.2), emphasizing the higher flexibility of the POP ligand.

Table 3.2: Bond angles and bond lengths surrounding the Cu(I) centre in [Cu(P[^]P)(Br₂phen)][PF₆] compounds. ^aFor [Cu(POP)(2,9-Br₂phen)][PF₆].0.5Et₂O and [Cu(POP)(4,7-Br₂phen)][PF₆].CH₂Cl₂ there are two independent ion pairs in the asymmetric unit. ^b τ_4 parameter as defined by Houser et al.. ^cThe N atoms are symmetry-related (symmetry code x, 1-y, z).

Cation in [Cu(P [^] P)(Br ₂ phen)][PF ₆] ^a	P–Cu–P/°	N–Cu–P/°	N–Cu–N/°	τ_4 ^b	P–Cu/Å	N–Cu/Å
[Cu(POP)(2,9-Br ₂ phen)] ⁺ cation 1	118.00(3)	106.47(6), 118.42(6), 109.57(6), 118.33(6)	79.61(8)	0.87	2.2742(7), 2.2416(7)	2.100(2), 2.135(2)
[Cu(POP)(2,9-Br ₂ phen)] ⁺ cation 2	116.47(3)	113.30(6), 118.81(6), 104.97(6), 118.45(6)	78.46(9)	0.87	2.2849(7), 2.2704(7)	2.149(2), 2.129(2)
[Cu(POP)(3,8-Br ₂ phen)] ⁺	115.65(7)	112.16(15), 107.46(15), 114.41(15), 120.32(16)	80.9(2)	0.88	2.2468(17), 2.2332(18)	2.055(6), 2.083(5)
[Cu(POP)(4,7-Br ₂ phen)] ⁺ cation 1	112.37(2)	105.08(6), 111.47(6), 110.95(6), 129.56(6)	80.22(7)	0.84	2.2622(7), 2.2377(7)	2.0797(19), 2.0607(19)
[Cu(POP)(4,7-Br ₂ phen)] ⁺ cation 2	112.52(3)	112.52(3), 104.92(6), 113.62(6), 113.62(6)	80.34(8)	0.85	2.2694(7), 2.2370(7)	2.088(2), 2.0683(19)
[Cu(xantphos)(2,9-Br ₂ phen)] ⁺	117.97(8)	121.55(12), 105.73(12)	79.2(2)	0.83	2.295(2), 2.2523(18)	2.115(4), 2.115(4) ^c
[Cu(xantphos)(3,8-Br ₂ phen)] ⁺	116.57(3)	109.79(6), 103.67(6), 119.92(6), 117.62(6)	80.45(8)	0.87	2.2495(7), 2.2752(7)	2.079(2), 2.122(2)
[Cu(xantphos)(4,7-Br ₂ phen)] ⁺	115.36(6)	109.97(12), 114.95(13), 121.66(13), 109.88(13)	80.29(16)	0.87	2.2619(15), 2.2591(15)	2.075(4), 2.069(5)

Figures 3.2 and 3.3 also show the distorted tetrahedral environment of the Cu(I) centre. Houser's τ_4 parameters for the complexes are between 0.83 and 0.88 (Table 2.2) suggesting a distortion towards C_{3v} symmetry.²¹⁹

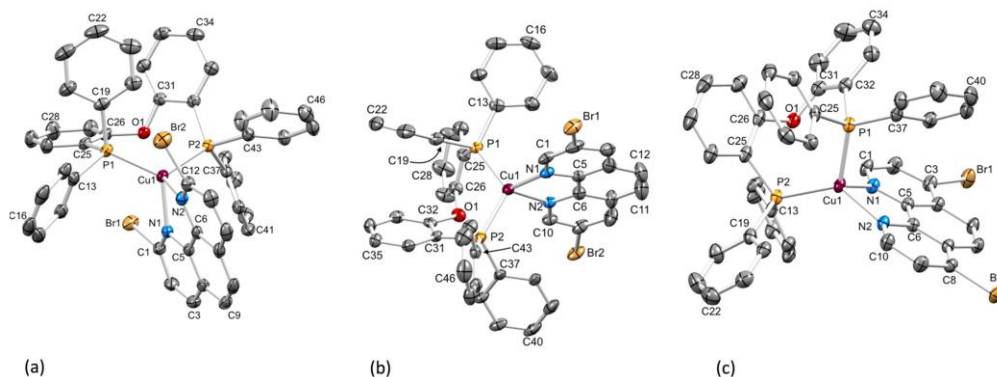


Figure 3.2: Cation structures of the POP containing complexes with H atoms omitted for clarity. (a) $[\text{Cu}(\text{POP})(2,9\text{-Br}_2\text{phen})]^+$ (ellipsoids plotted at 50% probability), (b) $[\text{Cu}(\text{POP})(3,8\text{-Br}_2\text{phen})]^+$ (ellipsoids plotted at 40% probability), (c) $[\text{Cu}(\text{POP})(4,7\text{-Br}_2\text{phen})]^+$ (ellipsoids plotted at 50% probability). For $[\text{Cu}(\text{POP})(2,9\text{-Br}_2\text{phen})][\text{PF}_6]\cdot 0.5\text{Et}_2\text{O}$ and $[\text{Cu}(\text{POP})(4,7\text{-Br}_2\text{phen})][\text{PF}_6]\cdot \text{CH}_2\text{Cl}_2$ there are two independent ion pairs in the asymmetric unit and only one cation is shown (see accompanying discussion and Table 3.2). Reproduced from reference 196 under the terms of the CC-BY license.

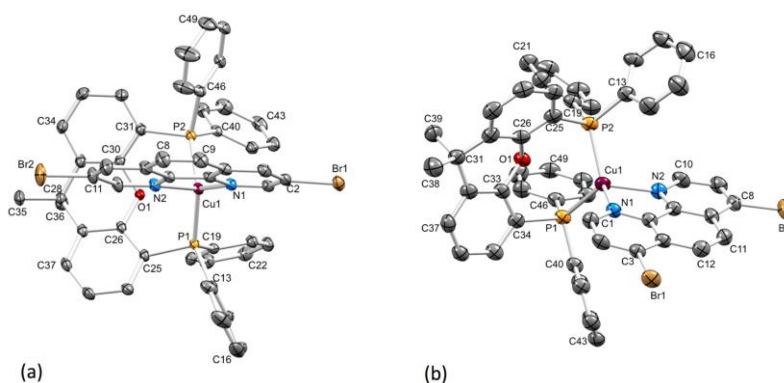


Figure 3.3: Cation structure of the POP containing complexes with H atoms omitted for clarity and ellipsoids plotted at 40% probability. (a) $[\text{Cu}(\text{POP})(3,8\text{-Br}_2\text{phen})]^+$, (b) $[\text{Cu}(\text{POP})(4,7\text{-Br}_2\text{phen})]^+$. Reproduced from reference 196 under the terms of the CC-BY license.

The asymmetric unit in $[\text{Cu}(\text{POP})(2,9\text{-Br}_2\text{phen})][\text{PF}_6]\cdot 0.5\text{Et}_2\text{O}$ and $[\text{Cu}(\text{POP})(4,7\text{-Br}_2\text{phen})][\text{PF}_6]\cdot \text{CH}_2\text{Cl}_2$ includes two independent ion-pairs. Bond lengths and angles are similar in both ions (Table 3.2). The overlay of the two $[\text{Cu}(\text{POP})(4,7\text{-Br}_2\text{phen})]^+$ cations is shown in Figure 3.4 with the two POP units approximately superimposed.

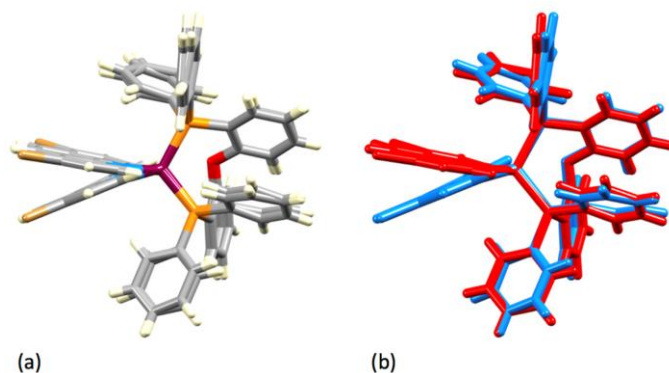


Figure 3.4: Overlay of the two independent cations in $[\text{Cu}(\text{POP})(4,7\text{-Br}_2\text{phen})][\text{PF}_6]\cdot\text{CH}_2\text{Cl}_2$ with the POP units approximately superimposed. (a) colouration by element colour, (b) coloured to show the two individual cations. Reproduced from reference 196 under the terms of the CC-BY license.

$[\text{Cu}(\text{POP})(\text{N}^{\wedge}\text{N})]^+$ and $[\text{Cu}(\text{xantphos})(\text{N}^{\wedge}\text{N})]^+$ cations often display intra-cation π -stacking interactions in the solid state. $[\text{Cu}(\text{xantphos})(\text{N}^{\wedge}\text{N})]^+$ tends to feature face-to-face π -stacking between two phenyl rings of the two different PPh_2 units, while in $[\text{Cu}(\text{POP})(\text{N}^{\wedge}\text{N})]^+$ the face-to-face π -stacking interactions occur between a phenyl ring of a PPh_2 unit and an arene ring of the POP backbone (see for example reference 116).

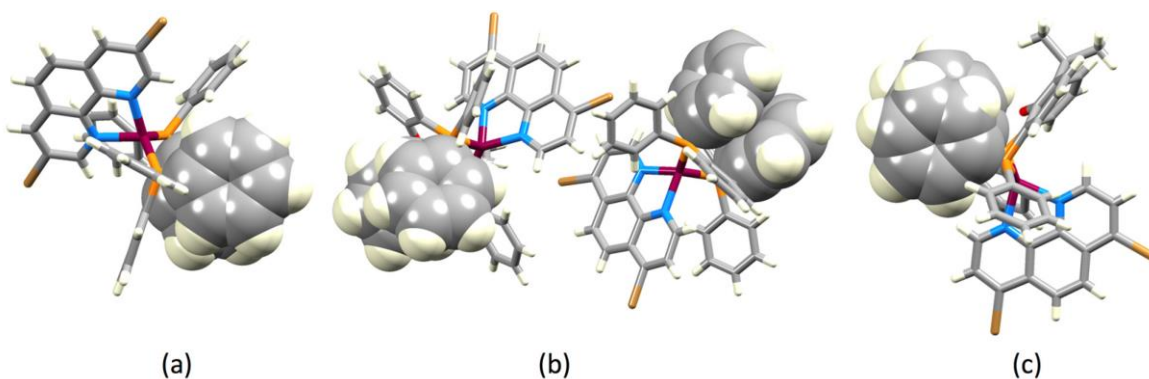


Figure 3.5: Space filling representations of the face-to-face π -stacking interactions between one phenyl ring of a PPh_2 group and an arene ring of the POP backbone in (a) in $[\text{Cu}(\text{POP})(3,8\text{-Br}_2\text{phen})]^+$ and (b) the two independent in $[\text{Cu}(\text{POP})(4,7\text{-Br}_2\text{phen})]^+$ cations. Space filling representation of the face-to-face π -stacking interactions between two phenyl ring of the two separate PPh_2 units on xantphos in (c) in $[\text{Cu}(\text{xantphos})(4,7\text{-Br}_2\text{phen})]^+$. Reproduced from reference 196 under the terms of the CC-BY license.

In the present complexes, the π -stacking interaction between the phenyl and arene ring of the POP can be observed in $[\text{Cu}(\text{POP})(3,8\text{-Br}_2\text{phen})]^+$ and $[\text{Cu}(\text{POP})(4,7\text{-Br}_2\text{phen})]^+$ (Figure 3.5a and 3.5b), with angles between the least squares planes of 27.7° and a centroid...centroid distance of 4.1 \AA for $[\text{Cu}(\text{POP})(3,8\text{-Br}_2\text{phen})]^+$ and 27.9° and 17.1° with centroid...centroid distances of 4.0 and 3.8 \AA for the two independent $[\text{Cu}(\text{POP})(4,7\text{-Br}_2\text{phen})]^+$ cations. Similar interactions were not observed for $[\text{Cu}(\text{POP})(2,9\text{-Br}_2\text{phen})]^+$. This might be associated with the bromo-substituents in 2,9-position having an influence on the positioning of the POP PPh_2 units. However, in cations in all the crystal structures are closely associated and there are clearly inter-cation and intra-cation interactions at play, as is exemplified by $[\text{Cu}(\text{POP})(2,9\text{-Br}_2\text{phen})][\text{PF}_6]\cdot 0.5\text{Et}_2\text{O}$ in Figure 3.6. The face-to-face π -stacking between two phenyl rings of the two different PPh_2 groups in xantphos can be observed in $[\text{Cu}(\text{POP})(4,7\text{-Br}_2\text{phen})]^+$ (Figure 3.5c). The angle

between the least squares plane is 28.0° and the centroid...centroid is 4.0 \AA , which is rather long for an efficient π -stacking contact.²⁴⁶

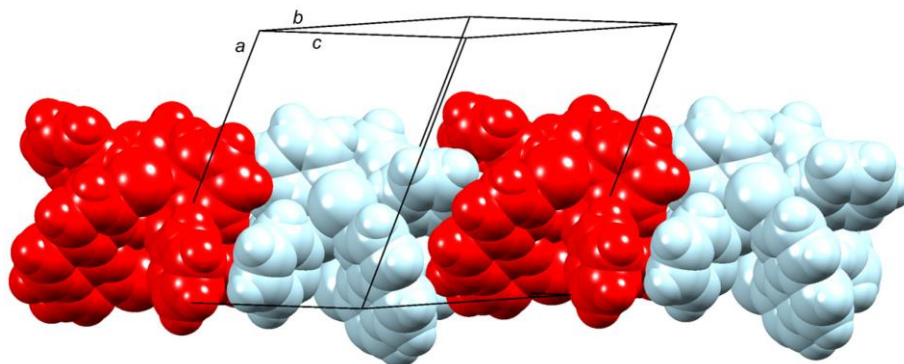


Figure 3.6: Packing of the independent cations (red and pale-blue) into chains in the crystal structure of $[\text{Cu}(\text{POP})(2,9\text{-Br}_2\text{phen})][\text{PF}_6] \cdot 0.5\text{Et}_2\text{O}$. Solvent molecules and PF_6^- anions are omitted for clarity. Reproduced from reference 196 under the terms of the CC-BY license.

3.4 Electrochemistry

The electrochemical behaviour of $[\text{Cu}(\text{P}^\wedge\text{P})(\text{Br}_2\text{phen})][\text{PF}_6]$ was investigated with cyclic voltammetry using CH_2Cl_2 solutions of the compounds. In the cyclic voltammograms, the first observed oxidation between $+0.79 \text{ V}$ and $+0.97 \text{ V}$ (referenced to $\text{Fc}/\text{Fc}^+ = +0.0 \text{ V}$) is assigned to the $\text{Cu}^+ \rightarrow \text{Cu}^{2+}$ oxidation and is either irreversible or partially reversible (Table 3.3). Experiments with the goal to enhance the reversibility of the Cu-oxidation with the exchange of CH_2Cl_2 with 4-methyl-1,3-dioxolan-2-one (propylene carbonate) were unsuccessful. A second, fully irreversible oxidation can be observed if the forward CV scan is taken beyond $+1.2 \text{ V}$ (with respect to $\text{Fc}/\text{Fc}^+ = +0.0 \text{ V}$), which is assigned to phosphane oxidation. The highest oxidation potentials are observed for the two $[\text{Cu}(\text{P}^\wedge\text{P})(2,9\text{-Br}_2\text{phen})][\text{PF}_6]$ compounds, which is consistent with the steric effects of the bromo-substituents *ortho* to the chelating N hindering the flattening of the copper geometry upon oxidation. This trend can also be observed on going from $[\text{Cu}(\text{POP})(\text{phen})][\text{BF}_4]$ to $[\text{Cu}(\text{POP})(2,9\text{-Me}_2\text{phen})][\text{BF}_4]$ with the respective $\text{Cu}^+/\text{Cu}^{2+}$ occurring at $+1.23 \text{ V}$ and $+1.38 \text{ V}$ (referenced to Ag/AgCl).²⁴⁷ The introduction of chloro- and bromo-substituents in the 6,6'-positions of bpy similarly shifts the $\text{Cu}^+/\text{Cu}^{2+}$ oxidation towards higher potentials.¹¹⁵ Several irreversible ligand based reduction processes can be observed for all the $[\text{Cu}(\text{P}^\wedge\text{P})(\text{Br}_2\text{phen})][\text{PF}_6]$ compounds (Table 3.3). This compares to only one reduction process for $[\text{Cu}(\text{POP})(\text{phen})][\text{PF}_6]$,²³⁷ indicating an involvement of the bromo-substituents in $[\text{Cu}(\text{P}^\wedge\text{P})(\text{Br}_2\text{phen})][\text{PF}_6]$.

Table 3.3: Cyclic voltammetry data for $[\text{Cu}(\text{P}^\wedge\text{P})(\text{Br}_2\text{phen})][\text{PF}_6]$ complexes in CH_2Cl_2 ($c \approx 2 \times 10^{-3} \text{ M}$, referenced to internal $\text{Fc}/\text{Fc}^+ = 0.0 \text{ V}$, $[\text{nBu}_4\text{N}][\text{PF}_6]$ as supporting electrolyte, scan rate = 0.1 V s^{-1}). ^aAll reductive processes are irreversible. irrev = irreversible.

Compounds	$\lambda_{\text{abs}}^{\text{max}}/\text{nm}$ ($\epsilon_{\text{max}}/\text{dm}^3 \text{ mol}^{-1} \text{ cm}^{-1}$)	
	Ligand-based absorptions	MLCT
$[\text{Cu}(\text{POP})(2,9\text{-Br}_2\text{phen})][\text{PF}_6]$	281 (31,100), 304 sh (19,800), 346 (2,900)	415 (2,400)
$[\text{Cu}(\text{POP})(3,8\text{-Br}_2\text{phen})][\text{PF}_6]$	283 (39,100), 302 sh (22,500), 319 sh (16,200), 346 (2,900)	418 (3,700)
$[\text{Cu}(\text{POP})(4,7\text{-Br}_2\text{phen})][\text{PF}_6]$	274 (52,000), 309 sh (17,000), 327 sh (5,000)	418 (5,100)
$[\text{Cu}(\text{xantphos})(2,9\text{-Br}_2\text{phen})][\text{PF}_6]$	280 (30,200), 304 sh (19,800), 346 (2,900)	415 (2,400)
$[\text{Cu}(\text{xantphos})(3,8\text{-Br}_2\text{phen})][\text{PF}_6]$	282 (41,700), 320 sh (12,500), 346 (2,900)	416 (3,400)
$[\text{Cu}(\text{xantphos})(4,7\text{-Br}_2\text{phen})][\text{PF}_6]$	275 (54,500), 309 sh (12,200), 327 sh (5,000)	420 (4,500)

3.5 Photophysical properties

3.5.1 UV-Vis absorption spectra

Table 3.4: Summary of the absorption maxima in the CH_2Cl_2 solution absorption spectra of $[\text{Cu}(\text{P}^\wedge\text{P})(\text{Br}_2\text{phen})][\text{PF}_6]$ complexes ($c = 1.75 \times 10^{-5}$ – 3.0×10^{-5} M).

Compounds	Oxidative Process			Reductive processes
	$E_{1/2}^{\text{ox}}/\text{V}$	E_{pc}/V	$E_{\text{pc}} - E_{\text{pa}}/\text{mV}$	E_{pa}/V^a
$[\text{Cu}(\text{POP})(2,9\text{-Br}_2\text{phen})][\text{PF}_6]$		+0.98 (irrev)		-2.23, -2.10, -1.92, -1.83
$[\text{Cu}(\text{POP})(3,8\text{-Br}_2\text{phen})][\text{PF}_6]$	+0.86		120	-2.20, -1.94, -1.83
$[\text{Cu}(\text{POP})(4,7\text{-Br}_2\text{phen})][\text{PF}_6]$	+0.79		130	-2.17, -1.93, -1.84
$[\text{Cu}(\text{xantphos})(2,9\text{-Br}_2\text{phen})][\text{PF}_6]$	+0.97		105	-2.08, -1.85, -1.74
$[\text{Cu}(\text{xantphos})(3,8\text{-Br}_2\text{phen})][\text{PF}_6]$		+0.87 (irrev)		-2.19, -1.90, -1.81
$[\text{Cu}(\text{xantphos})(4,7\text{-Br}_2\text{phen})][\text{PF}_6]$		+0.95 (irrev)		-2.17, -1.87, -1.77

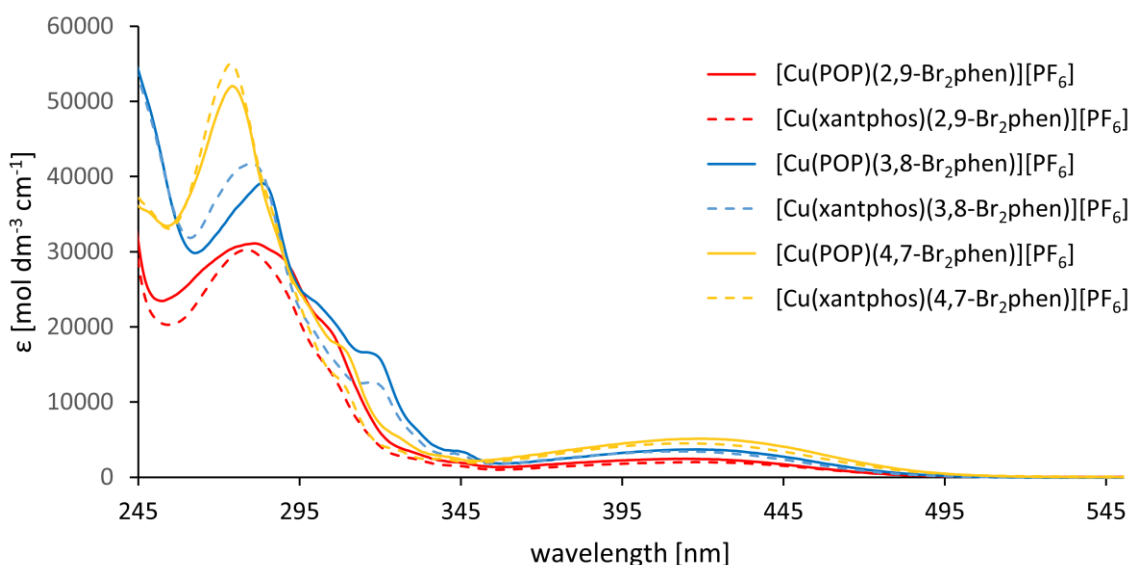


Figure 3.7: UV-Vis absorption spectra of $[\text{Cu}(\text{P}^\wedge\text{P})(\text{Br}_2\text{phen})][\text{PF}_6]$ complexes in CH_2Cl_2 with concentrations in the range of 1.75×10^{-5} – 3.0×10^{-5} M. Adapted from reference 196 under the terms of the CC-BY license.

CH_2Cl_2 solution absorption spectra of the Cu(I) complexes are presented in Figure 3.7 and the $\lambda_{\text{abs}}^{\text{max}}$ are summarized in Table 3.4. The broad, low energy absorption features with $\lambda_{\text{abs}}^{\text{max}}$ between 415–420 nm are typically assigned to MLCT transitions.¹¹⁵ Spin-allowed, ligand-centred transitions give rise to the high energy absorptions with $\lambda_{\text{abs}}^{\text{max}} < 345$ nm. The absorption spectrum profile of $[\text{Cu}(\text{xantphos})(3,8\text{-Br}_2\text{phen})][\text{PF}_6]$ is consistent the corresponding one reported for $[\text{Cu}(\text{xantphos})(3,8\text{-Br}_2\text{phen})][\text{ClO}_4]$.²⁴¹ The absorption profiles of the $[\text{Cu}(\text{P}^\wedge\text{P})(\text{Br}_2\text{phen})][\text{PF}_6]$ complexes form pairs with increasing values of ϵ_{max} ($2,9\text{-Br}_2\text{phen} < 3,8\text{-Br}_2\text{phen} < 4,7\text{-Br}_2\text{phen}$).

3.5.2 Solution emission properties

The $[\text{Cu}(\text{P}^\wedge\text{P})(\text{Br}_2\text{phen})][\text{PF}_6]$ complexes are weak yellow to orange emitters in argon-purged CH_2Cl_2 solution, when excited into the MLCT band (Figure 3.8 and Table 3.5). All PLQYs in solution were below 1%. Keller *et al.* investigated the origin of these emissions using computational methods. The unpaired-electron spin-density was calculated at the UB3LYP-D3 level and showed it being mostly located over the

metal and bpy ligand, suggesting a $^3\text{MLCT}$ nature for the T_1 state. Subsequent TD-DFT (TD = time dependent) calculations supported a LUMO \rightarrow HOMO $^3\text{MLCT}$ character of the emission and similar results were found by Yang *et al.*^{180,217} However, in their work Keller and co-workers stated that the calculated energy difference between the first excited singlet state (S_1) and the first excited triplet state (T_1) was in the range of 0.17–0.21 eV which would allow TADF to occur and therefore contributions of S_1 to the emission could not be excluded.²¹⁷ By analogy to the $[\text{Cu}(\text{P}^\wedge\text{P})(\text{N}^\wedge\text{N})][\text{PF}_6]$ complexes used by Keller *et al.* and Yang *et al.*, it can be assumed the solution emission in $[\text{Cu}(\text{P}^\wedge\text{P})(\text{Br}_2\text{phen})][\text{PF}_6]$ arises largely from similar $^3\text{MLCT}$ transitions.

Table 3.5: Summary of the emission photophysical data for $[\text{Cu}(\text{P}^\wedge\text{P})(\text{Br}_2\text{phen})][\text{PF}_6]$ compounds at room temperature. Concentration for deaerated solution measurements in $\text{CH}_2\text{Cl}_2 \approx 2.0 \times 10^{-5} \text{ M}$. $^a\lambda_{\text{exc}} = 365 \text{ nm}$ for $[\text{Cu}(\text{POP})(\text{Br}_2\text{phen})][\text{PF}_6]$ complexes and $\lambda_{\text{exc}} = 340 \text{ nm}$ for $[\text{Cu}(\text{xantphos})(\text{Br}_2\text{phen})][\text{PF}_6]$ complexes.

Compounds	Deaerated Solution		Powder		
	$\lambda_{\text{exc}}/\text{nm}$	$\lambda_{\text{em}}^{\text{max}}/\text{nm}$	$\lambda_{\text{em}}^{\text{max}}/\text{nm}^a$	PLQY/%	$\tau/\mu\text{s}$
$[\text{Cu}(\text{POP})(2,9\text{-Br}_2\text{phen})][\text{PF}_6]$	415	596	574	24	6.3
$[\text{Cu}(\text{POP})(3,8\text{-Br}_2\text{phen})][\text{PF}_6]$	420	655	578	3	0.9
$[\text{Cu}(\text{POP})(4,7\text{-Br}_2\text{phen})][\text{PF}_6]$	425	660	604	7	1.7
$[\text{Cu}(\text{xantphos})(2,9\text{-Br}_2\text{phen})][\text{PF}_6]$	425	582	554	45	9.9
$[\text{Cu}(\text{xantphos})(3,8\text{-Br}_2\text{phen})][\text{PF}_6]$	410	653	598	21	8.4
$[\text{Cu}(\text{xantphos})(4,7\text{-Br}_2\text{phen})][\text{PF}_6]$	420	657	574	12	4.2

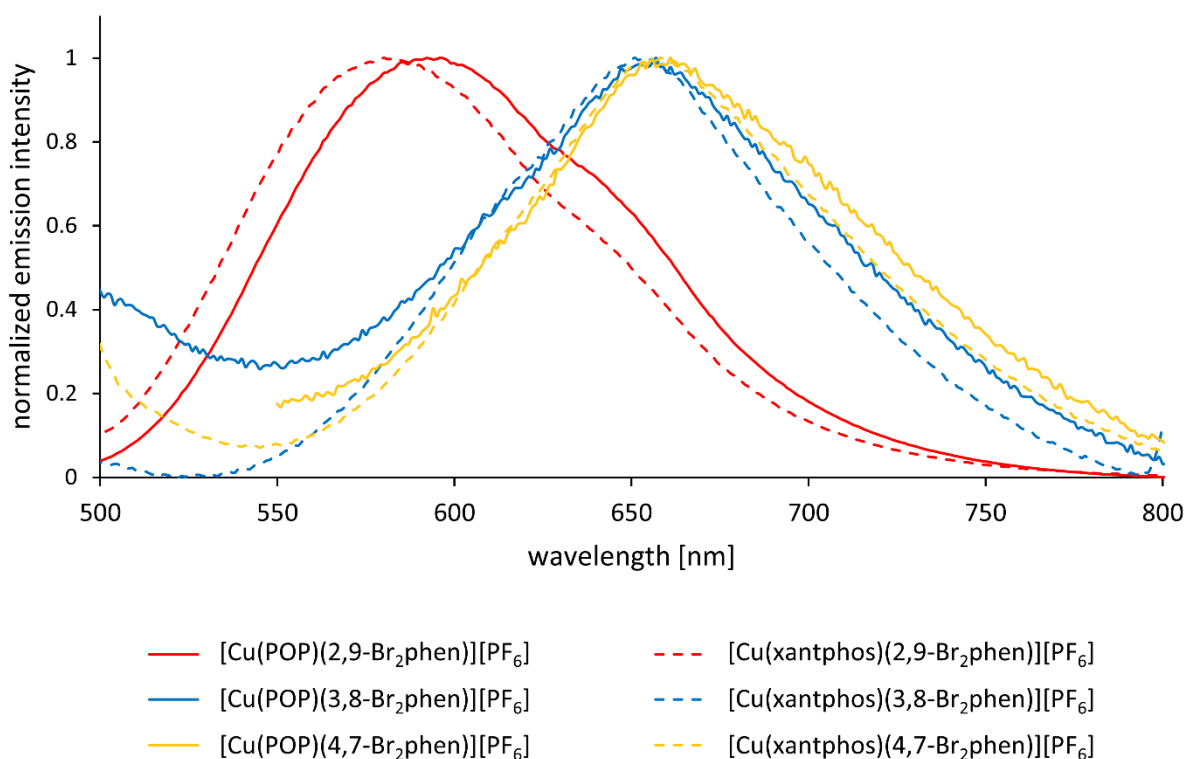


Figure 3.8: Normalized solution emission spectra of $[\text{Cu}(\text{P}^\wedge\text{P})(\text{Br}_2\text{phen})][\text{PF}_6]$ complexes in CH_2Cl_2 ($c = 1.5 \times 10^{-5} \text{ M} - 3.5 \times 10^{-5} \text{ M}$). λ_{exc} = see Table 3.5. Adapted from reference 196 under the terms of the CC-BY license.

Consistent with the higher oxidation potentials discussed in section 3.4, the emissions were significantly blue-shifted for [Cu(POP)(2,9-Br₂phen)][PF₆] and [Cu(xantphos)(2,9-Br₂phen)][PF₆] (λ_{em}^{max} = 596 and 582 nm, respectively) in comparison to the 3,8-Br₂phen and 4,7-Br₂phen compounds (λ_{em}^{max} between 653 and 660 nm, see Table 3.5). This suggests a higher energy level for the MLCT excited state of the two 2,9-Br₂phen complexes. Comparing the 2,9-Br₂phen complexes emission to the one of [Cu(POP)(2,9-Me₂phen)][BF₄] (λ_{em}^{max} = 570 nm) in CH₂Cl₂ at room temperature reveals a slight red-shift for the bromo substituted compounds.¹⁶⁷ It has to be noted, however, that the PLQY of the [Cu(POP)(2,9-Me₂phen)][BF₄] complex is significantly higher with 15% than the ones measured for [Cu(POP)(2,9-Br₂phen)][PF₆] and [Cu(xantphos)(2,9-Br₂phen)][PF₆] in solution (and similarly solid state, see next section). Exciplex quenching is a critical factor in the PLQY of Cu(I) complexes, which is suppressed by sterically demanding substituents on the phen ligand and especially the 2,9-positions,¹⁶⁷ but the similarities in the crystal structure of [Cu(POP)(2,9-Br₂phen)][PF₆].0.5Et₂O and [Cu(POP)(2,9-Me₂phen)][PF₆].0.5Et₂O (see section 3.4) makes steric effects unlikely to be the cause for the low PLQY of the 2,9-Br₂phen containing complexes. Similar conclusions were reached by Brown-Xu and co-workers when comparing different homoleptic bis-2,9-dihalophen Cu(I) complexes with [Cu(2,9-Me₂phen)₂][PF₆] and they stated that it is “difficult to rationalize only on steric grounds”.²⁴⁸

2.5.3 Solid-state emission properties

The emission of powder samples of [Cu(P[^]P)(Br₂phen)][PF₆] complexes are blue-shifted by 22–83 nm with respect to their solution emissions when excited at 365 nm (for [Cu(POP)(Br₂phen)][PF₆] complexes) or 340 nm (for [Cu(xantphos)(Br₂phen)][PF₆] complexes) (Figure 3.9). The blue-shift is common for a large part of the [Cu(P[^]P)(N[^]N)][PF₆] complexes in general and can be explained by the increased rigidity imposed by the environment, which hinders the geometrical relaxation of the excited complex towards a square-planar structure.¹¹⁵ The λ_{em}^{max} of [Cu(xantphos)(3,8-Br₂phen)][PF₆] at 598 nm is red-shifted with respect to that of the previously reported [Cu(xantphos)(3,8-Br₂phen)][ClO₄] at 565 nm, which may represent different solid state packing interactions.²⁴¹ Similar to the solution emission, the emissions of [Cu(POP)(2,9-Br₂phen)][PF₆] and [Cu(xantphos)(2,9-Br₂phen)][PF₆] are blue-shifted compared to their 3,8-Br₂phen and 4,7-Br₂phen-containing counterparts, although the shift to higher energies is not as prominent upon going from solution to the solid-state. [Cu(POP)(2,9-Br₂phen)][PF₆] and [Cu(xantphos)(2,9-Br₂phen)][PF₆] show the highest PLQY values in the solid-state with 24% and 45%, respectively. These are significantly higher than the ones for [Cu(POP)(2,9-Br₂bpy)][PF₆] and [Cu(xantphos)(2,9-Br₂bpy)][PF₆] (6.3% and 10.9%, respectively), however compared to 88% and 66% for [Cu(POP)(2,9-Me₂phen)][BARF] and [Cu(xantphos)(2,9-Me₂phen)][BARF] ([BARF] = tetrakis(bis-3,5-trifluoromethylphenyl)borate), respectively, reported by Smith *et al.*, the PLQY is substantially lower.^{217,247} For a powdered sample of [Cu(POP)(phen)][BF₄] a PLQY of 36.6% (λ_{em}^{max} = 566 nm) with an excited state lifetime of 12.75 μ s was reported which is similar to the τ value of [Cu(xantphos)(2,9-Br₂phen)][PF₆] with 9.9 μ s.

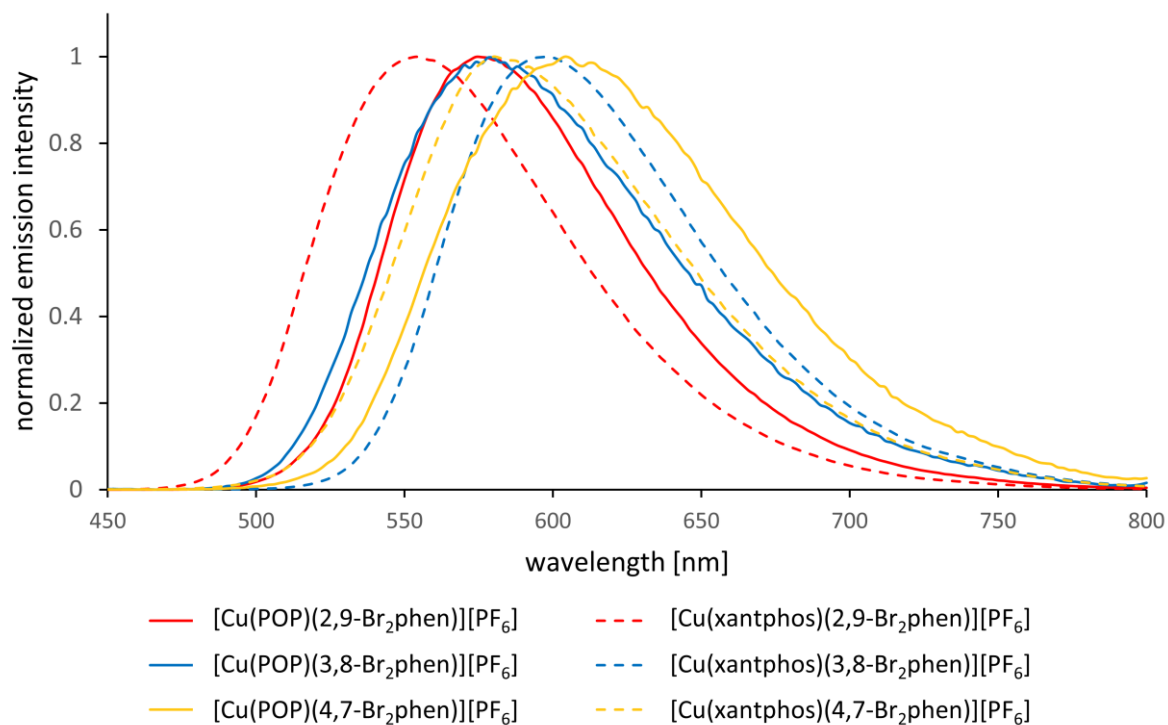


Figure 3.9: Normalized emission spectra of powder samples of $[Cu(P^A P)(Br_2phen)][PF_6]$ compounds when excited with $\lambda_{exc} = 365$ nm for $[Cu(POP)(Br_2phen)][PF_6]$ complexes and $\lambda_{exc} = 340$ nm for $[Cu(xantphos)(Br_2phen)][PF_6]$ complexes. Adapted from reference 196 under the terms of the CC-BY license.

Overall, the photophysical data indicate that the introduction of bromo-substituents in the 2,9-positions is not as beneficial as the presence of methyl groups.

3.6 Conclusion

Three $[Cu(POP)(Br_2phen)][PF_6]$ and three $[Cu(xantphos)(Br_2phen)][PF_6]$ complexes, in which Br_2phen represents 2,9- Br_2phen , 3,8- Br_2phen and 4,7- Br_2phen , were successfully synthesized and characterized. The formation of the heteroleptic complexes was confirmed by X-ray diffraction crystal structures and ESI-MS spectrometry. The 1H , $^{13}C\{^1H\}$ and $^{31}P\{^1H\}$ NMR spectra corroborate the stability of the Cu(I) complexes in solution over the course of a couple of hours. The compounds undergo a partially reversible or irreversible Cu^+/Cu^{2+} oxidation in CV measurements, with the highest potential measured for the 2,9- Br_2phen containing complexes, which is in agreement with the bromo-substituents in 2,9-position hindering the flattening of the pseudo-tetrahedral Cu(I) geometry upon oxidation. In solution, the compounds are weak yellow or orange emitters with a significant blue-shift in emission for the 2,9- Br_2phen containing complexes with respect to the 3,8- Br_2phen and 4,7- Br_2phen incorporating ones. In solid state the complexes are yellow or orange emitters. $[Cu(POP)(2,9-Br_2phen)][PF_6]$ and $[Cu(xantphos)(2,9-Br_2phen)][PF_6]$ still experience a blue-shift compared to the 3,8- Br_2phen and 4,7- Br_2phen containing complexes, but it is less pronounced. The highest PLQYs are observed for $[Cu(POP)(2,9-Br_2phen)][PF_6]$ and $[Cu(xantphos)(2,9-Br_2phen)][PF_6]$ with 24% ($\tau = 6.3 \mu s$) and 45% ($\tau = 9.9 \mu s$), respectively. Comparing the $[Cu(P^A P)(2,9-Br_2phen)][PF_6]$ to analogous heteroleptic Cu(I) complexes containing phen or dmp indicate that the introduction of the bromo-substituents has a detrimental effect on the photophysical properties

of such complexes. Taking into account the findings of Keller *et al.*¹¹⁵ with bromo-substituted bпыs together with our own results, the [Cu(P^A P)(Br₂phen)][PF₆] compounds were not tested in LEC devices.

3.7 Experimental

3.7.1 General synthesis procedures for Cu(I)-complex synthesis

POP-containing compounds were synthesized according to the following procedure. POP (1.1 eqv.) and [Cu(MeCN)₄][PF₆] (1.0 eqv.) were dissolved in CH₂Cl₂ (20 mL) and the reaction mixture was stirred for 1 h. Then the N^N ligand (1.0 eqv.) was added, and the reaction mixture was stirred for 1 h. The solvent was then removed under reduced pressure. The residue was washed with Et₂O. The crude product was purified by crystallization from CH₂Cl₂/Et₂O by vapour diffusion.

Compounds containing xantphos were prepared by the following procedure. A solution of the respective phen (1.0 eqv.) and xantphos (1.1 eqv.) in CH₂Cl₂ (10 mL) was added dropwise to a CH₂Cl₂ solution (10 mL) of [Cu(MeCN)₄][PF₆] (1.0 eqv.). The reaction mixture was then stirred for 90 min before the solvent was removed under reduced pressure. The residue was washed with Et₂O. The crude product was purified by crystallization from CH₂Cl₂/Et₂O by vapour diffusion.

3.7.1a [Cu(POP)(2,9-Br₂phen)][PF₆]

The reagents were POP (106 mg, 0.20 mmol), [Cu(MeCN)₄][PF₆] (66.5 mg, 0.18 mmol) and 2,9-Br₂phen (60.6 mg, 0.18 mmol). [Cu(POP)(2,9-Br₂phen)][PF₆] was isolated as an orange solid (170 mg, 0.16 mmol, 88%). ¹H NMR (500 MHz, acetone-*d*₆) δ/ppm 8.67 (d, *J* = 8.5 Hz, 2H, H^{A4}), 8.20 (s, 2H, H^{A5}), 8.11 (d, *J* = 8.5 Hz, 2H, H^{A3}), 7.46 (ddd, *J* = 8.3, 6.9, 2.1 Hz, 2H, H^{C4}), 7.37–7.29 (m, 4H, H^{C5+C6}), 7.29–7.24 (m, 4H, H^{D4}), 7.24–7.18 (m, 8H, H^{D2}), 7.16–7.10 (m, 8H, H^{D3}), 7.09–7.04 (m, 2H, H^{C3}). ¹³C{¹H} NMR (126 MHz, acetone-*d*₆) δ/ppm 159.4 (C^{C1}), 144.2 (C^{A10a}), 144.0 (C^{A2}), 141.3 (C^{A4}), 134.6 (C^{C3}), 134.1 (t, *J*_{PC} = 7.8 Hz, C^{D2}), 133.2 (C^{C5}), 132.8 (t, *J*_{PC} = 17.1 Hz, C^{D1}), 131.3 (C^{A3}), 130.6 (C^{D4}), 129.8 (C^{A4a}), 129.3 (t, *J*_{PC} = 4.7 Hz, C^{D3}), 128.2 (C^{A5}), 126.5 (C^{C2}), 125.9 (t, *J*_{PC} = 2 Hz, C^{C4}), 120.8 (t, *J*_{PC} = 2.0 Hz, C^{C6}). ³¹P{¹H} NMR (202 MHz, acetone-*d*₆, 298 K) δ/ppm -12.8 (POP), -144.2 (septet, *J*_{PF} = 707 Hz, PF₆⁻). ESI-MS positive mode *m/z* 939.02 [Cu(POP)(2,9-Br₂phen)]⁺ (calc. 938.98), 601.09 [Cu(POP)]⁺ (calc. 601.09). HR ESI-MS positive mode *m/z* 938.9775 [Cu(POP)(2,9-Br₂phen)]⁺ (calc. 938.9784). Satisfactory elemental analytical data were not obtained.

3.7.1b [Cu(POP)(3,8-Br₂phen)][PF₆]

The reagents were POP (297 mg, 0.55 mmol), [Cu(MeCN)₄][PF₆] (186 mg, 0.50 mmol) and 3,8-Br₂phen (168 mg, 0.50 mmol). [Cu(POP)(3,8-Br₂phen)][PF₆] was isolated as an orange solid (480 mg, 0.44 mmol, 89%). ¹H NMR (500 MHz, acetone-*d*₆) δ/ppm 8.99–8.95 (m, 4H, H^{A2+A4}), 8.24 (s, 2H, H^{A5}), 7.46 (ddd, *J* = 8.9, 7.6, 1.7 Hz, 2H, H^{C5}), 7.38–7.33 (m, 4H, H^{D4}), 7.27–7.19 (m, 10H, H^{C6+D3}), 7.19–7.14 (m, 8H, H^{D2}), 7.12 (t, *J* = 7.6 Hz, 2H, H^{C4}), 6.85–6.80 (m, 2H, H^{C3}). ¹³C{¹H} NMR (126 MHz, acetone-*d*₆) δ/ppm 159.1 (t, *J*_{PC} = 6.0 Hz, C^{C1}), 151.7 (C^{A2}), 142.3 (t, *J*_{PC} = 1.9 Hz, C^{A10a}), 140.3 (C^{A4}), 135.0 (C^{C3}), 134.1 (t, *J*_{PC} = 8.2 Hz, C^{D2}), 133.4 (C^{C5}), 131.5 (C^{A4a}), 131.3 (C^{D1}), 131.1 (C^{D4}), 129.6 (t, *J*_{PC} = 4.9 Hz, C^{D3}), 128.7 (C^{A5}), 126.3 (t, *J*_{PC} = 2.3 Hz, C^{C4}), 124.4 (t, *J*_{PC} = 15.4 Hz, C^{C2}), 121.6 (C^{A3}), 121.4 (t, *J*_{PC} = 2.0 Hz, C^{C6}). ³¹P{¹H} NMR (202 MHz, acetone-*d*₆, 298 K) δ/ppm -10.1 (POP), -144.2 (septet, *J*_{PF} = 707 Hz, PF₆⁻). ESI-MS positive mode *m/z* 938.96 [Cu(POP)(3,8-Br₂phen)]⁺ (calc. 938.98), 601.06 [Cu(POP)]⁺ (calc. 601.09). Found: C 50.79, H 3.40, N 2.56; C₄₈H₃₄Br₂CuF₆N₂OP₃·CH₂Cl₂ requires C 50.26, H 3.18, N 2.39.

3.7.1c [Cu(POP)(4,7-Br₂phen)][PF₆]

The reagents were POP (159 mg, 0.30 mmol), [Cu(MeCN)₄][PF₆] (99.7 mg, 0.27 mmol) and 4,7-Br₂phen (90.6 mg, 0.27 mmol). [Cu(POP)(4,7-Br₂phen)][PF₆] was isolated as an orange solid (270 mg, 0.25 mmol,

93%). ^1H NMR (500 MHz, acetone- d_6) δ /ppm 8.88 (d, J = 5.2 Hz, 2H, $\text{H}^{\text{A}2}$), 8.52 (s, 2H, $\text{H}^{\text{A}5}$), 8.21 (d, J = 5.2 Hz, 2H, $\text{H}^{\text{A}3}$), 7.45 (ddd, J = 8.2, 7.5, 1.7 Hz, 2H, $\text{H}^{\text{C}5}$), 7.36–7.30 (m, 4H, $\text{H}^{\text{D}4}$), 7.24–7.17 (m, 10H, $\text{H}^{\text{C}6+\text{D}3}$), 7.15–7.09 (m, 10H, $\text{H}^{\text{C}4+\text{D}2}$), 6.87–6.81 (m, 2H, $\text{H}^{\text{C}3}$). $^{13}\text{C}\{^1\text{H}\}$ NMR (126 MHz, acetone- d_6) δ /ppm 159.3 (t, J_{PC} = 6.1 Hz, $\text{C}^{\text{C}1}$), 151.1 ($\text{C}^{\text{A}2}$), 144.8 (t, J_{PC} = 2.1 Hz, $\text{C}^{\text{A}10\text{a}}$), 135.9 (t, J_{PC} = 1.1 Hz, $\text{C}^{\text{A}4}$), 135.1 ($\text{C}^{\text{C}3}$), 134.0 (t, J_{PC} = 8.2 Hz, $\text{C}^{\text{D}2}$), 133.3 ($\text{C}^{\text{C}5}$), 131.6 (t, J_{PC} = 17.2 Hz, $\text{C}^{\text{D}1}$), 131.0 ($\text{C}^{\text{D}4}$), 130.4 ($\text{C}^{\text{A}3/\text{A}4\text{a}}$), 130.3 ($\text{C}^{\text{A}3/\text{A}4\text{a}}$), 129.7 (t, J_{PC} = 4.8 Hz, $\text{C}^{\text{D}3}$), 127.8 ($\text{C}^{\text{A}5}$), 126.1 (t, J_{PC} = 2.3 Hz, $\text{C}^{\text{C}4}$), 124.4 (t, J_{PC} = 15.5 Hz, $\text{C}^{\text{C}2}$), 121.6 (t, J_{PC} = 2.1 Hz, $\text{C}^{\text{C}6}$). $^{31}\text{P}\{^1\text{H}\}$ NMR (202 MHz, acetone- d_6 , 298 K) δ /ppm -11.0 (POP), -144.2 (septet, J_{PF} = 708 Hz, PF_6^-). ESI-MS positive mode m/z 938.98 $[\text{Cu}(\text{POP})(4,7\text{-Br}_2\text{phen})]^+$ (calc. 938.98), 601.11 $[\text{Cu}(\text{POP})]^+$ (calc. 601.09). Found: C 50.67, H 3.26, N 2.59; $\text{C}_{48}\text{H}_{34}\text{Br}_2\text{CuF}_6\text{N}_2\text{OP}_3\cdot\text{CH}_2\text{Cl}_2$ requires C 50.26, H 3.18, N 2.39.

3.7.1d $[\text{Cu}(\text{xantphos})(2,9\text{-Br}_2\text{phen})][\text{PF}_6]$

The reagents were $[\text{Cu}(\text{MeCN})_4][\text{PF}_6]$ (66.3 mg, 0.18 mmol), 2,9- Br_2phen (60 mg, 0.18 mmol) and xantphos (113 mg, 0.20 mmol). $[\text{Cu}(\text{xantphos})(2,9\text{-Br}_2\text{phen})][\text{PF}_6]$ was isolated as a yellow solid (100 mg, 88.8 μmol , 50%). ^1H NMR (500 MHz, acetone- d_6) δ /ppm 8.61 (d, J = 8.4 Hz, 2H, $\text{H}^{\text{A}4}$), 8.14 (s, 2H, $\text{H}^{\text{A}5}$), 8.06 (d, J = 8.4 Hz, 2H, $\text{H}^{\text{A}3}$), 7.83 (d, J = 7.6 Hz, 2H, $\text{H}^{\text{C}5}$), 7.34–7.23 (m, 14H, $\text{H}^{\text{D}2+\text{D}4+\text{C}4}$), 7.16–7.07 (m, 10H, $\text{H}^{\text{D}3+\text{C}3}$), 1.74 (s, 6H, $\text{H}^{\text{xantphos-Me}}$). $^{13}\text{C}\{^1\text{H}\}$ NMR (126 MHz, acetone- d_6) δ /ppm 155.8 ($\text{C}^{\text{C}1}$), 143.8/143.2 ($\text{C}^{\text{A}2+\text{A}10\text{a}}$), 141.2 ($\text{C}^{\text{A}4}$), 134.3 ($\text{C}^{\text{C}6}$), 134.1 (t, J_{PC} = 7.6 Hz, $\text{C}^{\text{D}2}$), 132.1 (t, J_{PC} = 16.84 Hz, $\text{C}^{\text{D}1}$), 131.1 ($\text{C}^{\text{C}3}$), 130.9 ($\text{C}^{\text{A}3+\text{D}4}$), 129.8 ($\text{C}^{\text{A}4\text{a}}$), 129.4 (t, J_{PC} = 4.6 Hz, $\text{C}^{\text{D}3}$), 128.8 ($\text{C}^{\text{C}5}$), 128.1 ($\text{C}^{\text{A}5}$), 126.0 ($\text{C}^{\text{C}4}$), 122.6 ($\text{C}^{\text{C}2}$), 36.6 ($\text{C}^{\text{xantphos-bridge}}$), 29.2 ($\text{C}^{\text{xantphos-Me}}$). $^{31}\text{P}\{^1\text{H}\}$ NMR (202 MHz, acetone- d_6 , 298 K) δ /ppm -12.2 (xantphos), -144.2 (septet, J_{PF} = 707 Hz, PF_6^-). ESI-MS positive mode m/z 979.03 $[\text{Cu}(\text{xantphos})(2,9\text{-Br}_2\text{phen})]^+$ (calc. 979.01), 641.13 $[\text{Cu}(\text{xantphos})]^+$ (calc. 641.12). Found: C 54.06, H 3.56, N 2.62; $\text{C}_{51}\text{H}_{38}\text{Br}_2\text{CuF}_6\text{N}_2\text{OP}_3$ requires C 54.44, H 3.40, N 2.49.

3.7.1e $[\text{Cu}(\text{xantphos})(3,8\text{-Br}_2\text{phen})][\text{PF}_6]$

The reagents were $[\text{Cu}(\text{MeCN})_4][\text{PF}_6]$ (188 mg, 0.50 mmol), 3,8- Br_2phen (170 mg, 0.50 mmol) and xantphos (173 mg, 0.51 mmol). $[\text{Cu}(\text{xantphos})(3,8\text{-Br}_2\text{phen})][\text{PF}_6]$ was isolated as an orange solid (496 mg, 0.44 mmol, 87%). ^1H NMR (500 MHz, acetone- d_6) δ /ppm 8.99 (d, J = 2.0 Hz, 2H, $\text{H}^{\text{A}4}$), 8.55 (m, 2H, $\text{H}^{\text{A}2}$), 8.25 (s, 2H, $\text{H}^{\text{A}5}$), 7.95 (dd, J = 7.9 Hz, 1.3 Hz, 2H, $\text{H}^{\text{C}5}$), 7.34–7.28 (m, 6H, $\text{H}^{\text{D}4+\text{C}4}$), 7.16–7.11 (m, 8H, $\text{H}^{\text{D}3}$), 7.09–7.03 (m, 8H, $\text{H}^{\text{D}2}$), 6.69–6.61 (m, 2H, $\text{H}^{\text{C}3}$), 1.87 (s, 6H, $\text{H}^{\text{xantphos-Me}}$). $^{13}\text{C}\{^1\text{H}\}$ NMR (126 MHz, acetone- d_6) δ /ppm 155.9 ($\text{C}^{\text{C}1}$), 151.3 ($\text{C}^{\text{A}2}$), 142.4 ($\text{C}^{\text{A}10\text{a}}$), 140.6 ($\text{C}^{\text{A}4}$), 135.0 ($\text{C}^{\text{C}6}$), 133.8 (t, J_{PC} = 8.0 Hz, $\text{C}^{\text{D}2}$), 132.2 ($\text{C}^{\text{C}3}$), 131.8 ($\text{C}^{\text{D}1}$), 131.6 ($\text{C}^{\text{A}4\text{a}}$), 131.0 ($\text{C}^{\text{D}4}$), 129.7 (t, J_{PC} = 4.8 Hz, $\text{C}^{\text{D}3}$), 128.9 ($\text{C}^{\text{A}5+\text{C}5}$), 126.4 ($\text{C}^{\text{C}4}$), 121.7 ($\text{C}^{\text{A}3}$), 120.2 ($\text{C}^{\text{C}2}$), 37.1 ($\text{C}^{\text{xantphos-bridge}}$), 28.7 ($\text{C}^{\text{xantphos-Me}}$). $^{31}\text{P}\{^1\text{H}\}$ NMR (202 MHz, acetone- d_6 , 298 K) δ /ppm -11.0 (xantphos), -144.2 (septet, J_{PF} = 707 Hz, PF_6^-). ESI-MS positive mode m/z 979.00 $[\text{Cu}(\text{xantphos})(2,9\text{-Br}_2\text{phen})]^+$ (calc. 979.01), 641.12 $[\text{Cu}(\text{xantphos})]^+$ (calc. 641.12). Found: C 54.28, H 3.55, N 2.49; $\text{C}_{51}\text{H}_{38}\text{Br}_2\text{CuF}_6\text{N}_2\text{OP}_3$ requires C 54.44, H 3.40, N 2.49.

3.7.1f $[\text{Cu}(\text{xantphos})(4,7\text{-Br}_2\text{phen})][\text{PF}_6]$

The reagents were $[\text{Cu}(\text{MeCN})_4][\text{PF}_6]$ (64.9 mg, 0.17 mmol), 4,7- Br_2phen (58.8 mg, 0.17 mmol) and xantphos (111 mg, 0.19 mmol). $[\text{Cu}(\text{xantphos})(4,7\text{-Br}_2\text{phen})][\text{PF}_6]$ was isolated as orange solid (150 mg, 133 μmol , 77%). ^1H NMR (500 MHz, acetone- d_6) δ /ppm 8.60 (d, J = 5.2 Hz, 2H, $\text{H}^{\text{A}2}$), 8.50 (s, 2H, $\text{H}^{\text{A}5}$), 8.22 (d, J = 5.0 Hz, 2H, $\text{H}^{\text{A}3}$), 7.90 (dd, J = 7.8 Hz, 1.2 Hz, 2H, $\text{H}^{\text{C}5}$), 7.33–7.26 (m, 6H, $\text{H}^{\text{D}4+\text{C}4}$), 7.16–1.09 (m, 8H, $\text{H}^{\text{D}3}$), 7.09–7.01 (m, 8H, $\text{H}^{\text{D}2}$), 6.77–6.71 (m, 2H, $\text{H}^{\text{C}3}$), 1.81 (s, 6H, $\text{H}^{\text{xantphos-Me}}$). $^{13}\text{C}\{^1\text{H}\}$ NMR (126 MHz, acetone- d_6) δ /ppm 155.8 ($\text{C}^{\text{C}1}$), 150.7 ($\text{C}^{\text{A}2}$), 144.8 ($\text{C}^{\text{A}10\text{a}}$), 136.4/130.7 ($\text{C}^{\text{A}4+\text{A}4\text{a}}$), 135.1 ($\text{C}^{\text{C}6}$), 133.6 (t, J_{PC} = 8.0 Hz, $\text{C}^{\text{D}2}$), 132.2 ($\text{C}^{\text{D}1}$), 132.1 ($\text{C}^{\text{C}3}$), 131.0 ($\text{C}^{\text{D}4}$), 130.4 ($\text{C}^{\text{A}3}$), 129.6 (t, J_{PC} = 4.7 Hz, $\text{C}^{\text{D}3}$), 128.9 ($\text{C}^{\text{C}5}$), 127.9 ($\text{C}^{\text{A}5}$), 126.2 ($\text{C}^{\text{C}4}$), 120.3 ($\text{C}^{\text{C}2}$), 37.1 ($\text{C}^{\text{xantphos-bridge}}$), 28.7 ($\text{C}^{\text{xantphos-Me}}$). $^{31}\text{P}\{^1\text{H}\}$ NMR (202 MHz, acetone- d_6 , 298 K) δ /ppm -12.4 (xantphos), -144.3 (septet, J_{PF} = 707 Hz, PF_6^-). ESI-MS positive mode m/z 979.03

[Cu(xantphos)(2,9-Br₂phen)]⁺ (calc. 979.01), 641.15 [Cu(xantphos)]⁺ (calc. 641.12). Found: C 54.28, H 3.55, N 2.49; C₅₁H₃₈Br₂CuF₆N₂OP₃ requires C 54.44, H 3.40, N 2.49.

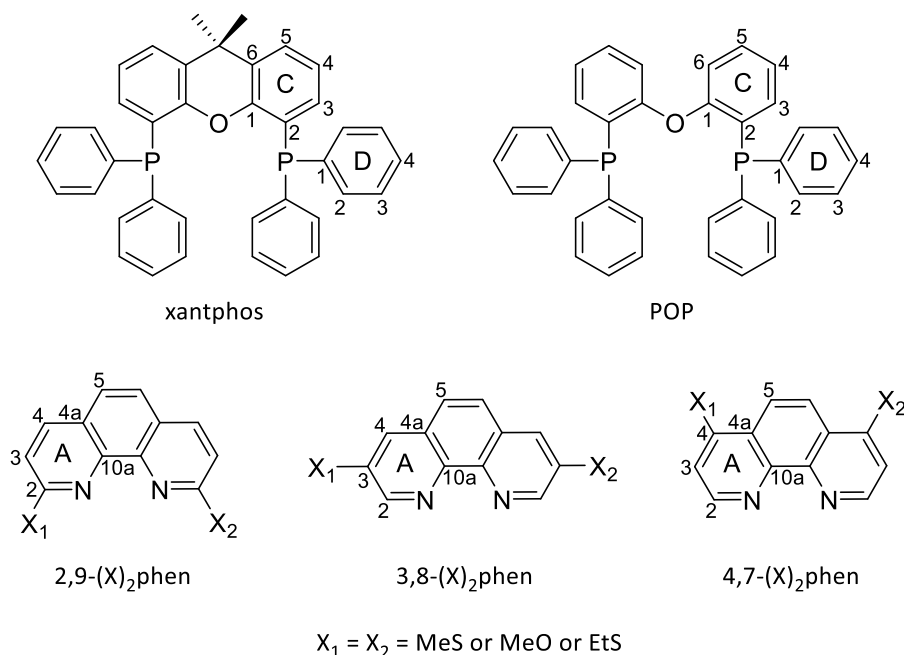
Chapter 4: The effect of alkylsulfanyl and alkyloxy substituents on 1,10-phenanthroline on the photophysical and electrochemical properties of $[\text{Cu}(\text{P}^{\wedge}\text{P})(\text{N}^{\wedge}\text{N})][\text{PF}_6]$ complexes.

Part of the synthesis and analytical measurements of this chapter were carried out by BSc. Aramis Keller during the course of his Wahlpraktikum.

4.1 Motivation

$[\text{Cu}(\text{POP})(\text{N}^{\wedge}\text{N})][\text{PF}_6]$ and $[\text{Cu}(\text{xantphos})(\text{N}^{\wedge}\text{N})][\text{PF}_6]$ compounds, with $\text{N}^{\wedge}\text{N}$ being a phen derivative substituted with a directly attached heteroatom to the phen backbone are rare in literature. In fact, the only reports for simple di-substituted (excluding alkyl substituents) phens are dibrominated phen ligands.²⁴¹ While there is a larger amount of analogous bpy derivatives $[\text{Cu}(\text{P}^{\wedge}\text{P})(\text{N}^{\wedge}\text{N})][\text{PF}_6]$,^{115,116,188} the use of such phen ligands is still a largely unexplored field.

A recent work by Alkan-Zambada *et al.* compared the effect of an array of mono-substituted $[\text{Cu}(\text{P}^{\wedge}\text{P})(6\text{-Rbpy})][\text{PF}_6]$ complexes, with R being different alkyloxy or alkylsulfanyl substituents, showed higher PLQYs, longer excited state lifetimes and a slight blue-shift for the alkylsulfanyl with respect to the alkyloxy substituted 6-Rbpy complexes in solid-state. In LEC devices, these complexes exhibited some interesting properties in comparison to $[\text{Cu}(\text{P}^{\wedge}\text{P})(\text{Etbpy})][\text{PF}_6]$, from relatively short turn-on times for $[\text{Cu}(\text{POP})(6\text{-MeSbpy})][\text{PF}_6]$ (MeS = methylsulfanyl) and $[\text{Cu}(\text{POP})(6\text{-EtSbpy})][\text{PF}_6]$ (EtS = ethylsulfanyl) with 0.4 and 0.3 h, respectively, and an increase in maximum luminance of 10 cd m^{-2} for $[\text{Cu}(\text{POP})(6\text{-EtObpy})][\text{PF}_6]$ (EtO = ethoxy) to a significantly increased device lifetime for $[\text{Cu}(\text{POP})(6\text{-MeObpy})][\text{PF}_6]$.¹¹⁶



Scheme 4.1: Structures of $\text{P}^{\wedge}\text{P}$ and $(\text{X})_2\text{phen}$ ligands used in the synthesis of $[\text{Cu}(\text{P}^{\wedge}\text{P})((\text{X})_2\text{phen})][\text{PF}_6]$ complexes with labelling scheme used for ^1H and ^{13}C NMR spectroscopic assignments.

With a widely unexplored territory, interesting results from Alkan-Zambada and co-workers, and readily available precursors with 2,9-Br₂phen or 2,9-Cl₂phen (2,9-dichloro-1,10-phenanthroline), 3,8-Br₂phen and 4,7-Br₂phen, we were inspired to investigate [Cu(P[^]P)(X)₂phen][PF₆] complexes with di-substituted MeO-, MeS- and EtS-phen ligands (Scheme 4.1).

4.2 Synthesis

4.2.1 Ligand synthesis

The synthesis of 2,9-(MeS)₂phen ligands has previously been reported²⁴⁹ and all other ligands were synthesized analogously, with differences in the reaction conditions for the synthesis of (EtS)₂phen and (MeO)₂phen (see section 4.7.1–4.7.3 for details). The solution ¹H and ¹³C{¹H} NMR spectra for the 2,9-(MeS)₂phen and 2,9-(MeO)₂phen 3,8-(MeO)₂phen and 4,7-(MeO)₂phen matched those previously reported.^{249–252} In the ESI-MS of the (EtS)₂phen, peaks were found at *m/z* 301.09 (for 2,9-(EtS)₂phen and 3,8-(EtS)₂phen) and *m/z* 301.08 (for 4,7-(EtS)₂phen) (calculated 301.08). The solution ¹H and ¹³C{¹H} NMR spectra of the (EtS)₂phen ligands were assigned using COSY, NOESY, HMQC and HMBC 2D NMR experiments and are consistent with the structure shown in Scheme 4.1.

4.2.2 Complex synthesis

Sequential (for POP containing complexes) and parallel (for xantphos containing complexes) synthesis protocols were applied to increase the yields of the complex syntheses. The total reaction time was 2 h for both procedures and the crude products were crystallized by vapour diffusion of Et₂O into a CH₂Cl₂ solution of the complexes. Isolating [Cu(xantphos)(2,9-(MeS)₂phen)][PF₆] and [Cu(POP)(2,9-(MeS)₂phen)][PF₆] required the addition of another equivalent of the respective diphosphane during the crystallisation process.

For each of the complexes the base peak in the ESI-MS was found to be the [Cu(P[^]P)(N[^]N)]⁺ cation peak (see section 4.7.4). The additional characteristic [Cu(POP)]⁺ and [Cu(xantphos)]⁺ peaks were found at *m/z* 601.1 and 641.1, respectively, with the exception of [Cu(POP)(2,9-(MeO)₂phen)][PF₆], [Cu(POP)(3,8-(MeO)₂phen)][PF₆], [Cu(POP)(4,7-(EtS)₂phen)][PF₆] and [Cu(xantphos)(4,7-(EtS)₂phen)][PF₆] where this peak was missing. The elemental composition of the complexes was confirmed by elemental analysis. For the compounds [Cu(POP)(2,9-(MeS)₂phen)][PF₆], [Cu(POP)(2,9-(MeO)₂phen)][PF₆], [Cu(POP)(4,7-(MeO)₂phen)][PF₆], [Cu(xantphos)(2,9-(EtS)₂phen)][PF₆] and [Cu(xantphos)(4,7-(EtS)₂phen)][PF₆], an HR ESI-MS was recorded (see section 4.7.4), since the elemental analysis data obtained was not satisfactory.

Solution ¹H, ¹³C{¹H} and ³¹P{¹H} NMR spectra were consistent with the proposed structure (Scheme 4.1) and, additionally, for [Cu(POP)(3,8-(MeS)₂phen)][PF₆], [Cu(xantphos)(3,8-(MeS)₂phen)][PF₆], [Cu(POP)(4,7-(MeS)₂phen)][PF₆], [Cu(POP)(2,9-(MeO)₂phen)][PF₆], [Cu(xantphos)(3,8-(EtS)₂phen)][PF₆] and [Cu(POP)(4,7-(EtS)₂phen)][PF₆] a crystal structure was obtained from X-ray diffraction experiments. For the discussion of the NMR assignment and crystal structures (see section 4.3.1 and 4.3.2, respectively).

4.3 Structural characterization

4.3.1 NMR spectroscopy

The solution ¹H, ¹³C{¹H}, ³¹P{¹H}, COSY, NOESY, HMQC and HMBC NMR spectra were recorded in acetone-*d*₆ at 298 K. In the case of [Cu(POP)(2,9-(MeO)₂phen)][PF₆] and [Cu(xantphos)(2,9-(MeO)₂phen)][PF₆], the NMR solvent was changed to CD₂Cl₂ as it gave improved peak resolution.

The septet at $\delta -144.2 \pm 0.1$ ppm (in acetone- d_6) and $\delta -144.6 \pm 0.1$ ppm (in CD_2Cl_2) was assigned to the PF_6^- anion. The coordinated diphosphane ligands gave rise to a broadened signal between $\delta -10.3$ and -13.1 ppm.

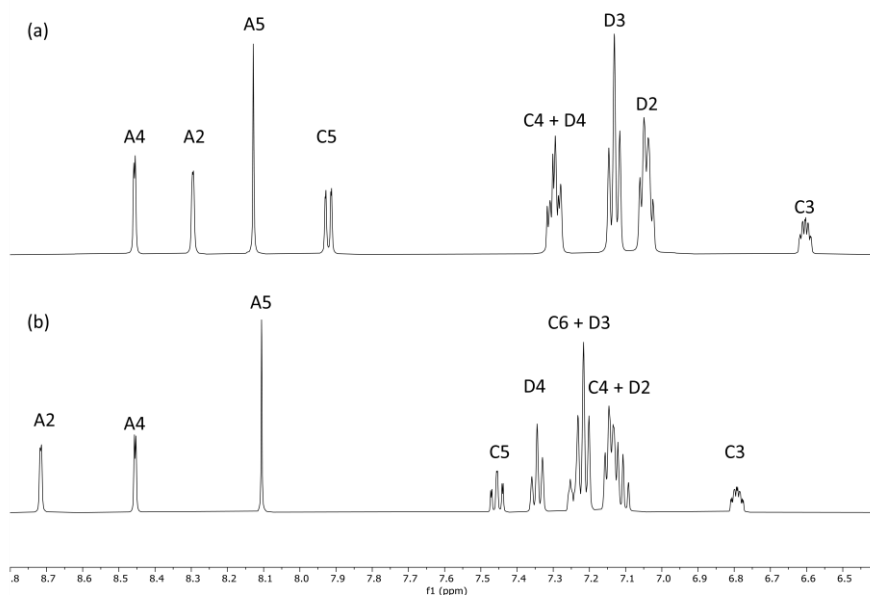


Figure 4.1: Aromatic region of the 1H NMR spectra (500 MHz, acetone- d_6 , 298 K) of (a) $[Cu(xantphos)(3,8-(MeS)_2phen)][PF_6]$ and $[Cu(POP)(3,8-(MeS)_2phen)][PF_6]$. Due to the introduction of the $C(Me)_2$ unit in xantphos, the signal for H^{C6} disappears in (b). Chemical shifts are given in δ/ppm ; for atom labelling see Scheme 4.1.

In the 1H NMR spectra, the same effects as have been described for the $[Cu(P^{\wedge}P)(Br_2phen)][PF_6]$ compounds in section 3.3.1 were observed: a significant shift downfield for H^{A2} when going from POP to the respective xantphos complex, with the exception of the complexes employing 2,9-substituted phens, due to the effect of the xanthene bowl. Furthermore, the disappearance of the signal of H^{C6} and the simultaneous appearance of the xantphos methyl groups are consistent with the introduction of the xantphos $C(Me)_2$ unit (Figure 4.1).

4.3.2 Crystal structures

Yellow single crystals of $[Cu(POP)(3,8-(MeS)_2phen)][PF_6] \cdot 1.5Me_2CO$, $[Cu(POP)(4,7-(MeS)_2phen)][PF_6] \cdot 0.5CH_2Cl_2 \cdot 0.5Me_2CO$, $[Cu(xantphos)(3,8-(MeS)_2phen)][PF_6]$, $[Cu(POP)(2,9-(EtS)_2phen)][PF_6] \cdot 0.5CH_2Cl_2$, $[Cu(xantphos)(3,8-(EtS)_2phen)][PF_6]$ and $[Cu(POP)(2,9-(MeO)_2phen)][PF_6] \cdot 1.5Et_2O$ were grown either from vapour diffusion of Et_2O into an acetone or CH_2Cl_2 solution of the complexes or by layering an acetone solution of the compounds with CH_2Cl_2 . Attempts to grow X-ray quality crystals of the other complexes were unsuccessful. The structures of the cations are shown in Figures 4.2 and 4.3, the crystallographic data are summarized in Table 4.1 and a summary of the bond angles and bond lengths surrounding the Cu(I) centres is given in Table 4.2. There are two independent ion pairs in the asymmetric unit of $[Cu(POP)(2,9-(EtS)_2phen)][PF_6] \cdot 0.5CH_2Cl_2$.

Table 4.1: Crystallographic data for [Cu(P[^]P)((X)₂phen)][PF₆] compounds.

Compound	[Cu(xantphos)(3,8-(MeS) ₂ phen)][PF ₆]	[Cu(POP)(3,8-(MeS) ₂ phen)][PF ₆] 1.5Me ₂ CO	[Cu(POP)(4,7-(MeS) ₂ phen)][PF ₆] 0.5CH ₂ Cl ₂ ·0.5Me ₂ CO
Formula	C ₅₆ H ₅₀ CuF ₆ N ₂ O ₂ P ₃ S ₂	C _{54.5} H ₅₂ CuF ₆ N ₂ O _{2.5} P ₃ S ₂	C ₅₂ H ₄₄ ClCuF ₆ H ₄₄ N ₂ O _{1.5} P ₃ S ₂
Formula weight	1117.55	1109.55	1090.91
Crystal colour and habit	triclinic	triclinic	triclinic
Crystal system	Yellow block	Yellow plate	Yellow needle
Space group	<i>P</i> -1	<i>P</i> -1	<i>P</i> -1
<i>a</i> , <i>b</i> , <i>c</i> /Å	12.8656(5), 13.1450(5), 16.3795(6)	11.3642(5), 14.8610(7), 15.8654(6)	12.3904(7), 13.8556(7), 17.0220(9)
α , β , γ /°	72.8760(10), 84.1450(10), 88.1130(10)	88.782(3), 80.982(3), 86.990(3)	92.964(4), 92.952(4), 114.617(3)
<i>V</i> /Å ³	2633.50(17)	2642.4(2)	2644.5(3)
<i>D_c</i> /Mg m ⁻³	1.409	1.395	1.370
<i>Z</i>	2	2	2
μ (Cu-K α)/mm ⁻¹	2.739	2.731	3.160
<i>T</i> /K	250	250	250
Refln. collected (<i>R</i> _{int})	23439 (0.0243)	31280 (0.05233)	34073 (0.0483)
Unique refln.	9436	9714	9670
Refln. for refinement	9027	7287	7381
Parameters	653	590	615
Threshold	2 σ	2 σ	2 σ
<i>R</i> ₁ (<i>R</i> ₁ all data)	0.0365 (0.0377)	0.0753 (0.0934)	0.0696 (0.0909)
<i>wR</i> ₂ (<i>wR</i> ₂ all data)	0.0970 (0.0980)	0.2045 (0.2229)	0.2257 (0.2503)
Goodness of fit	1.023	1.060	1.070
CCDC deposition number	1995591	1995592	1995593
Compound	[Cu(POP)(2,9-(EtS) ₂ phen)][PF ₆] 0.5CH ₂ Cl ₂	[Cu(xantphos)(3,8-(EtS) ₂ phen)][PF ₆]	[Cu(POP)(2,9-(MeO) ₂ phen)][PF ₆] 1.5Et ₂ O
Formula	C _{52.5} H ₄₅ ClCuF ₆ N ₂ OP ₃ S ₂	C ₅₅ H ₄₈ CuF ₆ N ₂ OP ₃ S ₂	C ₅₆ H ₅₃ CuF ₆ N ₂ O _{4.5} P ₃
Formula weight	1089.92	1087.52	1095.44
Crystal colour and habit	Yellow block	Yellow block	Colourless plate
Crystal system	Triclinic	Triclinic	monoclinic
Space group	<i>P</i> -1	<i>P</i> -1	<i>C</i> 2/ <i>c</i>
<i>a</i> , <i>b</i> , <i>c</i> /Å	17.5228(7), 18.3402(7), 19.2995(7)	11.5190(16), 12.5986(19), 17.766(3)	20.9991(111), 22.1089(8), 23.5390(13)
α , β , γ /°	112.3940(10), 103.8010(10), 108.8460(10)	88.369(9), 75.099(8), 89.303(8)	90, 111.628(4), 90
<i>V</i> /Å ³	4942.0(3)	2490.5(6)	1059.0(9)
<i>D_c</i> /Mg m ⁻³	1.465	1.450	1.432
<i>Z</i>	4	2	8
μ (Cu-K α)/mm ⁻¹	3.373	2.864	3.296
<i>T</i> /K	150	150	150
Refln. collected (<i>R</i> _{int})	36502 (0.0418)	23332 (0.0635)	73030 (0.1270)
Unique refln.	17709	8725	10834
Refln. for refinement	16125	6843	7548
Parameters	1238	635	588
Threshold	2 σ	2 σ	2 σ
<i>R</i> ₁ (<i>R</i> ₁ all data)	0.0604 (0.0560)	0.1111 (0.0877)	0.0753 (0.1007)
<i>wR</i> ₂ (<i>wR</i> ₂ all data)	0.1592 (0.1549)	0.2539 (0.2271)	0.2056 (0.2462)
Goodness of fit	1.034	1.096	1.117
CCDC deposition number			1900491

In [Cu(POP)(3,8-(MeS)₂phen)]⁺ one of the methylsulfanyl groups is disordered and has been modelled over two sites with equal occupancies. The methyl group is thereby either facing towards or away from the copper centre but stays in the plane of the phen backbone. The N–Cu–N angle is limited to about 80° due to the rigidity of the phen unit and falls below that value in the 2,9-substituted phen incorporating complexes. A search in the CSD v.5.41²³⁵ reveals that the N–Cu–N angle for the overwhelming majority of [Cu(P[^]P)(phen)]⁺ compounds lies between 79.1 and 81.9° (Figure 4.2). The small N–Cu–N angle measured for [Cu(POP)(2,9-(MeO)₂phen)]⁺ and [Cu(POP)(2,9-

(EtS)₂phen)]⁺ may be an effect of an interaction between the Cu and the O or S atom of the substituents and steric effects.

Table 4.23: Bond angles and bond lengths surrounding the Cu(I) centre in [Cu(P^{^A}P)((X)₂phen)][PF₆] compounds. ^a For [Cu(POP)(2,9-(EtS)₂phen)][PF₆] there are two independent ion pairs in the asymmetric unit.

Cation in [Cu(P ^{^A} P)((X) ₂ phen)][PF ₆] ^a	P–Cu–P/ ^o	N–Cu–P/ ^o	N–Cu–N/ ^o	τ ₄ ^b	P–Cu/Å	N–Cu/Å
[Cu(xantphos)(3,8-(MeS) ₂ phen)] ⁺	116.068(19)	107.78(4), 110.19(5), 110.13(4), 125.01(5)	80.92(6)	0.84	2.2782(5), 2.2481(5)	2.0906(15), 2.0723(16)
[Cu(POP)(3,8-(MeS) ₂ phen)] ⁺	110.96(4)	117.44(11), 116.95(11), 120.87(11), 105.28(10)	81.43(15)	0.86	2.2295(11), 2.2555(11)	2.062(4), 2.077(3)
[Cu(POP)(4,7-(MeS) ₂ phen)] ⁺	117.90(4)	106.49(10), 99.92(10), 119.36(9), 125.82(9)	80.34(12)	0.81	2.2862(13), 2.2109(10)	2.060(3), 2.068(3)
[Cu(POP)(2,9-(EtS) ₂ phen)] ⁺ cation 1	113.63(3)	116.14(7), 118.74(7), 109.48(8), 115.20(8)	78.60(12)	0.89	2.2998(8), 2.2848(8)	2.157(3), 2.106(3)
[Cu(POP)(2,9-(EtS) ₂ phen)] ⁺ cation 2	111.26(3)	121.01(7), 111.35(6), 113.69(7), 117.78(7)	78.54(9)	0.86	2.2866(8), 2.3072(7)	2.141(2), 2.132(2)
[Cu(xantphos)(3,8-(EtS) ₂ phen)] ⁺	119.48(5)	132.65(12), 98.63(12), 112.59(13), 104.46(17)	80.38(16)	0.77	2.2326(14), 2.3072(15)	2.088(4), 2.103(4)
[Cu(POP)(2,9-(MeO) ₂ phen)] ⁺	113.15(4)	116.35(10), 113.15(4), 118.80(10), 111.23(10)	78.57(12)	0.89	2.2577(11), 2.2630(12)	2.091(3), 2.099(3)

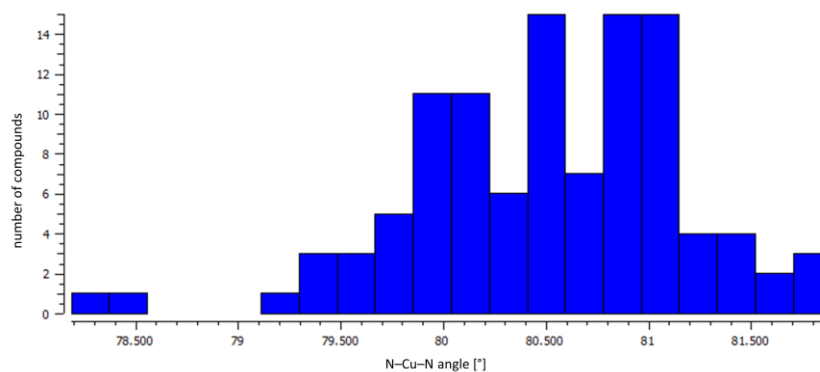


Figure 4.2: Distribution of N–Cu–N angles in [Cu(P^{^A}P)(N^{^A}N)]⁺ cations in the CSD version 2021.1.0.²³⁵ Searched with Conquest version 2021.1.0.²³⁶

The Cu⋯S (3.346–3.492 Å) and Cu⋯O (3.148 and 3.205 Å) distances are within the sum of van der Waals radii taken from Batsanov and Hu,^{220,221} and would support the occurrence of such interactions. The P–Cu–P angle is larger for the xantphos containing complexes, consistent with the higher rigidity of xantphos. The angles surrounding the Cu(I) centre deviate from the perfect tetrahedral 109.5° angle and the Houser τ₄ parameter in the range of 0.77–0.89 suggests a distortion towards C_{3v} geometry.

Face-to-face π-stacking interactions between the phenyl ring of a PPh₂ unit and the arene ring of the POP can be observed in the cation of [Cu(POP)(3,8-(MeS)₂phen)]⁺, in the two independent [Cu(POP)(2,9-(EtS)₂phen)]⁺ cations and the cation of [Cu(POP)(2,9-(MeO)₂phen)]⁺. (Figure 4.3). The angle between the least squares planes are 21.5° and 14.4° for the two independent [Cu(POP)(2,9-(EtS)₂phen)]⁺ cations with a centroid⋯centroid distance of 3.8 Å and 3.9 Å. For [Cu(POP)(3,8-(MeS)₂phen)]⁺ the angle between the least squares planes accounts for 22.6° with a

centroid...centroid distance of 3.9 Å and for $[\text{Cu}(\text{POP})(2,9\text{-(MeO)}_2\text{phen})]^+$ the measured values were 22.6° and 3.8 Å.

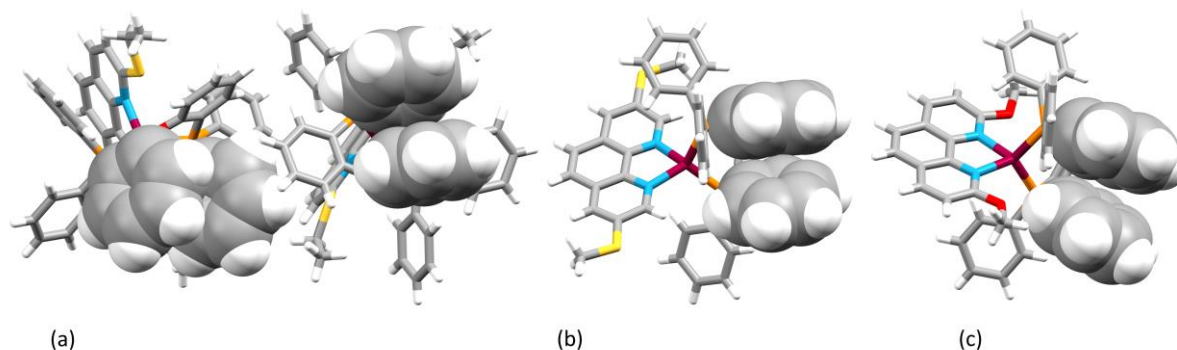


Figure 4.3: Space-filling representation of face-to-face π -stacking between a phenyl ring on a PPh_2 unit and an arene ring of the POP backbone in a) the two independent cations of $[\text{Cu}(\text{POP})(2,9\text{-(EtS)}_2\text{phen})]^+$ and b) the cation of $[\text{Cu}(\text{POP})(2,9\text{-(MeS)}_2\text{phen})]^+$. The face-to-face π -stacking between two phenyl rings of separate PPh_2 units of the xantphos in $[\text{Cu}(\text{xantphos})(3,8\text{-(MeS)}_2\text{phen})]^+$.

The π -stacking interactions between the two separate PPh_2 units on xantphos can be found in the cation of $[\text{Cu}(\text{xantphos})(3,8\text{-(MeS)}_2\text{phen})]^+$. The angle between the two phenyl rings amounts to 20° with a centroid...centroid distance of 4.1 Å.

$[\text{Cu}(\text{POP})(4,7\text{-(MeS)}_2\text{phen})]^+$ and $[\text{Cu}(\text{xantphos})(3,8\text{-(EtS)}_2\text{phen})]^+$ feature π -stacking interactions between a phenyl ring of a PPh_2 unit and the phenanthroline (Figure 4.5). In the former the phenyl ring is located over the middle of the phenanthroline in an offset alignment with an angle between the least squares planes of 15.5° and a centroid...centroid distance of 3.6 Å. In $[\text{Cu}(\text{xantphos})(3,8\text{-(EtS)}_2\text{phen})][\text{PF}_6]$ the phenyl ring is placed over one of the lateral rings of phenanthroline in a face-to-face alignment with an angle between the least squares planes of 7.43° and a centroid...centroid distance of 3.5 Å. Analogous interactions have been observed in $[\text{Cu}(\text{P}^\wedge\text{P})(\text{N}^\wedge\text{N})]^+$ cations, where the N^\wedgeN ligand is a 2-(pyridin-2yl)quinoline.²⁵³

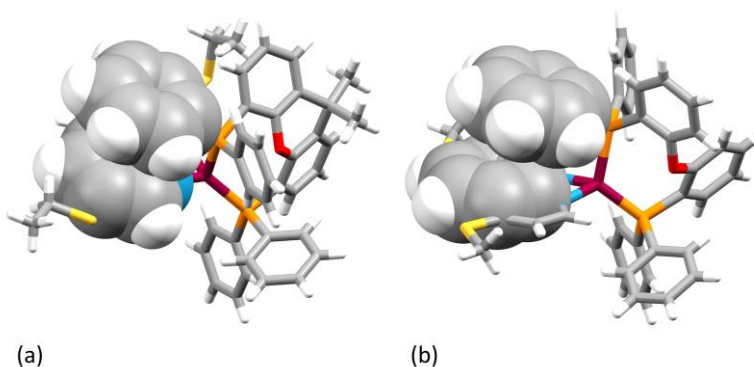


Figure 4.4: Space-filling representation of face-to-face π -stacking between a phenyl ring on a PPh_2 unit and the phenanthroline ligand in a) $[\text{Cu}(\text{xantphos})(3,8\text{-(EtS)}_2\text{phen})]^+$ and b) $[\text{Cu}(\text{POP})(4,7\text{-(MeS)}_2\text{phen})]^+$.

In $[\text{Cu}(\text{xantphos})(3,8\text{-(MeS)}_2\text{phen})]^+$ C–H... π interactions can be observed.^{254,255} In this cation, one phenyl ring which incorporates C43, of a PPh_2 group is aligned almost perpendicular (angle between least

squares plane = 85.8°) with respect to the phen unit, while the phenyl ring containing C16, which is part of the other PPh₂ unit, is situated below the central phen ring (Figure 4.5). The C–H···centroid distances (the centroid being for the middle ring of the phen unit) to H43 (above phen) and H16 (below phen) are 4.3 Å and 3.3 Å, respectively.

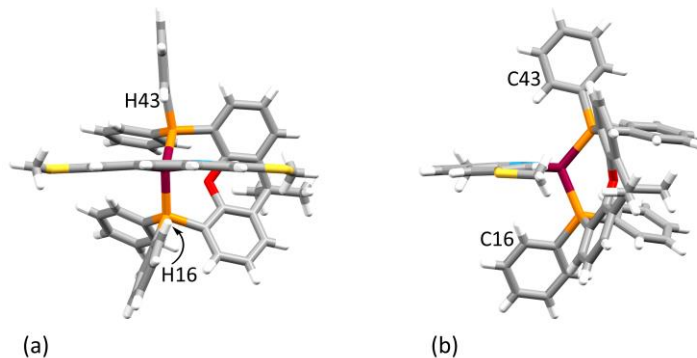


Figure 4.5: Side and front view onto the phen of [Cu(xantphos)(3,8-(MeS)₂phen)]⁺ cation, showing edge-to-face π -interactions between two independent phenyl rings and the central ring of phen.

All crystal structures, except [Cu(POP)(2,9-(MeO)₂phen)][PF₆]-1.5Et₂O, feature π -stacking interactions between two neighbouring phen units with an offset alignment. The phen moieties are always coplanar with the least squares planes of the phens being separated by 3.4 – 3.6 Å. Lastly, the orientation of the EtS substituents in [Cu(xantphos)(3,8-(EtS)₂phen)][PF₆] is worthy of note. The EtS group facing towards the ‘xanthene-bowl’ only has very limited space and therefore comes out of the phen plane, while the one facing away from the bowl stays in plane (Figure 4.6).

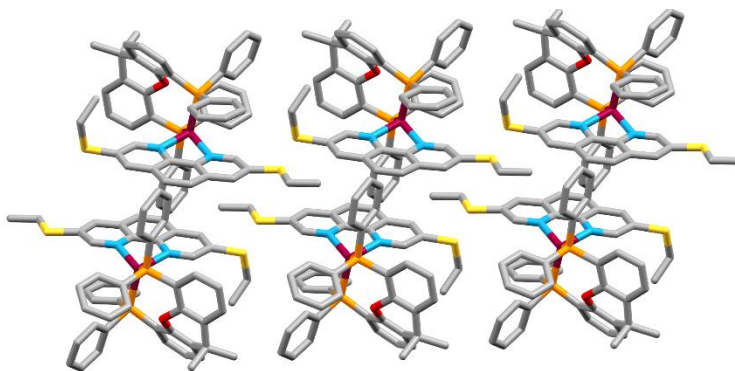


Figure 4.6: π -Stacking interactions between phenanthroline units of independent cations in the crystal structure of [Cu(xantphos)(3,8-(EtS)₂phen)][PF₆]. H atoms and PF₆⁻ anions omitted.

4.4 Electrochemistry

Electrochemical investigation of the $[\text{Cu}(\text{P}^{\wedge}\text{P})(\text{X})_2\text{phen}][\text{PF}_6]$ complexes were carried out with cyclic voltammetry in CH_2Cl_2 solution, with $[\text{nBu}_4\text{N}][\text{PF}_6]$ as a supporting electrolyte and referenced to $\text{Fc}/\text{Fc}^+ = 0.0$ V. A partially reversible or irreversible $\text{Cu}^+ \rightarrow \text{Cu}^{2+}$ oxidation can be observed between +0.65 and +0.83 V, all the data are summarized in Table 4.3 and a representative example of a cyclic voltammogram is shown in Figure 4.7. If the forward scan is taken beyond +1.2 V a second, irreversible process can be observed, typically assigned to phosphane oxidation.

In comparison to the $[\text{Cu}(\text{P}^{\wedge}\text{P})(\text{Br}_2\text{phen})][\text{PF}_6]$ compounds discussed in the previous chapter, the differences between the different substitution patterns do not lead to as pronounced a difference in $\text{Cu}^+/\text{Cu}^{2+}$ oxidation potentials. One thing that is notable, is the lower oxidation potential for complexes incorporating the 4,7-substituted phen. This indicates that the 3,8-substituents are still able to stabilize the Cu(I) geometry to a degree while the 4,7-substituents – pointing away from the copper centre – do that to a lesser extent, if at all.

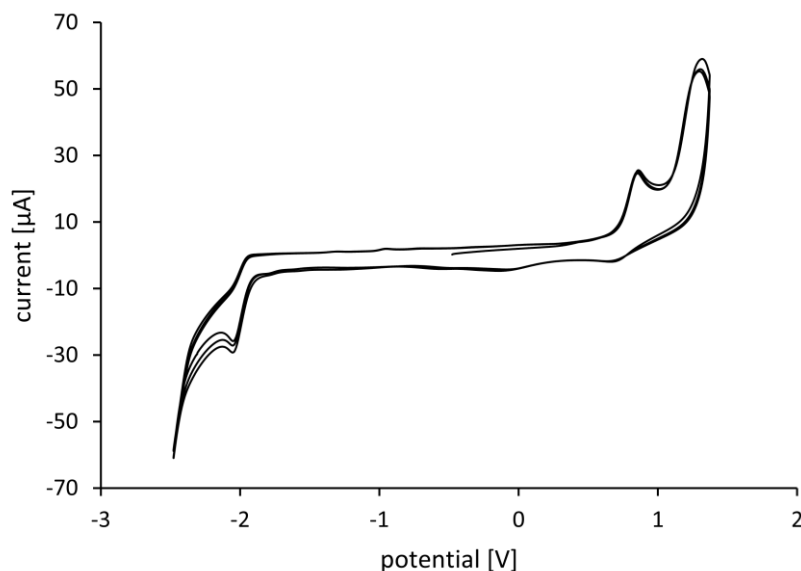


Figure 4.7: Three successive cycles in the voltammogram of $[\text{Cu}(\text{POP})(3,8-(\text{MeS})_2\text{phen})][\text{PF}_6]$ in CH_2Cl_2 ($c \approx 2 \times 10^{-5}$ M, referenced to $\text{Fc}/\text{Fc}^+ = 0$ V, $[\text{nBu}_4\text{N}][\text{PF}_6]$ as supporting electrolyte, scan rate = 0.1 V s^{-1}).

On the other hand, taking the $\text{Cu}^+/\text{Cu}^{2+}$ -oxidation potentials of the $[\text{Cu}(\text{P}^{\wedge}\text{P})((\text{MeO})_2\text{phen})][\text{PF}_6]$ into account, the argument based on pure sterics fails, since $[\text{Cu}(\text{POP})(2,9-(\text{MeO})_2\text{phen})][\text{PF}_6]$ would be expected to have the highest oxidation potential $[\text{Cu}(\text{POP})((\text{MeO})_2\text{phen})][\text{PF}_6]$ compounds, but in fact $[\text{Cu}(\text{POP})(3,8-(\text{MeO})_2\text{phen})][\text{PF}_6]$ takes this spot with +0.79 V. Considering the relatively high $\text{Cu}^+/\text{Cu}^{2+}$ -oxidation potentials of $[\text{Cu}(\text{P}^{\wedge}\text{P})(\text{Br}_2\text{phen})][\text{PF}_6]$ complexes, and the differences in oxidation potential of the di(alkylsulfanyl)phen containing compounds vs. the di(methoxy)phen incorporating ones, the ability of the substituents to either withdraw or donate electrons, respectively, is likely to play an important role. Substituents with a more negative σ -Hammett parameter on the phen moiety in $[\text{Cu}(\text{P}^{\wedge}\text{P})(\text{N}^{\wedge}\text{N})][\text{PF}_6]$ complexes thereby lead to lower Cu-oxidation potentials.

Table 4.3: Cyclic voltammetry data for [Cu(P[^]P)((X)₂phen)][PF₆] complexes in CH₂Cl₂ (c ≈ 2 × 10⁻³ M, referenced to internal Fc/Fc⁺ = 0.0 V, [nBu₄N][PF₆] as supporting electrolyte, scan rate = 0.1 V s⁻¹). ^aAll reductive processes are irreversible. irrev = irreversible.

Compounds	Oxidative Process			Reductive processes
	$E_{1/2}^{ox}/V$	E_{pa}/V	$E_{pa} - E_{pc}/mV$	E_{pc}/V
[Cu(POP)(2,9-(MeS) ₂ phen)][PF ₆]	+0.81		104	-2.14
[Cu(POP)(3,8-(MeS) ₂ phen)][PF ₆]	+0.80		102	-2.04
[Cu(POP)(4,7-(MeS) ₂ phen)][PF ₆]	+0.67		101	-2.15
[Cu(xantphos)(2,9-(MeS) ₂ phen)][PF ₆]	+0.83		102	-2.17
[Cu(xantphos)(3,8-(MeS) ₂ phen)][PF ₆]		+0.77 (irrev)		-1.96, -2.57, -2.69, -2.98
[Cu(xantphos)(4,7-(MeS) ₂ phen)][PF ₆]		+0.67 (irrev)		-2.01, -2.39, -2.61
[Cu(POP)(2,9-EtS) ₂ phen)][PF ₆]	+0.77		141	-2.23
[Cu(POP)(3,8-(EtS) ₂ phen)][PF ₆]	+0.80		184	-2.12
[Cu(POP)(4,7-(EtS) ₂ phen)][PF ₆]		+0.65 (irrev)		-2.13
[Cu(xantphos)(2,9-(EtS) ₂ phen)][PF ₆]	+0.81		150	-2.24
[Cu(xantphos)(3,8-(EtS) ₂ phen)][PF ₆]	+0.82		171	-1.81
[Cu(xantphos)(4,7-(EtS) ₂ phen)][PF ₆]	+0.69		100	-2.12
[Cu(POP)(2,9-(MeO) ₂ phen)][PF ₆]	+0.69		92	-2.28, -2.50
[Cu(POP)(3,8-(MeO) ₂ phen)][PF ₆]	+0.79		99	-2.30
[Cu(POP)(4,7-(MeO) ₂ phen)][PF ₆]	+0.64		94	-2.54
[Cu(xantphos)(2,9-(MeO) ₂ phen)][PF ₆]	+0.75		100	-2.08, -2.27, -2.46

One note has to be made about the peak-to-peak separation $E_{pa} - E_{pc}$, which is an indicator of the reversibility of the redox process. For a perfectly reversible system this value would be 59 mV at 298 K, which is derived from the Nernst equation. While the complexes presented in this chapter clearly deviate from this value, the differences are particularly striking for the [Cu(P[^]P)((EtS)₂phen)][PF₆] complexes, indicating an especially low reversibility of the Cu⁺/Cu²⁺ process.

All complexes show one or multiple irreversible ligand-based reduction processes. It was observed for all [Cu(P[^]P)(N[^]N)][PF₆] compounds presented in this chapter.

4.5 Photophysical properties

4.5.1 UV-Vis absorption spectra

Table 4.4: Summary of the absorption maxima in the CH₂Cl₂ solution absorption spectra of [Cu(P[^]P)((X)₂phen)][PF₆] complexes (c = 1.5 × 10⁻⁵–3.0 × 10⁻⁵ M).

Compounds	λ_{abs}^{max}/nm ($\epsilon_{max}/dm^2 mol^{-1} cm^{-1}$)	
	Ligand-based absorptions	MLCT
[Cu(POP)(2,9-(MeS) ₂ phen)][PF ₆]	261 (38000), 280 sh (26900), 342 (19800)	425 (2100)
[Cu(POP)(3,8-(MeS) ₂ phen)][PF ₆]	272 (50000), 354 (23200)	405 (3300)
[Cu(POP)(4,7-(MeS) ₂ phen)][PF ₆]	275 (35400), 281 sh (35200), 309 (32400)	390 (9500)
[Cu(xantphos)(2,9-(MeS) ₂ phen)][PF ₆]	263 (41600), 290 sh (27400), 343 (20400)	420 (2300)
[Cu(xantphos)(3,8-(MeS) ₂ phen)][PF ₆]	273 (50600), 353 (23000)	400 (3700)
[Cu(xantphos)(4,7-(MeS) ₂ phen)][PF ₆]	263 (38900), 285 sh (34700), 309 (26900)	390 (8100)
[Cu(POP)(2,9-EtS) ₂ phen)][PF ₆]	261 (35600), 343 (20000)	420 (1870)
[Cu(POP)(3,8-(EtS) ₂ phen)][PF ₆]	273 (32700), 353 (19000)	410 (2500)
[Cu(POP)(4,7-(EtS) ₂ phen)][PF ₆]	275 (29700), 310 (24900)	399 (6600)
[Cu(xantphos)(2,9-(EtS) ₂ phen)][PF ₆]	265 (38400), 344 (19800)	412 (2100)
[Cu(xantphos)(3,8-(EtS) ₂ phen)][PF ₆]	274 (42600), 352 (20100)	410 (2600)
[Cu(xantphos)(4,7-(EtS) ₂ phen)][PF ₆]	275 (36100), 310 (24810)	390 (7800)
[Cu(POP)(2,9-(MeO) ₂ phen)][PF ₆]	295 (30400)	415 (3100)
[Cu(POP)(3,8-(MeO) ₂ phen)][PF ₆]	246 (42600), 285 (22400), 320 (13400)	380 (2700)
[Cu(POP)(4,7-(MeO) ₂ phen)][PF ₆]	260 (41200), 307 sh (15400)	371 (5400)
[Cu(xantphos)(2,9-(MeO) ₂ phen)][PF ₆]	286 (38400)	411 (3800)

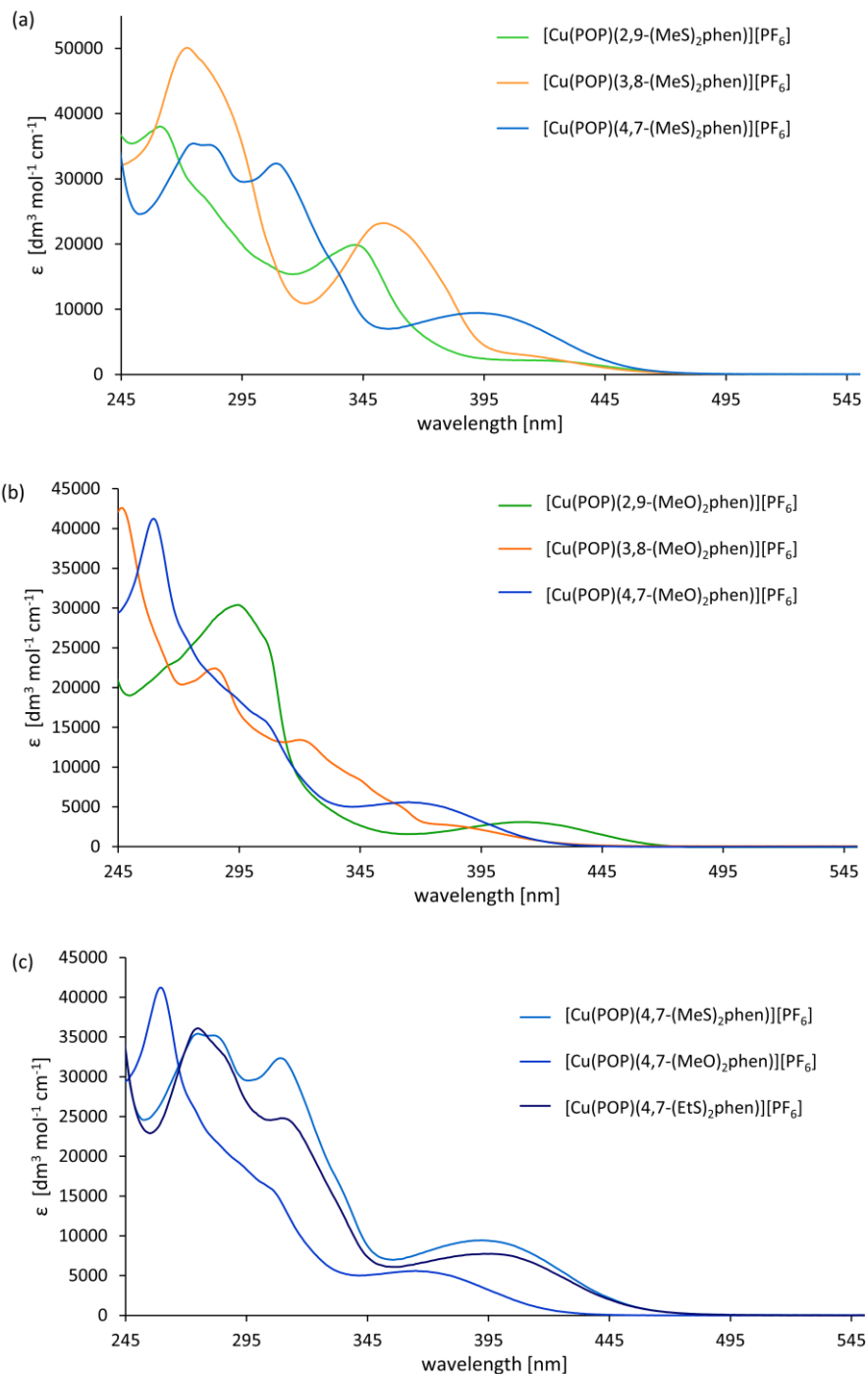


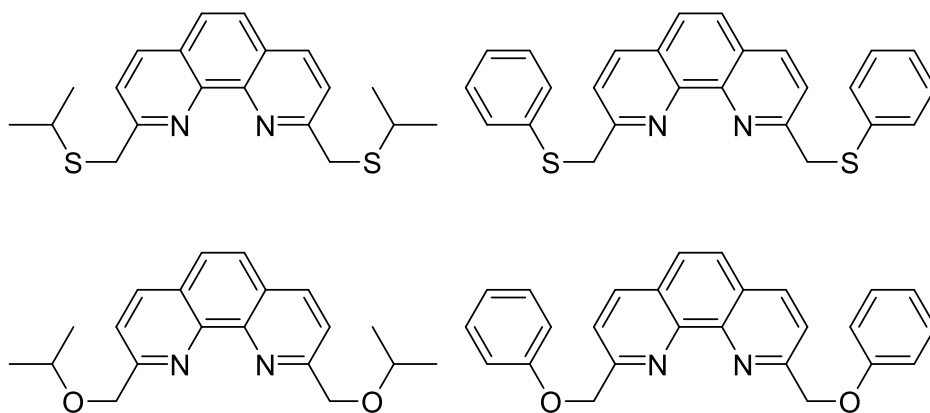
Figure 4.8: UV-Vis absorption spectra of a) $[\text{Cu}(\text{POP})((\text{MeS})_2\text{phen})][\text{PF}_6]$, b) $[\text{Cu}(\text{POP})((\text{MeO})_2\text{phen})][\text{PF}_6]$ and c) a comparison of $[\text{Cu}(\text{POP})(4,7-(X)_2\text{phen})][\text{PF}_6]$ in CH_2Cl_2 with concentrations in the range of 1.75×10^{-5} – 3.0×10^{-5} M.

UV-Vis absorption spectra were recorded in CH_2Cl_2 . Additionally, for $[\text{Cu}(\text{P}^\wedge\text{P})((\text{MeS})_2\text{phen})][\text{PF}_6]$ and $[\text{Cu}(\text{P}^\wedge\text{P})((\text{MeO})_2\text{phen})][\text{PF}_6]$ measurements in THF (tetrahydrofuran) solutions of the complexes were carried out. The $\lambda_{\text{abs}}^{\text{max}}$ are summarized in Table 4.4. The absorptions bands >300 nm clearly depend on the substitution pattern of the phen (Figure 4.8a and b), while the use of O instead of S shifts the absorptions to higher energies (Figure 4.8c). In this series, the effect of the 4,7-substitution pattern on the band around

400 nm, which normally is assigned to MLCT transitions, is striking. Commonly this band in Cu(I) complexes has ϵ values of $<6000 \text{ M}^{-1} \text{ cm}^{-1}$.^{116,196,256–258} This value is surpassed by all complexes employing 4,7-substituted phen with an alkylsulfanyl substituent, by a factor of 1.75 or more when compared to the other complexes in the respective series. The intensity of this absorption indicates a mixed nature of these bands.

Another feature, unique to the (MeS)₂phen and (EtS)₂phen containing complexes is the intense absorption band between 300 and 400 nm. Such intense absorptions in this region have rarely been reported for [Cu(P[^]P)(N[^]N)]⁺ complexes,²⁵⁹ and only a few examples where the N[^]N ligand involves an extended π -system show similarly intense absorption bands in this region.^{191,260,261} Similar behaviour can be found in the mono-substituted bpy with alkoxy or alkylsulfanyl substituents, investigated by Alkan-Zambada *et al.*, where the alkylsulfanyl substituted bpy featured an additional absorption band with a $\lambda_{\text{abs}}^{\text{max}}$ between 330 and 340 nm.¹¹⁶ The use of different chalcogens on the N[^]N moiety clearly gives a tool to tune the electronic structure of the N[^]N ligands and with it the associated absorption bands of [Cu(P[^]P)(N[^]N)]⁺ complexes.

As a final note, the direct connection of the chalcogen to the phen backbone seems to play an important role in the emergence of the intense absorption band between 310 and 360 nm (for (MeS)₂phen and (EtS)₂phen containing complexes). Rentschler and co-workers reported some [Cu(xantphos)(N[^]N)][PF₆] complexes where the N[^]N ligand is a 2,9-substituted phen with –CH₂SiPr, –CH₂SPh, –CH₂O^{*i*}Pr and –CH₂OPh substituents (Scheme 4.2). Even though there is a sulfur included in the N[^]N ligand, no additional intense absorption bands in the range between 300–400 nm were reported.²⁶²



Scheme 4.2: Structures of the N[^]N ligand used in the [Cu(xantphos)(N[^]N)][PF₆] complexes synthesized by Rentschler *et al.*²⁶²

4.5.2 Solution emission properties

Solution emission spectra were recorded in CH₂Cl₂, and for [Cu(P[^]P)((MeS)₂phen)][PF₆] and [Cu(P[^]P)((MeO)₂phen)][PF₆] additionally solutions of the complexes in THF. The complexes are yellow to red emitters and only compounds incorporating a 2,9-substituted phen exhibited any significant (<2%) PLQY in argon purged CH₂Cl₂ solution (Table 4.5). The $\lambda_{\text{em}}^{\text{max}}$ for the [Cu(P[^]P)((MeO)₂phen)][PF₆] are all remarkably close grouped in a range between 610 and 630 nm. In comparison, $\lambda_{\text{em}}^{\text{max}}$ for [Cu(P[^]P)((EtS)₂phen)][PF₆] are spread over a range of 50 nm and, even more noteworthy, the range

amounts to 140 nm for $[\text{Cu}(\text{P}^\wedge\text{P})((\text{MeS})_2\text{phen})][\text{PF}_6]$ compounds. The large range for the $[\text{Cu}(\text{P}^\wedge\text{P})((\text{MeS})_2\text{phen})][\text{PF}_6]$ mainly originates from remarkably blue shifted emissions of the two $[\text{Cu}(\text{P}^\wedge\text{P})(2,9-(\text{MeS})_2\text{phen})][\text{PF}_6]$ complexes, with respect to the $[\text{Cu}(\text{P}^\wedge\text{P})(3,8-(\text{MeS})_2\text{phen})][\text{PF}_6]$ and $[\text{Cu}(\text{P}^\wedge\text{P})(4,7-(\text{MeS})_2\text{phen})][\text{PF}_6]$ compounds (Figure 4.9).

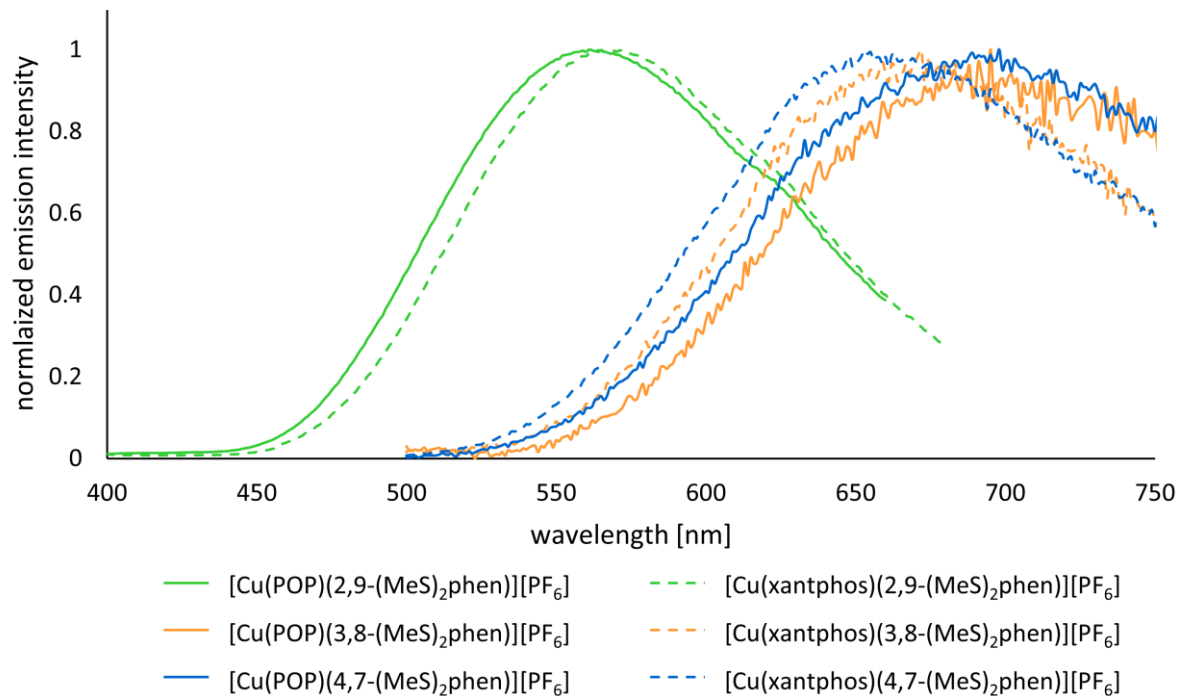


Figure 4.9: Normalized solution emission spectra for $[\text{Cu}(\text{P}^\wedge\text{P})((\text{MeS})_2\text{phen})][\text{PF}_6]$ in CH_2Cl_2 solution. ($c = 1.75 \times 10^{-5}$ – 3.0×10^{-5} M). λ_{exc} = see Table 4.5.

The comparison of $[\text{Cu}(\text{P}^\wedge\text{P})((\text{MeS})_2\text{phen})][\text{PF}_6]$ and $[\text{Cu}(\text{P}^\wedge\text{P})((\text{EtS})_2\text{phen})][\text{PF}_6]$ shows only very small shifts of the $\lambda_{\text{em}}^{\text{max}}$ (Table 4.5) with the largest shift of 18 nm between $[\text{Cu}(\text{xantphos})(4,7-(\text{EtS})_2\text{phen})][\text{PF}_6]$ and $[\text{Cu}(\text{xantphos})(4,7-(\text{MeS})_2\text{phen})][\text{PF}_6]$. However, the PLQY and the associated excited state lifetime show clear differences. While for $[\text{Cu}(\text{P}^\wedge\text{P})(3,8-(\text{MeS})_2\text{phen})][\text{PF}_6]$ no PLQY could be detected, a weak luminescence was measured for $[\text{Cu}(\text{P}^\wedge\text{P})(3,8-(\text{EtS})_2\text{phen})][\text{PF}_6]$, with very short (<300 ns) excited state lifetime. The PLQY for $[\text{Cu}(\text{P}^\wedge\text{P})(2,9-(\text{EtS})_2\text{phen})][\text{PF}_6]$ is considerably enhanced compared to their $[\text{Cu}(\text{P}^\wedge\text{P})(2,9-(\text{MeS})_2\text{phen})][\text{PF}_6]$ counterparts. This and the longer τ for the $[\text{Cu}(\text{P}^\wedge\text{P})(2,9-(\text{EtS})_2\text{phen})][\text{PF}_6]$ complexes is consistent with the EtS substituents hindering the flattening of the copper geometry upon photo-excitation better than the MeS substituents.

The relative blue-shift of $[\text{Cu}(\text{POP})(3,8-(\text{MeO})_2\text{phen})][\text{PF}_6]$ and $[\text{Cu}(\text{POP})(4,7-(\text{MeO})_2\text{phen})][\text{PF}_6]$ compared to $[\text{Cu}(\text{P}^\wedge\text{P})(3,8-(\text{MeS})_2\text{phen})][\text{PF}_6]$ and $[\text{Cu}(\text{P}^\wedge\text{P})(4,7-(\text{MeS})_2\text{phen})][\text{PF}_6]$, and the comparatively short excited state lifetimes in THF for the two latter complexes (30–80 ns) is in agreement with the energy gap law. Furthermore, the red-shift also leads to an increase in non-radiative decays for $[\text{Cu}(\text{P}^\wedge\text{P})(3,8-(\text{MeS})_2\text{phen})][\text{PF}_6]$ and $[\text{Cu}(\text{P}^\wedge\text{P})(4,7-(\text{MeS})_2\text{phen})][\text{PF}_6]$ thus the PLQY stayed below the detection limit of 1%, while the PLQY of $[\text{Cu}(\text{P}^\wedge\text{P})(3,8-(\text{MeO})_2\text{phen})][\text{PF}_6]$ and $[\text{Cu}(\text{P}^\wedge\text{P})(4,7-(\text{MeO})_2\text{phen})][\text{PF}_6]$ were 1.5% and 1.8%, respectively. The σ -Hammett parameters for MeO and MeS in *ortho* and *para* positions are more

negative for the MeO substituent,²⁶³ a blue-shift for the (MeO)₂phen containing complexes with an associated increase in PLQY is also consistent with the experimental values.

Table 4.54: Summary of the solution emission data of [Cu(P^P)((X)₂phen)][PF₆] complexes in deaerated CH₂Cl₂ solution. ^a Excitation occurred at 410 nm. ^b Excitation occurred at 365 nm. ^c not measured since PLQY <1%. ^d not observed due to poor solubility.

Compounds	CH ₂ Cl ₂				THF ^a		77 K 2-Me-THF ^a	
	λ _{exc} /nm	λ _{em} ^{max} /nm	PLQY/%	τ/μs ^b	λ _{em} ^{max} /nm	τ/μs	λ _{em} ^{max} /nm	τ/ms
[Cu(POP)(2,9-(MeS) ₂ phen)][PF ₆]	425	561	15	8.3	596	5.2	530	0.8
[Cu(POP)(3,8-(MeS) ₂ phen)][PF ₆]	425	695	<1	^c	710	0.04	535, 499	2.0, 2.1
[Cu(POP)(4,7-(MeS) ₂ phen)][PF ₆]	405	698	<1	^c	704	0.08	547, 505	3.1, 4.2
[Cu(xantphos)(2,9-(MeS) ₂ phen)][PF ₆]	425	568	5.0	2.1	579	4.3	528, 498	3.2, 3.3
[Cu(xantphos)(3,8-(MeS) ₂ phen)][PF ₆]	425	672	<1	^c	680	0.03	529, 490	2.5, 2.7
[Cu(xantphos)(4,7-(MeS) ₂ phen)][PF ₆]	405	653	<1	^c	677	0.06	550, 510	3.5, 4.2
[Cu(POP)(2,9-EtS) ₂ phen)][PF ₆]	420	558	23	9.4				
[Cu(POP)(3,8-(EtS) ₂ phen)][PF ₆]	410	703	1.5	<0.01				
[Cu(POP)(4,7-(EtS) ₂ phen)][PF ₆]	400	695	<1	^c				
[Cu(xantphos)(2,9-(EtS) ₂ phen)][PF ₆]	410	559	13	9.5				
[Cu(xantphos)(3,8-(EtS) ₂ phen)][PF ₆]	410	679	2.2	0.3				
[Cu(xantphos)(4,7-(EtS) ₂ phen)][PF ₆]	395	671	<1	^c				
[Cu(POP)(2,9-(MeO) ₂ phen)][PF ₆]	410	625	5.5	1.5	618	2.1	544	0.5
[Cu(POP)(3,8-(MeO) ₂ phen)][PF ₆]	320	610	1.5	<0.01	662	0.37	^d	^d
[Cu(POP)(4,7-(MeO) ₂ phen)][PF ₆]	365	631	1.8	<0.01	642	0.28	^d	^d
[Cu(xantphos)(2,9-(MeO) ₂ phen)][PF ₆]	420	625	6.0	0.36	611	3.3	537	0.4

The small Stokes shift (energy difference, λ_{abs}^{max} – λ_{em}^{max}) between the lowest energy absorption and the emission of around 0.75 eV (6050 cm⁻¹) for the [Cu(POP)(2,9-(MeS)₂phen)][PF₆] and [Cu(xantphos)(2,9-(MeS)₂phen)][PF₆] are quite remarkable and one of the smallest observed for [Cu(P^P)(N^N)]⁺ complexes.

^{264–266} The small energy difference suggests that the pseudo-tetrahedral Cu(I) geometry is retained to a significant degree for these two complexes, leading to an only minimal energy loss upon photoexcitation. Consistent with this observation, the excited state of the 2,9-substituted phen incorporating complexes are the longest-lived ones in the series.

Comparing the emissive properties of the complexes employing (MeS)₂phen with the ones carrying (MeO)₂phen, it is clear that the choice of the employed chalcogen plays an important role in the solution emission of these complexes. The higher PLQY and longer excited state lifetimes when comparing [Cu(POP)(2,9-(MeS)₂phen)][PF₆] to [Cu(POP)(2,9-(MeO)₂phen)][PF₆] may be a result of an increased steric demand of the MeS vs. MeO group (atomic radii for O and S: 0.6 Å vs. 1.0 Å²⁶⁷, covalent radii: 0.66 Å vs. 1.05 Å²⁶⁸ and van der Waals radii: 1.63 Å vs 1.86 Å²²⁰), which more effectively prevents the flattening of the Cu(I) coordination sphere upon excitation and consequently decreases the number of non-radiative decay pathways. Furthermore, Cu(I) exhibits an affinity for sulfur,^{269,270} which may lead to interactions between the copper centre and the sulfur atom in [Cu(P^P)(2,9-(MeS)₂phen)]⁺ thereby stabilizing the tetrahedral geometry with respect to the [Cu(P^P)(2,9-(MeO)₂phen)]⁺ analogues. While crystallographic data of [Cu(POP)(2,9-(MeS)₂phen)][PF₆] are not available, the data for [Cu(POP)(2,9-(MeO)₂phen)][PF₆] with a Cu...O distance of 3.2 Å and the Cu...S distance of 3.5 Å in [Cu(POP)(2,9-(EtS)₂phen)][PF₆], which are both smaller than the sum of van der Waals radii postulated by Batsanov,²²⁰ indicate that such an interaction between the copper and sulfur is plausible.

The improvements of the PLQY are only observed for $[\text{Cu}(\text{POP})(2,9\text{-(MeS)}_2\text{phen})][\text{PF}_6]$ compared to $[\text{Cu}(\text{POP})(2,9\text{-(MeO)}_2\text{phen})][\text{PF}_6]$ (15% vs. 5.5%), but not when comparing $[\text{Cu}(\text{xantphos})(2,9\text{-(MeS)}_2\text{phen})][\text{PF}_6]$ to $[\text{Cu}(\text{xantphos})(2,9\text{-(MeO)}_2\text{phen})][\text{PF}_6]$ (5.0% vs. 6.0%), an observation that has been made before for bpy-derivative containing $[\text{Cu}(\text{P}^\wedge\text{P})(\text{N}^\wedge\text{N})][\text{PF}_6]$ complexes.¹⁸⁴ This may originate in the higher rigidity of the xantphos ligand which constrains the complexes to a larger degree than POP.

4.5.2a Emission properties in THF solution and in frozen glass matrices at 77 K

Commonly, more polar solvents stabilize the MLCT state due to improved stabilisation of the charges which would lead to a red-shift of the complexes' emission in CH_2Cl_2 when compared to the less polar THF.²⁷¹ Comparing the emission spectra of $[\text{Cu}(\text{P}^\wedge\text{P})(\text{MeS})_2\text{phen}][\text{PF}_6]$ and $[\text{Cu}(\text{P}^\wedge\text{P})(\text{MeO})_2\text{phen}][\text{PF}_6]$ in these two solvents reveals, however, that this only holds true for $[\text{Cu}(\text{POP})(2,9\text{-(MeO)}_2\text{phen})][\text{PF}_6]$ and $[\text{Cu}(\text{xantphos})(2,9\text{-(MeO)}_2\text{phen})][\text{PF}_6]$ (Table 4.5). For all the other compounds the $\lambda_{\text{em}}^{\text{max}}$ is blue-shifted in CH_2Cl_2 when compared to the emission in THF. This observation supports the that the absorption bands around 400 nm are not purely of MLCT character.

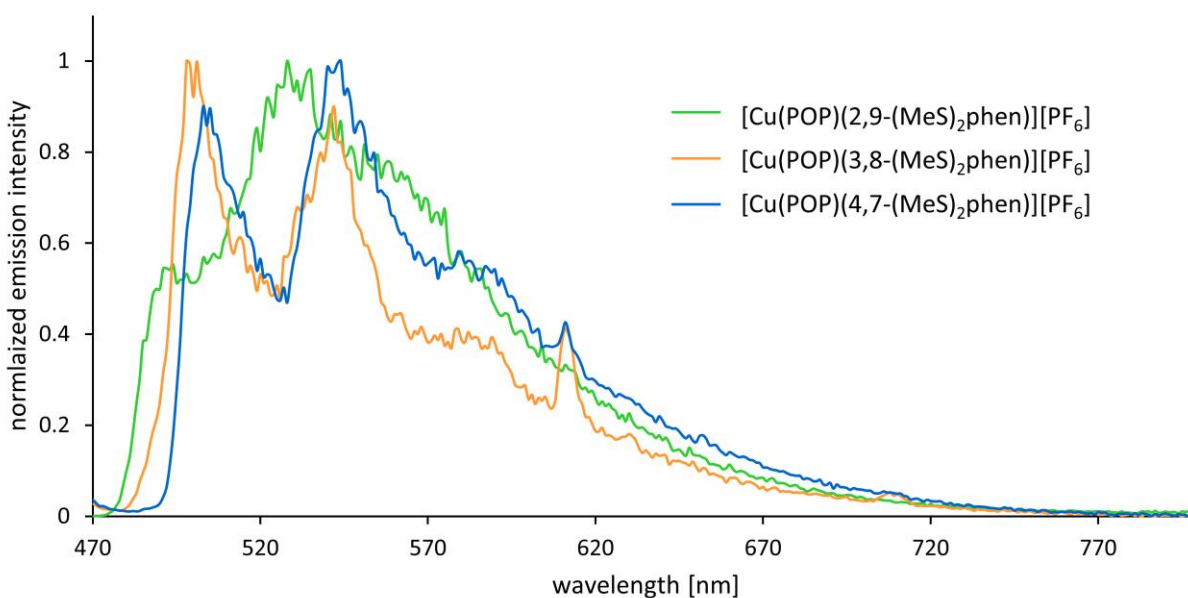


Figure 4.10: Normalized frozen matrix emission spectra of $[\text{Cu}(\text{POP})(\text{MeS})_2\text{phen}][\text{PF}_6]$ complexes in 2-Me-THF. ($c = 1.75 \times 10^{-5}$ – 3.0×10^{-5} M). $\lambda_{\text{exc}} = 425$ nm.

In order to investigate the nature of the transitions around 400 nm in more detail, measurements at 77 K in frozen 2-Me-THF (2-methyltetrahydrofuran) were carried out. $[\text{Cu}(\text{POP})(2,9\text{-(MeS)}_2\text{phen})][\text{PF}_6]$, $[\text{Cu}(\text{POP})(2,9\text{-(MeO)}_2\text{phen})][\text{PF}_6]$ and $[\text{Cu}(\text{xantphos})(2,9\text{-(MeO)}_2\text{phen})][\text{PF}_6]$ exhibit one emission band with a $\lambda_{\text{em}}^{\text{max}}$ at 530, 544 and 537 nm, respectively. In contrast to that, all the other complexes, with the exception of $[\text{Cu}(\text{POP})(3,8\text{-(MeO)}_2\text{phen})][\text{PF}_6]$ which could not be measured due to poor solubility, feature two distinct emission bands (Table 4.5 and Figure 4.10). The emissions of all the complexes are significantly blue-shifted, with the compounds incorporating 2,9-substituted phens exhibiting the smallest shifts ($\Delta\lambda_{\text{em}}^{\text{max}} = 40\text{--}88$ nm), while the complexes carrying 3,8- and 4,7-substituted phens show a $\Delta\lambda_{\text{em}}^{\text{max}}$ of up to

194 nm. Furthermore, with excited state lifetimes of 2.0 to 4.2 ms, these dual emissions are extraordinarily long lived. In comparison, the excited state lifetimes of [Cu(POP)(2,9-(MeS)₂phen)][PF₆], [Cu(POP)(2,9-(MeO)₂phen)][PF₆] and [Cu(xantphos)(2,9-(MeO)₂phen)][PF₆] with 0.8 μs, 0.5 μs and 0.4 ms, respectively, are considerably shorter.

The shape of the emission spectrum at 77 K is clearly influenced by the substitution pattern of the phen ligand, while the choice of P[^]P ligand has only a negligible influence. Most notably, only 2,9-substituted phen ligands lead to a single emission band at 77 K. This single emission most likely originates from a ¹MLCT state, and the [Cu(P[^]P)(2,9-(MeS)₂phen)][PF₆] and [Cu(P[^]P)(2,9-(MeO)₂phen)][PF₆] complexes notably also exhibit the least overlap with possible ligand-based absorption bands around 400 nm (Figure 4.8).

4.5.3 Solid-state emission properties

Table 4.6: Solid-state emission data for [Cu(P[^]P)(X)₂phen)][PF₆] complexes. ^aExcitation occurred at 405 nm. ^bExcitation occurred at 365 nm.

Compounds	Powder		
	λ_{em}^{max}/nm	PLQY/% ^a	$\tau/\mu s^b$
[Cu(POP)(2,9-(MeS) ₂ phen)][PF ₆]	539	26	3.7
[Cu(POP)(3,8-(MeS) ₂ phen)][PF ₆]	540	5.5	19
[Cu(POP)(4,7-(MeS) ₂ phen)][PF ₆]	564	1.5	3.4
[Cu(xantphos)(2,9-(MeS) ₂ phen)][PF ₆]	576	9.0	4
[Cu(xantphos)(3,8-(MeS) ₂ phen)][PF ₆]	540	5.0	2.6
[Cu(xantphos)(4,7-(MeS) ₂ phen)][PF ₆]	603	3.5	2.4
[Cu(POP)(2,9-EtS) ₂ phen)][PF ₆]	550	60	14
[Cu(POP)(3,8-(EtS) ₂ phen)][PF ₆]	600	7.0	4.1
[Cu(POP)(4,7-(EtS) ₂ phen)][PF ₆]	594	5.9	2.4
[Cu(xantphos)(2,9-(EtS) ₂ phen)][PF ₆]	550	37	13
[Cu(xantphos)(3,8-(EtS) ₂ phen)][PF ₆]	590	10	4.9
[Cu(xantphos)(4,7-(EtS) ₂ phen)][PF ₆]	596	1.6	2.0
[Cu(POP)(2,9-(MeO) ₂ phen)][PF ₆]	523	39	11
[Cu(POP)(3,8-(MeO) ₂ phen)][PF ₆]	562	11	8.8
[Cu(POP)(4,7-(MeO) ₂ phen)][PF ₆]	550	13 ^b	6.2
[Cu(xantphos)(2,9-(MeO) ₂ phen)][PF ₆]	550	15	7.6

In the solid-state, all complexes are yellow or orange emitters with an λ_{em}^{max} between 523 and 603 nm. [Cu(POP)(2,9-(MeS)₂phen)][PF₆], [Cu(POP)(2,9-(MeO)₂phen)][PF₆], [Cu(POP)(2,9-(EtS)₂phen)][PF₆] and [Cu(xantphos)(2,9-(EtS)₂phen)][PF₆] exhibit significant PLQY (>20%, Table 4.6), however all compounds show an increase in PLQY when compared to deaerated solution measurements. This and the accompanying blue-shift of all the emissions in the solid-state except for [Cu(xantphos)(2,9-(MeS)₂phen)][PF₆], with respect to the emissions in solution, are consistent with the higher rigidity of the medium and, in case of the [Cu(P[^]P)(2,9-(EtS)₂phen)][PF₆] compounds, of the higher steric demand of the EtS vs. MeS substituents, leading to a hindering of the relaxation of the copper coordination sphere upon excitation.

As a series, the (MeO)₂phen incorporating complexes feature the most advantageous photophysical properties in solid-state. Previous reports have described [Cu(P[^]P)(N[^]N)]⁺ complexes carrying a phen ligand and POP feature higher quantum yields in solid-state than their analogous xantphos counterpart, this is in contrast to corresponding bpy containing complexes.^{217,247} This observation holds true for the herein reported compounds. However, the electronic influence of the sulfanyl substituents clearly affects

the emissive properties of the complexes to a larger degree than the methoxy substituents and clear trends are hard to discern for the complexes employing (MeS)₂phen and (EtS)₂phen.

Excited state lifetimes are featured in the μs regime with [Cu(POP)(3,8-(MeO)₂phen)][PF₆] having a remarkably long excited state lifetime of 19 μs (Table 4.6). Although Smith *et al.* reported a lifetime of 26 μs for [Cu(POP)(2,9-(Me)₂phen)][tfbp] (tfbp = tetrakis[3,5-bis(trifluoromethyl)phenyl]borate), they carried out their measurement under N₂ atmosphere with O₂ exclusion. In pure O₂ atmosphere the same complex featured a τ of 6.4 μs and a considerably decreased PLQY (88% in N₂, 19% in O₂). Indeed, already 10 mol% O₂ in N₂ lead to a noticeable decrease in luminescence.²⁴⁷ Although not explicitly stated, it can be assumed that the decrease in luminescence goes hand in hand with a shortened excited state lifetime, as can be observed for excited state lifetimes of [Cu(P[^]P)(N[^]N)]⁺ complexes in solution.^{179,217} While the PLQY for [Cu(POP)(3,8-(MeO)₂phen)][PF₆] is not particularly high, with 5.5%, the long excited state lifetime indicates for this single complex may suggest that this complex is not as vulnerable to oxygen quenching in solid-state as other complexes.

The longer excited state lifetimes for the [Cu(P[^]P)(2,9-(EtS)₂phen)][PF₆] compounds, when compared to [Cu(P[^]P)(2,9-(MeS)₂phen)][PF₆] are consistent with the increase in PLQY, based on the higher steric demands of the N[^]N ligand.

4.5.4 Comparison of solid-state and 77 K frozen matrix emission measurements

The differences between the room temperature solid-state measurements and the measurements at 77 K in 2-Me-THF are quite striking. The τ values increase by two to three orders of magnitude for all complexes. These longer excited state lifetimes upon cooling down are consistent with TADF behaviour,^{101,164} however, the accompanying red-shift, that is expected for TADF compounds at lower temperatures, is only observed for [Cu(POP)(2,9-(MeO)₂phen)][PF₆]. Nevertheless, for [Cu(POP)(2,9-(MeS)₂phen)][PF₆] and [Cu(xantphos)(2,9-(MeO)₂phen)][PF₆], the blue-shift in solid-state compared to the frozen matrix is quite small ($\leq 13\text{nm}$), especially when compared to the blue-shift between the solid-state emission and the higher energy emission at 77 K of the dual emitting complexes. It is remarkable that only complexes with 2,9-substituted phens show one emission band at 77 K, which also does not shift as much as the emission bands of the other complexes. Furthermore, [Cu(POP)(2,9-(MeS)₂phen)][PF₆], [Cu(POP)(2,9-(MeO)₂phen)][PF₆] and [Cu(xantphos)(2,9-(MeO)₂phen)][PF₆], exhibit the shortest excited state lifetimes at in the frozen matrix measurements. From the gathered data it is likely that the single emission of [Cu(POP)(2,9-(MeS)₂phen)][PF₆], [Cu(POP)(2,9-(MeO)₂phen)][PF₆] and [Cu(xantphos)(2,9-(MeO)₂phen)][PF₆] at 77 K originates from a ¹MLCT state. It is of note, that a blue-shift in frozen matrix was observed for several [Cu(P[^]P)(N[^]N)][PF₆] complexes, with N[^]N being a substituted bpy, reported by Keller *et al.* which was explained by “intermolecular matrix effects in the Me-THF glass”.^{115,179}

4.6 Conclusion

A series of [Cu(P[^]P)((X)₂phen)][PF₆] complexes bearing POP or xantphos as P[^]P ligand and a alkylsulfanyl or alkyloxy substituted phen as the N[^]N ligand was successfully synthesized and characterized.

The introduction of the MeS, MeO or EtS substituents on the phen ligand has a considerable effect on the photophysical properties of the [Cu(P[^]P)(N[^]N)][PF₆] complexes. All complexes incorporating an

(MeS)₂phen or (EtS)₂phen feature intense absorption ligand-based bands in the region between 300–400 nm.

When excited in the band around 400 nm, which is usually assigned to an MLCT transition, the complexes emit with an $\lambda_{\text{em}}^{\text{max}}$ between 561 and 703 nm, but only complexes employing a 2,9-substituted phen feature PLQYs > 5%. The complexes employing 2,9-(MeS)₂phen instead of 2,9-(MeO)₂phen feature a strikingly small Stokes shift, which may be attributed to the larger S atom, compared to O, and interactions between the copper centre the S atom, preventing the relaxation of the pseudo-tetrahedral Cu(I) geometry towards square-planar upon excitation. The introduction of the larger EtS substituent has a significant effect on the PLQY and excited state lifetime, which indicates an even more effective hindering of the relaxation of the copper geometry upon excitation.

When measuring the luminescence of the complexes at 77 K in 2-Me-THF, most of the complexes feature two distinct emission maxima with extraordinary long lifetimes between 2–4.2 ms. The three complexes ([Cu(POP)(2,9-(MeS)₂phen)][PF₆], [Cu(POP)(2,9-(MeO)₂phen)][PF₆] and [Cu(xantphos)(2,9-(MeS)₂phen)][PF₆]) that only feature one distinct emission maximum, have considerably shorter lifetimes (0.8, 0.5 and 0.4 ms), however these are still two orders of magnitude longer than the τ at room temperature in THF.

In the solid-state, the complexes are yellow to orange emitters with PLQYs up to 60% with lifetimes in the μs regime. The high PLQY, longer excited state lifetimes and blue-shift, compared to solution values, are consistent with the higher rigidity of the medium and the environmentally imposed stabilisation of the Cu(I) geometry.

To get a better insight into the photophysical behaviour of these complexes, computational methods would be beneficial, however it was not able to carry such out over the course of this work. Similarly, especially the [Cu(P[^]P)(2,9-(EtS)₂phen)][PF₆] complexes feature intriguing properties and their incorporation into LEC devices may be warranted, but because of time constraints this was not possible.

4.7 Experimental

4.7.1 (MeS)₂phen ligand synthesis

The synthesis of 2,9-(MeS)₂phen has been previously reported²⁴⁹ and each ligand preparation was carried out in an analogous manner (see later for details). The respective Br₂phen (1.0 equiv.) was dissolved in DMF and sodium thiomethoxide (3.5 equiv.) was added. The reaction was heated to 50 °C and stirred for 20 h. Then water was added, and the resulting precipitate was collected by filtration and washed with water.

4.7.1a 3,8-(MeS)₂phen

The reagents were 3,8-dibromophenanthroline (350 mg, 1.04 mmol), and sodium thiomethoxide (269 mg, 3.64 mmol). 3,8-(MeS)₂phen was isolated as a yellow solid (220 mg, 0.81 mmol, 77.7%). Melting point 268 °C. ¹H NMR (500 MHz, CDCl₃) δ /ppm 9.03 (d, *J* = 2.3 Hz, 2H, H^{A2}), 7.97 (d, *J* = 2.4 Hz, 2H, H^{A4}), 7.71 (2H, H^{A5}), 2.66 (s, 6H, H^{A-Me}). ¹³C{¹H} NMR (126 MHz, CDCl₃) δ /ppm 149.4 (C^{A2}) 143.6 (C^{A10a}), 135.2 (C^{A3}) 131.6 (C^{A4}), 128.1 (C^{A4a}), 126.6 (C^{A5}), 15.8 (C^{A-Me}). ESI-MS positive mode *m/z* 273.01 [3,8-(MeS)₂phen + H]⁺ (calc. 273.05), 295.01 [3,8-(MeS)₂phen + Na]⁺ (calc. 295.03).

4.7.1b 4,7-(MeS)₂phen

The reagents were 4,7-dibromophenanthroline (351 mg, 1.04 mmol), and sodium thiomethoxide (269 mg, 3.64 mmol). 4,7-(MeS)₂phen was isolated as yellow solid (220 mg, 0.81 mmol, 77.7%). Melting point 247 °C. ¹H NMR (500 MHz, CD₂Cl₂) δ/ppm 8.94 (d, *J* = 4.9 Hz, 2H, H^{A2}), 8.13 (s, 2H, H^{A5}), 7.39 (d, *J* = 2.4 Hz, 2H, H^{A3}), 2.68 (s, 6H, H^{A-Me}). ¹³C{¹H} NMR (126 MHz, CD₂Cl₂) δ/ppm 149.8 (C^{A2}), 149.3 (C^{A4}) 146.0 (C^{A10a}), 126.6 (C^{A4a}), 122.0 (C^{A5}), 117.6 (C^{A3}), 14.8 (C^{A-Me}). ESI-MS positive mode *m/z* 273.04 [4,7-(MeS)₂phen + H]⁺ (calc. 273.05), 295.03 [4,7-(MeS)₂phen + Na]⁺ (calc. 295.03).

4.7.2 (MeO)₂phen ligand synthesis

The respective Br₂phen (1.0 equiv.) was placed in a microwave vial which was subsequently sealed. The vial was evacuated three times and backfilled with N₂. The Br₂phen was partially dissolved in DMF, and then freshly prepared sodium methanolate solution (8.0 equiv.) was added. The reaction was allowed to run for 6 h at 120 °C in the microwave. The solvents were removed under reduced pressure and the resulting precipitate was dissolved in CH₂Cl₂ and extracted with water to yield the desired product.

4.7.3 (EtS)₂phen ligand synthesis

The respective Br₂phen (1.0 equiv.) was dissolved in DMF and sodium thioethoxide (3.5 equiv.) was added. The reaction was heated to 80 °C and stirred for 16 h. Then water was added, and the resulting precipitate was collected by filtration and washed with water.

4.7.3a 2,9-(EtS)₂phen

The reagents were 2,9-Dibromo-1,10-phenanthroline (100 mg, 0.28 mmol), sodium thioethoxide (82.7 mg, 0.98 mmol). 2,9-(EtS)₂phen was isolated as an ochre solid (83.8 mg, 0.28 mmol, 99%). Melting point 128 °C. ¹H NMR (500 MHz, CDCl₃) δ/ppm 7.95 (d, *J* = 8.5 Hz, 2H, H^{A4}), 7.62 (s, 2H, H^{A5}), 7.41 (d, *J* = 8.5 Hz, 2H, H^{A3}), 3.57 (q, *J* = 7.4 Hz, 4H, H^{Et-CH₂}), 1.57 (t, *J* = 7.4 Hz, 6H, H^{Et-CH₃}). ¹³C{¹H} NMR (126 MHz, CDCl₃) δ/ppm 159.7 (C^{A2}), 145.3 (C^{A10a}), 135.5 (C^{A4}), 126.3 (C^{A4a}), 124.9 (C^{A5}), 122.5 (C^{A3}), 24.5 (C^{Et-CH₂}), 15.1 (C^{Et-CH₃}). ESI-MS positive mode *m/z* 301.09 [2,9-(EtS)₂phen + H]⁺ (base peak, calc. 301.08), 323.07 [2,9-(EtS)₂phen + Na]⁺ (calc. 323.07), 339.03 [2,9-(EtS)₂phen + K]⁺ (calc. 339.04), 623.09 [2 x 2,9-(EtS)₂phen + Na]⁺ (calc. 623.14).

4.7.3b 3,8-(EtS)₂phen

The reagents were 3,8-Dibromo-1,10-phenanthroline (300 mg, 0.89 mmol), sodium thioethoxide (261 mg, 3.11 mmol). 3,8-(EtS)₂phen was isolated as an off-yellow solid (233 mg, 0.78 mmol, 87%). Melting point 129 °C. ¹H NMR (500 MHz, CDCl₃) δ/ppm 9.06 (d, *J* = 2.3 Hz, 2H, H^{A2}), 8.08 (d, *J* = 2.4 Hz, 2H, H^{A4}), 7.71 (s, 2H, H^{A5}), 3.12 (q, *J* = 7.3 Hz, 4H, H^{Et-CH₂}), 1.40 (t, *J* = 7.4 Hz, 6H, H^{Et-CH₃}). ¹³C{¹H} NMR (126 MHz, CDCl₃) δ/ppm 151.0 (C^{A2}), 144.0 (C^{A10a}), 134.6 (C^{A4}), 133.6 (C^{A5}), 128.5 (C^{A4a}), 126.7 (C^{A5}), 27.8 (C^{Et-CH₂}), 14.4 (C^{Et-CH₃}). ESI-MS positive mode *m/z* 301.09 [3,8-(EtS)₂phen + H]⁺ (base peak, calc. 301.08).

4.7.3c 4,7-(EtS)₂phen

The reagents were 4,7-Dibromo-1,10-phenanthroline (300 mg, 0.89 mmol), sodium thioethoxide (249 mg, 2.96 mmol). 4,7-(EtS)₂phen was isolated as an ochre solid (251.2 mg, 0.84 mmol, 99%). Decomposition temperature 135 °C. ¹H NMR (500 MHz, CDCl₃) δ/ppm 8.97 (d, *J* = 4.9 Hz, 2H, H^{A2}), 8.14 (s, 2H, H^{A5}), 7.40 (d, *J* = 4.9 Hz, 2H, H^{A3}), 3.18 (q, *J* = 7.4 Hz, 4H, H^{Et-CH₂}), 1.51 (t, *J* = 7.4 Hz, 6H,

H^{Et-CH₃}). ¹³C{¹H} NMR (126 MHz, CDCl₃) δ/ppm 149.4 (C^{A2}), 147.9 (C^{A4}), 145.9 (C^{A10a}), 126.7 (C^{4a}), 121.9 (C^{A5}), 118.2 (C^{A3}), 25.8 (C^{Et-CH₂}), 13.6 (C^{Et-CH₃}). ESI-MS positive mode *m/z* 301.08 [4,7-(EtS)₂phen + H]⁺ (base peak, calc. 301.08), 323.07 [4,7-(EtS)₂phen + Na]⁺ (calc. 323.07).

4.7.4 Complex synthesis

POP-containing compounds were synthesized according to the following procedure. POP (1.1 eqv.) and [Cu(MeCN)₄][PF₆] (1.0 eqv.) were dissolved in CH₂Cl₂ (20 mL) and the reaction mixture was stirred for 1 h. Then the N^AN ligand (1.0 eqv.) was added, and the reaction mixture was stirred for 1 h. The solvent was then removed under reduced pressure. The residue was washed with Et₂O. The crude product was purified by crystallisation from CH₂Cl₂/Et₂O by vapour diffusion.

Compounds containing xantphos were prepared by the following procedure. A solution of the respective phen (1.0 eqv.) and xantphos (1.1 eqv.) in CH₂Cl₂ (10 mL) was added dropwise to a CH₂Cl₂ solution (10 mL) of [Cu(MeCN)₄][PF₆] (1.0 eqv.). The reaction mixture was then stirred for 2 h before the solvent was removed under reduced pressure. The residue was washed with Et₂O. The crude product was purified by crystallisation from CH₂Cl₂/Et₂O by vapour diffusion.

4.7.4a [Cu(POP)(2,9-(MeS)₂phen)][PF₆]

The reagents were POP (106 mg, 0.20 mmol), [Cu(MeCN)₄][PF₆] (66.5 mg, 0.18 mmol) and 2,9-(MeS)₂phen (60.6 mg, 0.18 mmol). One additional equivalent of POP was added for the crystallisation process to precipitate the desired compound. [Cu(POP)(2,9-(MeS)₂phen)][PF₆] was isolated as an orange solid (170 mg, 0.16 mmol, 88%). ¹H NMR (500 MHz, acetone-*d*₆) δ/ppm 8.56 (d, *J* = 8.7 Hz, 2H, H^{A4}), 7.95 (s, 2H, H^{A5}), 7.80 (d, *J* = 8.7 Hz, 2H, H^{A3}), 7.40 (td, *J* = 8.2, 1.6 Hz, 2H, H^{C5}), 7.29–7.17 (overlapping m, 14H, H^{C4+D2+D4}), 7.18–7.09 (overlapping m, 10H, H^{C3+D3}), 7.02 (dt, *J* = 8.2, 1.6 Hz, 2H, H^{C5}), 2.37 (s, 6H, H^{SMe}). ¹³C{¹H} NMR (126 MHz, acetone-*d*₆) δ/ppm 165.2 (C^{A2}), 159.2 (C^{C1}), 143.5 (C^{A10a}), 138.7 (C^{A4}), 134.4 (t, *J*_{PC} = 8 Hz, C^{D2}), 134.3 (C^{C3}), 133.1 (C^{D1}), 132.8 (C^{C5}), 130.4 (C^{C4}), 129.1 (t, *J*_{PC} = 5 Hz, C^{D3}), 127.7 (C^{A4a}), 127.6 (C^{C2}), 126.3 (C^{A5}), 125.4 (C^{D4}), 122.0 (C^{A3}), 120.4 (C^{C6}), 15.4 (C^{SMe}). ³¹P{¹H} NMR (202 MHz, acetone-*d*₆) δ/ppm –12.8 (POP), –144.2 (septet, *J*_{PF} = 707 Hz, PF₆[–]). ESI-MS positive mode *m/z* 873.09 [Cu(POP)(2,9-(MeS)₂phen)]⁺ (calc. 873.14), 601.07 [Cu(POP)]⁺ (calc. 601.09). HR ESI-MS positive mode *m/z* 873.1335 [Cu(POP)(2,9-(MeS)₂phen)]⁺ (calc. 873.1353). Satisfactory elemental analytical data were not obtained.

4.7.4b [Cu(POP)(3,8-(MeS)₂phen)][PF₆]

The reagents were POP (297 mg, 0.55 mmol), [Cu(MeCN)₄][PF₆] (186 mg, 0.50 mmol) and 3,8-(MeS)₂phen (168 mg, 0.50 mmol). [Cu(POP)(3,8-(MeS)₂phen)][PF₆] was isolated as an orange solid (480 mg, 0.44 mmol, 89%). ¹H NMR (500 MHz, acetone-*d*₆) δ/ppm 8.71 (d, *J* = 2.1 Hz, 2H, H^{A2}), 8.46 (d, *J* = 2.0 Hz, 2H, H^{A4}), 8.11 (s, 2H, H^{A5}), 7.46 (td, *J* = 8.1, 1.6 Hz, 2H, H^{C5}), 7.34 (m, 4H, H^{D4}), 7.27–7.19 (overlapping m, 10H, H^{C6+D3}), 7.17–7.08 (overlapping m, 10H, H^{C4+D2}), 6.83–6.75 (m, 2H, H^{C3}), 2.53 (s, 2H, H^{SMe}). ¹³C{¹H} NMR (126 MHz, acetone-*d*₆) δ/ppm 159.0 (C^{C1}), 148.5 (C^{A2}), 141.1 (C^{A10a}), 139.0 (C^{A3}), 133.1 (C^{A4}), 135.1 (C^{C3}), 134.2 (t, *J*_{PC} = 8.2 Hz, C^{D2}), 133.2 (C^{C5}), 130.0 (C^{A4a}), 131.7 (C^{D1}), 131.1 (C^{D4}), 129.6 (t, *J*_{PC} = 5 Hz, C^{D3}), 128.2 (C^{A5}), 126.3 (C^{C4}), 124.5 (C^{C2}), 121.5 (C^{C6}), 15.1 (C^{SMe}). ³¹P{¹H} NMR (202 MHz, acetone-*d*₆) δ/ppm –10.5 (POP), –144.2 (septet, *J*_{PF} = 707 Hz, PF₆[–]). ESI-MS positive mode *m/z* 873.06 [Cu(POP)(3,8-(MeS)₂phen)]⁺ (calc. 873.14), 601.07 [Cu(POP)]⁺ (calc. 601.09). Found: C 58.70, H 4.06, N 2.85; C₅₀H₄₀CuF₆N₂OP₃S₂ requires C 58.91, H 3.96, N 2.75.

4.7.4.c [Cu(POP)(4,7-(MeS)₂phen)][PF₆]

The reagents were POP (159 mg, 0.30 mmol), [Cu(MeCN)₄][PF₆] (99.7 mg, 0.27 mmol) and 4,7-(MeS)₂phen (90.6 mg, 0.27 mmol). [Cu(POP)(4,7-(MeS)₂phen)][PF₆] was isolated as an orange solid (270 mg, 0.25 mmol, 93%). ¹H NMR (500 MHz, acetone-*d*₆) δ/ppm 8.75 (d, *J* = 5.3 Hz, 2H, H^{A2}), 8.29 (s, 2H, H^{A5}), 7.59 (d, *J* = 5.5 Hz, 2H, H^{A3}), 7.44 (td, *J* = 7.8, 1.2 Hz, 2H, H^{C5}), 7.33 (m, 4H, H^{D4}), 7.20 (overlapping m, 10H, H^{D3+C6}), 7.14–7.08 (overlapping m, 10H, H^{D2+C4}), 6.83–6.77 (m, 2H, H^{C3}), 2.77 (s, 6H, H^{SMe}). ¹³C{¹H} NMR (126 MHz, acetone-*d*₆) δ/ppm 159.4 (t, *J*_{PC} = 6.3 Hz, C^{C1}), 153.0 (C^{A4}), 149.8 (C^{A2}), 143.3 (C^{A10a}), 135.1 (C^{C3}), 134.0 (t, *J*_{PC} = 8 Hz, C^{D2}), 133.1 (C^{C5}), 131.6 (t, *J*_{PC} = 17 Hz, C^{D1}), 130.9 (C^{D4}), 127.6 (C^{A4a}), 119.5 (C^{A3}), 129.6 (t, *J*_{PC} = 5 Hz, C^{D3}), 122.9 (C^{A5}), 126.0 (C^{C4}), 124.7 (C^{C2}), 121.5 (C^{C6}), 14.24 (C^{SMe}). ³¹P{¹H} NMR (202 MHz, acetone-*d*₆) δ/ppm –11.8 (POP), –144.3 (septet, *J*_{PF} = 708 Hz, PF₆[–]). ESI-MS positive mode *m/z* 873.08 [Cu(POP)(4,7-(MeS)₂phen)]⁺ (calc. 873.14), 601.06 [Cu(POP)]⁺ (calc. 601.09). Found: C 58.90, H 4.04, N 2.85; C₅₀H₄₀CuF₆N₂OP₃S₂ requires C 58.91, H 3.96, N 2.75.

4.7.4d [Cu(xantphos)(2,9-(MeS)₂phen)][PF₆]

The reagents were [Cu(MeCN)₄][PF₆] (41 mg, 0.11 mmol), 2,9-(MeS)₂phen (30 mg, 0.11 mmol) and xantphos (64 mg, 0.11 mmol). One additional equivalent of xantphos was added for the crystallisation process to precipitate the desired compound. [Cu(xantphos)(2,9-(MeS)₂phen)][PF₆] was isolated as a yellow solid (85 mg, 0.09 mmol, 86%). ¹H NMR (500 MHz, acetone-*d*₆) δ/ppm 8.49 (d, *J* = 8.6 Hz, 2H, H^{A4}), 7.88 (s, 2H, H^{A5}), 7.79 (dd, *J* = 7.8, 1.4 Hz, 2H, H^{C5}), 7.72 (d, *J* = 8.6 Hz, 2H, H^{A3}), 7.31–7.20 (m, 14H, H^{D2+D4+C4}), 7.11–7.06 (m, 8H, H^{D3}), 7.01–6.95 (m, 2H, H^{C3}), 2.30 (s, 6H, H^{SMe}), 1.75 (s, 6H, H^{Cxantphos-Me}). ¹³C{¹H} NMR (126 MHz, acetone-*d*₆) δ/ppm 164.2 (C^{A2}), 156.5 (C^{C1}), 143.1 (C^{A10a}), 138.5 (C^{A4}), 134.3 (t, *J*_{PC} = 8 Hz, C^{D2}), 134.1 (C^{C6}), 132.7 (C^{D1}), 130.6 (C^{C3}), 130.6 (C^{D4}), 127.3 (C^{A4a}), 129.1 (t, *J*_{PC} = 5 Hz, C^{D3}), 128.1 (C^{C5}), 126.1 (C^{A5}), 125.7 (C^{C4}), 125.6 (C^{C2}), 36.8 (C^{xantphos-bridge}), 28.7 (C^{xantphos-Me}), 15.1 (C^{SMe}). ³¹P{¹H} NMR (202 MHz, acetone-*d*₆) δ/ppm –11.2 (xantphos), –144.3 (septet, *J*_{PF} = 707 Hz, PF₆[–]). ESI-MS positive mode *m/z* 913.10 [Cu(xantphos)(2,9-(MeS)₂phen)]⁺ (calc. 913.17), 641.08 [Cu(xantphos)]⁺ (calc. 641.12). Found: C 60.08, H 4.23, N 2.64; C₅₃H₄₄CuF₆N₂OP₃S₂ requires C 60.08, H 4.19, N 2.64.

4.7.4e [Cu(xantphos)(3,8-(MeS)₂phen)][PF₆]

The reagents were [Cu(MeCN)₄][PF₆] (41 mg, 0.11 mmol), 3,8-(MeS)₂phen (30 mg, 0.11 mmol) and xantphos (63.6 mg, 0.11 mmol). [Cu(xantphos)(3,8-(MeS)₂phen)][PF₆] was isolated as a yellow solid (106 mg, 0.1 mmol, 91%). ¹H NMR (500 MHz, acetone-*d*₆) δ/ppm 8.45 (d, *J* = 2.0 Hz, 2H, H^{A4}), 8.29 (m, 2H, H^{A2}), 8.13 (s, 2H, H^{A5}), 7.92 (dd, *J* = 7.9, 1.1 Hz, 2H, H^{C5}), 7.32–7.28 (overlapping m, 6H, H^{D4+C4}), 7.15–7.12 (m, 8H, H^{D3}), 7.06–7.02 (m, 8H, H^{D2}), 6.63–6.58 (m, 2H, H^{C3}), 2.48 (s, 6H, H^{SMe}), 1.85 (s, 6H, H^{xantphos-Me}). ¹³C{¹H} NMR (126 MHz, acetone-*d*₆) δ/ppm 155.9 (C^{C1}), 148.1 (C^{A2}), 141.1 (C^{A10a}), 139.3 (C^{A3}), 135.1 (C^{C6}), 133.8 (t, *J*_{PC} = 8.0 Hz, C^{D2}), 133.0 (C^{A4}), 132.15 (C^{C3}), 132.1 (t, *J*_{PC} = 17 Hz, C^{D1}), 131.0 (C^{D4}), 130.2 (C^{A4a}), 129.6 (t, *J*_{PC} = 5 Hz, C^{D3}), 128.6 (C^{C5}), 128.3 (C^{A5}), 126.3 (C^{C4}), 120.7 (C^{C2}), 37.1 (C^{xantphos-bridge}), 28.4 (C^{xantphos-Me}), 14.9 (C^{SMe}). ³¹P{¹H} NMR (202 MHz, acetone-*d*₆) δ/ppm –11.3 (xantphos), –144.2 (septet, *J*_{PF} = 707 Hz, PF₆[–]). ESI-MS positive mode *m/z* 913.11 [Cu(xantphos)(3,8-(MeS)₂phen)]⁺ (calc. 913.17), 641.07 [Cu(xantphos)]⁺ (calc. 641.12). Found: C 59.88, H 4.36, N 2.70; C₅₃H₄₄CuF₆N₂OP₃S₂ requires C 60.08, H 4.19, N 2.64.

4.7.4f [Cu(xantphos)(4,7-(MeS)₂phen)][PF₆]

The reagents were [Cu(MeCN)₄][PF₆] (41 mg, 0.11 mmol), 4,7-(MeS)₂phen (30 mg, 0.11 mmol) and xantphos (63.6 mg, 0.11 mmol). [Cu(xantphos)(4,7-(MeS)₂phen)][PF₆] was isolated as a yellow solid (68 mg, 0.06 mmol, 58%). ¹H NMR (500 MHz, acetone-*d*₆) δ/ppm 8.47 (d, *J* = 5.3 Hz, 2H, H^{A2}), 8.30 (s, 2H,

H^{A5}), 7.88 (dd, $J = 7.8, 1.2$ Hz, 2H, H^{C5}), 7.58 (d, $J = 5.3$ Hz, 2H, H^{A3}), 7.31–7.26 (overlapping m, 6H, H^{D4+C4}), 7.14–7.11 (m, 8H, H^{D3}), 7.06–7.01 (m, 8H, H^{D2}), 6.66–6.63 (m, 2H, H^{C3}), 2.76 (s, 6H, H^{SMe}), 1.81 (s, 6H, H^{xantphos-Me}). ¹³C{¹H} NMR (126 MHz, acetone-*d*₆) δ /ppm 155.9 (C^{C1}), 153.2 (C^{A4}), 149.4 (C^{A2}), 143.3 (C^{A10a}), 135.1 (C^{C6}), 133.7 (t, $J_{PC} = 8$ Hz, C^{D2}), 132.6 (t, $J_{PC} = 17$ Hz, C^{D2}), 131.9 (C^{C3}), 130.9 (C^{D4}), 127.7 (C^{A4a}), 129.6 (t, $J_{PC} = 5$ Hz, C^{D3}), 128.6 (C^{C5}), 126.1 (C^{C4}), 123.0 (C^{A5}), 120.9 (C^{C2}), 119.7 (C^{A3}), 36.5 (C^{xantphos-bridge}), 28.5 (C^{xantphos-Me}), 14.2 (C^{SMe}). ³¹P{¹H} NMR (202 MHz, acetone-*d*₆) δ /ppm –13.1 (xantphos), –144.3 (septet, $J_{PF} = 707$ Hz, PF₆[–]). ESI-MS positive mode m/z 913.11 [Cu(xantphos)(4,7-(MeS)₂phen)]⁺ (calc. 913.17), 641.08 [Cu(xantphos)]⁺ (calc. 641.12). Found: C 59.81, H 4.35, N 2.64; C₅₃H₄₄CuF₆N₂OP₃S₂ requires C 60.08, H 4.19, N 2.64.

4.7.4g [Cu(POP)(2,9-(MeO)₂phen)][PF₆]

The reagents were POP (67.3 mg, 0.125 mmol), [Cu(MeCN)₄][PF₆] (46.6 mg, 0.125 mmol) and 2,9-(MeO)₂phen (30 mg, 0.125 mmol). [Cu(POP)(2,9-(MeO)₂phen)][PF₆] was isolated as a yellow solid (98 mg, 0.16 mmol, 79%). ¹H NMR (500 MHz, CD₂Cl₂) δ /ppm 8.46 (d, $J = 8.8$ Hz, 2H, H^{A4}), 7.81 (s, 2H, H^{A5}), 7.26–7.19 (overlapping m, 8H, H^{A3+C5+D4}), 7.17 (d, $J = 8.8$ Hz, 2H, H^{A3}), 7.14–7.06 (m, 16H, H^{D2+D3}), 7.00 (td, $J = 7.5, 1.1$ Hz, 2H, H^{C4}), 6.94–6.90 (m, 2H, H^{C6}), 6.83–6.76 (m, 2H, H^{C3}), 3.58 (s, 6H, H^{OMe}). ¹³C{¹H} NMR (126 MHz, CD₂Cl₂) δ /ppm 163.2 (C^{A2}), 159.0 (C^{C1}), 142.1 (C^{A10a}), 141.7 (C^{A4}), 134.4 (C^{C3}), 133.8 (t, $J_{PC} = 8$ Hz, C^{D2}), 132.6 (C^{D1}), 132.0 (C^{D4}), 130.1 (C^{C5}), 128.8 (t, $J_{PC} = 5$ Hz, C^{D3}), 125.7 (C^{A4a/C2}), 125.0 (C^{A4a/C2}), 124.9 (C^{C4}), 124.3 (C^{A5}), 120.9 (C^{C6}), 109.4 (C^{A3}), 55.9 (C^{OMe}). ³¹P{¹H} NMR (202 MHz, CD₂Cl₂) δ /ppm –11.6 (POP), –144.7 (septet, $J_{PF} = 710$ Hz, PF₆[–]). ESI-MS positive mode m/z 841.14 [Cu(POP)(2,9-(MeO)₂phen)]⁺ (calc. 841.18), 601.06 [Cu(POP)]⁺ (calc. 601.09). HR ESI-MS positive mode m/z 841.1809 [Cu(POP)(2,9-(MeO)₂phen)]⁺ (calc. 841.1805). Satisfactory elemental analytical data were not obtained.

4.7.4h [Cu(POP)(3,8-(MeO)₂phen)][PF₆]

The reagents were POP (87.5 mg, 0.163 mmol), [Cu(MeCN)₄][PF₆] (46.6 mg, 0.163 mmol) and 3,8-(MeO)₂phen (30 mg, 0.125 mmol). [Cu(POP)(3,8-(MeO)₂phen)][PF₆] was isolated as a yellow solid (42 mg, 0.04 mmol, 34%). ¹H NMR (500 MHz, acetone-*d*₆) δ /ppm 8.57 (d, $J = 2.6$ Hz, 2H, H^{A2}), 8.13 (d, $J = 2.7$ Hz, 2H, H^{A4}), 8.11 (s, 2H, H^{A5}), 7.46 (td, $J = 8.1, 1.6$ Hz, 2H, H^{C5}), 7.37–7.31 (m, 4H, H^{D4}), 7.28–7.18 (overlapping m, 10H, H^{C6+D2}), 7.16–7.07 (overlapping m, 10H, H^{C4+D3}), 6.76–6.73 (m, 2H, H^{C3}), 3.94 (s, 2H, H^{OMe}). ¹³C{¹H} NMR (126 MHz, acetone-*d*₆) δ /ppm 159.6 (C^{C1}), 157.0 (C^{A3}), 142.5 (C^{A2}), 138.7 (C^{A10a}), 135.2 (C^{C3}), 134.1 (t, $J_{PC} = 9$ Hz, C^{D2}), 132.8 (C^{C5}), 132.0 (C^{D1}), 131.0 (C^{D4}), 130.0 (C^{A4a}), 129.7 (t, $J_{PC} = 5$ Hz, C^{D3}), 128.4 (C^{A5}), 125.9 (C^{C4}), 124.9 (C^{C2}), 121.3 (C^{C6}), 117.5 (C^{A4}), 56.8 (C^{OMe}). ³¹P{¹H} NMR (202 MHz, acetone-*d*₆) δ /ppm –11.0 (POP), –144.2 (septet, $J_{PF} = 710$ Hz, PF₆[–]). ESI-MS positive mode m/z 841.12 [Cu(POP)(3,8-(MeO)₂phen)]⁺ (calc. 841.18). Found: C 60.52, H 4.64, N 2.64; C₅₀H₄₀CuF₆N₂O₃P₃ requires C 60.83, H 4.08, N 2.84.

4.7.4i [Cu(POP)(4,7-(MeO)₂phen)][PF₆]

The reagents were POP (100 mg, 0.186 mmol), [Cu(MeCN)₄][PF₆] (57.8 mg, 0.155 mmol) and 4,7-(MeO)₂phen (37.2 mg, 0.155 mmol). [Cu(POP)(4,7-(MeO)₂phen)][PF₆] was isolated as an orange solid (87 mg, 0.09 mmol, 57%). ¹H NMR (500 MHz, acetone-*d*₆) δ /ppm 8.81 (d, $J = 5.7$ Hz, 2H, H^{A2}), 8.30 (s, 2H, H^{A5}), 7.44 (t, $J = 7.8, 1.6$ Hz, 2H, H^{C5}), 7.35–7.30 (m, 4H, H^{D4}), 7.29 (d, $J = 5.8$ Hz, 2H, H^{A3}), 7.23–7.18 (overlapping m, 10H, H^{D3+C6}), 7.13–7.07 (overlapping m, 10H, H^{D2+C4}), 6.83–6.74 (m, 2H, H^{C3}), 4.21 (s, 6H, H^{OMe}). ¹³C{¹H} NMR (126 MHz, acetone-*d*₆) δ /ppm 164.2 (C^{A4}), 159.3 (C^{C1}), 151.9 (C^{A2}), 145.1 (C^{A10a}), 135.1 (C^{C3}), 134.1 (t, $J_{PC} = 8$ Hz, C^{D2}), 133.0 (C^{C5}), 132.3 (C^{D1}), 130.9 (C^{D4}), 122.4 (C^{A4a}), 105.6 (C^{A3}), 129.5 (t, $J_{PC} = 5$ Hz, C^{D3}), 120.5 (C^{A5}), 129.4 (C^{C4}), 121.7 (C^{C2}), 133.7 (C^{C6}), 57.4 (C^{OMe}). ³¹P{¹H} NMR (202 MHz, acetone-*d*₆)

δ /ppm -12.0 (POP), -144.3 (septet, $J_{PF} = 710$ Hz, PF_6^-). ESI-MS positive mode m/z 841.16 [Cu(POP) (4,7-(MeO)₂phen)]⁺ (calc. 841.18), 811.13 [Cu(POP)(4-(MeO)phen)]⁺ (calc. 811.17), 601.08 [Cu(POP)]⁺ (calc. 601.09). HR ESI-MS positive mode m/z 841.1809 [Cu(4,7-(POP)(MeO)₂phen)]⁺ (calc. 841.1805). Satisfactory elemental analytical data were not obtained.

4.7.4j [Cu(xantphos)(2,9-(MeO)₂phen)][PF₆]

The reagents were [Cu(MeCN)₄][PF₆] (mg, 0.18 mmol), 2,9-(MeO)₂phen (60 mg, 0.18 mmol) and xantphos (113 mg, 0.20 mmol). [Cu(xantphos)(2,9-(MeO)₂phen)][PF₆] was isolated as a yellow solid (102 mg, 0.10 mmol, 79%). ¹H NMR (500 MHz, CD₂Cl₂) δ /ppm 8.46 (d, $J = 8.8$ Hz, 2H, H^{A4}), 7.80 (s, 2H, H^{A5}), 7.70 (dd, $J = 7.8, 1.5$ Hz, 2H, H^{C5}), 7.26–7.22 (overlapping m, 6H, H^{A3+D4}), 7.19 (t, $J = 7.6$ Hz, 2H, H^{C4}), 7.07–7.03 (overlapping m, 16H, H^{D2+D3}), 6.74–6.69 (m, 2H, H^{C3}), 3.51 (s, 6H, H^{OMe}), 1.75 (s, 6H, H^{xantphos-Me}). ¹³C{¹H} NMR (126 MHz, CD₂Cl₂) δ /ppm 163.2 (C^{A2}), 156.4 (C^{C1}), 142.0 (C^{A10a}), 141.7 (C^{A4}), 134.1 (C^{C6}), 133.5 (t, $J_{PC} = 8$ Hz, C^{D2}), 132.8 (C^{D1}), 131.3 (C^{C3}), 130.1 (C^{D4}), 128.8 (t, $J_{PC} = 5$ Hz, C^{D3}), 127.7 (C^{C5}), 125.9 (C^{A4a}), 125.1 (C^{C4}), 124.4 (C^{A5}), 122.0 (C^{C2}), 56.1 (C^{OMe}), 36.6 (C^{xantphos-bridge}), 28.5 (C^{xantphos-Me}). ³¹P{¹H} NMR (202 MHz, CD₂Cl₂) δ /ppm -12.1 (xantphos), -144.5 (septet, $J_{PF} = 710$ Hz, PF_6^-). ESI-MS positive mode m/z 881.16 [Cu(xantphos)(2,9-(MeO)₂phen)]⁺ (calc. 881.21), 641.08 [Cu(xantphos)]⁺ (calc. 641.12). Found: C 61.11, H 4.59, N 2.62; C₅₂H₄₄CuF₆N₂O₃P₃ requires C 61.96, H 4.32, N 2.73.

4.7.4k [Cu(POP)(2,9-(EtS)₂phen)][PF₆]

The reagents were POP (47.4 mg, 0.88 mmol), [Cu(MeCN)₄][PF₆] (29.8 mg, 0.80 mmol), 2,9-(EtS)₂phen (24 mg, 0.80 mmol). [Cu(POP)(2,9-(EtS)₂phen)][PF₆] was isolated as a yellow solid (67.3 mg, 0.64 mmol, 80%). ¹H NMR (500 MHz, acetone-*d*₆) δ /ppm 8.53 (d, $J = 8.7$ Hz, 2H, H^{A4}), 7.93 (s, 2H, H^{A5}), 7.79 (d, $J = 8.7$ Hz, 2H, H^{A3}), 7.44–7.39 (m, 2H, H^{C5}), 7.28–7.17 (m, 16H, H^{C4,C6,D2,D4}), 7.12 (t, $J = 7.3$ Hz, 8H, H^{D3}), 7.05–7.01 (m, 2H, H^{C3}), 2.95 (q, $J = 7.4$ Hz, 4H, H^{Et-CH₂}), 1.03 (t, $J = 7.4$ Hz, 6H, H^{Et-CH₃}). ¹³C{¹H} NMR (126 MHz, acetone-*d*₆) δ /ppm 164.8 (C^{A2}), 160.6 (C^{C1}), 143.5 (C^{A10b}), 138.6 (C^{A4}), 134.4 (t, $J_{PC} = 7.7$ Hz, C^{D2}), 134.3 (C^{D1}), 132.77 (C^{C5}), 130.4 (C^{D4}), 129.0 (t, $J_{PC} = 4.6$ Hz, C^{D3}), 127.5 (C^{C2}), 127.1 (C^{A5}), 126.2 (C^{C4}), 125.6 (C^{C6}), 122.3 (C^{A3}), 120.7 (C^{C3}), 26.9 (C^{Et-CH₂}), 13.5 (C^{Et-CH₃}). ³¹P{¹H} NMR (202 MHz, acetone-*d*₆) δ /ppm -12.6 (POP), -144.3 (septet, $J_{PF} = 707$ Hz, PF_6^-). ESI-MS positive mode m/z 901.10 [Cu(POP) (2,9-(EtS)₂phen)]⁺ (calc. 901.16), 601.03 [Cu(POP)]⁺ (calc. 601.09). Found: C 59.20, H 4.15, N 2.90; C₅₂H₄₄CuF₆N₂O₃P₃S₂ requires C 59.62, H 4.23, N 2.67.

4.7.4l [Cu(POP)(3,8-(EtS)₂phen)][PF₆]

The reagents were POP (68.1 mg, 0.13 mmol), [Cu(MeCN)₄][PF₆] (42.9 mg, 0.12 mmol), 3,8-(EtS)₂phen (34.6 mg, 0.12 mmol). [Cu(POP)(3,8-(EtS)₂phen)][PF₆] was isolated as an orange solid (116 mg, 0.11 mmol, 96%). ¹H NMR (500 MHz, acetone-*d*₆) δ /ppm 8.75 (dt, $J = 1.9, 0.9$ Hz, 2H, H^{A2}), 8.55 (d, $J = 2.1$ Hz, 2H, H^{A4}), 8.12 (s, 2H, H^{A5}), 7.49–7.43 (m, 2H, H^{C5}), 7.37–7.32 (m, 4H, H^{D4}), 7.26–7.19 (m, 10H, H^{C6+D3}), 7.16–7.09 (m, 10H, H^{C4+D2}), 6.83–6.78 (m, 2H, H^{C3}), 2.99 (q, $J = 7.4$ Hz, 4H, H^{Et-CH₂}), 1.23 (t, $J = 7.3$ Hz, 6H, H^{Et-CH₃}). ¹³C{¹H} NMR (126 MHz, acetone-*d*₆) δ /ppm 159.2 (C^{C1}), 149.9 (C^{A2}), 141.5 (C^{A10b}), 137.4 (C^{A3}), 135.4 (C^{A4a}), 135.1 (C^{A4}), 134.1 (t, $J_{PC} = 8.2$ Hz, C^{D2}), 133.3 (C^{C5}), 131.7 (t, $J_{PC} = 17.2$ Hz, C^{D1}), 131.1 (C^{D4}), 129.6 (t, $J_{PC} = 4.9$ Hz, C^{D3}), 128.2 (C^{A5}), 126.2 (C^{C4}), 121.5 (C^{C6}), 27.4 (C^{Et-CH₂}), 14.3 (C^{Et-CH₃}). ³¹P{¹H} NMR (202 MHz, acetone-*d*₆) δ /ppm -10.3 (POP), -144.2 (septet, $J_{PF} = 707$ Hz, PF_6^-). ESI-MS positive mode m/z 901.05 [Cu(POP)(3,8-(EtS)₂phen)]⁺ (base peak, calc. 901.16), 601.05 [Cu(POP)]⁺ (calc. 601.09). HR ESI-MS positive mode m/z 901.1661 [Cu(POP)(3,8-(EtS)₂phen)]⁺ (calc. 901.1666). Satisfactory elemental analytical data were not obtained.

4.7.4.m [Cu(POP)(4,7-(EtS)₂phen)][PF₆]

The reagents were POP (68.1 mg, 0.13 mmol), [Cu(MeCN)₄][PF₆] (42.9 mg, 0.12 mmol), 4,7-(EtS)₂phen (34.6 mg, 0.12 mmol). [Cu(POP)(4,7-(EtS)₂phen)][PF₆] was isolated as an orange solid (71.1 mg, 0.68 mmol, 59%). ¹H NMR (500 MHz, acetone-*d*₆) δ/ppm 8.73 (d, *J* = 5.3 Hz, 2H, H^{A2}), 8.29 (s, 2H, H^{A5}), 7.64 (d, *J* = 5.4 Hz, 2H, H^{A3}), 7.46–7.42 (m, 2H, H^{C5}), 7.32 (t, *J* = 7.4 Hz, 4H, H^{D4}), 7.22–7.18 (m, 10H, H^{D3+C6}), 7.14–7.08 (m, 10H, H^{D2+C4}), 6.83–6.78 (m, 2H, H^{C3}), 3.33 (q, *J* = 7.4 Hz, 4H, H^{Et-CH₂}), 1.47 (t, *J* = 7.3 Hz, 6H, H^{Et-CH₃}). ¹³C{¹H} NMR (126 MHz, acetone-*d*₆) δ/ppm 159.4 (C^{C1}), 151.8 (C^{A4}), 149.7 (C^{A2}), 143.6 (C^{A10b}), 135.1 (C^{C3}), 134.0 (t, *J*_{PC} = 8.2 Hz, C^{D2}), 133.1 (C^{C5}), 132.2 (C^{D1}), 130.9 (C^{D4}), 129.6 (t, *J*_{PC} = 4.7 Hz, C^{D3}), 127.8 (C^{A4a}), 126.1 (C^{C4}), 125.0 (C^{C2}), 123.0 (C^{A5}), 121.5 (C^{C6}), 120.1 (C^{A3}), 25.9 (C^{Et-CH₂}), 13.5 (C^{Et-CH₃}). ³¹P{¹H} NMR (202 MHz, acetone-*d*₆) δ/ppm –11.4 (POP), –144.2 (septet, *J*_{PF} = 707 Hz, PF₆[–]). ESI-MS positive mode *m/z* 901.08 [Cu(POP)(4,7-(EtS)₂phen)]⁺ (calc. 901.16). Found: C 60.19, H 4.95, N 2.29; C₅₂H₄₄CuF₆N₂OP₃S₂ requires C 59.62, H 4.23, N 2.67.

4.7.4.n [Cu(xantphos)(2,9-(EtS)₂phen)][PF₆]

The reagents were xantphos (49 mg, 0.85 mmol), [Cu(MeCN)₄][PF₆] (28.7 mg, 0.08 mmol), 2,9-(EtS)₂phen (23.1 mg, 0.08 mmol). [Cu(xantphos)(2,9-(EtS)₂phen)][PF₆] was isolated as a yellow solid (78 mg, 0.07 mmol, 93%). ¹H NMR (500 MHz, acetone-*d*₆) δ/ppm 8.45 (d, *J* = 8.7 Hz, 2H, H^{A4}), 7.85 (s, 2H, H^{A5}), 7.79 (dd, *J* = 7.8, 1.4 Hz, 2H, H^{C5}), 7.73 (d, *J* = 8.7 Hz, 2H, H^{A3}), 7.32–7.23 (m, 14H, H^{C4,D2,D4}), 7.12–7.07 (m, 8H, H^{D3}), 7.06–7.01 (m, 2H, H^{C3}), 2.88 (q, *J* = 7.4 Hz, 4H, H^{Et-CH}), 1.74 (s, 6H, H^{xantphos-Me}), 0.95 (t, *J* = 7.4 Hz, 6H, H^{Et-CH₃}). ¹³C{¹H} NMR (126 MHz, acetone-*d*₆) δ/ppm 163.5 (C^{A10b}), 156.6 (C^{C1}), 143.3 (C^{A2}), 138.4 (C^{A4}), 134.9 (C^{C6}), 134.4 (t, *J*_{PC} = 7.7 Hz, C^{D2}), 133.0 (C^{D1}), 130.9 (C^{C3}), 130.6 (C^{D4}), 129.1 (t, *J*_{PC} = 4.5 Hz, C^{D3}), 128.0 (C^{C5}), 127.5 (C^{A4a}), 126.0 (C^{A5}), 125.7 (C^{C4}), 124.0 (C^{C2}), 121.7 (C^{A3}), 36.8 (C^{xantphos-bridge}), 28.7 (C^{xantphos-Me}), 26.6 (C^{Et-CH₂}), 13.7 (C^{Et-CH₃}). ³¹P{¹H} NMR (202 MHz, acetone-*d*₆) δ/ppm –11.8 (xantphos), –144.2 (septet, *J*_{PF} = 707 Hz, PF₆[–]). ESI-MS positive mode *m/z* 941.13 [Cu(xantphos)(2,9-(EtS)₂phen)]⁺ (calc. 941.20), 641.08 [Cu(xantphos)]⁺ (calc. 641.12). Found: C 60.15, H 4.45, N 2.58; C₅₅H₄₈CuF₆N₂OP₃S₂ requires C 60.74, H 5.37, N 2.58.

4.7.4.o [Cu(xantphos)(3,8-(EtS)₂phen)][PF₆]

The reagents were xantphos (70.7 mg, 0.12 mmol), [Cu(MeCN)₄][PF₆] (41.4 mg, 0.11 mmol), 3,8-(EtS)₂phen (33.3 mg, 0.11 mmol). [Cu(xantphos)(3,8-(EtS)₂phen)][PF₆] was isolated as an orange solid (103 mg, 0.09 mmol, 86%). ¹H NMR (500 MHz, acetone-*d*₆) δ/ppm 8.55 (d, *J* = 2.1 Hz, 2H, H^{A4}), 8.35 (d, *J* = 2.1 Hz, 2H, H^{A2}), 8.13 (s, 2H, H^{A5}), 7.93 (dd, *J* = 7.8, 1.4 Hz, 2H, H^{C5}), 7.34–7.27 (m, 6H, H^{C4,D4}), 7.14 (t, *J* = 7.5 Hz, 8H, H^{D3}), 7.09–7.01 (m, 8H, H^{D2}), 6.66–6.62 (m, 2H, H^{C3}), 2.94 (q, *J* = 7.3 Hz, 4H, H^{Et-CH₂}), 1.85 (s, 6H, H^{xantphos-Me}), 1.18 (t, *J* = 7.3 Hz, 6H, H^{Et-CH₃}). ¹³C{¹H} NMR (126 MHz, acetone-*d*₆) δ/ppm 155.9 (C^{C1}), 149.6 (C^{A2}), 141.6 (C^{A10b}), 137.6 (C^{A3}), 136.1 (C^{A4a}), 135.6 (C^{A4}), 135.1 (C^{C6}), 133.8 (t, *J*_{PC} = 8.1 Hz, C^{D2}), 132.26 (C^{C3}), 132.1 (t, *J*_{PC} = 17.5 Hz, C^{D1}), 131.0 (C^{D4}), 129.6 (t, *J*_{PC} = 4.8 Hz, C^{D3}), 128.7 (C^{C5}), 128.4 (C^{A5}), 126.3 (t, C^{C4}), 120.6 (C^{C2}), 37.1 (C^{xantphos-bridge}), 28.5 (C^{xantphos-Me}), 27.3 (C^{Et-CH₂}), 14.1 (C^{Et-CH₃}). ³¹P{¹H} NMR (202 MHz, acetone-*d*₆) δ/ppm –11.4 (xantphos), –144.3 (septet, *J*_{PF} = 707 Hz, PF₆[–]). ESI-MS positive mode *m/z* 941.07 [Cu(xantphos)(3,8-(EtS)₂phen)]⁺ (base peak, calc. 941.20), 641.12 [Cu(xantphos)]⁺ (calc. 641.12). Found: C 60.74, H 5.04, N 2.79; C₅₅H₄₈CuF₆N₂OP₃S₂ requires C 60.74, H 5.37, N 2.58.

4.7.4.p [Cu(xantphos)(4,7-(EtS)₂phen)][PF₆]

The reagents were xantphos (70.7 mg, 0.12 mmol), [Cu(MeCN)₄][PF₆] (41.4 mg, 0.11 mmol), 4,7-(EtS)₂phen (33.3 mg, 0.11 mmol). [Cu(xantphos)(4,7-(EtS)₂phen)][PF₆] was isolated as an orange solid (93.5 mg,

0.09 mmol, 78%). ^1H NMR (500 MHz, acetone- d_6) δ /ppm 8.46 (d, $J = 5.3$ Hz, 2H, $\text{H}^{\text{A}2}$), 8.29 (s, 2H, $\text{H}^{\text{A}5}$), 7.88 (dd, $J = 7.8, 1.4$ Hz, 2H, $\text{H}^{\text{C}5}$), 7.63 (d, $J = 5.3$ Hz, 2H, $\text{H}^{\text{A}3}$), 7.31–7.26 (m, 6H, $\text{H}^{\text{C}4+\text{D}4}$), 7.15–7.10 (m, 8H, $\text{H}^{\text{D}3}$), 7.07–7.01 (m, 8H, $\text{H}^{\text{D}2}$), 6.69–6.67 (m, 2H, $\text{H}^{\text{C}3}$), 3.31 (q, $J = 7.4$ Hz, 4H, $\text{H}^{\text{Et-CH}_2}$), 1.80 (s, 6H, $\text{H}^{\text{xantphos-Me}}$), 1.46 (t, $J = 7.4$ Hz, 6H, $\text{H}^{\text{Et-CH}_3}$). $^{13}\text{C}\{^1\text{H}\}$ NMR (126 MHz, acetone- d_6) δ /ppm 155.9 ($\text{C}^{\text{C}1}$), 152.2 ($\text{C}^{\text{A}4}$), 149.3 ($\text{C}^{\text{A}2}$), 143.5 ($\text{C}^{\text{A}10\text{b}}$), 135.1 ($\text{C}^{\text{C}6}$), 133.7 (t, $J_{\text{PC}} = 8.0$ Hz, $\text{C}^{\text{D}2}$), 132.0 ($\text{C}^{\text{C}3}$), 130.9 ($\text{C}^{\text{D}4}$), 129.6 (t, $J_{\text{PC}} = 4.8$ Hz, $\text{C}^{\text{D}3}$), 128.6 ($\text{C}^{\text{C}5}$), 127.9 ($\text{C}^{\text{A}4\text{a}}$), 126.1 ($\text{C}^{\text{C}4}$), 123.1 ($\text{C}^{\text{A}5}$), 120.8 (m, $\text{C}^{\text{C}2}$), 119.9 ($\text{C}^{\text{A}3}$), 37.0 ($\text{C}^{\text{xantphos-bridge}}$), 28.5 ($\text{C}^{\text{xantphos-Me}}$), 25.9 ($\text{C}^{\text{Et-CH}_2}$), 13.4 ($\text{C}^{\text{Et-CH}_3}$). $^{31}\text{P}\{^1\text{H}\}$ NMR (202 MHz, acetone- d_6) δ /ppm –13.1(xantphos), –144.2 (septet, $J_{\text{PF}} = 707$ Hz, PF_6^-). ESI-MS positive mode m/z 941.10 $[\text{Cu}(\text{xantphos})(4,7\text{-}(\text{EtS})_2\text{phen})]^+$ (calc. 941.20). HR ESI-MS positive mode m/z 941.1974 $[\text{Cu}(\text{xantphos})(4,7\text{-}(\text{EtS})_2\text{phen})]^+$ (calc. 941.1979). Satisfactory elemental analytical were could not be obtained.

Conclusion and Outlook

In this work, the syntheses and characterisation of heteroleptic Cu(I) complexes with the general formula $[\text{Cu}(\text{P}^{\wedge}\text{P})(\text{N}^{\wedge}\text{S})][\text{PF}_6]$, where $\text{N}^{\wedge}\text{S}$ is either a 2-(alkylsulfanyl)pyridine or a 2-(thiophen-2-yl)pyridine, or $[\text{Cu}(\text{P}^{\wedge}\text{P})(\text{N}^{\wedge}\text{N})][\text{PF}_6]$, where $\text{N}^{\wedge}\text{N}$ is a phen with a heteroatom substituent have been presented. In both cases, $\text{P}^{\wedge}\text{P}$ describes the two diphosphanes POP and xantphos.

In Chapter 2 the focus lay on the $\text{N}^{\wedge}\text{S}$ ligands. The complexes carrying 2-(alkylsulfanyl)pyridine ligands did not feature any significant photoluminescence. They did, however, exhibit interesting solution dynamic behaviour at room temperature which was investigated using ^1H NMR spectroscopy. To investigate this, experiments at 248 K, 238 K and 198 K were carried out. It was shown that the stereogenic centre at the coordinated sulfur still undergoes fast inversion at 198 K, while the inversion of the xanthene bowl and the motion of the POP backbone are frozen out and this leads to two sets of signals at low temperatures. In contrast to the 2-(alkylsulfanyl)pyridine carrying complexes, those employing a 2-(thiophen-2-yl)pyridine exhibited interesting photophysical behaviour. In the solid state, they featured moderate PLQYs of up to 10.8% for $[\text{Cu}(\text{xantphos})(\text{ThPy})][\text{PF}_6]$. Contrary to what would be expected, these complexes feature blue-shifted emissions and, in some cases, also higher PLQYs in argon-purged CH_2Cl_2 solution in comparison to solid-state. Furthermore, these complexes exhibit two distinct emission bands. Based on the emission maxima of the free $\text{N}^{\wedge}\text{S}$ ligands, and the excitation spectra of the complexes, it is likely that there is significant ligand character in the emission of the complexes in solution. The $\text{N}^{\wedge}\text{S}$ binding mode of the ligands was confirmed with crystal structures of the complexes. However, the stability of these complexes is always a key issue since competitive complexation reactions can easily take place. It was shown that in the presence of a coordinating solvent, such as MeCN, the $\text{N}^{\wedge}\text{S}$ ligand is removed and crystals of $[\text{Cu}(\text{xantphos})(\text{MeCN})_2][\text{PF}_6]$ could be isolated. Additional experiments included the addition of increasing amounts of $[\text{nBu}_4\text{N}]\text{Cl}$, leading to a significant change in the UV-Vis absorption spectrum in CH_2Cl_2 and shifts in the ^1H NMR spectrum for several proton signals of $[\text{Cu}(\text{POP})(\text{MeThPy})][\text{PF}_6]$. Using a Job's plot, the 1:1 ratio of complex to Cl^- ion was determined and analysing the methyl resonance yielded a K_d value of 0.14 ± 0.03 mM, which suggests the formation of an ion pair rather than the coordination of the chloride ion. The use of $[\text{Cu}(\text{xantphos})(\text{ThPy})][\text{PF}_6]$ as the electrolumiphore in a LEC did not lead to electroluminescence even under a high bias of 18 V; this was possibly due to poor charge transport characteristics in a device configuration.

In Chapter 3, $[\text{Cu}(\text{P}^{\wedge}\text{P})(\text{N}^{\wedge}\text{N})][\text{PF}_6]$ complexes with isomeric Br_2phen ligands as electron donating ligands were investigated. They feature an absorption band in the visible region between 415 and 420 nm, assigned to an MLCT transition. Although the complexes are non-emissive in deaerated CH_2Cl_2 solution, they are luminescent in the solid state. The two complexes $[\text{Cu}(\text{POP})(2,9\text{-Br}_2\text{phen})][\text{PF}_6]$ and $[\text{Cu}(\text{xantphos})(2,9\text{-Br}_2\text{phen})][\text{PF}_6]$ are noteworthy, with a blue-shifted emission, higher PLQY up to 45% and longer excited state lifetimes than their 3,8- Br_2phen and 4,7- Br_2phen counterparts. Furthermore, these two complexes also feature the highest oxidation potential for $\text{Cu}^+ \rightarrow \text{Cu}^{2+}$ in cyclic voltammetry measurements. All these findings can be attributed to the bromo substituents in the 2,9-positions hindering the flattening of the pseudo-tetrahedral Cu(I) coordination sphere upon excitation. However, when compared to $[\text{Cu}(\text{POP})(2,9\text{-Me}_2\text{phen})][\text{BARF}]$ and $[\text{Cu}(\text{xantphos})(2,9\text{-Me}_2\text{phen})][\text{BARF}]$, the 2,9- Br_2phen carrying complexes have not as favourable properties. Because the methyl substituent generally seems to lead to higher energy $\lambda_{\text{em}}^{\text{max}}$, higher PLQY and longer excited state lifetimes, at least in pure N_2

atmosphere, coupled with the findings for $[\text{Cu}(\text{P}^\wedge\text{P})(6,6'\text{-Br}_2\text{bpy})][\text{PF}_6]$ by Keller et al., the $[\text{Cu}(\text{P}^\wedge\text{P})(\text{Br}_2\text{phen})][\text{PF}_6]$ complexes were not investigated in LEC devices.

In Chapter 4, the effect of introducing methylsulfanyl, ethylsulfanyl and methoxy substituents into the phen backbone was explored. The lowest energy absorption band for the $[\text{Cu}(\text{P}^\wedge\text{P})(\text{RX})_2\text{phen}][\text{PF}_6]$ complexes, which generally has an ϵ_{max} value of $< 6000 \text{ M}^{-1} \text{ cm}^{-1}$ in $[\text{Cu}(\text{P}^\wedge\text{P})(\text{N}^\wedge\text{N})][\text{PF}_6]$, was measured to be remarkably strong, especially in case of the complexes coordinating 4,7-substituted phens. Such an intense absorption suggests a mixed nature of the absorption band. Furthermore, the complexes feature an intense absorption in the region between 300 and 400 nm, highlighting further that chalcogens give a useful tool to tune the electronic structure of the diimine ligands. In argon-purged CH_2Cl_2 solution, the complexes are weak yellow or orange emitters and only the compounds employing a 2,9- X_2phen featured PLQYs $< 5\%$, whereby the $[\text{Cu}(\text{P}^\wedge\text{P})(2,9\text{-(EtS)}_2\text{phen})][\text{PF}_6]$ featured the highest PLQY and excited state lifetime. When measured in deaerated THF solution a blue-shift for all complexes but $[\text{Cu}(\text{POP})(2,9\text{-(MeO)}_2\text{phen})][\text{PF}_6]$ and $[\text{Cu}(\text{xantphos})(2,9\text{-(MeO)}_2\text{phen})][\text{PF}_6]$ was observed, which supports the mixed nature of the absorption band around 400 nm. The relatively high PLQY in deaerated CH_2Cl_2 solution and small Stokes shift for the 2,9-alkylsulfanylphen carrying complexes, and particularly for $[\text{Cu}(\text{POP})(2,9\text{-(MeS)}_2\text{phen})][\text{PF}_6]$, may indicate an interaction between the copper centre and the sulfur, in addition to the effect that the bulkier S, compared to O, may have on the relaxation of the Cu(I) coordination sphere upon photoexcitation. Although the crystal structure of $[\text{Cu}(\text{POP})(2,9\text{-(MeS)}_2\text{phen})][\text{PF}_6]$ could not be obtained, the Cu...O distance in $[\text{Cu}(\text{POP})(2,9\text{-(MeO)}_2\text{phen})][\text{PF}_6]$ and the Cu...S in $[\text{Cu}(\text{POP})(2,9\text{-(EtS)}_2\text{phen})][\text{PF}_6]$ distance are both shorter than the sum of van der Waals radii postulated by Batsanov,²²⁰ and would support the occurrence of such an interaction. In the solid-state, the complexes are yellow to orange emitters with a PLQY of up to 60% and excited state lifetimes between 2–19 μs . The highest PLQYs were measured for $[\text{Cu}(\text{P}^\wedge\text{P})(2,9\text{-(EtS)}_2\text{phen})][\text{PF}_6]$ which is consistent with the higher steric demand of the substituents and consequently better stabilisation of the Cu(I) geometry. Contrary to what would be expected for TADF emitters, most of the complexes exhibit a blue-shifted emission in 2-Me-THF at 77 K. The only complexes that do not shift significantly are $[\text{Cu}(\text{POP})(2,9\text{-(MeS)}_2\text{phen})][\text{PF}_6]$ and $[\text{Cu}(\text{xantphos})(2,9\text{-(MeO)}_2\text{phen})][\text{PF}_6]$ while for $[\text{Cu}(\text{POP})(2,9\text{-(MeO)}_2\text{phen})][\text{PF}_6]$ a red shift of about 20 nm is observed. Coincidentally, these three complexes are also the only ones with a single emission maximum at 77 K, while all others feature two distinct emission maxima. The gathered data for the three mentioned complexes indicate that the emission of those complexes originates from a $^1\text{MLCT}$ state.

One of the main problems of LECs is the device stability and the chemical stability of the emitting species.^{117,190} For $[\text{Cu}(\text{P}^\wedge\text{P})(\text{N}^\wedge\text{N})]^+$ complexes the additional issue of the dominant yellow to orange emission arises. While the latter issue was not solved by the complexes in this work, the complexes carrying an alkylsulfanylphen may give an indication how to address the former. If there is indeed an interaction between the S and the Cu centre, then it seems likely, that this interaction would not only hinder the flattening of the complex geometry upon excitation, but also might stabilise the complex structure as a whole and limit or prevent ligand dissociation. In that case, $[\text{Cu}(\text{P}^\wedge\text{P})(2,9\text{-(alkylsulfanyl)phen})]^+$ complexes may play an important role, at least as a steppingstone, for the development of a generation of complexes with increased stability and moderately high PLQY. On the other hand, since high PLQY values do not necessarily correlate to bright electroluminescence,^{161,164} a

definitive statement about the suitability of the $[\text{Cu}(\text{P}^{\wedge}\text{P})(2,9\text{-alkylsulfanylphen})]^+$ complexes cannot be made before testing them in LEC devices.

Bibliography

1. SAINT-8.34A-2013, *Software for the Integration of CCD Detector System Bruker Analytical X-ray Systems*, Bruker axs, Madison, WI, 2013.
2. *Software for the Integration of CCD Detector System Bruker Analytical X-ray Systems*, Bruker axs, Madison, WI, 2013.
3. L. Palatinus and G. Chapuis, *J. Appl. Crystallogr.*, 2007, **40**, 786–790.
4. P. W. Betteridge, J. R. Carruthers, R. I. Cooper, K. Prout, and D. J. Watkin, *J. Appl. Crystallogr.*, 2003, **36**, 1487–1487.
5. O. V. Dolomanov, L. J. Bourhis, R. J. Gildea, J. A. K. Howard, and H. Puschmann, *J. Appl. Crystallogr.*, 2009, **42**, 339–341.
6. G. M. Sheldrick, *Acta Crystallogr. A Found. Adv.*, 2015, **71**, 3–8.
7. G. M. Sheldrick, *Acta Crystallogr. C Struct. Chem.*, 2015, **71**, 3–8.
8. C. F. Macrae, P. R. Edgington, P. McCabe, E. Pidcock, G. P. Shields, R. Taylor, M. Towler, and J. van de Streek, *J. Appl. Crystallogr.*, 2006, **39**, 453–457.
9. C. F. Macrae, I. J. Bruno, J. A. Chisholm, P. R. Edgington, P. McCabe, E. Pidcock, L. Rodriguez-Monge, R. Taylor, J. van de Streek, and P. A. Wood, *J. Appl. Crystallogr.*, 2008, **41**, 466–470.
10. C. F. Macrae, I. Sovago, S. J. Cottrell, P. T. A. Galek, P. McCabe, E. Pidcock, M. Platings, G. P. Shields, J. S. Stevens, M. Towler, and P. A. Wood, *J. Appl. Crystallogr.*, 2020, **53**, 226–235.
11. A. L. Spek, *Acta Crystallogr. C Struct. Chem.*, 2015, **71**, 9–18.
12. *Spartan 16*, Wavefunction, Inc, Irvine, CA, USA, 2017.
13. G. J. Kubas, B. Monzyk, and A. L. Crumblis, in *Inorganic syntheses: reagents for transition metal complex and organometallic syntheses*, ed. R. J. Angelici, John Wiley & Sons, Inc., Hoboken, NJ, USA, 1990, pp. 68–70.
14. M. S. Shur and R. Zukauskas, *Proc. IEEE.*, 2005, **93**, 1691–1703.
15. US Department of Energy, Arc Lamp , <https://www.energy.gov/articles/history-light-bulb>, (accessed March 3, 2021).
16. C. J. Humphreys, *MRS Bull.*, 2008, **33**, 459–470.
17. A. Kemmler and T. Spillmann, *Analyse des schweizerischen Energieverbrauchs 2000–2019 nach Verwendungszwecken*, Im Auftrag des Bundesamtes für Energie, Bern, 2020.
18. T. Abergel, Lighting – Analysis - IEA, <https://www.iea.org/reports/lighting>, (accessed June 2, 2021).
19. 2018 Global Status Report (English and other languages) – Analysis - IEA, <https://www.iea.org/reports/2018-global-status-report>, (accessed June 2, 2021).

20. Electricity Information 2019 – Analysis - IEA, <https://www.iea.org/reports/electricity-information-overview>, (accessed June 14, 2021).
21. M. Joos and I. Staffell, *Renew. Sustain. Energy Rev.*, 2018, **86**, 45–65.
22. L. Bird, D. Lew, M. Milligan, E. M. Carlini, A. Estanqueiro, D. Flynn, E. Gomez-Lazaro, H. Holttinen, N. Menemenlis, A. Orths, P. B. Eriksen, J. C. Smith, L. Soder, P. Sorensen, A. Altiparmakis, Y. Yasuda, and J. Miller, *Renew. Sustain. Energy Rev.*, 2016, **65**, 577–586.
23. H. J. Round, *Electr. World*, 1907, **49**, 309.
24. N. Zheludev, *Nat. Photonics.*, 2007, **1**, 189–192.
25. N. Holonyak and S. F. Bevacqua, *Appl. Phys. Lett.*, 1962, **1**, 82–83.
26. I. L. Azevedo, M. G. Morgan, and F. Morgan, *Proc. IEEE.*, 2009, **97**, 481–510.
27. G. B. Nair and S. J. Dhoble, *Luminescence*, 2015, **30**, 1167–1175.
28. P. Xiao, T. Dong, J. Xie, D. Luo, J. Yuan, and B. Liu, *Appl. Sci.*, 2018, **8**, 299.
29. M. Pope, H. P. Kallmann, and P. Magnante, *J. Chem. Phys.*, 1963, **38**, 2042–2043.
30. C. W. Tang and S. A. VanSlyke, *Appl. Phys. Lett.*, 1987, **51**, 913–915.
31. M. Kodan, *OLED displays and lighting*, John Wiley & Sons, Ltd, Chichester, UK, 2016.
32. J. Kido, K. Hongawa, K. Okuyama, and K. Nagai, *Appl. Phys. Lett.*, 1994, **64**, 815–817.
33. S. Reineke, F. Lindner, G. Schwartz, N. Seidler, K. Walzer, B. Lüssem, and K. Leo, *Nature*, 2009, **459**, 234–238.
34. R. D. Costa, E. Ortí, H. J. Bolink, F. Monti, G. Accorsi, and N. Armadori, *Angew. Chem. Int. Ed.*, 2012, **51**, 8178–8211.
35. C. E. Housecroft and A. G. Sharpe, in *Inorganic Chemistry*, Pearson, Harlow, England, 5th edn., 2018, pp. 687–737.
36. R. Pellow and M. Vala, *J. Chem. Phys.*, 1989, **90**, 5612–5621.
37. S. Franzen, *The Spin-orbit coupling Hamiltonian*, 2020.
38. S. Koseki, N. Matsunaga, T. Asada, M. W. Schmidt, and M. S. Gordon, *J. Phys. Chem. A*, 2019, **123**, 2325–2339.
39. P.-T. Chou and Y. Chi, *Chem. Eur. J.*, 2007, **13**, 380–395.
40. H. Xu, R. Chen, Q. Sun, W. Lai, Q. Su, W. Huang, and X. Liu, *Chem. Soc. Rev.*, 2014, **43**, 3259–3302.
41. G. Méhes, A. S. D. Sandanayaka, J.-C. Ribierre, and K. Goushi, in *Handbook of Organic Light-Emitting Diodes*, eds. C. Adachi, R. Hattori, H. Kaji, and T. Tsujimura, Springer Japan, Tokyo, 2020, pp. 1–73.

42. M. A. Baldo, D. F. O'Brien, Y. You, A. Shoustikov, S. Sibley, M. E. Thompson, and S. R. Forrest, *Nature*, 1998, **395**, 151–154.
43. C. W. Tang, S. A. VanSlyke, and C. H. Chen, *J. Appl. Phys.*, 1989, **65**, 3610–3616.
44. C. Adachi, M. A. Baldo, M. E. Thompson, and S. R. Forrest, *J. Appl. Phys.*, 2001, **90**, 5048–5051.
45. S. Lamansky, P. Djurovich, D. Murphy, F. Abdel-Razzaq, H. E. Lee, C. Adachi, P. E. Burrows, S. R. Forrest, and M. E. Thompson, *J. Am. Chem. Soc.*, 2001, **123**, 4304–4312.
46. J. P. Spindler, W. J. Begley, T. K. Hatwar, and D. Y. Kondakov, *Dig. Tech. Pap. - SID Int. Symp.*, 2009, **40**, 420.
47. C. Rothe, A. Werner, O. Fadhel, M. Limmert, T. W. Canzler, and J. Birnstock, *Dig. Tech. Pap. - SID Int. Symp.*, 2009, **40**, 495.
48. D. Y. Kondakov, T. D. Pawlik, T. K. Hatwar, and J. P. Spindler, *J. Appl. Phys.*, 2009, **106**, 124510.
49. A. Endo, K. Sato, K. Yoshimura, T. Kai, A. Kawada, H. Miyazaki, and C. Adachi, *Appl. Phys. Lett.*, 2011, **98**, 083302.
50. H. Uoyama, K. Goushi, K. Shizu, H. Nomura, and C. Adachi, *Nature*, 2012, **492**, 234–238.
51. C. Li, C. Duan, C. Han, and H. Xu, *Adv. Mater.*, 2018, **30**, e1804228.
52. J.-X. Chen, W.-W. Tao, W.-C. Chen, Y.-F. Xiao, K. Wang, C. Cao, J. Yu, S. Li, F.-X. Geng, C. Adachi, C.-S. Lee, and X.-H. Zhang, *Angew. Chem. Int. Ed.*, 2019, **58**, 14660–14665.
53. J. Zhao, C. Zheng, Y. Zhou, C. Li, J. Ye, X. Du, W. Li, Z. He, M. Zhang, H. Lin, S. Tao, and X. Zhang, *Mater. Horiz.*, 2019, **6**, 1425–1432.
54. B. Walker, A. Tamayo, J. Yang, J. Z. Brzezinski, and T.-Q. Nguyen, *Appl. Phys. Lett.*, 2008, **93**, 063302.
55. C. Adachi, R. Hattori, H. Kaji, and T. Tsujimura, Eds., *Handbook of Organic Light-Emitting Diodes*, Springer Japan, Tokyo, 2020.
56. U. Giovanella, M. Pasini, and C. Botta, in *Applied photochemistry: when light meets molecules*, eds. G. Bergamini and S. Silvi, Springer International Publishing, Cham, 2016, vol. 92, pp. 145–196.
57. K. S. Yook and J. Y. Lee, *Adv. Mater.*, 2014, **26**, 4218–4233.
58. T. M. Brown, R. H. Friend, I. S. Millard, D. J. Lacey, T. Butler, J. H. Burroughes, and F. Cacialli, *J. Appl. Phys.*, 2003, **93**, 6159–6172.
59. A. R. Brown, D. D. C. Bradley, J. H. Burroughes, R. H. Friend, N. C. Greenham, P. L. Burn, A. B. Holmes, and A. Kraft, *Appl. Phys. Lett.*, 1992, **61**, 2793–2795.
60. R. H. Friend, R. W. Gymer, A. B. Holmes, J. H. Burroughes, R. N. Marks, C. Taliani, D. D. C. Bradley, D. A. D. Santos, J. L. Brédas, M. Lögdlund, and W. R. Salaneck, *Nature*, 1999, **397**, 121–128.
61. J. Lee, N. Aizawa, M. Numata, C. Adachi, and T. Yasuda, *Adv. Mater.*, 2017, **29**.

62. X. Zhang, C. Fuentes-Hernandez, Y. Zhang, M. W. Cooper, S. Barlow, S. R. Marder, and B. Kippelen, *J. Appl. Phys.*, 2018, **124**, 055501.
63. H. S. Kim, S.-R. Park, and M. C. Suh, *J. Phys. Chem. C*, 2017, **121**, 13986–13997.
64. Y. Kawamura, J. Brooks, J. J. Brown, H. Sasabe, and C. Adachi, *Phys. Rev. Lett.*, 2006, **96**, 017404.
65. J. C. Ribierre, A. Ruseckas, K. Knights, S. V. Staton, N. Cumpstey, P. L. Burn, and I. D. W. Samuel, *Phys. Rev. Lett.*, 2008, **100**, 017402.
66. H. Kuhn, *J. Chem. Phys.*, 1970, **53**, 101–108.
67. Y.-Y. Lyu, J. Kwak, W. S. Jeon, Y. Byun, H. S. Lee, D. Kim, C. Lee, and K. Char, *Adv. Funct. Mater.*, 2009, **19**, 420–427.
68. P.-I. Shih, C.-H. Chien, C.-Y. Chuang, C.-F. Shu, C.-H. Yang, J.-H. Chen, and Y. Chi, *J. Mater. Chem.*, 2007, **17**, 1692.
69. F.-M. Hsu, C.-H. Chien, C.-F. Shu, C.-H. Lai, C.-C. Hsieh, K.-W. Wang, and P.-T. Chou, *Adv. Funct. Mater.*, 2009, **19**, 2834–2843.
70. Y. Tao, S. Gong, Q. Wang, C. Zhong, C. Yang, J. Qin, and D. Ma, *Phys. Chem. Chem. Phys.*, 2010, **12**, 2438–2442.
71. Y. Tao, C. Yang, and J. Qin, *Chem. Soc. Rev.*, 2011, **40**, 2943–2970.
72. D. H. Kim, N. S. Cho, H.-Y. Oh, J. H. Yang, W. S. Jeon, J. S. Park, M. C. Suh, and J. H. Kwon, *Adv. Mater.*, 2011, **23**, 2721–2726.
73. C. L. Ho, W. Y. Wong, G. J. Zhou, B. Yao, Z. Xie, and L. Wang, *Adv. Funct. Mater.*, 2007, **17**, 2925–2936.
74. J.-X. Cai, T.-L. Ye, X.-F. Fan, C.-M. Han, H. Xu, L.-L. Wang, D.-G. Ma, Y. Lin, and P.-F. Yan, *J. Mater. Chem.*, 2011, **21**, 15405.
75. M. A. Baldo, S. Lamansky, P. E. Burrows, M. E. Thompson, and S. R. Forrest, *Appl. Phys. Lett.*, 1999, **75**, 4–6.
76. C. Wu, H.-F. Chen, K.-T. Wong, and M. E. Thompson, *J. Am. Chem. Soc.*, 2010, **132**, 3133–3139.
77. G. Xie, X. Li, D. Chen, Z. Wang, X. Cai, D. Chen, Y. Li, K. Liu, Y. Cao, and S.-J. Su, *Adv. Mater.*, 2016, **28**, 181–187.
78. P. Chen, L.-P. Wang, W.-Y. Tan, Q.-M. Peng, S.-T. Zhang, X.-H. Zhu, and F. Li, *ACS Appl. Mater. Interfaces*, 2015, **7**, 2972–2978.
79. C. Tang, T. Yang, X. Cao, Y. Tao, F. Wang, C. Zhong, Y. Qian, X. Zhang, and W. Huang, *Adv. Opt. Mater.*, 2015, **3**, 786–790.
80. L. Yu, Z. Wu, G. Xie, C. Zhong, Z. Zhu, H. Cong, D. Ma, and C. Yang, *Chem. Commun.*, 2016, **52**, 11012–11015.

81. Y.-H. Kim, C. Wolf, H. Cho, S.-H. Jeong, and T.-W. Lee, *Adv. Mater.*, 2016, **28**, 734–741.
82. Q. Zhang, H. Kuwabara, W. J. Potscavage, S. Huang, Y. Hatae, T. Shibata, and C. Adachi, *J. Am. Chem. Soc.*, 2014, **136**, 18070–18081.
83. Y. Wada, K. Shizu, S. Kubo, K. Suzuki, H. Tanaka, C. Adachi, and H. Kaji, *Appl. Phys. Lett.*, 2015, **107**, 183303.
84. M. Idris, S. C. Kapper, A. C. Tadle, T. Batagoda, D. S. Muthiah Ravinson, O. Abimbola, P. I. Djurovich, J. Kim, C. Coburn, S. R. Forrest, and M. E. Thompson, *Adv. Opt. Mater.*, 2021, **9**, 2001994.
85. J. Lee, C. Jeong, T. Batagoda, C. Coburn, M. E. Thompson, and S. R. Forrest, *Nat. Commun.*, 2017, **8**, 15566.
86. A. Arjona-Esteban, B. Szafranowska, and J. Ochsmann, in *Luminescence - OLED Technology and Applications*, ed. S. Pyshkin, IntechOpen, 2020.
87. W. Zhang, Y.-X. Zhang, X.-Q. Zhang, X.-Y. Liu, J. Fan, and L.-S. Liao, *Org. Electron.*, 2018, **58**, 238–244.
88. J. Li, X. Liao, H. Xu, L. Li, J. Zhang, H. Wang, and B. Xu, *Dyes and Pigments*, 2017, **140**, 79–86.
89. X. Liang, H.-B. Han, Z.-P. Yan, L. Liu, Y.-X. Zheng, H. Meng, and W. Huang, *New J. Chem.*, 2018, **42**, 4317–4323.
90. Y. Wada, S. Kubo, and H. Kaji, *Adv. Mater.*, 2018, **30**, 1705641.
91. C. F. Madigan and V. Bulović, *Phys. Rev. Lett.*, 2003, **91**, 247403.
92. M. A. Baldo, Z. G. Soos, and S. R. Forrest, *Chem. Phys. Lett.*, 2001, **347**, 297–303.
93. G. Candiotto, R. Giro, B. A. C. Horta, F. P. Rosselli, M. de Cicco, C. A. Achete, M. Cremona, and R. B. Capaz, *Phys. Rev. B*, 2020, **102**, 235401.
94. Q. Pei, G. Yu, C. Zhang, Y. Yang, and A. J. Heeger, *Science*, 1995, **269**, 1086–1088.
95. P. Matyba, K. Maturova, M. Kemerink, N. D. Robinson, and L. Edman, *Nat. Mater.*, 2009, **8**, 672–676.
96. S. van Reenen, R. A. J. Janssen, and M. Kemerink, *Org. Electron.*, 2011, **12**, 1746–1753.
97. N. Kaihovirta, C. Larsen, and L. Edman, *ACS Appl. Mater. Interfaces*, 2014, **6**, 2940–2947.
98. S. van Reenen and M. Kemerink, in *Light-Emitting Electrochemical Cells*, ed. R. D. Costa, Springer International Publishing, Cham, 2017, pp. 3–45.
99. A. Asadpoordarvish, A. Sandström, C. Larsen, R. Bollström, M. Toivakka, R. Österbacka, and L. Edman, *Adv. Funct. Mater.*, 2015, **25**, 3238–3245.
100. G. Hernandez-Sosa, S. Tekoglu, S. Stolz, R. Eckstein, C. Teusch, J. Trapp, U. Lemmer, M. Hamburger, and N. Mechau, *Adv. Mater.*, 2014, **26**, 3235–3240.

101. A. Sandström, A. Asadpoordarvish, J. Enevold, and L. Edman, *Adv. Mater.*, 2014, **26**, 4975–4980.
102. C.-C. Shih, C.-W. Huang, M. Gao, C.-C. Chueh, and W.-C. Chen, *J. Mater. Chem. C*, 2017, **5**, 11421–11428.
103. J. C. deMello, N. Tessler, S. C. Graham, and R. H. Friend, *Phys. Rev. B*, 1998, **57**, 12951–12963.
104. G. G. Malliaras, J. D. Slinker, J. A. DeFranco, M. J. Jaquith, W. R. Silveira, Y.-W. Zhong, J. M. Moran-Mirabal, H. G. Craighead, H. D. Abruña, and J. A. Marohn, *Nat. Mater.*, 2008, **7**, 168–168.
105. S. Tang and L. Edman, *Top. Curr. Chem.*, 2016, **374**, 40.
106. S. van Reenen, P. Matyba, A. Dzwilewski, R. A. J. Janssen, L. Edman, and M. Kemerink, *J. Am. Chem. Soc.*, 2010, **132**, 13776–13781.
107. J. D. Slinker, J. A. DeFranco, M. J. Jaquith, W. R. Silveira, Y. Zhong, J. M. Moran-Mirabal, H. G. Craighead, H. D. Abruña, J. A. Marohn, and G. G. Malliaras, *Nat. Mater.*, 2007, **6**, 894–899.
108. Q. Pei and A. J. Heeger, *Nat. Mater.*, 2008, **7**, 167–167.
109. J. M. Leger, S. A. Carter, and B. Ruhstaller, *J. Appl. Phys.*, 2005, **98**, 124907.
110. T. J. Mills and M. C. Lonergan, *Phys. Rev. B*, 2012, **85**, 035203.
111. F. Dumur, in *Luminescence in Electrochemistry*, eds. F. Miomandre and P. Audebert, Springer International Publishing, Cham, 2017, pp. 327–361.
112. J. Slinker, D. Bernards, P. L. Houston, H. D. Abruña, S. Bernhard, and G. G. Malliaras, *Chem. Commun.*, 2003, 2392–2399.
113. M. Elie, F. Sguerra, F. Di Meo, M. D. Weber, R. Marion, A. Grimault, J.-F. Lohier, A. Stallivieri, A. Brosseau, R. B. Pansu, J.-L. Renaud, M. Linares, M. Hamel, R. D. Costa, and S. Gaillard, *ACS Appl. Mater. Interfaces*, 2016, **8**, 14678–14691.
114. S. Keller, F. Brunner, J. M. Junquera-Hernández, A. Pertegás, M.-G. La-Placa, A. Prescimone, E. C. Constable, H. J. Bolink, E. Ortí, and C. E. Housecroft, *ChemPlusChem*, 2018, **83**, 217–229.
115. S. Keller, A. Prescimone, H. Bolink, M. Sessolo, G. Longo, L. Martínez-Sarti, J. M. Junquera-Hernández, E. C. Constable, E. Ortí, and C. E. Housecroft, *Dalton Trans.*, 2018, **47**, 14263–14276.
116. M. Alkan-Zambada, S. Keller, L. Martínez-Sarti, A. Prescimone, J. M. Junquera-Hernández, E. C. Constable, H. J. Bolink, M. Sessolo, E. Ortí, and C. E. Housecroft, *J. Mater. Chem.*, 2018, **6**, 8460–8471.
117. D. Tordera, S. Meier, M. Lenes, R. D. Costa, E. Ortí, W. Sarfert, and H. J. Bolink, *Adv. Mater.*, 2012, **24**, 897–900.
118. S. van Reenen, T. Akatsuka, D. Tordera, M. Kemerink, and H. J. Bolink, *J. Am. Chem. Soc.*, 2013, **135**, 886–891.

119. C. V. Hoven, H. Wang, M. Elbing, L. Garner, D. Winkelhaus, and G. C. Bazan, *Nat. Mater.*, 2010, **9**, 249–252.
120. Y. Shen, D. D. Kuddes, C. A. Naquin, T. W. Hesterberg, C. Kusmierz, B. J. Holliday, and J. D. Slinker, *Appl. Phys. Lett.*, 2013, **102**, 203305.
121. L. D. Bastatas and J. D. Slinker, in *Light-Emitting Electrochemical Cells*, ed. R. D. Costa, Springer International Publishing, Cham, 2017, pp. 93–119.
122. C. H. Lyons, E. D. Abbas, J. K. Lee, and M. F. Rubner, *J. Am. Chem. Soc.*, 1998, **120**, 12100–12107.
123. S. T. Parker, J. D. Slinker, M. S. Lowry, M. P. Cox, S. Bernhard, and G. G. Malliaras, *Chem. Mater.*, 2005, **17**, 3187–3190.
124. S. Park, D. Moon, S. C. Damodharan, M. Chandran, and Y. Choe, *Mater. Res. Bull.*, 2012, **47**, 2807–2810.
125. R. D. Costa, A. Pertegás, E. Ortí, and H. J. Bolink, *Chem. Mater.*, 2010, **22**, 1288–1290.
126. C. D. Sunesh, O. Sunseong, M. Chandran, D. Moon, and Y. Choe, *Mater. Chem. Phys.*, 2012, **136**, 173–178.
127. L. D. Bastatas, K.-Y. Lin, M. D. Moore, K. J. Suhr, M. H. Bowler, Y. Shen, B. J. Holliday, and J. D. Slinker, *Langmuir*, 2016, **32**, 9468–9474.
128. S. B. Meier, S. van Reenen, B. Lefevre, D. Hartmann, H. J. Bolink, A. Winnacker, W. Sarfert, and M. Kemerink, *Adv. Funct. Mater.*, 2013, **23**, 3531–3538.
129. G. Yu, Y. Cao, C. Zhang, Y. Li, J. Gao, and A. J. Heeger, *Appl. Phys. Lett.*, 1998, **73**, 111–113.
130. W. Zhao, C.-Y. Liu, Q. Wang, J. M. White, and A. J. Bard, *Chem. Mater.*, 2005, **17**, 6403–6406.
131. M. Schaer, F. Nüesch, D. Berner, W. Leo, and L. Zuppiroli, *Adv. Funct. Mater.*, 2001, **11**, 116–121.
132. H. Rudmann and M. F. Rubner, *J. Appl. Phys.*, 2001, **90**, 4338–4345.
133. A. A. Gorodetsky, S. Parker, J. D. Slinker, D. A. Bernards, M. H. Wong, G. G. Malliaras, S. Flores-Torres, and H. D. Abruña, *Appl. Phys. Lett.*, 2004, **84**, 807–809.
134. J. H. Shin, P. Matyba, N. D. Robinson, and L. Edman, *Electrochim. Acta.*, 2007, **52**, 6456–6462.
135. J. Xu, A. Sandström, E. M. Lindh, W. Yang, S. Tang, and L. Edman, *ACS Appl. Mater. Interfaces.*, 2018, **10**, 33380–33389.
136. D. Hohertz and J. Gao, *Adv. Mater.*, 2008, **20**, 3298–3302.
137. J. Fang, P. Matyba, N. D. Robinson, and L. Edman, *J. Am. Chem. Soc.*, 2008, **130**, 4562–4568.
138. J. Fang, P. Matyba, and L. Edman, *Adv. Funct. Mater.*, 2009, **19**, 2671–2676.
139. J. H. Shin, S. Xiao, and L. Edman, *Adv. Funct. Mater.*, 2006, **16**, 949–956.

140. K. Chu, J. R. Adsetts, C. Moore, and Z. Ding, *ACS Appl. Electron. Mater.*, 2020, **2**, 3825–3830.
141. M. Di Marcantonio, F. Vollkommer, G. Bacher, and E. Nannen, *J. Mater. Chem. C*, 2018, **6**, 9742–9748.
142. J. M. Hodgkiss, S. Albert-Seifried, A. Rao, A. J. Barker, A. R. Campbell, R. A. Marsh, and R. H. Friend, *Adv. Funct. Mater.*, 2012, **22**, 1567–1577.
143. S. M. King, D. Dai, C. Rothe, and A. P. Monkman, *Phys. Rev. B.*, 2007, **76**, 085204.
144. S. van Reenen, M. V. Vitorino, S. C. J. Meskers, R. A. J. Janssen, and M. Kemerink, *Phys. Rev. B*, 2014, **89**, 205206.
145. J. Kalinowski, W. Stampor, J. Szmytkowski, D. Virgili, M. Cocchi, V. Fattori, and C. Sabatini, *Phys. Rev. B*, 2006, **74**, 085316.
146. J. D. Slinker, J. Rivnay, J. S. Moskowitz, J. B. Parker, S. Bernhard, H. D. Abruña, and G. G. Malliaras, *J. Mater. Chem.*, 2007, **17**, 2976–2988.
147. H. Rudmann, S. Shimada, and M. F. Rubner, *J. Am. Chem. Soc.*, 2002, **124**, 4918–4921.
148. N. Kaihovirta, A. Asadpoordarvish, A. Sandström, and L. Edman, *ACS Photonics*, 2014, **1**, 182–189.
149. N. Kaihovirta, G. Longo, L. Gil-Escrig, H. J. Bolink, and L. Edman, *Appl. Phys. Lett.*, 2015, **106**, 103502.
150. S. K. Lee, D. H. Hwang, B. J. Jung, N. S. Cho, J. Lee, J. D. Lee, and H. K. Shim, *Adv. Funct. Mater.*, 2005, **15**, 1647–1655.
151. Y. Xiong, L. Li, J. Liang, H. Gao, S. Chou, and Q. Pei, *Mater. Horiz.*, 2015, **2**, 338–343.
152. Y. Yang and Q. Pei, *J. Appl. Phys.*, 1997, **81**, 3294–3298.
153. Y. Shao, G. C. Bazan, and A. J. Heeger, *Adv. Mater.*, 2007, **19**, 365–370.
154. J. Yang, K. C. Gordon, Y. Zidon, and Y. Shapira, *J. Appl. Phys.*, 2003, **94**, 6391–6395.
155. E. S. Handy, A. J. Pal, and M. F. Rubner, *J. Am. Chem. Soc.*, 1999, **121**, 3525–3528.
156. C. E. Housecroft and E. C. Constable, *Coord. Chem. Rev.*, 2017.
157. F. De Angelis, S. Fantacci, N. Evans, C. Klein, S. M. Zakeeruddin, J.-E. Moser, K. Kalyanasundaram, H. J. Bolink, M. Grätzel, and M. K. Nazeeruddin, *Inorg. Chem.*, 2007, **46**, 5989–6001.
158. J. L. Rodríguez-Redondo, R. D. Costa, E. Ortí, A. Sastre-Santos, H. J. Bolink, and F. Fernández-Lázaro, *Dalton Trans.*, 2009, 9787–9793.
159. Periodic Table – Royal Society of Chemistry, <https://www.rsc.org/periodic-table/>, (accessed June 15, 2021).
160. Daily Metal Price: Free Metal Price Tables and Charts, <https://www.dailymetalprice.com/>, (accessed June 15, 2021).

161. M. Elie, S. Gaillard, and J.-L. Renaud, in *Light-Emitting Electrochemical Cells*, ed. R. D. Costa, Springer International Publishing, Cham, 2017, pp. 287–327.
162. D. R. McMillin, M. T. Buckner, and B. Tae. Ahn, *Inorg. Chem.*, 1977, **16**, 943–945.
163. M. C. Rosko, K. A. Wells, C. E. Hauke, and F. N. Castellano, *Inorg. Chem.*, 2021, **60**, 8394–8403.
164. C. E. Housecroft and E. C. Constable, in *Light-Emitting Electrochemical Cells*, ed. R. D. Costa, Springer International Publishing, Cham, 2017, pp. 167–202.
165. M. T. Buckner and D. R. McMillin, *J. Chem. Soc., Chem. Commun.*, 1978, 759.
166. Y. Zhang, M. Schulz, M. Wächtler, M. Karnahl, and B. Dietzek, *Coord. Chem. Rev.*, 2018, **356**, 127–146.
167. D. G. Cuttell, S.-M. Kuang, P. E. Fanwick, D. R. McMillin, and R. A. Walton, *J. Am. Chem. Soc.*, 2002, **124**, 6–7.
168. S.-M. Kuang, D. G. Cuttell, D. R. McMillin, P. E. Fanwick, and R. A. Walton, *Inorg. Chem.*, 2002, **41**, 3313–3322.
169. E. C. Riesgo, Y. Z. Hu, F. Bouvier, R. P. Thummel, D. V. Scaltrito, and G. J. Meyer, *Inorg. Chem.*, 2001, **40**, 3413–3422.
170. S. Garakyaraghi, E. O. Danilov, C. E. McCusker, and F. N. Castellano, *J. Phys. Chem. A*, 2015, **119**, 3181–3193.
171. C. T. Cunningham, K. L. H. Cunningham, J. F. Michalec, and D. R. McMillin, *Inorg. Chem.*, 1999, **38**, 4388–4392.
172. S. Keller, A. Prescimone, E. C. Constable, and C. E. Housecroft, *Photochem. Photobiol. Sci.*, 2018, **17**, 375–385.
173. F. Brunner, A. Babaei, A. Pertegás, J. M. Junquera-Hernández, A. Prescimone, E. C. Constable, H. J. Bolink, M. Sessolo, E. Ortí, and C. E. Housecroft, *Dalton Trans.*, 2019, **48**, 446–460.
174. L. Bergmann, J. Friedrichs, M. Mydlak, T. Baumann, M. Nieger, and S. Bräse, *Chem. Commun.*, 2013, **49**, 6501–6503.
175. T. Hofbeck, U. Monkowius, and H. Yersin, *J. Am. Chem. Soc.*, 2015, **137**, 399–404.
176. R. Czerwieniec, K. Kowalski, and H. Yersin, *Dalton Trans.*, 2013, **42**, 9826–9830.
177. R. Czerwieniec and H. Yersin, *Inorg. Chem.*, 2015, **54**, 4322–4327.
178. R. D. Costa, D. Tordera, E. Ortí, H. J. Bolink, J. Schönle, S. Graber, C. E. Housecroft, E. C. Constable, and J. A. Zampese, *J. Mater. Chem.*, 2011, **21**, 16108.
179. S. Keller, A. Prescimone, M.-G. La Placa, J. M. Junquera-Hernández, H. J. Bolink, E. C. Constable, M. Sessolo, E. Ortí, and C. E. Housecroft, *RSC Adv.*, 2020, **10**, 22631–22644.

180. L. Yang, J.-K. Feng, A.-M. Ren, M. Zhang, Y.-G. Ma, and X.-D. Liu, *Eur. J. Inorg. Chem.*, 2005, **2005**, 1867–1879.
181. R. Czerwieniec, J. Yu, and H. Yersin, *Inorg. Chem.*, 2011, **50**, 8293–8301.
182. C. Yi, S. Xu, J. Wang, F. Zhao, H. Xia, and Y. Wang, *Eur. J. Inorg. Chem.*, 2016, **2016**, 4885–4890.
183. F. Brunner, S. Graber, Y. Baumgartner, D. Häussinger, A. Prescimone, E. C. Constable, and C. E. Housecroft, *Dalton Trans.*, 2017, **46**, 6379–6391.
184. F. Brunner, L. Martínez-Sarti, S. Keller, A. Pertegás, A. Prescimone, E. C. Constable, H. J. Bolink, and C. E. Housecroft, *Dalton Trans.*, 2016, **45**, 15180–15192.
185. N. Armaroli, G. Accorsi, M. Holler, O. Moudam, J. F. Nierengarten, Z. Zhou, R. T. Wegh, and R. Welter, *Adv. Mater.*, 2006, **18**, 1313–1316.
186. M. Heberle, S. Tschierlei, N. Rockstroh, M. Ringenberg, W. Frey, H. Junge, M. Beller, S. Lochbrunner, and M. Karnahl, *Chem. Eur. J.*, 2017, **23**, 312–319.
187. E. Fresta and R. D. Costa, *J. Mater. Chem. C*, 2017, **5**, 5643–5675.
188. M. D. Weber, M. Viciano-Chumillas, D. Armentano, J. Cano, and R. D. Costa, *Dalton Trans.*, 2017, **46**, 6312–6323.
189. G. U. Mahoro, J. Fernandez-Cestau, J. Renaud, P. B. Coto, R. D. Costa, and S. Gaillard, *Adv. Opt. Mater.*, 2020, **8**, 2000260.
190. M. Mohankumar, M. Holler, E. Meichsner, J.-F. Nierengarten, F. Niess, J.-P. Sauvage, B. Delavaux-Nicot, E. Leoni, F. Monti, J. M. Malicka, M. Cocchi, E. Bandini, and N. Armaroli, *J. Am. Chem. Soc.*, 2018, **140**, 2336–2347.
191. E. Fresta, M. D. Weber, J. Fernandez-Cestau, and R. D. Costa, *Adv. Opt. Mater.*, 2019, **7**, 1900830.
192. R. Marion, F. Sguerra, F. Di Meo, E. Sauvageot, J.-F. Lohier, R. Daniellou, J.-L. Renaud, M. Linares, M. Hamel, and S. Gaillard, *Inorg. Chem.*, 2014, **53**, 9181–9191.
193. R. Marion, F. Sguerra, F. Di Meo, E. Sauvageot, J.-F. Lohier, R. Daniellou, J.-L. Renaud, M. Linares, M. Hamel, and S. Gaillard, *Inorg. Chem.*, 2016, **55**, 4068–4068.
194. M. Elie, M. D. Weber, F. Di Meo, F. Sguerra, J.-F. Lohier, R. B. Pansu, J.-L. Renaud, M. Hamel, M. Linares, R. D. Costa, and S. Gaillard, *Chem. Eur. J.*, 2017, **23**, 16328–16337.
195. M. D. Weber, E. Fresta, M. Elie, M. E. Miehllich, J.-L. Renaud, K. Meyer, S. Gaillard, and R. D. Costa, *Adv. Funct. Mater.*, 2018, **28**, 1707423.
196. I. Nohara, A. Keller, N. Tarassenko, A. Prescimone, E. C. Constable, and C. E. Housecroft, *Inorganics*, 2020, **8**, 4.
197. I. Nohara, A. Prescimone, D. Häussinger, C. E. Housecroft, and E. C. Constable, *RSC Adv.*, 2019, **9**, 13646–13657.

198. I. Nohara, A. Prescimone, C. E. Housecroft, and E. C. Constable, *Inorganics*, 2019, **7**, 11.
199. P. Arce, C. Vera, D. Escudero, J. Guerrero, A. Lappin, A. Oliver, D. H. Jara, G. Ferraudi, and L. Lemus, *Dalton Trans.*, 2017, **46**, 13432–13445.
200. H.-B. Song, Z.-Z. Zhang, and T. C. W. Mak, *J. Chem. Soc., Dalton Trans.*, 2002, 1336–1343.
201. P. Coburger, J. Schulz, J. Klose, B. Schwarze, M. B. Sárosi, and E. Hey-Hawkins, *Inorg. Chem.*, 2017, **56**, 292–304.
202. T. S. Lobana, M. Kaushal, R. K. Virk, I. Garcia-Santos, and J. P. Jasinski, *Polyhedron*, 2018, **152**, 49–54.
203. R. Ramachandran, G. Prakash, P. Vijayan, P. Viswanathamurthi, and J. Grzegorz Malecki, *Inorg. Chim. Acta*, 2017, **464**, 88–93.
204. T. S. Lobana, R. Sharma, G. Bawa, and S. Khanna, *Coord. Chem. Rev.*, 2009, **253**, 977–1055.
205. C. Pettinari, C. di Nicola, F. Marchetti, R. Pettinari, B. W. Skelton, N. Somers, A. H. White, W. T. Robinson, M. R. Chierotti, R. Gobetto, and C. Nervi, *Eur. J. Inorg. Chem.*, 2008, **2008**, 1974–1984.
206. T. S. Lobana, S. Indoria, M. Sharma, J. Nandi, A. K. Jassal, M. S. Hundal, and A. Castineiras, *Polyhedron*, 2014, **80**, 34–40.
207. M. Trivedi, S. K. Ujjain, G. Singh, A. Kumar, S. K. Dubey, and N. P. Rath, *J. Organomet. Chem.*, 2014, **772–773**, 202–209.
208. T. S. Lobana, A. K. Sandhu, R. Sultana, A. Castineiras, R. J. Butcher, and J. P. Jasinski, *RSC Adv.*, 2014, **4**, 30511.
209. C. Amari, S. Ianelli, C. Pelizzi, G. Pelizzi, and G. Predieri, *Inorg. Chim. Acta.*, 1993, **211**, 89–94.
210. H. Gökce and S. Bahçeli, *Spectrochim. Acta A Mol. Biomol. Spectrosc.*, 2012, **96**, 139–147.
211. L. Canovese, F. Visentin, P. Uguagliati, G. Chessa, and A. Pesce, *J. Organomet. Chem.*, 1998, **566**, 61–71.
212. K. Garg, S. I. M. Paris, and J. J. Rack, *Eur. J. Inorg. Chem.*, 2013, **2013**, 1142–1148.
213. A. Tsuboyama, H. Iwawaki, M. Furugori, T. Mukaide, J. Kamatani, S. Igawa, T. Moriyama, S. Miura, T. Takiguchi, S. Okada, M. Hoshino, and K. Ueno, *J. Am. Chem. Soc.*, 2003, **125**, 12971–12979.
214. S. W. Thomas, K. Venkatesan, P. Müller, and T. M. Swager, *J. Am. Chem. Soc.*, 2006, **128**, 16641–16648.
215. J. Yuasa, M. Dan, and T. Kawai, *Dalton Trans.*, 2013, **42**, 16096–16101.
216. G. Tárkányi, P. Király, G. Pálinkás, and A. Deák, *Magn. Reson. Chem.*, 2007, **45**, 917–924.
217. S. Keller, A. Pertegás, G. Longo, L. Martínez, J. Cerdá, J. M. Junquera-Hernández, A. Prescimone, E. C. Constable, C. E. Housecroft, E. Ortí, and H. J. Bolink, *J. Mater. Chem. C*, 2016, **4**, 3857–3871.

218. D. Neuhaus and M. P. Williamson, *The nuclear Overhauser effect in stereochemical and conformational analysis*, Wiley-VCH, New York, NY, USA, 2nd edn., 2000.
219. L. Yang, D. R. Powell, and R. P. Houser, *Dalton Trans.*, 2007, 955–964.
220. S. S. Batsanov, *Springer Science and Business Media LLC.*, 2001.
221. S.-Z. Hu, Z.-H. Zhou, and B. E. Robertson, *Zeitschrift für Kristallographie*, 2009, **224**, 375–383.
222. C. Sivasankar, N. Sadhukhan, J. K. Bera, and A. G. Samuelson, *New J. Chem.*, 2007, **31**, 385–393.
223. A. V. Mitin, J. Baker, and P. Pulay, *J. Chem. Phys.*, 2003, **118**, 7775–7782.
224. T. Ansbacher, H. K. Srivastava, J. M. L. Martin, and A. Shurki, *J. Comput. Chem.*, 2010, **31**, 75–83.
225. X. Ma, R. Sun, J. Cheng, J. Liu, F. Gou, H. Xiang, and X. Zhou, *J. Chem. Educ.*, 2016, **93**, 345–350.
226. L. Le Bras, K. Chaitou, S. Aloïse, C. Adamo, and A. Perrier, *Phys. Chem. Chem. Phys.*, 2018, **21**, 46–56.
227. P. J. Spellane, R. J. Watts, and C. J. Curtis, *Inorg. Chem.*, 1983, **22**, 4060–4062.
228. G. Nord, A. C. Hazell, R. G. Hazell, and O. Farver, *Inorg. Chem.*, 1983, **22**, 3429–3434.
229. B. Butschke, M. Schlangen, D. Schröder, and H. Schwarz, *Chem. Eur. J.*, 2008, **14**, 11050–11060.
230. B. Butschke and H. Schwarz, *Organometallics*, 2010, **29**, 6002–6011.
231. E. C. Constable and K. R. Seddon, *J. Chem. Soc., Chem. Commun.*, 1982, 34–36.
232. G. E. Schneider, H. J. Bolink, E. C. Constable, C. D. Ertl, C. E. Housecroft, A. Pertegàs, J. A. Zampese, A. Kanitz, F. Kessler, and S. B. Meier, *Dalton Trans.*, 2014, **43**, 1961–1964.
233. W. M. Ward, B. H. Farnum, M. Siegler, and G. J. Meyer, *J. Phys. Chem. A*, 2013, **117**, 8883–8894.
234. M. P. Williamson, *Prog. nucl. magn. reson. spectrosc.*, 2013, **73**, 1–16.
235. C. R. Groom, I. J. Bruno, M. P. Lightfoot, and S. C. Ward, *Acta Crystallogr. B Struct. Sci. Cryst. Eng. Mater.*, 2016, **72**, 171–179.
236. I. J. Bruno, J. C. Cole, P. R. Edgington, M. Kessler, C. F. Macrae, P. McCabe, J. Pearson, and R. Taylor, *Acta Crystallogr. B*, 2002, **58**, 389–397.
237. E. Leoni, J. Mohanraj, M. Holler, M. Mohankumar, I. Nierengarten, F. Monti, A. Sournia-Saquet, B. Delavaux-Nicot, J. F. Nierengarten, and N. Armaroli, *Inorg. Chem.*, 2018, **57**, 15537–15549.
238. C. Minozzi, A. Caron, J.-C. Grenier-Petel, J. Santandrea, and S. K. Collins, *Angew. Chem. Int. Ed.*, 2018, **57**, 5477–5481.
239. J. D. Roberts and M. C. Caserio, in *Basic Principles of Organic Chemistry*, Addison-Wesley, Menlo Park, CA, 2nd edn., 1977, pp. 1287–1341.

240. E. Fresta, G. Volpi, M. Milanese, C. Garino, C. Barolo, and R. D. Costa, *Inorg. Chem.*, 2018, **57**, 10469–10479.
241. X.-Y. Feng, X.-L. Xin, Y.-M. Guo, L.-L. Chen, Y.-Y. Liang, M. Xu, and X.-L. Li, *Polyhedron*, 2015, **101**, 23–28.
242. J. M. Carbonell-Vilar, E. Fresta, D. Armentano, R. D. Costa, M. Viciano-Chumillas, and J. Cano, *Dalton Trans.*, 2019, **48**, 9765–9775.
243. X.-L. Li, Y.-B. Ai, B. Yang, J. Chen, M. Tan, X.-L. Xin, and Y.-H. Shi, *Polyhedron*, 2012, **35**, 47–54.
244. X.-L. Xin, M. Chen, Y. Ai, F. Yang, X.-L. Li, and F. Li, *Inorg. Chem.*, 2014, **53**, 2922–2931.
245. H. C. Guo, R. H. Zheng, and H. J. Jiang, *Org. Prep. Proced. Int.*, 2012, **44**, 392–396.
246. C. Janiak, *J. Chem. Soc., Dalton Trans.*, 2000, 3885–3896.
247. C. S. Smith, C. W. Branham, B. J. Marquardt, and K. R. Mann, *J. Am. Chem. Soc.*, 2010, **132**, 14079–14085.
248. S. Brown-Xu, M. Fumanal, C. Gourlaouen, L. Gimeno, A. Quatela, C. Thobie-Gautier, E. Blart, A. Planchat, F. Riobé, C. Monnereau, L. X. Chen, C. Daniel, and Y. Pellegrin, *Inorg. Chem.*, 2019, **58**, 7730–7745.
249. A. P. Krapcho, S. Sparapani, A. Leenstra, and J. D. Seitz, *Tetrahedron Lett.*, 2009, **50**, 3195–3197.
250. M. Levis, U. Lüning, M. Müller, and M. Schmittel, *Z. Naturforsch.*, 1993, **49b**, 675–682.
251. C. Boldron, M. Pitié, and B. Meunier, *Synlett*, 2001, 1629–1631.
252. A. P. Krapcho and S. Sparapani, *J. Heterocycl. Chem.*, 2008, **45**, 1167–1170.
253. S. Keller, M. Alkan-Zambada, A. Prescimone, E. C. Constable, and C. E. Housecroft, *Crystals*, 2020, **10**, 255.
254. M. Nishio, *Phys. Chem. Chem. Phys.*, 2011, **13**, 13873–13900.
255. M. Nishio, *CrystEngComm.*, 2004, **6**, 130.
256. V. Balzani and S. Campagna, Eds., *Photochemistry and Photophysics of Coordination Compounds I*, Springer Berlin Heidelberg, Berlin, Heidelberg, 2007.
257. H. Takeda, K. Ohashi, A. Sekine, and O. Ishitani, *J. Am. Chem. Soc.*, 2016, **138**, 4354–4357.
258. L.-Z. Sun, X.-N. Kuang, S. Lin, L. Zhao, X. Yu, Z.-F. Li, Min-Liu, X.-L. Xin, Y.-P. Yang, and Q.-H. Jin, *Polyhedron*, 2020, **175**, 114177.
259. J. I. Mapley, D. A. W. Ross, C. J. McAdam, K. C. Gordon, and J. D. Crowley, *J. Coord. Chem.*, 2019, **72**, 1378–1394.
260. Z.-J. Yu, H. Chen, A. J. J. Lennox, L.-J. Yan, X.-F. Liu, D.-D. Xu, F. Chen, L.-X. Xu, Y. Li, Q.-A. Wu, and S.-P. Luo, *Dyes and Pigments*, 2019, **162**, 771–775.

261. X. Liu, R. Li, L. Ma, X. Feng, and Y. Ding, *New J. Chem.*, 2016, **40**, 619–625.
262. M. Rentschler, M.-A. Schmid, W. Frey, S. Tschierlei, and M. Karnahl, *Inorg. Chem.*, 2020, **59**, 14762–14771.
263. Hammett Sigma Constants, <http://www.wiredchemist.com/data/hammett-sigma-constants> (accessed August 17, 2021).
264. R. Liu, M.-M. Huang, X.-X. Yao, H.-H. Li, F.-L. Yang, and X.-L. Li, *Inorg. Chim. Acta*, 2015, **434**, 172–180.
265. S.-X. Xu, J.-L. Wang, F. Zhao, H.-Y. Xia, and Y. Wang, *Transition Met. Chem.*, 2015, **40**, 723–732.
266. A. V. Rozhkov, S. N. Eliseeva, S. V. Baykov, L. E. Zelenkov, D. O. Goriachiy, and I. V. Taydakov, *New J. Chem.*, 2020, **44**, 110–120.
267. J. C. Slater, *J. Chem. Phys.*, 1964, **41**, 3199–3204.
268. B. Cordero, V. Gómez, A. E. Platero-Prats, M. Revés, J. Echeverría, E. Cremades, F. Barragán, and S. Alvarez, *Dalton Trans.*, 2008, 2832–2838.
269. J. Ortíz-Corona and F. J. Rodríguez-Gómez, *Trans. Nonferrous Met. Soc. China*, 2019, **29**, 2646–2657.
270. Z. Zhao, L. Xiao, F. Sun, G. Huo, and H. Li, *Int. J. Refract. Met. Hard Mater.*, 2010, **28**, 503–507.
271. U. S. Raikar, C. G. Renuka, Y. F. Nadaf, B. G. Mulimani, A. M. Karguppikar, and M. K. Soudagar, *Spectrochim. Acta A Mol. Biomol. Spectrosc.*, 2006, **65**, 673–677.

Appendix

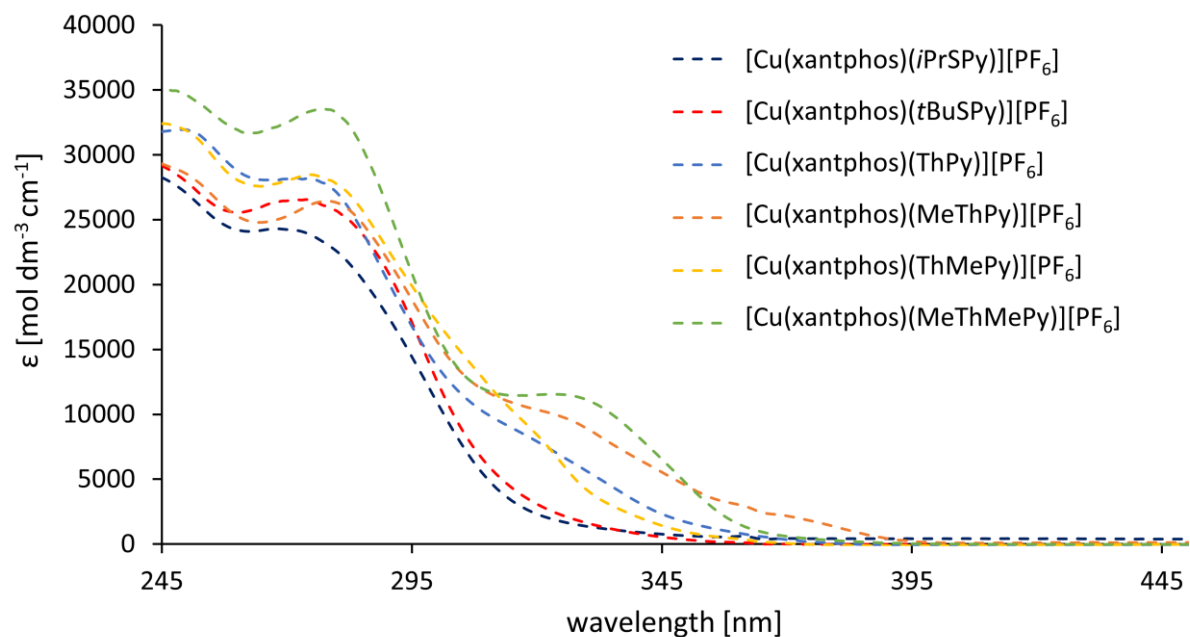


Figure A.1: UV-Vis absorption spectra of $[\text{Cu}(\text{xantphos})(N^S)]\text{PF}_6$ complexes in CH_2Cl_2 with $c = 2.5 \times 10^{-5} \text{ M}$ for $[\text{Cu}(\text{xantphos})(i\text{PrSPy})]\text{PF}_6$ and $[\text{Cu}(\text{xantphos})(t\text{BuSPy})]\text{PF}_6$, for all other complexes $c = 5 \times 10^{-5} \text{ M}$.

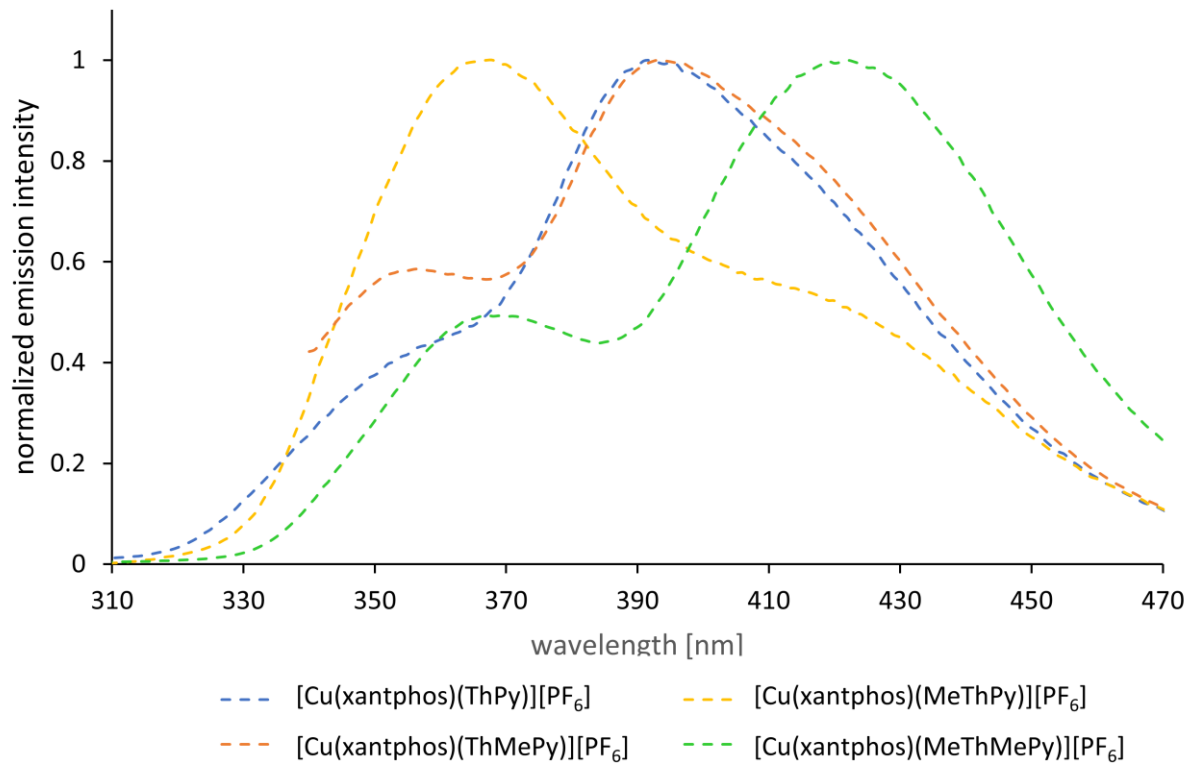


Figure A.2: Normalized solution emission spectra of $[\text{Cu}(\text{POP})(N^S)]\text{PF}_6$ complexes in CH_2Cl_2 ($c = 2.5 \times 10^{-5}$ – $5 \times 10^{-5} \text{ M}$). $\lambda_{\text{exc}} = 275 \text{ nm}$ for ThPy, 275 nm for MeThPy, 320 nm for ThMePy and 280 nm for MeThMePy. $\lambda_{\text{exc}} = 360 \text{ nm}$

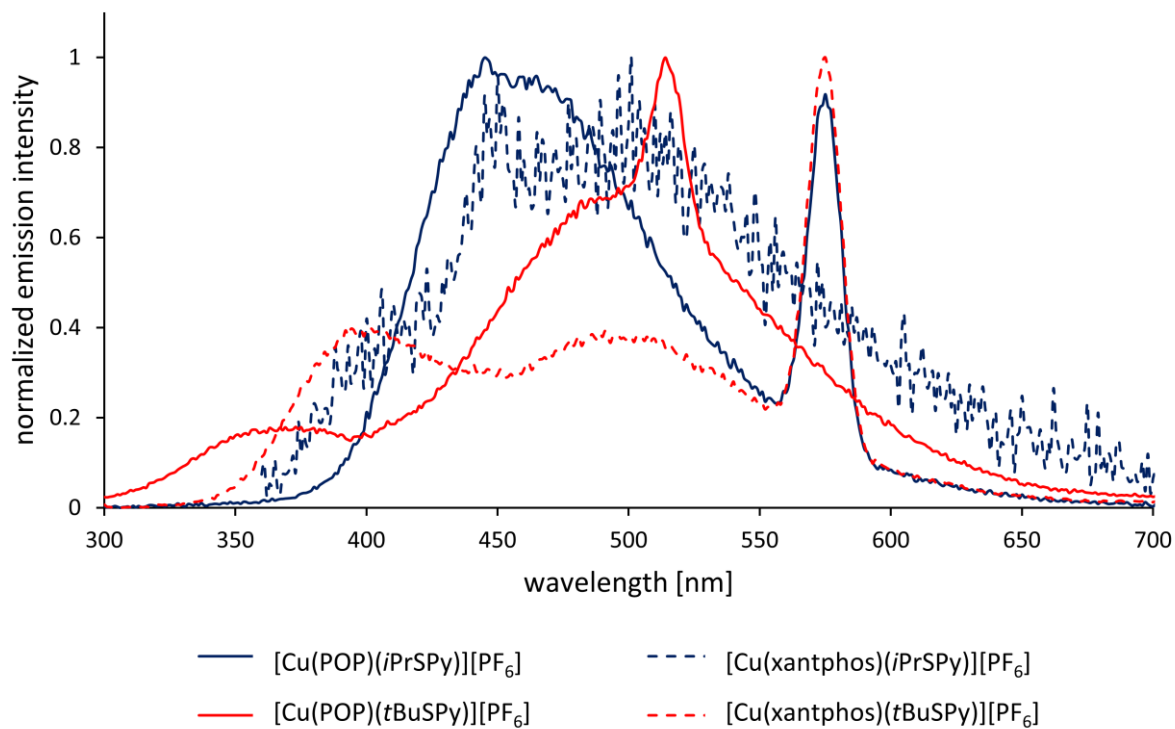


Figure A.3: Normalized emission spectra of powder samples of $[\text{Cu}(\text{P}^{\wedge}\text{P})(i\text{PrSPy})][\text{PF}_6]$ and $[\text{Cu}(\text{P}^{\wedge}\text{P})(t\text{BuSPy})][\text{PF}_6]$ compounds when excited with $\lambda_{\text{exc}} = 280 \text{ nm}$.

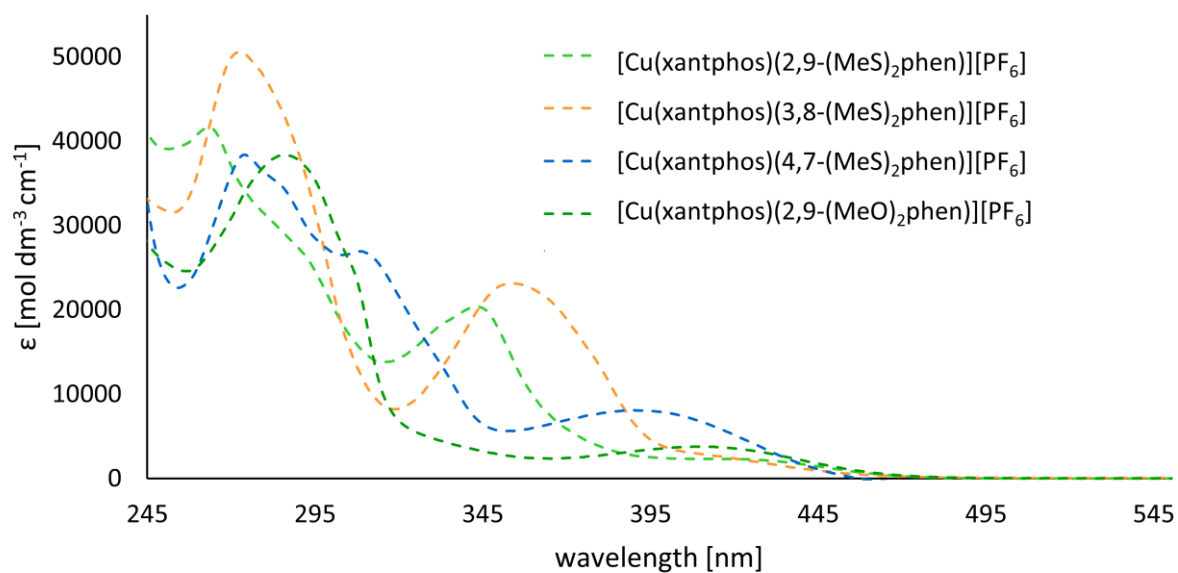


Figure A.4: UV-Vis absorption spectra of $[\text{Cu}(\text{xantphos})((\text{MeX})_2\text{phen})][\text{PF}_6]$ in CH_2Cl_2 with concentrations in the range of 1.75×10^{-5} – $3.0 \times 10^{-5} \text{ M}$.

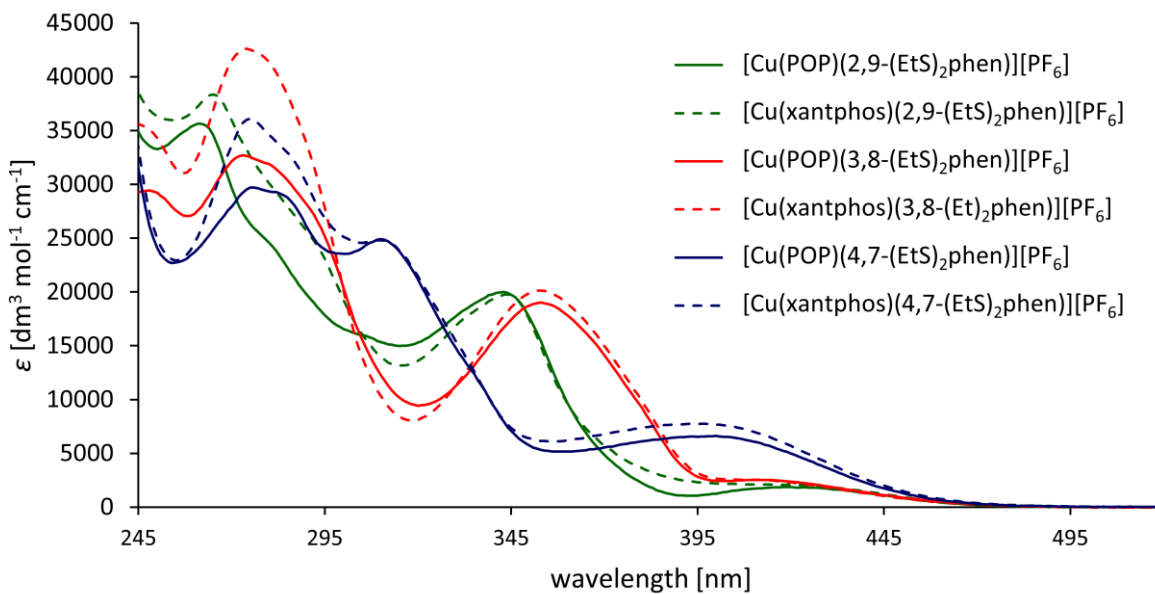


Figure A.5: UV-Vis absorption spectra of $[\text{Cu}(\text{P}^{\wedge}\text{P})((\text{EtS})_2\text{phen})][\text{PF}_6]$ in CH_2Cl_2 with concentrations in the range of 1.5×10^{-5} – 3.0×10^{-5} M.

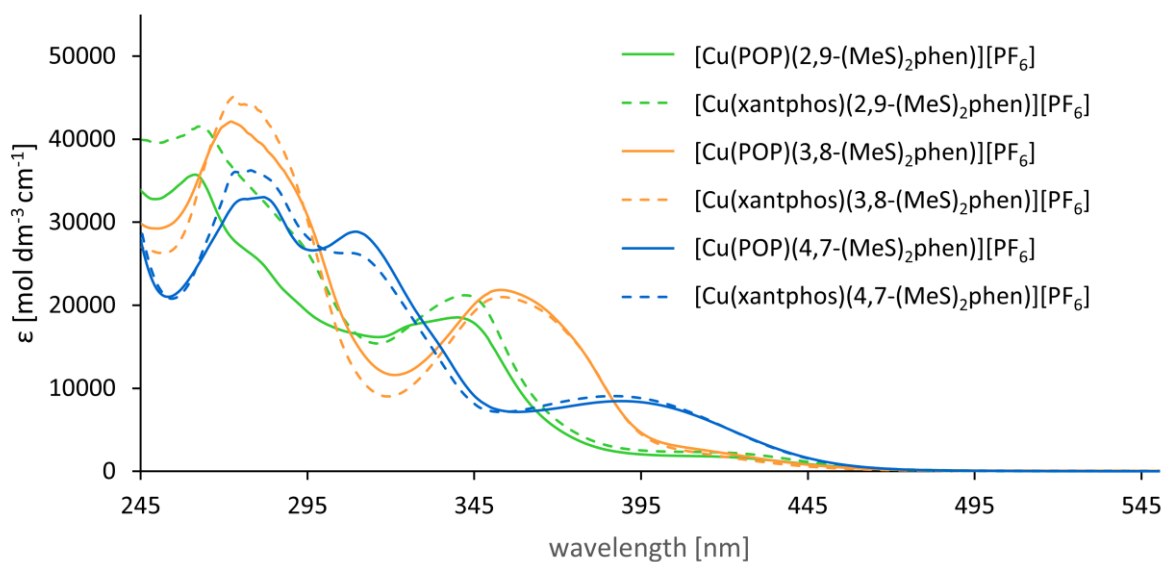


Figure A.6: UV-Vis absorption spectra of $[\text{Cu}(\text{P}^{\wedge}\text{P})((\text{MeS})_2\text{phen})][\text{PF}_6]$ in THF with concentrations in the range of 1.75×10^{-5} – 3.0×10^{-5} M.

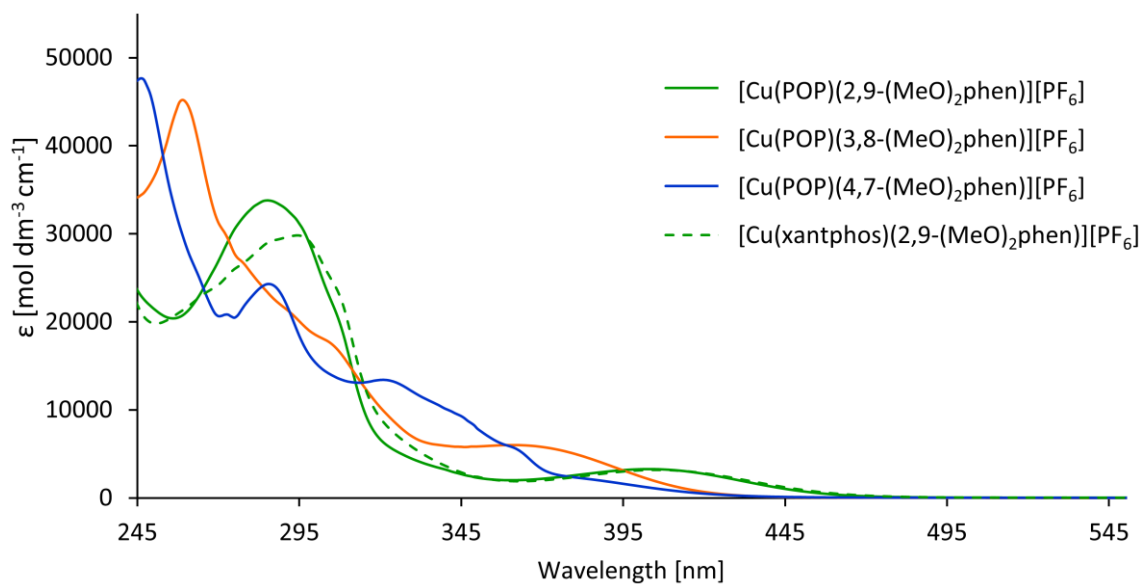


Figure A.7: UV-Vis absorption spectra of $[\text{Cu}(\text{P}^{\wedge}\text{P})((\text{MeO})_2\text{phen})][\text{PF}_6]$ in THF with concentrations in the range of 1.75×10^{-5} – 3.0×10^{-5} M.

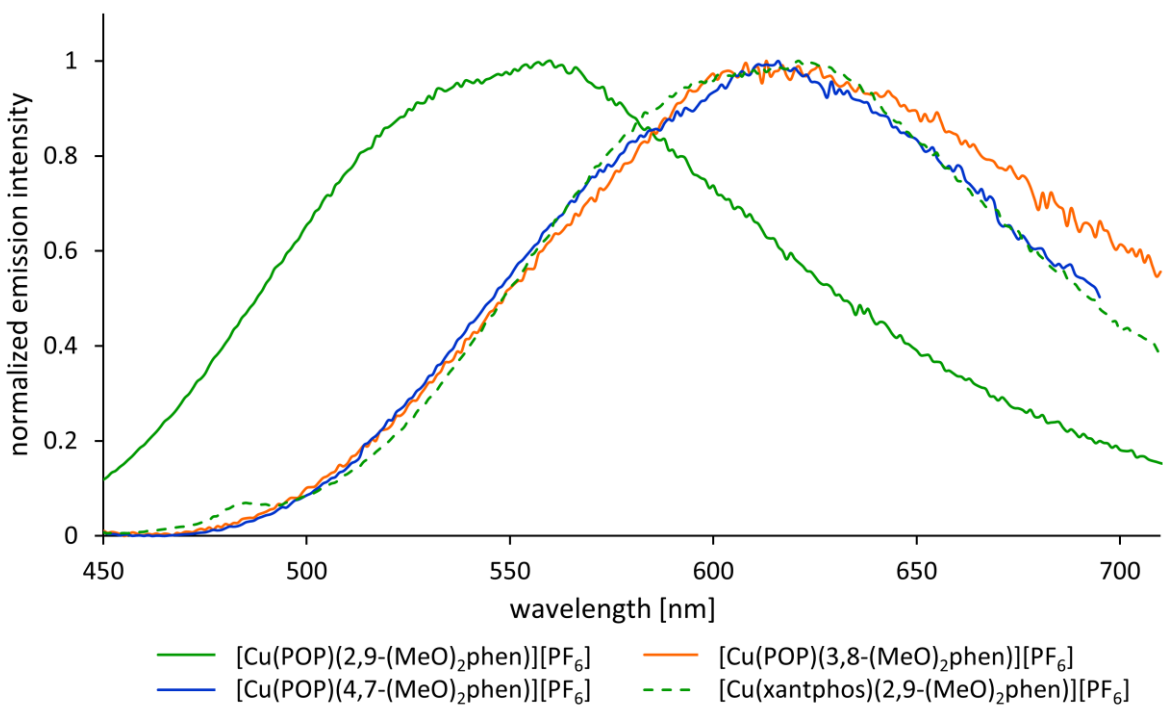


Figure A.8: Normalized solution emission spectra for $[\text{Cu}(\text{P}^{\wedge}\text{P})((\text{MeO})_2\text{phen})][\text{PF}_6]$ in CH_2Cl_2 solution. ($c = 1.75 \times 10^{-5}$ – 3.0×10^{-5} M). λ_{exc} : $[\text{Cu}(\text{POP})(2,9-(\text{MeO})_2\text{phen})][\text{PF}_6] = 410$ nm, $[\text{Cu}(\text{POP})(3,8-(\text{MeO})_2\text{phen})][\text{PF}_6] = 320$ nm, $[\text{Cu}(\text{POP})(4,7-(\text{MeO})_2\text{phen})][\text{PF}_6] = 365$ nm, $[\text{Cu}(\text{xantphos})(3,8-(\text{MeO})_2\text{phen})][\text{PF}_6] = 420$ nm

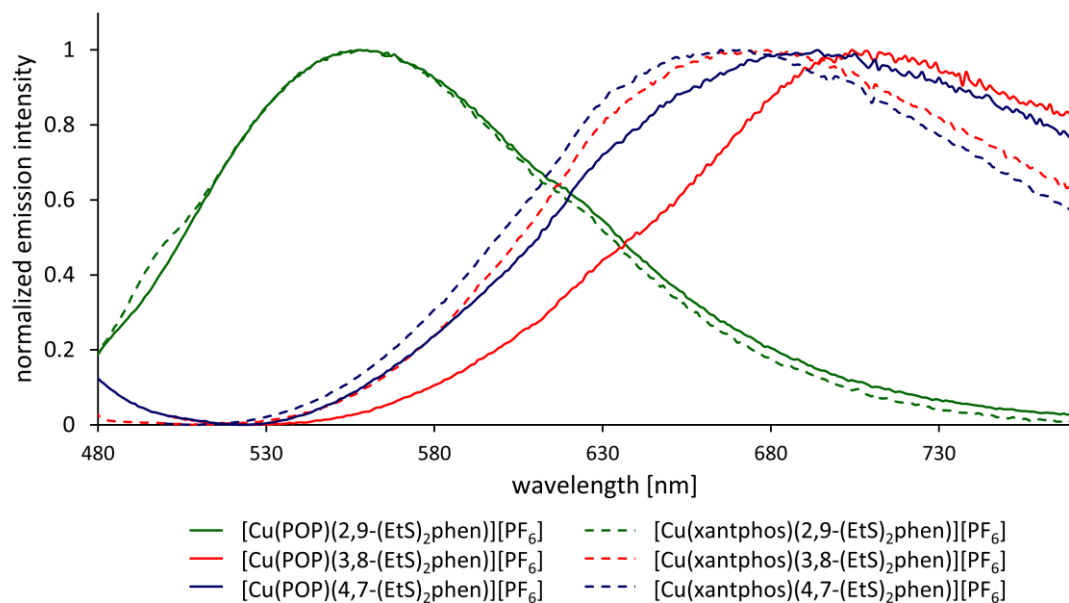


Figure A.9: Normalized solution emission spectra for $[\text{Cu}(\text{P}^{\text{A}}\text{P})(\text{EtS})_2\text{phen}][\text{PF}_6]$ in CH_2Cl_2 solution. ($c = 1.5 \times 10^{-5}$ – 3.0×10^{-5} M). λ_{exc} : $[\text{Cu}(\text{POP})(2,9\text{-(EtS)}_2\text{phen})][\text{PF}_6] = 420$ nm, $[\text{Cu}(\text{POP})(3,8\text{-(EtS)}_2\text{phen})][\text{PF}_6] = 410$ nm, $[\text{Cu}(\text{POP})(4,7\text{-(EtS)}_2\text{phen})][\text{PF}_6] = 400$ nm, $[\text{Cu}(\text{xantphos})(2,9\text{-(EtS)}_2\text{phen})][\text{PF}_6] = 410$ nm, $[\text{Cu}(\text{xantphos})(3,8\text{-(EtS)}_2\text{phen})][\text{PF}_6] = 410$ nm, $[\text{Cu}(\text{xantphos})(4,7\text{-(EtS)}_2\text{phen})][\text{PF}_6] = 395$ nm.

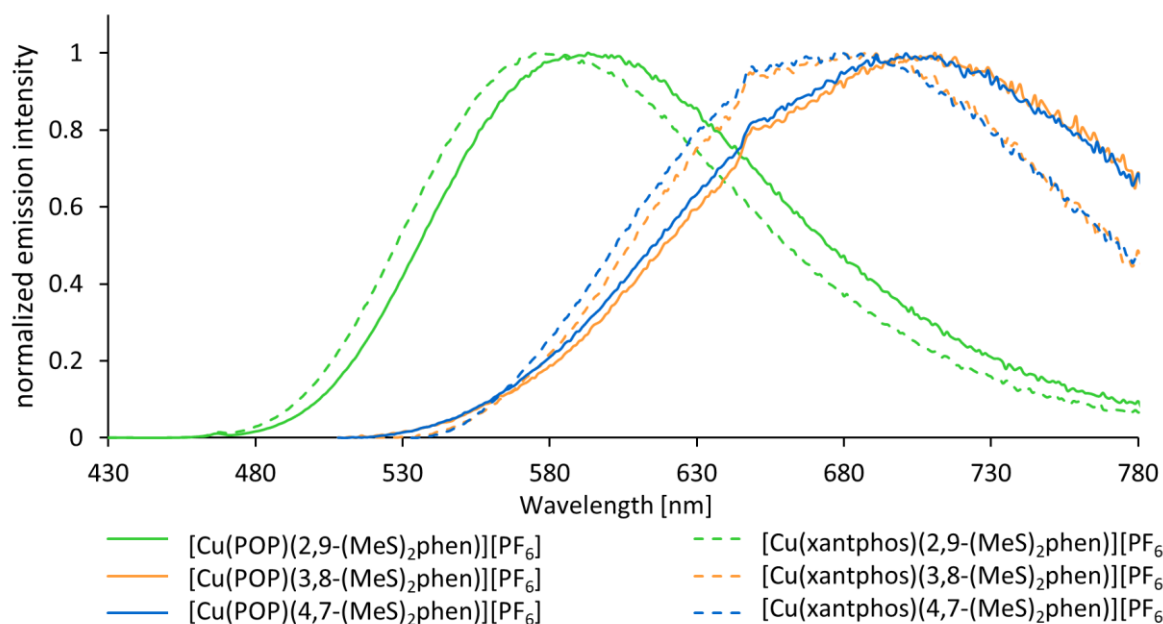


Figure A.10: Normalized solution emission spectra for $[\text{Cu}(\text{P}^{\text{A}}\text{P})(\text{MeS})_2\text{phen}][\text{PF}_6]$ in THF solution. ($c = 1.0 \times 10^{-5}$ – 2.5×10^{-5} M). $\lambda_{\text{exc}} = 410$ nm.

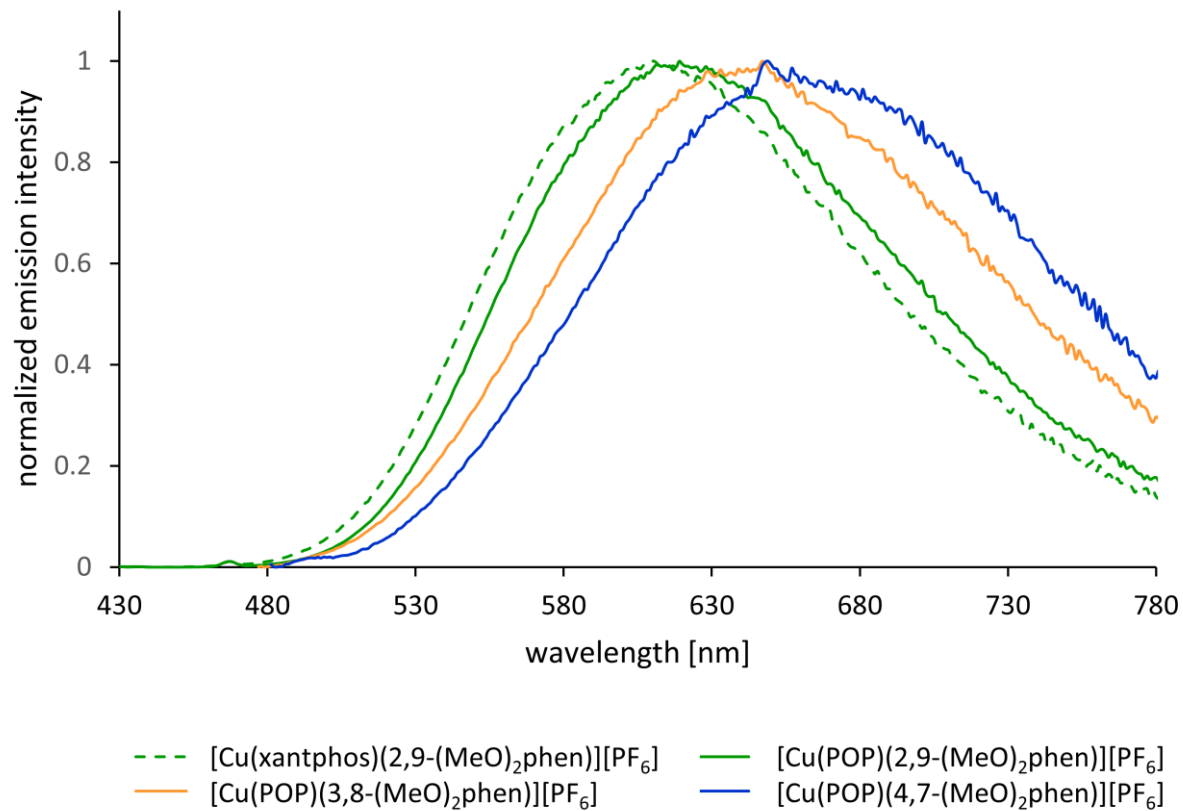


Figure A.11: Normalized solution emission spectra for $[\text{Cu}(\text{P}^{\wedge}\text{P})((\text{MeO})_2\text{phen})][\text{PF}_6]$ in THF solution. ($c = 1.0 \times 10^{-5} - 2.5 \times 10^{-5} \text{ M}$). $\lambda_{\text{exc}} := 410 \text{ nm}$.

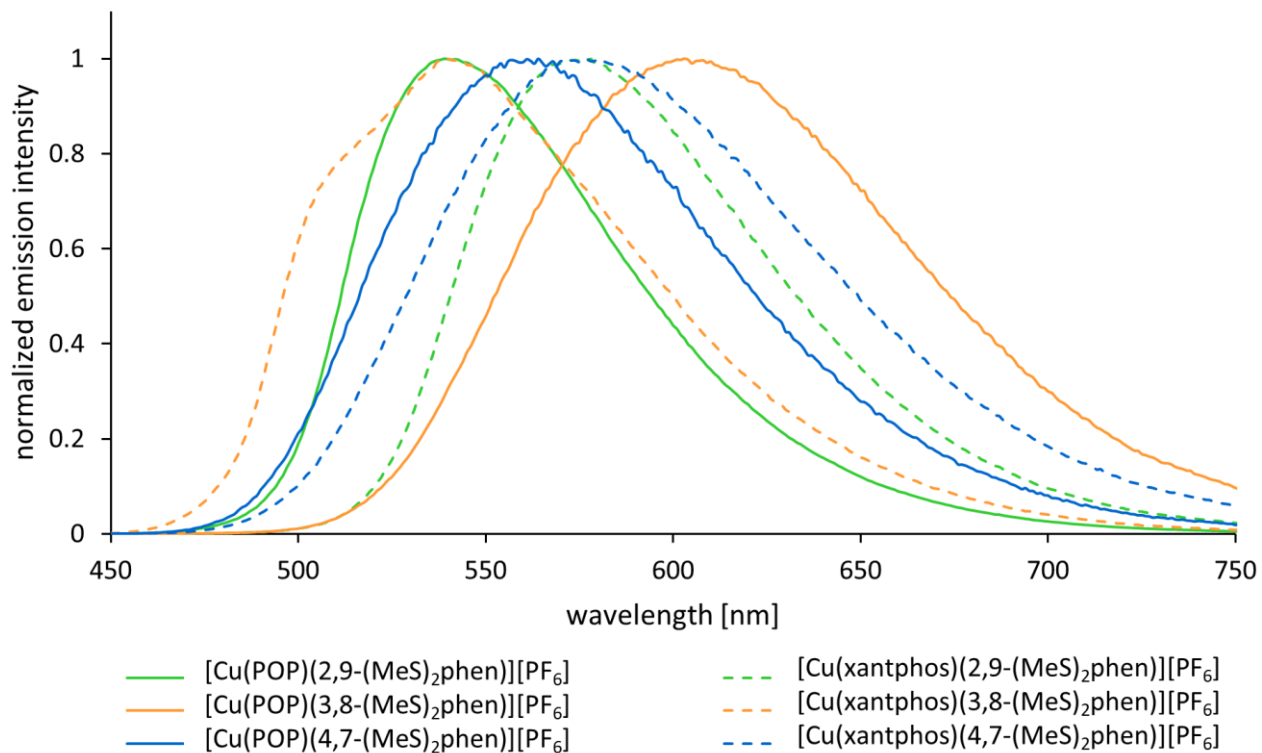


Figure A.12: Normalized emission spectra of powdered samples of $[\text{Cu}(\text{P}^{\wedge}\text{P})((\text{MeS})_2\text{phen})][\text{PF}_6]$. $\lambda_{\text{exc}} = 405 \text{ nm}$.

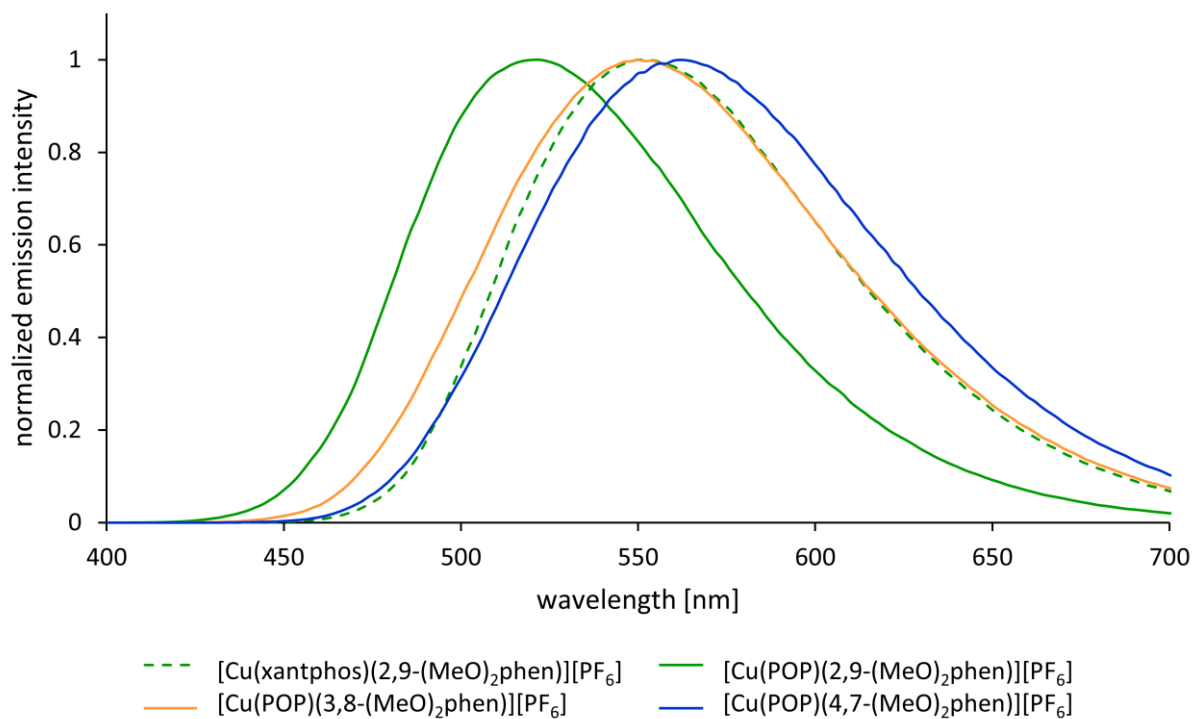


Figure A.13: Normalized emission spectra of powdered samples of $[\text{Cu}(\text{P}^{\wedge}\text{P})((\text{MeO})_2\text{phen})][\text{PF}_6]$. $\lambda_{\text{exc}} = 405 \text{ nm}$; λ_{exc} for $[\text{Cu}(\text{POP})(3,8-(\text{MeO})_2\text{phen})][\text{PF}_6] = 365 \text{ nm}$.

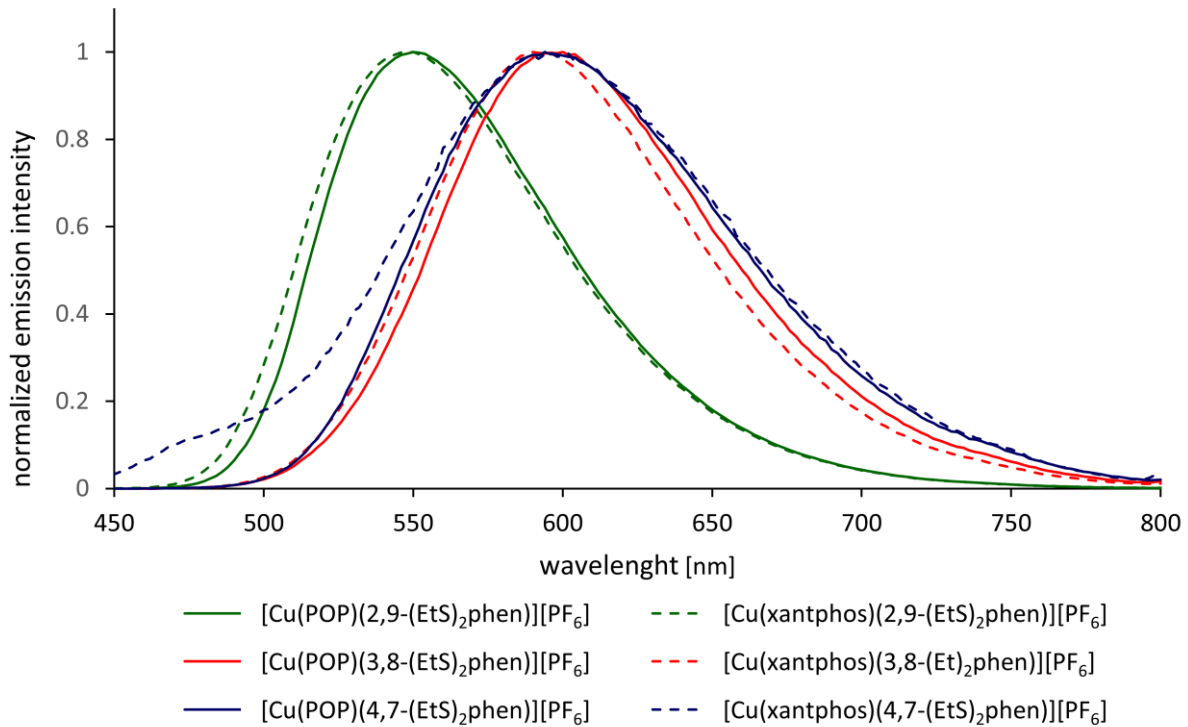


Figure A.14: Normalized emission spectra of powdered samples of $[\text{Cu}(\text{P}^{\wedge}\text{P})((\text{EtS})_2\text{phen})][\text{PF}_6]$. $\lambda_{\text{exc}} = 405 \text{ nm}$.

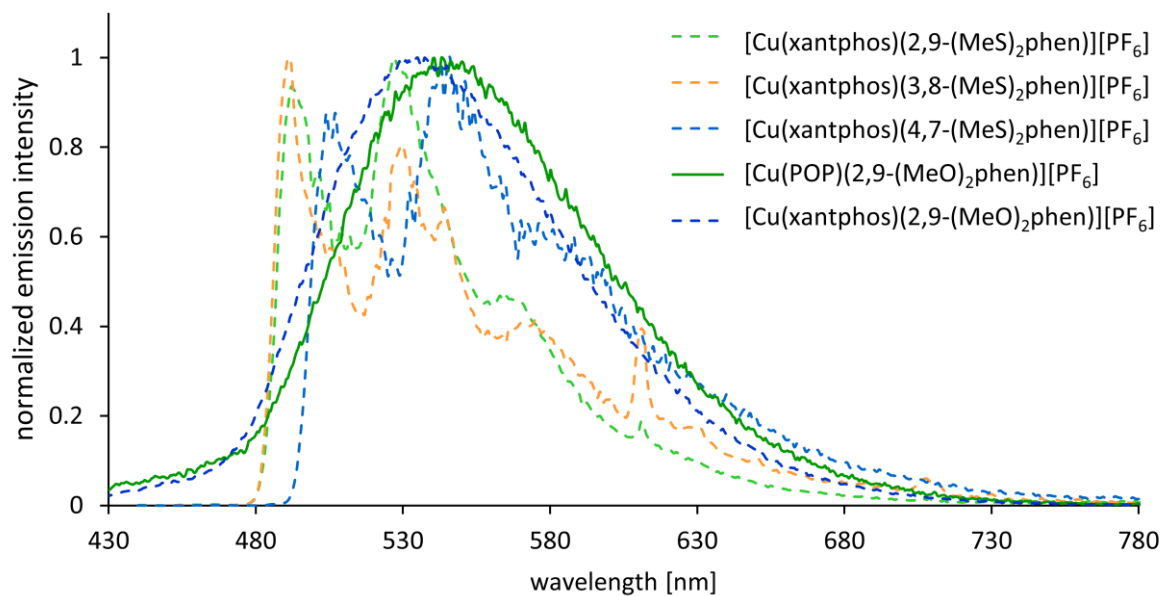


Figure A.15: Normalized frozen matrix emission spectra of $[\text{Cu}(\text{P}^{\wedge}\text{P})((\text{MeX})_2\text{phen})][\text{PF}_6]$ complexes in 2-Me-THF. ($c = 1.75 \times 10^{-5} - 3.0 \times 10^{-5} \text{ M}$). $\lambda_{\text{exc}} = 425 \text{ nm}$.

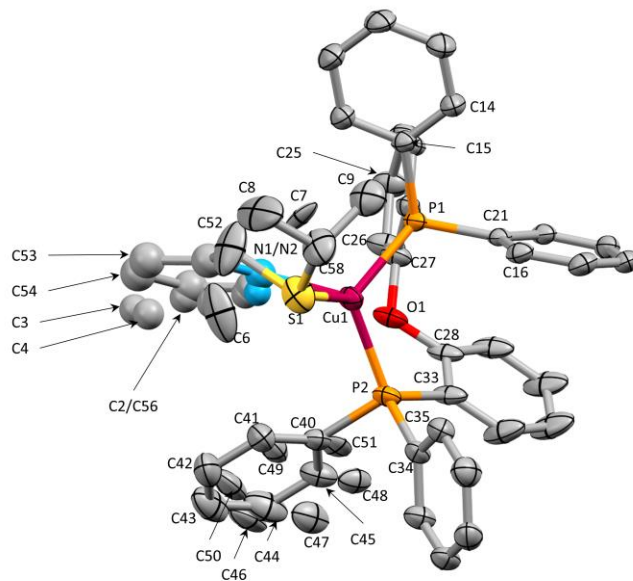


Figure A.16: Cation structure of the $[Cu(POP)(iPrSPy)]^+$ cation with H atoms omitted for clarity at ellipsoids plotted at 40%.

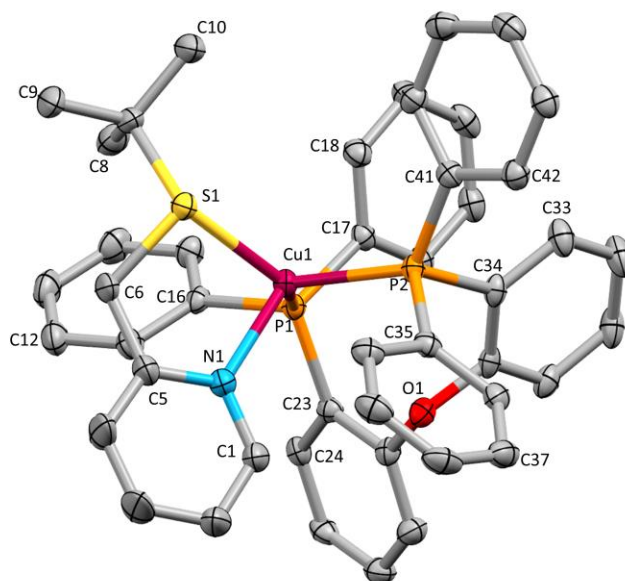


Figure A.17: Cation structure of the $[Cu(POP)(tBuSPy)]^+$ cation with H atoms omitted for clarity at ellipsoids plotted at 40%.

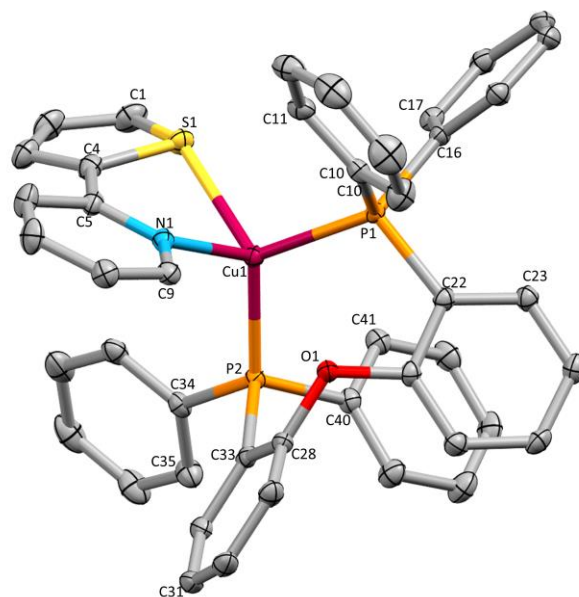


Figure A.18: Cation structure of the $[Cu(POP)(ThPy)]^+$ cation with H atoms omitted for clarity at ellipsoids plotted at 40%.

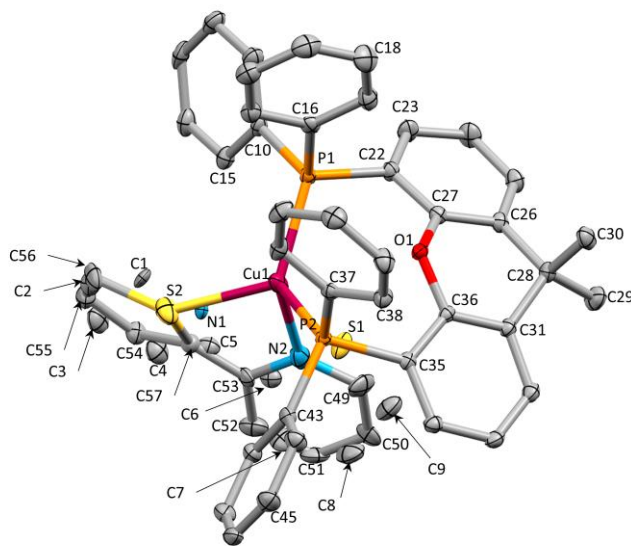


Figure A.19: Cation structure of the $[Cu(xantphos)(ThPy)]^+$ cation with H atoms omitted for clarity at ellipsoids plotted at 40%. The N^S ligand is disordered and has been modeled over 2 sites with 0.75:0.25 occupancy.

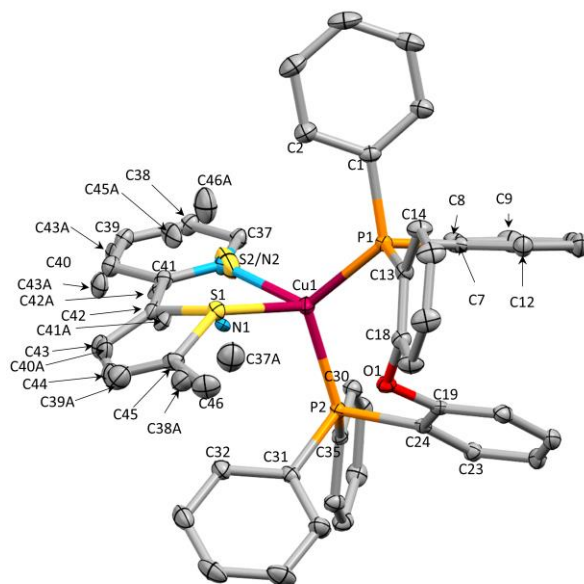


Figure A.20: Cation structure of the $[Cu(POP)(MeThPy)]^+$ cation with H atoms omitted for clarity at ellipsoids plotted at 40%. The N^S ligand is disordered and has been modeled over 2 sites with 0.8:0.2 occupancy.

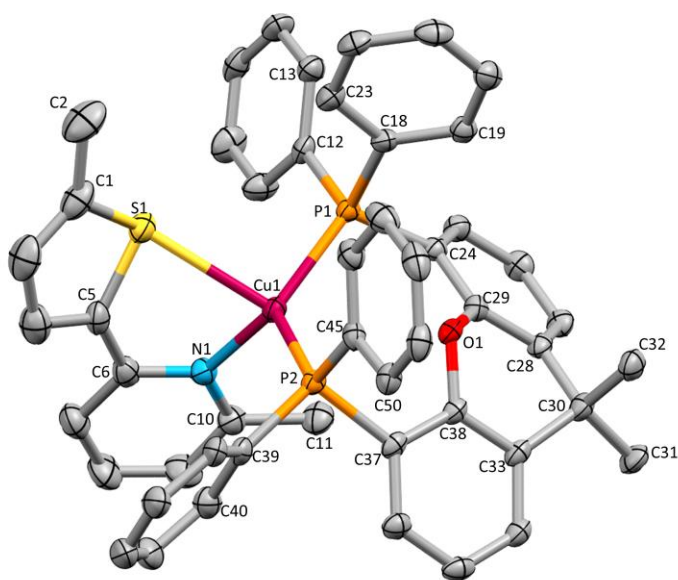


Figure A.21: Cation structure of the $[Cu(xantphos)(MeThMePy)]^+$ cation with H atoms omitted for clarity at ellipsoids plotted at 40%.

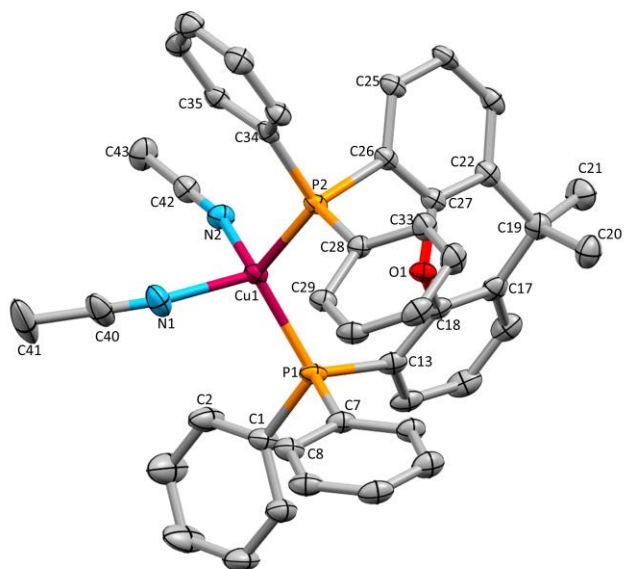


Figure A.22: Cation structure of the $[Cu(xantphos)(MeCN)_2]^+$ cation with H atoms omitted for clarity at ellipsoids plotted at 40%.

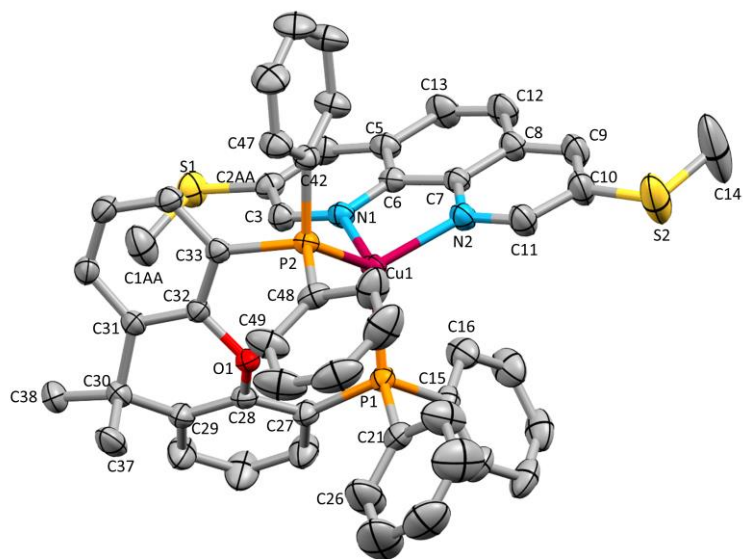


Figure A.23: Cation structure of the $[Cu(xantphos)(3,8-(MeS)_2phen)]^+$ cation with H atoms omitted for clarity at ellipsoids plotted at 40%.

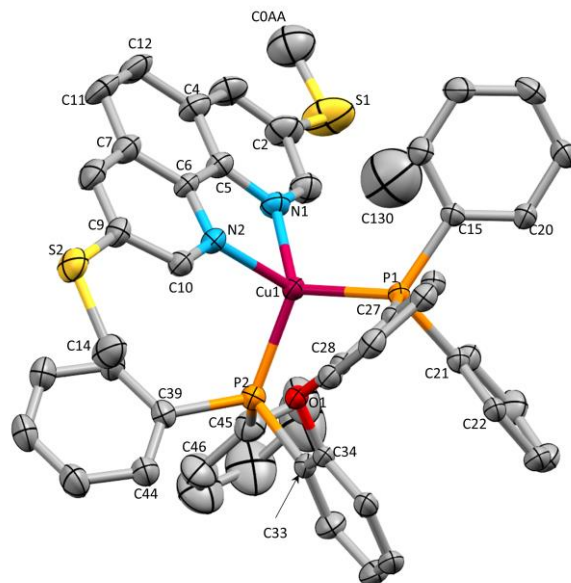


Figure A.24: Cation structure of the $[Cu(POP)(3,8-(MeS)_2phen)]^+$ cation with H atoms omitted for clarity at ellipsoids plotted at 40%.

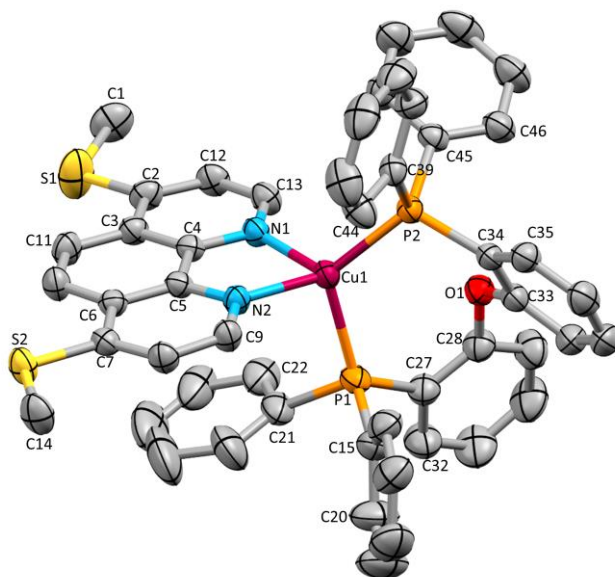


Figure A.25: Cation structure of the $[Cu(POP)(4,7-(MeS)_2phen)]^+$ cation with H atoms omitted for clarity at ellipsoids plotted at 40%.

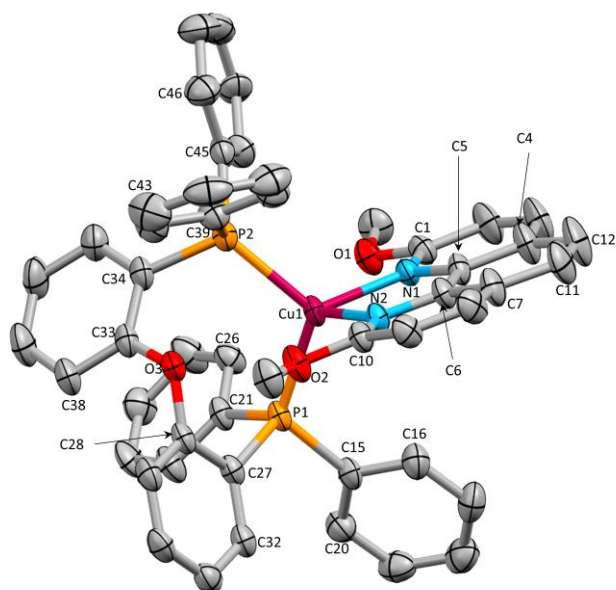


Figure A.26: Cation structure of the $[Cu(POP)(2,9-(MeO)_2phen)]^+$ cation with H atoms omitted for clarity at ellipsoids plotted at 40%.

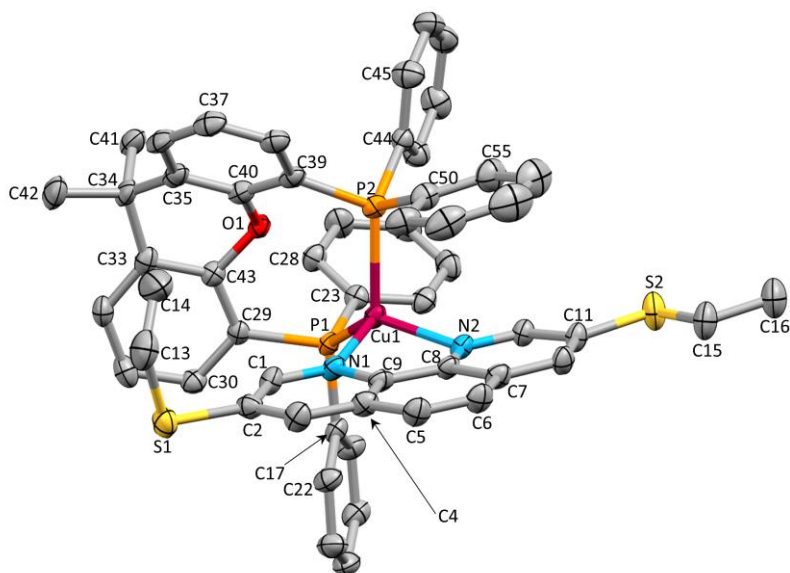


Figure A.27: Cation structure of the $[Cu(xantphos)(3,8-(EtS)_2phen)]^+$ cation with H atoms omitted for clarity at ellipsoids plotted at 40%.

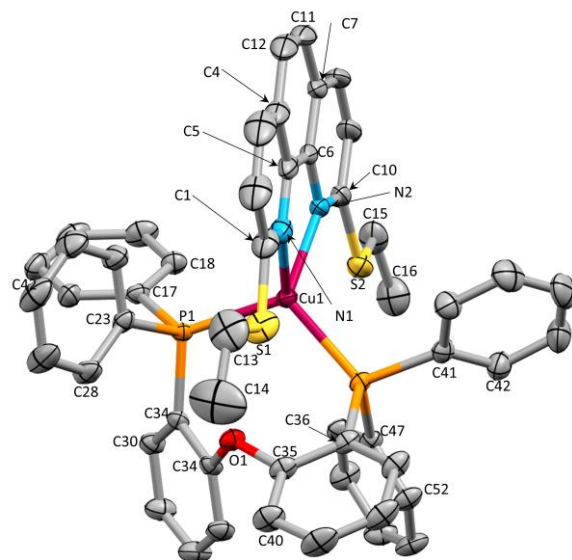


Figure A.28: Cation structure of the $[Cu(POP)(2,9-(EtS)_2phen)]^+$ cation 1 with H atoms omitted for clarity at ellipsoids plotted at 40%.

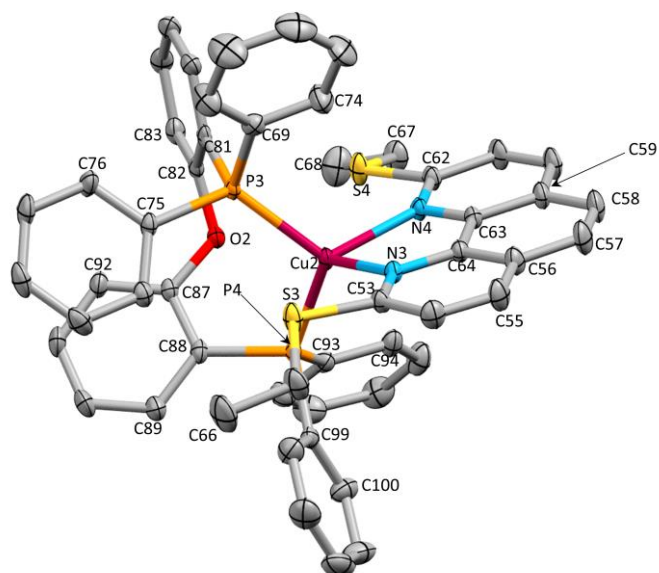


Figure A.30: Cation structure of the $[Cu(POP)(2,9-(EtS)_2phen)]^+$ cation 2 with H atoms omitted for clarity and ellipsoids plotted at 40%.